

Gold(II) Porphyrins as Key Intermediates in Novel Artificial Photosynthetic Systems

Synthesis, Understanding and
Application

Dissertation

Zur Erlangung des Grades
„Doktor der Naturwissenschaften“
im Promotionsfach Chemie

am Fachbereich Chemie, Pharmazie, Geographie
und Geowissenschaften
der Johannes Gutenberg-Universität Mainz

Sebastian Preiß

geboren in Wuppertal

Mainz, 2019

Die vorliegende Arbeit wurde unter Betreuung von [REDACTED] in der Zeit von Oktober 2013 bis Februar 2019 am Institut für Anorganische Chemie und Analytische Chemie der Johannes Gutenberg-Universität Mainz angefertigt.

Mainz, Februar 2019

Dekan: [REDACTED]

1. Berichterstatter: [REDACTED]

2. Berichterstatter: [REDACTED]

Tag der mündlichen Prüfung: 03.05.2019

Ich, Sebastian Preiß, versichere, dass ich meine Promotionsarbeit selbständig verfasst und keine anderen als die angegebenen schriftlichen und elektronischen Quellen, sowie andere Hilfsmittel benutzt habe. Alle Ausführungen, die anderen Schriften wörtlich oder sinngemäß entnommen wurden, habe ich kenntlich gemacht.

Datum:

Unterschrift:

Abstract

As the largest usable energy source for life on earth, the sun supplies an impressive amount of energy of about 1.5×10^{18} kWh per year. The largest proportion of this so-called solar energy is attributed to global warming which guarantees the biological existence in the near-surface area. This is followed by the photosynthesis process, the conversion of solar energy into chemical energy, of algae and plants. Most of the higher life forms (including humans) are directly dependent on this unique energy conversion process, since algae and plants are located at the beginning of the food chain. The elucidation of the underlying chemical reaction, namely the photoinduced electron transfer (PET) inside the reaction centres (RC) of plants, is therefore of great scientific and economical interest. Over the past years, a promising approach to illuminate the first steps of photosynthesis was achieved by the design and preparation of artificial photosynthetic RCs, composed of donor-acceptor model compounds, mimicking the energy conversion process.

In this context, this work aims to elucidate the role of gold(III) porphyrins as a potent cationic electron acceptor in such artificial photosynthetic systems. Particularly, the site of gold(III) porphyrin reduction is discussed controversially in the literature, since it could be ligand centred or metal centred. The approach chosen here was the preparation and characterisation of a *meso*-tetraarylporphyrinato gold(III) cation reference system, bearing functional groups at the aryl substituents with variable electron-donating and electron-withdrawing behaviour (COOMe, COOH, NO₂, NH₂, NHAc, H, O^{*t*}Bu, CF₃) to examine their influence on the site of gold(III) porphyrin reduction. The obtained gold(III) porphyrins were treated with the reducing agent cobaltocene and probed by electron paramagnetic resonance (EPR) spectroscopy to determine the preferred location of the spin density (Au^{II}: 5d⁹ metallo radical; (P^{•-}): organic π -radical anion). Gratifyingly, the chemical one-electron reduction of the gold(III) porphyrins yielded the corresponding gold(II) porphyrin complexes with a characteristic EPR pattern revealing hyperfine coupling to ¹⁹⁷Au and ¹⁴N and is therefore clearly preferred over the porphyrin π -radical anion. However, the broad Au^{II} resonances were superimposed by a sharp resonance, which has been assigned to the porphyrin π -radical anion. During the one-electron reduction of a nitro derivative, an additional radical species was observed and could be assigned to a nitro π -radical anion.

Encouraged by the unexpected high stability of the aforementioned gold(II) porphyrin complexes and to further investigate this usually elusive species, a mononuclear gold(II) porphyrin

was successfully synthesized. This has been achieved via chemical reduction of a gold(III) porphyrin with stoichiometric amounts of KC_8 or cobaltocene and by an excess of 1-benzyl-1,4-dihydronicotinamide (BNAH) in the presence of a base. The latter was employed as an NADH model compound to illustrate the potential mode-of-action of gold(III) porphyrins inside tumor cells, since they are used as potent anti-cancer drugs. Furthermore, it was possible to isolate and purify this mononuclear gold(II) complex by means of recrystallization or sublimation. This enabled the first thorough investigation of a thermodynamically stable mononuclear gold(II) species by using a combination of spectroscopic and theoretical methods. These indicate that the porphyrin macrocycle provides unprecedented stability to the gold(II) core by blocking the usual reaction pathways (dimerization and disproportionation) of other labile gold(II) species. In addition, reactivity studies towards water, acids, oxygen and nitrosobenzene could be realised.

Further, the knowledge obtained from the aforementioned studies has been exploited for the synthesis and examination of three novel amide-bridged donor-acceptor dyads designed to undergo ultrafast PET. For this purpose, zinc(II) porphyrin amino acid derivatives were utilised as chromophores and electron donors and gold(III) porphyrin amino acid derivatives as electron acceptors $[\text{Zn}(\text{P})\text{-Au}^{\text{III}}(\text{P})][\text{PF}_6]$. The individual building blocks were equipped with electron-donating and electron-withdrawing *meso*-aryl groups (4- $\text{C}_6\text{H}_4\text{O}^n\text{Bu}$, 4- $\text{C}_6\text{H}_4\text{CF}_3$) with the intent to influence the driving force of the forward PET and the backward electron transfer (BET). The dyads were synthesized via coupling of free-base amine-substituted porphyrins with cationic gold(III) porphyrin acids by means of the potent coupling agent HATU (2-(7-aza-1H-benzotriazole-1-yl)-1,1,3,3-tetramethyluronium hexafluorophosphate). The intended zinc(II)-gold(III) dyads were obtained via subsequent metalation with zinc(II) acetate dihydrate. The PET processes were successfully investigated via time-resolved spectroscopic techniques and they revealed a charge-shifted (CSh) state $[\text{Zn}(\text{P}^{\bullet+})\text{-Au}^{\text{II}}(\text{P})]^+$ featuring a gold(II) core for all the dyads. Since the transferred electron is located in a σ -type orbital of gold ($5d_{x^2-y^2}$) relative to the porphyrine plane, the direct back-electron transfer to the a_{2u} SOMO of the zinc(II) porphyrin is hindered, resulting in a relatively long lifetime of the CSh state. As a consequence, the CSh states have been successfully exploited for bimolecular reactions with amines as sacrificial electron donors yielding a stable gold(II) species $\text{Zn}(\text{P})\text{-Au}^{\text{II}}(\text{P})$ as confirmed by using a combination of spectroscopic and theoretical methods. Furthermore, this stable gold(II) species was competent to reduce aromatic azides to amines during a photoredox experiment, whereby the initial gold(III) dyad was restored and thus a catalytic cycle was closed.

Zusammenfassung

Die Sonne ist die größte und wichtigste Energiequelle für das Leben auf der Erde und liefert mit ca. 1.5×10^{18} kWh pro Jahr eine beeindruckende Energiemenge. Der größte Teil dieser Sonnenenergie wird der globalen Erwärmung zugeschrieben, welche die biologische Existenz im oberflächennahen Bereich ermöglicht. Darauf folgt der Photosynthese-Prozess, der die Umwandlung von Sonnenenergie in chemische Energie innerhalb von Algen und Pflanzen ermöglicht. Die meisten höheren Lebensformen (einschließlich des Menschen) sind von diesem einzigartigen Prozess der Energieumwandlung abhängig, da sich Algen und Pflanzen am Anfang der Nahrungskette befinden. Die Aufklärung der zugrundeliegenden chemischen Reaktion, des photoinduzierten Elektronentransfers (PET) innerhalb der Reaktionszentren (RC) von Pflanzen, ist daher von großem wissenschaftlichen und ökonomischen Interesse. Ein vielversprechender Ansatz zur Aufklärung der ersten Schritte des photosynthetischen Prozesses wurde in den vergangenen Jahren mit Hilfe von künstlichen RCs ermöglicht. Diese bestehen aus Donor-Akzeptor-Modellverbindungen und können den Energieumwandlungsprozess nachahmen.

In diesem Zusammenhang soll in dieser Arbeit die Rolle von Gold(III)-Porphyrinen als potenter kationischer Elektronenakzeptor in solchen künstlichen Photosynthese-Systemen untersucht werden. Insbesondere wird der Charakter der Gold(III)-Porphyrin-Reduktion in der Fachliteratur bisher kontrovers diskutiert, da diese liganden- oder metallzentriert ablaufen kann. Der hier gewählte Ansatz basiert auf der Darstellung und Charakterisierung eines *meso*-Tetraarylporphyrinato-Gold(III)-Kation Bezugssystems. Dieses besitzt funktionelle Gruppen mit unterschiedlichen elektronenziehenden und -schiebenden Eigenschaften an den Aryl-Substituenten (COOMe, COOH, NO₂, NH₂, NHAc, H, OⁿBu, CF₃), um deren Einfluss auf den Ort der Gold(III)-Porphyrin-Reduktion untersuchen zu können. Die so erhaltenen Gold(III)-Porphyrine wurden mit dem Reduktionsmittel Cobaltocen versetzt und mittels elektronenparamagnetischer Resonanzspektroskopie (EPR) untersucht, um die bevorzugte Lage der Spindichte zu bestimmen (Au^{II}: 5d⁹-Metallradikal; (P^{•-}): organisches π-Radikalanion). Erfreulicherweise ergab die chemische Einelektronen-Reduktion der Gold(III)-Porphyrine die entsprechenden Gold(II)-Porphyrin-Komplexe mit einem charakteristischen EPR-Muster, sowie Hyperfeinkopplungen zu ¹⁹⁷Au und ¹⁴N und ist somit gegenüber einem Porphyrin-π-Radikalanion klar bevorzugt. Allerdings wurden die breiten Au^{II}-Resonanzen von einer scharfen Resonanz überlagert, die dem Porphyrin-π-Radikalanion zugeordnet wurde. Während der Einelektronen-Reduktion des Nitro-Derivates wurde eine zusätzliche Radikalspezies beobachtet, welche einem Nitro-π-Radikalanion zugeordnet werden konnte.

Ermöglicht durch die unerwartet hohe Stabilität der zuvor genannten Gold(II)-Porphyrin-Komplexe, und zur weiteren Untersuchung dieser normalerweise schwer fassbaren Spezies, wurde ein mononuklearer Gold(II)-Porphyrin-Komplex synthetisiert. Dies gelang mittels chemischer Reduktion eines Gold(III)-Porphyrins mit stöchiometrischen Mengen an KC_8 , Cobaltocen oder durch einen Überschuss an 1-Benzyl-1,4-dihydrinicotinamid in Gegenwart einer Base. Letzteres wurde als NADH-Modellverbindung eingesetzt, um die mögliche Wirkungsweise von Gold(III)-Porphyrinen in Tumorzellen zu veranschaulichen, da diese als wirksame Krebsmedikamente eingesetzt werden. Außerdem konnte dieser einkernige Gold(II)-Komplex mittels Sublimation oder Rekristallisation isoliert und gereinigt werden. Dies ermöglichte die erste tiefgehende Untersuchung einer thermodynamisch stabilen mononuklearen Gold(II)-Spezies mittels spektroskopischer und theoretischer Methoden. Diese deuten darauf hin, dass der Porphyrin-Makrozyklus dem Gold(II)-Kern eine beispiellose Stabilität verleiht, indem die üblichen Reaktionspfade anderer labiler Gold(II)-Spezies (Dimerisierung und Disproportionierung) blockiert werden. Darüber hinaus konnten Reaktivitätsuntersuchungen gegenüber Wasser, Säuren, Sauerstoff und Nitrosobenzol durchgeführt werden.

Die Erkenntnisse aus den oben genannten Studien wurden für die Synthese und Untersuchung von drei neuartigen Amid-verbrückten Donor-Akzeptor Dyaden genutzt, um einen sehr schnellen PET zu ermöglichen. Zu diesem Zweck wurden Zink(II)-Porphyrin-Aminosäurederivate als Chromophore und Elektronendonatoren und Gold(III)-Porphyrin-Aminosäurederivate als Elektronenakzeptoren verwendet $[\text{Zn}(\text{P})-\text{Au}^{\text{III}}(\text{P})][\text{PF}_6]$. Die einzelnen Bausteine wurden mit elektroschiebenden und -ziehenden *meso*-Aryl-Gruppen ($4\text{-C}_6\text{H}_4\text{O}^n\text{Bu}$, $4\text{-C}_6\text{H}_4\text{CF}_3$) ausgestattet, um die Triebkraft des vorwärts gerichteten PETs und des rückwärts gerichteten Elektronentransfers (BET) beeinflussen zu können. Die Dyaden wurden mittels Kupplung von „free-base“-aminsubstituierten Porphyrinen mit kationischen Gold(III)-Porphyrin-Säuren unter Zuhilfenahme des potenten Kupplungsreagenzes HATU (*O*-(7-Azabenzotriazol-1-yl)-*N,N,N',N'*-tetramethyluroniumhexafluorophosphat) synthetisiert. Die gewünschten Zink(II)-Gold(III)-Dyaden wurden durch anschließende Metallierung mit Zink(II)-Acetat Dihydrat erhalten. Die PET-Prozesse wurden erfolgreich mittels zeitaufgelösten spektroskopischen Methoden verfolgt und offenbarten für alle Dyaden einen ladungsverschobenen (CSh) Zustand $[\text{Zn}(\text{P}^{\bullet+})-\text{Au}^{\text{II}}(\text{P})]^+$ mit einem Gold(II)-Kern. Da sich das transferierte Elektron in einem σ -artigen Orbital ($5d_{x^2-y^2}$) von Gold (relativ zur Porphyrin-Ebene) befindet, ist der direkte Elektronen-Rücktransport zum a_{2u} SOMO des Zink(II)-Porphyrins gehemmt, was zu einer relativ langen Lebensdauer des CSh-Zustands führt. Infolgedessen

wurden die CSh-Zustände erfolgreich für bimolekulare Reaktionen mit Aminen als Opferelektroendonatoren eingesetzt, was in einer stabilen Gold(II)-Spezies $\text{Zn(P)-Au}^{\text{II}}(\text{P})$ resultierte. Darüber hinaus konnte diese Gold(II)-Dyade erfolgreich für die Reduktion von aromatischen Aziden während eines Photoredox-Experimentes verwendet werden, wobei die anfängliche Gold(III)-Dyade regeneriert und somit ein katalytischer Zyklus geschlossen wurde.



Contents

Abstract	I
Zusammenfassung	III
Contents	VII
Abbreviations	IX
1 Introduction	1
1.1 Porphyrins	2
1.1.1 <i>Photophysical Properties of Porphyrins</i>	3
1.1.2 <i>Synthetic Routes to Artificial Porphyrins</i>	6
1.2 Mononuclear Gold(II) Complexes	10
1.2.1 <i>Mononuclear Open-Shell Gold(II) Complexes</i>	12
1.2.2 <i>Suggested Mononuclear Gold(II) Complexes</i>	14
1.3 The Electron Transfer Process	16
1.3.1 <i>The Marcus Theory of Electron Transfer</i>	16
1.3.2 <i>The Marcus-Hush Theory of Electron Transfer</i>	19
1.4 Photosynthesis	22
1.4.1 <i>Primary Processes in Photosynthesis</i>	23
1.4.2 <i>From Natural to Artificial Photosynthesis</i>	26
2 Aim of Work	31
3 Results and Discussion	33

3.1	Gold(III) tetraarylporphyrin amino acid derivatives: ligand or metal centred redox chemistry?	35
3.2	Structure and reactivity of a mononuclear gold(II) complex	51
3.3	Gold(II) porphyrins in photoinduced electron transfer reactions	59
3.4	Intrinsic superoxide dismutase activity of MnO nanoparticles enhances the magnetic resonance imaging contrast	71
4	Summary and Outlook	79
5	References	85
6	Appendix	91
6.1	Supporting Information to 3.1: Gold(III) tetraarylporphyrin amino acid derivatives: ligand or metal centred redox chemistry?	91
6.2	Supporting Information to 3.2: Structure and reactivity of a mononuclear gold(II) complex	107
6.3	Supporting Information to 3.3: Gold(II) porphyrins in photoinduced electron transfer reactions	141
6.4	Supporting Information to 3.4: Intrinsic superoxide dismutase activity of MnO nanoparticles enhances magnetic resonance imaging contrast	173
7	Acknowledgements	183
8	Curriculum Vitae	185
8.1	List of Publications	187
8.2	Conference Contributions	188

Abbreviations

ΔG^*	activation energy
ΔG°	Gibbs free energy
δ	chemical shift (NMR) [ppm]
ϵ	molar extinction coefficient [$M^{-1} \text{ cm}^{-1}$]
λ	wavelength or reorganisation energy depending on the context
Φ	quantum yield
τ	fluorescence lifetime
A	acceptor or relative amplitude depending on the context
Ac	acetyl
Ar	aryl substituent
a.u.	arbitrary units
B	bridge
BNAH	1-benzyl-1,4-dihydronicotinamide
Bu	butyl
calcd.	calculated
$^\circ\text{C}$	degree Celsius
CDCl_3	deuterated chloroform
Cp	cyclopentadienyl
COSY	correlated spectroscopy
CR	charge recombination
CS	charge separation
CSh	charge shift
CV	cyclic voltammetry
D	donator
DDQ	2,3-dichloro-5,6-dicyano-1,4-benzoquinone
DFT	Density Functional Theory
DMF	dimethylformamide
$E_{1/2}$	halfwave potential
e.g.	<i>exempli gratia</i> (for example)
EnT	energy transfer
eq.	equivalent

V	electronic coupling matrix element
EPR	electron paramagnetic resonance
ESI	electrospray ionization (mass spectrometry)
ET	electron transfer
eV	electron volt
Fc	ferrocenyl (C ₅ H ₄ FeC ₅ H ₅)
FD	field desorption (mass spectrometry)
g	gram
G	Gauss
<i>g</i>	<i>g</i> -value (EPR)
h	hour
HATU	2-(7-aza-1H-benzotriazole-1-yl)-1,1,3,3-tetramethyluronium hexafluorophosphate
HOMO	highest occupied molecular orbital
HMBC	heteronuclear multiple bond correlation (NMR)
HSQC	heteronuclear single quantum coherence (NMR)
HR	high resolution (mass spectrometry)
IC	internal conversion
IR	infrared
IVCT	intervalence charge transfer
ISC	intersystem crossing
ⁿ <i>J</i>	coupling constant (NMR)
<i>k</i>	rate constant
K	Kelvin
<i>k</i> _B	Boltzmann constant = 1.381×10 ⁻²³ [J/K]
L	liter
LHC	light-harvesting antenna complex
LUMO	lowest unoccupied molecular orbital
m	milli
M	molarity or metal depending on the context
M ⁺	metal cation or base peak depending on the context
Me	methyl
MS	mass spectrometry
<i>m/z</i>	mass-to-charge ratio

NADH	nicotinamide adenine dinucleotide
NADP ⁺	nicotinamide adenine dinucleotide phosphate
NADPH	reduced form of NADP ⁺
NIR	near infrared
nm	nanometer
NMR	nuclear magnetic resonance spectroscopy
ns	nanosecond
P	porphyrin or product depending on the context
PET	photoinduced electron transfer
Ph	phenyl
ppm	parts per million
q	reaction coordinate
R	reactant
RC	reaction centre
ROS	reactive oxygen species
S	singlet state
SP	“special pair”
SWV	squarewave voltammetry
T	temperature or triplet state depending on context
TEA	triethylamine
TFA	trifluoroacetic acid
TPP	tetraphenylporphyrinato(2-)
UV	ultra-violet (light)
Vis	visible (light)
$\tilde{\nu}$	wavenumber
XANES	X-ray absorption near edge structure
XRD	X-ray diffraction

1 Introduction

The elegantly constructed porphyrinoid ligand has been selected in the course of evolution as the key functional pigment without which life itself could not be maintained.^[1] For instance, the iron-porphyrin complexes hemoglobin and myoglobin are involved in dioxygen uptake inside the lungs, transport in the blood stream and subsequent storage in the muscle tissue.^[2-4] Its role in photosynthesis, the probably most important biochemical process on earth for life, is even more essential and unique. Chlorophylls and bacteriochlorophylls, which possess a porphyrinoid backbone, are involved in light harvesting, energy transfer, charge separation and electron transport.^[5-8] These complexes (see **Figure 1.1**) belong to the most prominent bioinorganic compounds and their organic syntheses as well as their structural and functional examinations were therefore rewarded with Nobel Prizes in Chemistry. For instance, J. Deisenhofer, R. Huber and H. Michel in 1988 for their X-ray structure examinations of a heme- and bacteriochlorophyll-containing photosynthetic reaction centre from purple bacteria.^[2,8]

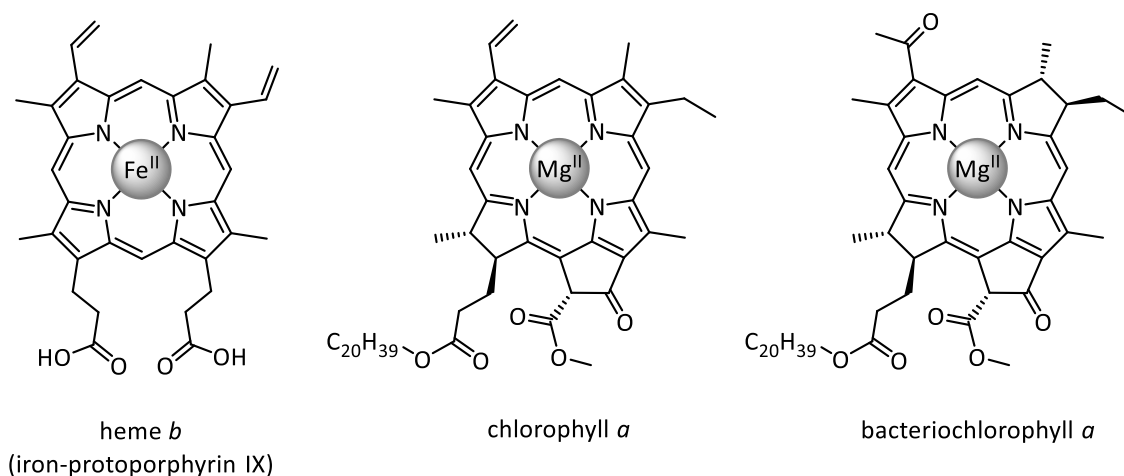


Figure 1.1 Heme *b*, chlorophyll *a* and bacteriochlorophyll *a*.

A large part of the enhanced endeavours to understand the molecular mechanisms of photosynthesis and to make that knowledge utilizable for mankind results from our dependence on unsustainable and potentially dangerous energy sources, such as fossil fuels or nuclear power.^[2]

The rational design of porphyrin-based artificial photosynthesis systems is directly linked with a profound understanding of the photophysical properties and the molecular structure of the porphyrin macrocycle. Hence, this will be further discussed in the following section.

1.1 Porphyrins

The simplest porphyrin is porphine, which follows the general IUPAC nomenclature of tetrapyrroles^[9] (see **Figure 1.2**) and represents the skeleton of naturally occurring and synthetic porphyrin macrocycles. The first synthesis was reported by Fischer in 1936, who prepared porphine by adding pyrrole- α -aldehyde to boiling formic acid.^[10,11]

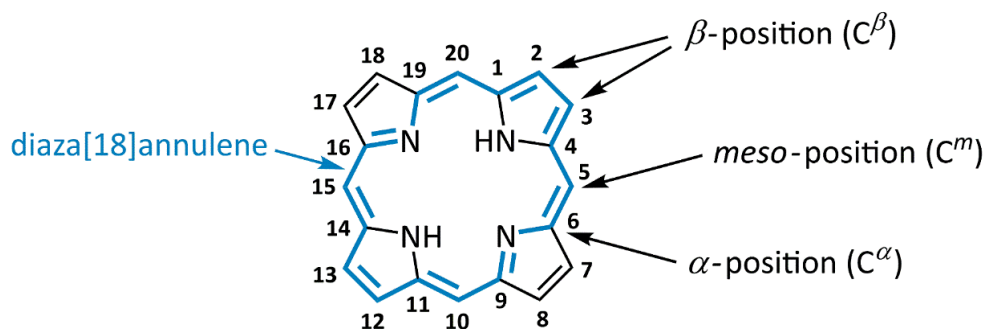


Figure 1.2 Porphine structure, IUPAC nomenclature and illustration of the aromatic diaza[18]annulene system (indicated in blue).

The core structure consists of four pyrrole units joined together via methine bridges and contains a particularly stabilized cyclic heteroaromatic π -system, including 18 delocalized π -electrons in the inner 16-membered ring. Therefore, it fulfills the $(4n+2)$ Hückel rule for aromaticity and can be described as diaza[18]annulene.^[12] As a consequence, the nearly planar ring system possesses a significant thermal stability, as indicated by the presence of porphyrin complexes in sediments or crude mineral oil.^[2,13,14]

Porphyrin is a prototypical amphoteric compound. The basic character is most obvious by the formation of the stable and doubly protonated $[H_4P]^{2+}$ form.^[15] The acidic nature of the porphyrin is given by the loss of the inner NH protons to form the dianion $[P]^{2-}$ and subsequent complexation of even substitutionally labile divalent metal ions like Mg^{2+} or Ca^{2+} .^[16] The stability of the resulting tetradentate chelate complexes can be readily justified, since dissociation is only possible if the M-L bonds are broken simultaneously, which is not probable.^[2]

The conjugated π -system leads to a narrowing of the π frontier orbital gap, which facilitates the uptake and release of electrons and consequently, porphyrins can behave “non-innocently”, resulting in quite stable anion or cation radical complexes. This redox behavior is essential regarding the most important biological processes, such as photosynthesis or the cytochrome-P450 monooxygenase reactions of xenobiotic substances.^[2,17,18]

1.1.1 Photophysical Properties of Porphyrins

Porphyrins are very rich coloured, bioactive compounds, which led to their description as “pigments of life”.^[2] They show a characteristic absorption pattern, dominated by π - π^* transitions, namely the very intense B band (or so-called Soret band) in the near UV region and multiple relatively weak Q bands in the visible part of the spectrum. The UV/vis absorption spectra of the free-base porphyrin *meso*-tetraphenylporphyrin ($H_2(TPP)$) and the metalloporphyrin zinc(II) *meso*-tetraphenylporphyrin ($Zn(TPP)$) are exemplarily illustrated in **Figure 1.3**.

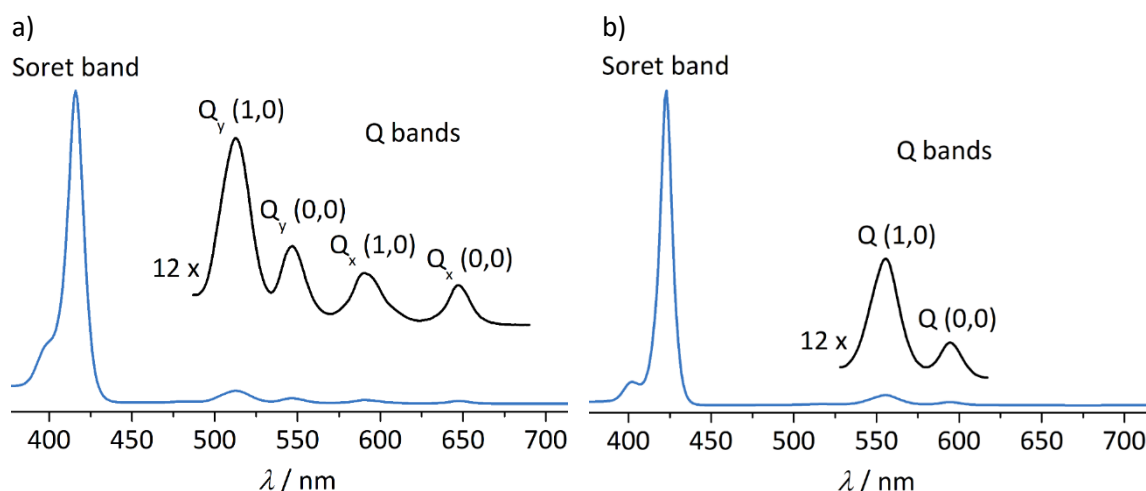


Figure 1.3 UV/vis absorption spectra of a) $H_2(TPP)$ and b) $Zn(TPP)$ in THF at room temperature.

The significant absorption features can be successfully described via π - π^* transitions between the porphyrins' two highest occupied (HOMO and HOMO-1) and two lowest unoccupied (LUMO and LUMO+1) frontier orbitals as demonstrated in **Figure 1.4**, according to Gouterman's four-orbital model.^[19–21] In D_{4h} -symmetric metalloporphyrin chromophores, the two HOMOs possess a_{2u} and a_{1u} symmetry with accidentally similar energies (a_{2u} having a slightly higher energy), while the two LUMOs are degenerate and can be labelled $e_{g,x}$ and $e_{g,y}$ to distinguish their orientation. Additionally, Gouterman introduced the more general notations b_1/b_2 for the HOMOs and c_1/c_2 for the LUMOs to consider lower symmetric systems, such as D_{2h} free-base porphyrin chromophores (see **Figure 1.5a**).^[20]

The four possible electronic transitions between the frontier orbitals result in two degenerate excited states with x-polarisation, namely $^1(a_{1u}, e_{g,y})$ and $^1(a_{2u}, e_{g,x})$ and two degenerate excited states with y-polarisation, $^1(a_{1u}, e_{g,x})$ and $^1(a_{2u}, e_{g,y})$. Due to similar symmetry and energy levels, the excited states are capable of mixing, which results in two degenerate high energy

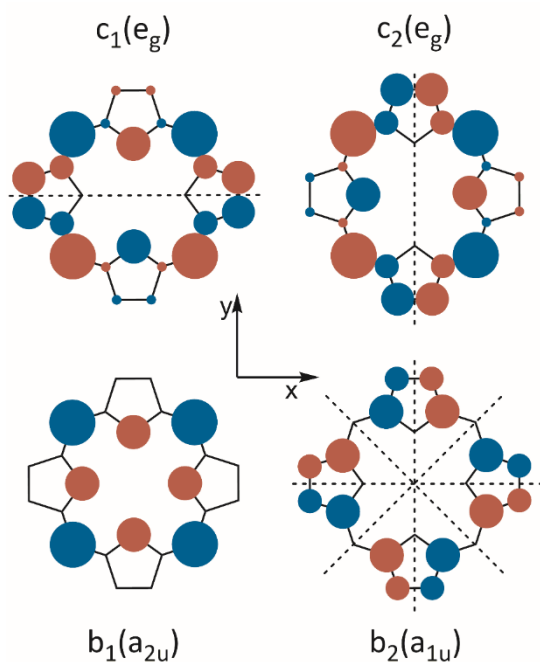


Figure 1.4 The frontier orbitals relevant to the Gouterman's four orbital model.

transitions (${}^1E_{u,a}$) with parallel transition dipoles leading to the intense Soret or rather B_x/B_y absorption and two degenerate low energy transitions (${}^1E_{u,b}$) which possess anti-parallel transition dipoles leading to the low intensity Q_x/Q_y absorption, as shown in **Figure 1.5b**. A further Q-band transition, assigned to a vibrational overtone, often increases the number of Q bands detected.^[22]

Regarding the free-base porphyrins absorption spectra, it has to be considered that they possess lower D_{2h} symmetry, due to the two protons, which are connected to the two nitrogen atoms

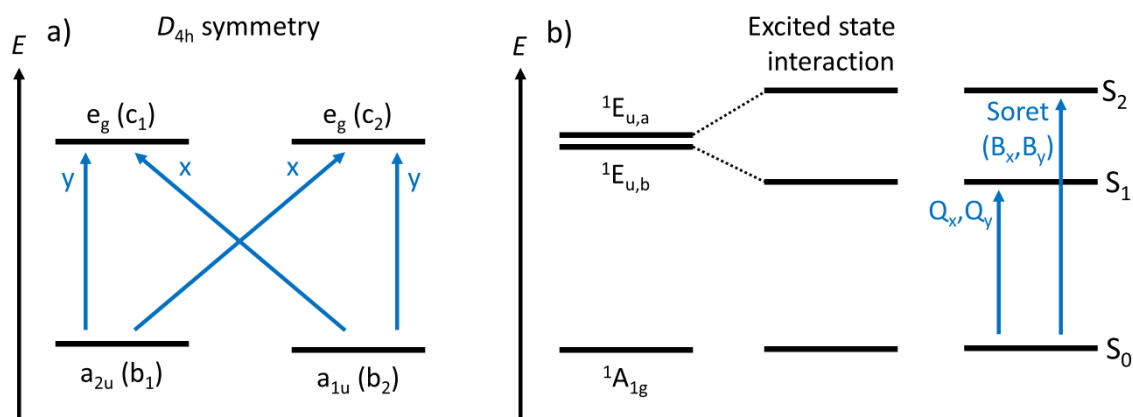


Figure 1.5 a) Schematic orbital description of possible electronic transitions for D_{4h} symmetric metalloporphyrins, such as Zn(TPP); b) molecular energy levels involved in the electron transitions, which generate the prototypical absorption pattern of metalloporphyrins.

and subsequently break the LUMO c_1/c_2 degeneracy. The c_2 level is stabilized as compared to c_1 , resulting in the separation of the Q_x/Q_y and B_x/B_y bands, respectively. In conjunction with the vibronic progression one can detect four Q bands as shown in **Figure 1.3a**, whereas the B_x/B_y energy splitting is usually too small to be observed.^[23]

Additionally, metalloporphyrins can be divided in three classes of electronic spectra: *normal*, *hypso* and *hyper*. The *hyper* spectra can be further divided into d-type and p-type depending on occupation and energy levels of the d-orbitals of the particular metal inside the porphyrin ligand.^[24–26]

Normal spectra are observed for metalloporphyrins with metals having d^0 or d^{10} configuration (for instance Mg^{2+} or Zn^{2+}). Due to the weak interaction of the metal with the a_{2u} and e_g orbitals, only small shifts of the B and Q band positions are observed. Furthermore, the a_{1u} orbital has nodes at the coordinating nitrogen atoms (see **Figure 1.4**) and consequently there is no interaction with the metal orbitals. As a result, the absorbances arise primarily from coupling of the $\pi-\pi^*$ electron transitions between the HOMOs and LUMOs, as mentioned before.^[24]

Hypso spectra resemble *normal* porphyrin spectra but the Q-bands are blue shifted to wavelengths of less than 570 nm for transition metals with d^6 to d^9 configuration having $e_g(d_{xz}, d_{yz})$ orbitals partially filled. Popular examples are Rh^{2+} , Pd^{2+} , Pt^{2+} , Cu^{2+} and Au^{3+} .^[24,25,27] One can explain the hypsochromic shift via mixing of the $e_g(\pi^*)$ LUMOs of the porphyrin ligand with the filled $e_g(d_{xz}, d_{yz})$ metal orbitals as exemplarily shown for Cu^{2+} (d^9) in **Figure 1.6**. This interaction

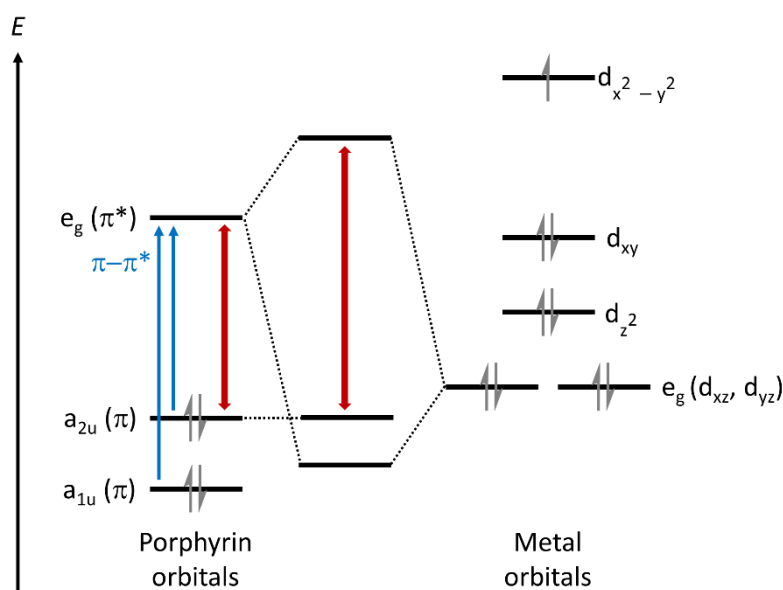


Figure 1.6 Schematic illustration of important orbitals for *hypso* metalloporphyrins showing the interaction between TPP^{2-} and Cu^{2+} (d^9).

raises the energy of the porphyrin LUMOs resulting in a larger $\pi-\pi^*$ energy gap (red arrows) and may be characterized as metal-to-ligand π -backbonding. The largest blue shifts are observed for 4d and 5d metals, due to a better orbital overlap.^[24]

The optical spectra of *hyper* porphyrins show another intense charge transfer absorption in the near UV region, in addition to Soret and Q bands. D-type *hyper* spectra are common for d^1 to d^6 transition metal ions, e.g. Cr^{3+} , Mn^{3+} , Fe^{3+} , with vacancies in the $e_g(d_{xz}, d_{yz})$ orbitals and low reduction potentials concerning the change of metal oxidation state. Here, one can observe extra bands via a ligand-to-metal charge transfer (LMCT) with $a_{1u}(\pi), a_{2u}(\pi) \rightarrow e_g(d_{xz}, d_{yz})$ character. On the contrary, p-type *hyper* spectra are observed for metalloporphyrins with main group elements, e.g. Sn^{2+} , Pb^{2+} , As^{2+} , Sb^{3+} , in low oxidation states. The extra bands are of $a_{2u}(np_z) \rightarrow e_g(\pi^*)$ character and can be described as metal-to-ligand charge transfer (MLCT).^[24,25]

1.1.2 Synthetic Routes to Artificial Porphyrins

Three main types of porphyrins can be distinguished, concerning the substitution pattern: β -substituted, *meso*-substituted and *dodeca*-substituted porphyrins as illustrated in **Figure 1.7**.

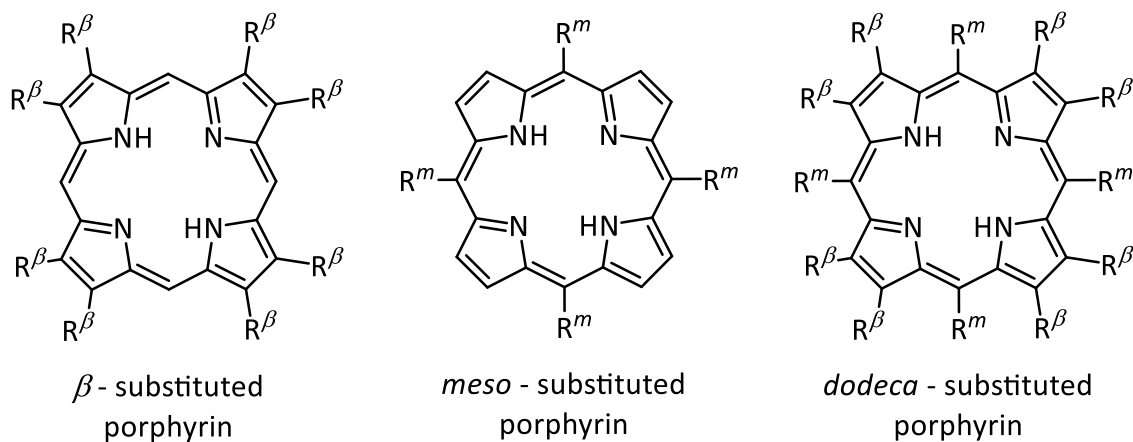


Figure 1.7 Distinct substitution patterns of porphyrins.

From a historical point of view, the primary studies by Küster, Stoll, Willstätter and Fischer entirely focused on naturally occurring chlorophylls, hemes and their structural elucidation. This was followed by Fischer's total syntheses of chlorophyll and vitamin B₁₂ derivatives as well as related β -substituted porphyrins.^[28,29] The β -substituents need to be introduced via the respective pyrrole derivatives, which often requires vast synthetic effort. Therefore, most practical applications apply *meso*-substituted porphyrins, since functionalization can be achieved in a straightforward way by the use of distinct aldehydes whose chemistry is more accessible.^[28,30]

The first example of a symmetric, *meso*-substituted A_4 porphyrin is *meso*-tetraphenylporphyrin and was published by Rothmund in 1936.^[31] The synthetic approach is based on the condensation of pyrrole with specific aldehydes at high temperatures (see **Figure 1.8a**). However, various current research areas mandate the use of unsymmetric *meso*-substituted porphyrins, e.g. donor–acceptor systems for solar energy conversion or amphiphilic systems for the use as photosensitizers.^[32–35] Hence, ingenious synthetic routes to *trans*- A_2B_2 and *trans*- AB_2C porphyrins (see **Figure 1.8b** and **1.8c**) have been developed via prefunctionalized dipyrromethanes, significantly so by the groups of McDonald and Lindsey.^[36,37]

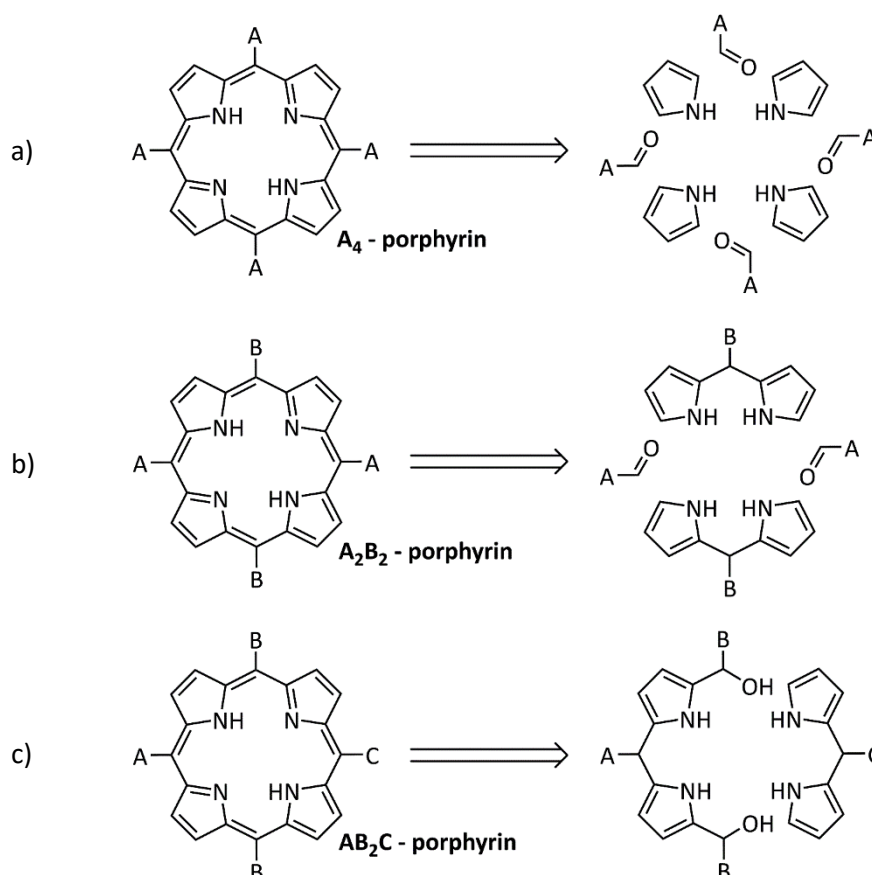


Figure 1.8 Retrosynthetic analysis for the synthesis of a) A_4 b) *trans*- A_2B_2 and c) *trans*- AB_2C porphyrins.

The so-called McDonald condensation towards *trans*- A_2B_2 -porphyrins requires the selective preparation of dipyrromethanes bearing one of the *meso*-substituents (B) which are subsequently connected with aldehydes bearing the other *meso*-substituent (A).^[37] Lindsey optimized this synthetic approach by applying an AB_2 -substituted dipyrromethane-dicarbinal together with a dipyrromethane bearing the C-substituent and consequently lowering the symmetry to *trans*- AB_2C -porphyrins.^[36]

Porphyrin amino acids, bearing the aforementioned *trans*-AB₂C substitution pattern, are especially suitable as key building blocks for the synthesis of artificial photosynthetic reaction centres. These building blocks are easily connected via amide bridges and hence resembling the structure of natural peptide chains. The amide linker guarantees a rigid and stable multiporphyrin system as well as an inherent asymmetry regarding electronic communication and energy/electron transfer directions.^[38]

However, the synthesis of distinct *trans*-AB₂C porphyrins with satisfactory yields is still very challenging. Heinze and co-workers established a Lindsey-based route to prepare ester protected *trans*-AB₂C porphyrin amino acid derivatives in comparatively good yields, as illustrated in **Figure 1.9**.^[38,39]

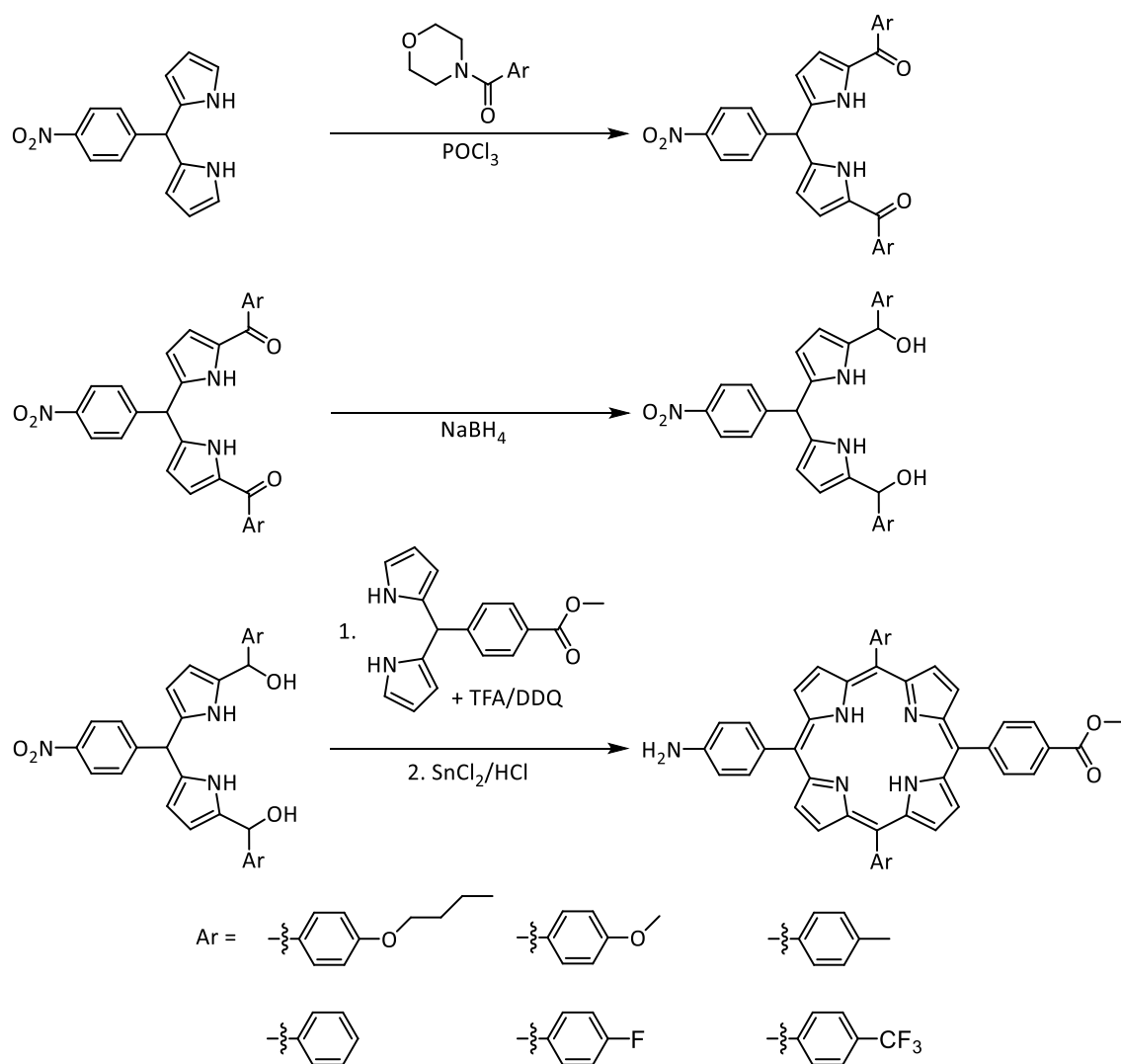


Figure 1.9 Synthesis of *trans*-AB₂C porphyrin amino acid ester building blocks.

The diacylation under Vilsmeier conditions turned out to be the key step for the selective synthesis of *trans*-AB₂C porphyrin amino acid derivatives, since there is no disturbing formation of the monoacylated dipyrromethane as in the Grignard-based approach of Lindsey.^[36] Subsequent reduction with NaBH₄ yielded the corresponding dipyrromethanedicarbinol. After acid catalysed condensation with the ester functionalised dipyrromethane followed by oxidation with DDQ and successive reduction of the NO₂-function with SnCl₂/HCl, the *trans*-AB₂C porphyrin amino acid ester was formed.^[39]

By using this route, a large series of porphyrin amino acid esters bearing different electron donating and withdrawing substituents at the B position is accessible. The shifts observed so far for porphyrin oxidation and reduction amount to 0.34 V for the first oxidation and 0.25 V for the first reduction.^[34,38] This allows the fine-tuning of the redox potentials regarding each individual building block of artificial photosynthetic systems.

1.2 Mononuclear Gold(II) Complexes

Since the early years of humanity, gold has been of particular importance. Due to the scarcity, stability and fascinating golden shine, it has been used for jewellery, coinage and several other arts throughout the recorded history. Many properties of gold and gold compounds, such as the unique colour, aurophilicity, luminescence or the coordination geometry can be attributed to strong relativistic effects.^[40–45] The heavy gold core induces a strong acceleration of the inner electrons close to the speed of light. This leads to a relativistic increase in mass along with a subsequent contraction and energetic stabilisation of s- and p-shells. Since these contracted orbitals shield the nuclear charge more effectively, the d- and f-shells destabilise and therefore expand, as illustrated in **Figure 1.10**.^[43]

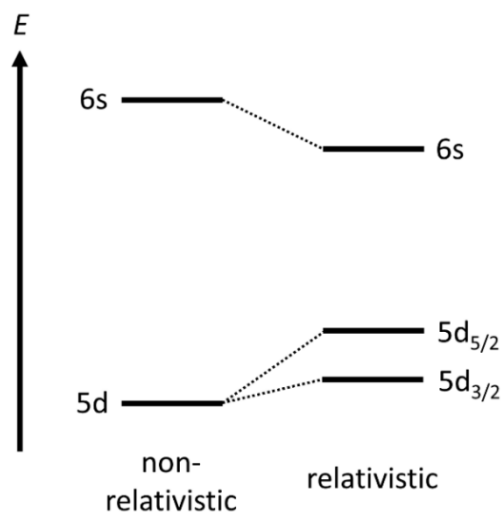


Figure 1.10 Comparison of non-relativistic and relativistic valence orbital energies (calculated for AuH).^[43]

The resulting smaller energy gap between the 5d and 6s orbitals facilitates the formation of the most common linear ($5d^{10}$, oxidation state +I) and square-planar ($5d^8$, oxidation state +III) gold complexes.^[46] This relativistic effect together with the lanthanide contraction provides a possible explanation for aurophilicity, the interatomic attraction between two gold(I) centres. The strength of gold(I)–gold(I) attractive interactions has been estimated via NMR experiments to be in the same order of magnitude such as typical hydrogen bonds ($29\text{--}33\text{ kJ mol}^{-1}$).^[47] The aurophilicity plays a decisive role in the formation of di- and trinuclear gold complexes as well as gold clusters.^[48]

Gold provides a wide area of application such as potent drugs based on gold(I) or gold(III) complexes. Auranofin, an effective drug for the treatment of rheumatoid arthritis, consists of a thi-

olato phosphane gold(I) complex and is used successfully since the 1980s. Furthermore, gold(III) complexes ($[\text{Au}^{\text{III}}(\text{TPP})][\text{X}]$) have been developed as anti-cancer drugs, inspired by the great success of cisplatin ($\text{cis-}[\text{PtCl}_2(\text{NH}_3)_2]$) in the treatment of tumors.^[41,49–52]

In contrast, gold complexes with the formal oxidation state +II and particularly mononuclear gold(II) complexes (5d^9) are a very elusive species. Due to relativistic effects (see **Figure 1.10**), the half-filled $5\text{d}_{x^2-y^2}$ orbital is relatively high in energy, which probably explains the great instability of the latter, as compared to copper(II) and silver(II) complexes. Indeed, disproportionation to mixed-valence compounds comprising of Au^{I} and Au^{III} ions is highly preferred. Particularly pseudo-gold(II) halides “ AuX_2 ” (**Figure 1.11** left) and the halido aurates $\text{M}_2\text{Au}_2\text{X}_6$ are mixed-valence compounds.^[41,53,54]

Favoured by the aforementioned aurophilicity, gold(II) can be stabilised by dimerization, forming a $\text{Au}^{\text{II}}-\text{Au}^{\text{II}}$ bond. A good example for the latter was realised by Bochmann and co-workers and is given by the dinuclear gold(II) pincer complex $[\text{Au}(\text{C}^{\wedge}\text{N}^{\wedge}\text{C})]_2$ together with a comparatively short $\text{Au}^{\text{II}}-\text{Au}^{\text{II}}$ bond length of $2.4941(4)$ Å (**Figure 1.11** right).^[55] The homolytic bond cleavage of the $\text{Au}^{\text{II}}-\text{Au}^{\text{II}}$ bond requires an energy of 198 ± 1 kJ mol⁻¹ and has been determined experimentally by electrochemical methods. Therefore, the $\text{Au}^{\text{II}}-\text{Au}^{\text{II}}$ bond is remarkably stable (even in the presence of O_2) and thermal disproportionation into Au^{I} and Au^{III} is not detected.^[56] Unfortunately, the $\text{Au}^{\text{II}}-\text{Au}^{\text{II}}$ dimer disproportionates on irradiation to give an $\text{Au}^{\text{I}}_4\text{Au}^{\text{III}}_4$ mixed-valence macrocyclic structure and thus no mononuclear gold(II) complex was obtained.^[41,57]

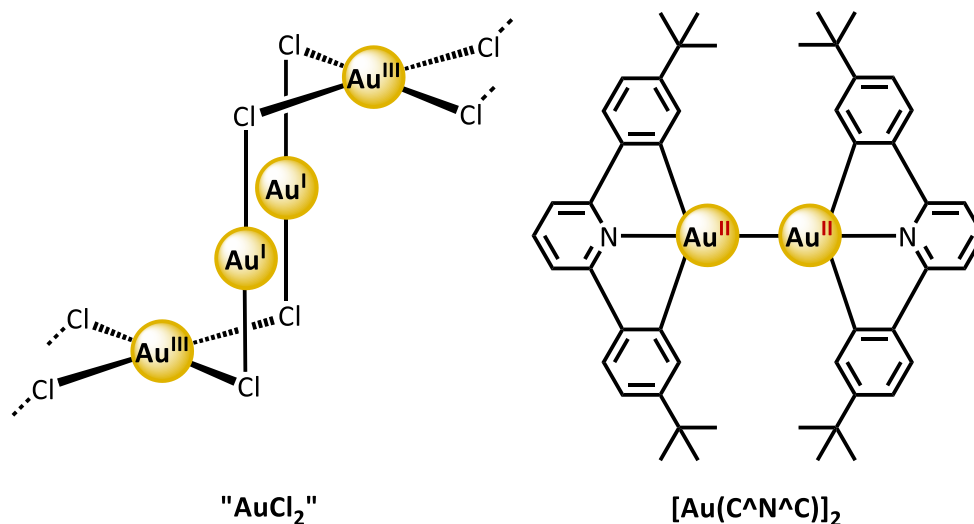


Figure 1.11 Pseudo-gold(II) halide “ AuCl_2 ” (left) and dinuclear gold(II) pincer complex $[\text{Au}(\text{C}^{\wedge}\text{N}^{\wedge}\text{C})]_2$ (right).^[53,55]

It appears, that mononuclear open-shell gold(II) complexes are very difficult to capture. However, a thorough understanding of this elusive species would be of great importance, since gold(II) has been proposed as key intermediate in photoinduced gold-catalysed reactions as well as in artificial photosynthetic reaction centres bearing gold(III) complexes as electron acceptors.^[41,58–69]

For instance, Hashmi and co-workers proposed a highly speculative mechanism that accounts for the visible-light-mediated gold-catalysed synthesis of α -aryl ketones via 1,2-difunctionalization of alkynes (see **Figure 1.12**).^[58] The reaction is initiated by gold-induced single electron transfer (SET) to the aryl diazonium salt, yielding a gold(II) species and an aryl diazo radical. In the next step, the gold(II) intermediate recombines with the phenyldiazonium radical, yielding a cationic gold(III) complex. After several further steps, reductive elimination provides an arylated enol ether, which delivers the final product via hydrolysis.^[58] However, gold(II) species have not yet been observed spectroscopically in reactions of this type.

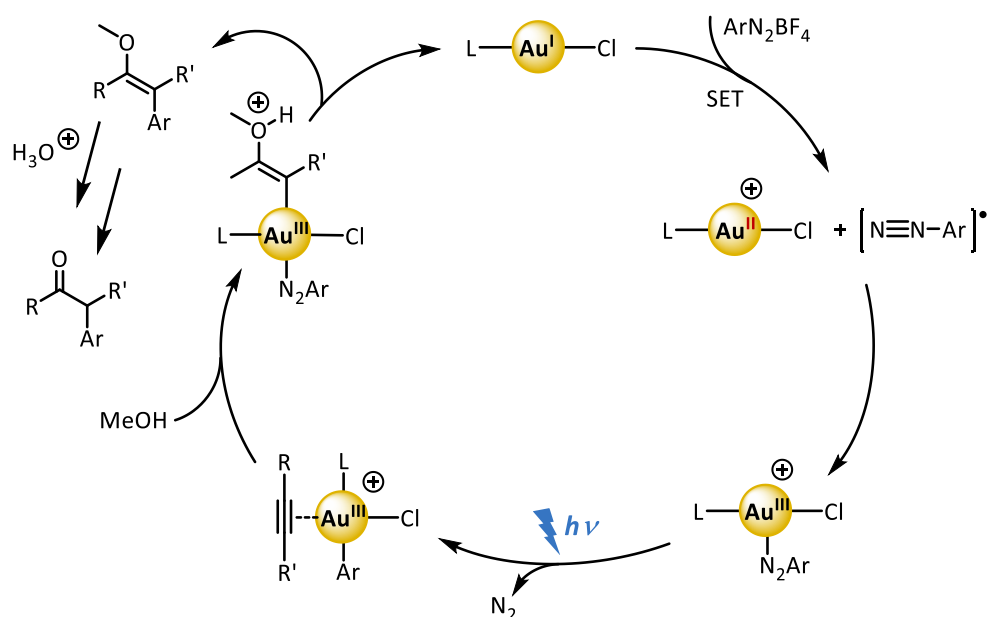


Figure 1.12 Proposed mechanism involving an intermediate gold(II) species.^[58]

1.2.1 Mononuclear Open-Shell Gold(II) Complexes

Among the few literature-known examples of true mononuclear open-shell gold(II) complexes are the prominent ionic gold(II) xenon complexes $[AuXe_n]^{2+}$ such as $[Au^{II}Xe_4][Sb_2F_{11}]_2$ or $[trans-AuXe_2][SbF_6]_2$, synthesized by Seppelt and co-workers.^[70–72] However, these xenon complexes could only be stabilised in HF/SbF_5 mixtures at low temperatures and under xenon atmosphere to prevent decomposition. Consequently, their reactivity could not be examined. Nevertheless, it was possible to structurally characterise these mononuclear gold(II) compounds.^[41,70–72]

Furthermore, the groups of Seppelt and Bartlett succeeded to isolate and structurally characterise the ionic compounds $[\text{Au}(\text{HF})_2][\text{SbF}_6]_2$ and $\text{Au}[\text{SbF}_6]_2$, which exhibit a $[\text{AuF}_4]^n$ coordination mode. As before, stabilisation of these complexes could be achieved in HF/SbF_5 mixtures at low temperatures, but in the absence of xenon.^[41,73,74] Another gold(II) complex with the $[\text{AuF}_4]^n$ motive is given by the mixed-valence compound $\text{Au}^{\text{II}}[\text{Au}^{\text{III}}\text{F}_4]_2$, isolated by Müller and co-workers during examinations of $\text{Ce}^{4+}/\text{AuF}_3$ systems.^[75] Representative structurally characterized mononuclear gold(II) compounds with Au–Xe and Au–F bonds are shown in **Figure 1.13** (left).^[72]

The first structurally characterised mononuclear gold(II) complex was realized by the group of Schröder in 1990. They utilised the chelating thioether ligand 1,4,7-trithiacyclononane $[\text{9}] \text{aneS}_3$, which entirely encapsulates the gold(II) ion (see **Figure 1.13** right). This six-coordinate thioether environment efficiently impedes the usual dimerization and disproportionation pathways of the otherwise highly reactive gold(II) species.^[41,76] The crystal structure of the $[\text{Au}^{\text{II}}([\text{9}] \text{aneS}_3)_2]^{2+}$ cation revealed an elongated octahedral complex geometry, which can be explained by the first-order Jahn-Teller effect of the open-shell $5d^9$ electronic configuration.^[77] Furthermore, they observed an intense signal in the EPR spectrum at $g_{\text{av}} = 2.010$ (at 77 K) together with a hyperfine

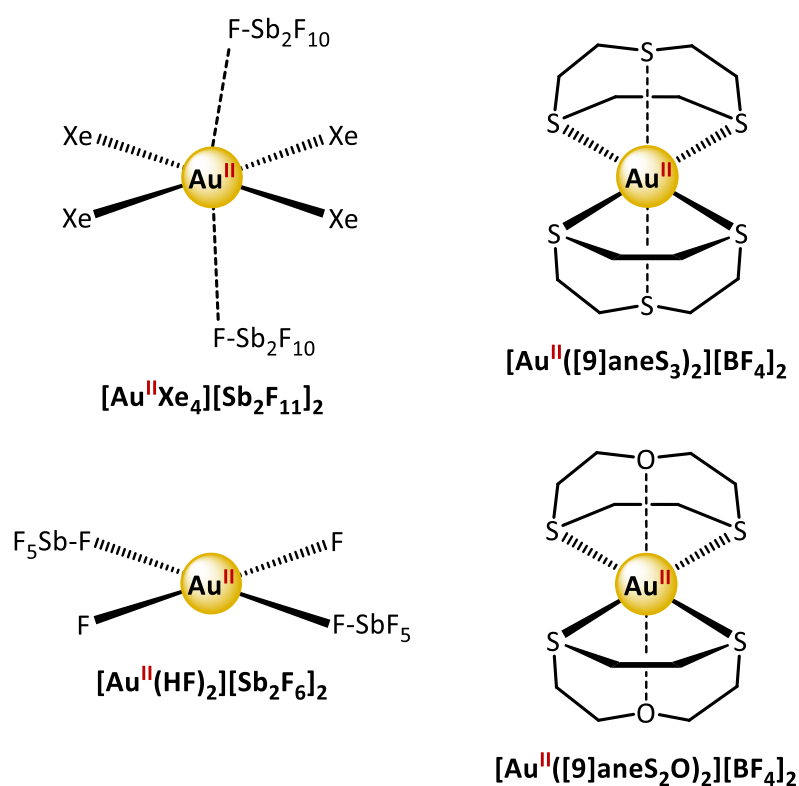


Figure 1.13 Selection of structurally characterized mononuclear gold(II) complexes.^[72,74,76,79]

coupling to ^{197}Au ($I = 3/2$; 100 %) of $A_{\text{av}}(^{197}\text{Au}) = 57.3$ G, affirming the gold(II) description. Noteworthy is the rather low g anisotropy due to a relatively weak spin-orbit coupling ($g_{zz} = 2.032$; $g_{yy} = 1.980$; $g_{xx} = 1.999$), assuming that g_{zz} is perpendicular to the equatorial AuS_4 plane.^[41,78]

A similar outcome was obtained by modifying the ligand $[\text{9}]_{\text{ane}}\text{S}_3$ to $[\text{9}]_{\text{ane}}\text{S}_2\text{O}$ via incorporation of an ether O-donor, yielding the analogous complex $[\text{Au}([\text{9}]_{\text{ane}}\text{S}_2\text{O})_2][\text{BF}_4]_2$ as illustrated in **Figure 1.13** (right).^[41,79] Once more the EPR spectroscopic measurements indicated a mononuclear gold(II) species with $g_{\text{iso}} = 2.0182$ and $A_{\text{av}}(^{197}\text{Au}) = 47.0$ G, along with a rather low g anisotropy ($g_{zz} = 2.037$; $g_{yy} = 2.006$; $g_{xx} = 2.010$).^[41,79]

1.2.2 Suggested Mononuclear Gold(II) Complexes

Recently, mononuclear gold(II) trihalide complexes $[\text{AuCl}_3]^-$ and $[\text{AuBr}_3]^-$ have been detected via mass spectrometry during gas-phase experiments with monoalkyl gold(III) complexes $[\text{PPh}_4][\text{Au}(\text{CF}_3)\text{X}_3]$ (see **Figure 1.14a**). DFT calculations revealed a T-shaped structure as energy minima for the $[\text{AuX}_3]^-$ anions.^[80] However, neither further structural nor spectroscopic evidence for such elusive low-coordinate gold(II) complexes has been provided thus far.

Furthermore, three-coordinate mononuclear gold(II) species have been repetitively proposed as intermediates in gold-catalysed photoredox experiments involving radical reaction steps, such as $\text{Au}(\text{PPh}_3)(\text{Ph})(\text{Cl})$ in the course of a gold-catalysed ring expansion–arylation reaction, conducted by the group of Toste (see **Figure 1.14b**)^[41,58–63,66]. But up until now, the participation of gold(II) species in photocatalytic cycles lacks any spectroscopic or structural evidence and an explicit assignment of oxidation states is challenging.

Roduner and co-workers stabilised the bis(ethylenediamine) gold(II) complex $[\text{Au}(\text{en})_2]^{2+}$ inside a zeolite Y supercage (see **Figure 1.14c**), since the confinement in the zeolite pores effectively prevents the gold(II) species from undergoing disproportionation.^[81] The oxidation state +II could be verified via EPR spectroscopy with $g_{zz} = 2.239$, $g_{xx,yy} = 2.051$, $A_{zz}(^{197}\text{Au}) = 188$ G and $A_{xx,yy}(^{197}\text{Au}) = 22$ G, indicating a clear axial characteristics and thus a square planar coordination geometry. Noteworthy is the large g -anisotropy revealing a considerable spin-orbit coupling. But again, further spectroscopic, structural or reactivity data is missing.^[41,81]

The group of Koski published a paper about the synthesis of a gold(II) phthalocyanine complex $\text{Au}(\text{Pc})$ in 1965, which has been regarded as a rare example of a paramagnetic gold(II) complex (see **Figure 1.14d**). However, the reported data was limited to UV/vis measurements and an incomplete EPR spectrum showing only the perpendicular part ($g_{\perp} = 1.996$), probably due to the

bad solubility of such unsubstituted phthalocyaninato metal compounds.^[82] Shimizu, Kobayashi, Leznoff and co-workers tried to verify the aforementioned assumptions. Their synthetic approach was based on the route of Kashi by using 1,3-diiminoisoindoline and a gold salt (AuCl or KAuCl) in 1-chloronaphthalene at 200°C. But except of a triphyrin-like species with a square-planar gold(III) center, gold(III) phthalocyanine and several oligomers of phthalonitril, no gold(II) phthalocyanine could be observed.^[83] Indeed, DFT calculations revealed, that Au^{II}(Pc) can be better interpreted as Au^{III}(Pc³⁻) with the spin density located in the π -system of the radical anion ligand.^[41,84]

Spectroelectrochemical EPR experiments (295 K) of an *in situ* generated one-electron reduced gold(III) corrole complex (see **Figure 1.14e**), which has been synthesized by Sarkar, Kar and co-workers, revealed the formation of a gold(III) corrole π -anion radical with $g_{iso} = 1.995$. This was further supported by spin density calculations, demonstrating an almost entirely ligand centred spin density.^[41,85] Contrary to this, earlier studies on one-electron reduction of the corresponding copper(III) and silver(III) corrole complexes had clearly shown the generation of Cu^{II} and Ag^{II}, respectively. This can be probably explained via a large ligand field splitting of the gold(III) corrole complex, pushing the $5d_{x^2-y^2}$ orbital to such high energy, that it becomes unattainable for the one-electron reduction process.^[85-87]

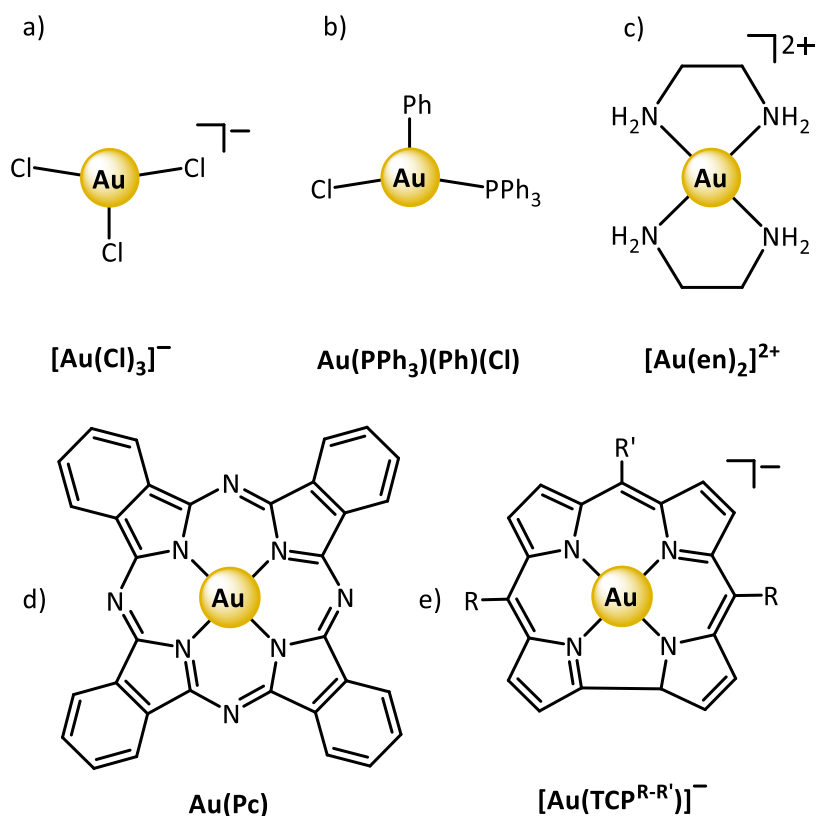


Figure 1.14 Putative three- and four-coordinate mononuclear gold(II) species with Au–C, Au–P, Au–Cl and Au–N coordination (Ph = phenyl group).^[41,61,80,81,82,85]

1.3 The Electron Transfer Process

Electron transfer (ET) processes are fundamental for the chemistry of life, such as photosynthesis or nitrogen fixation. Therefore, the knowledge about such an elementary process affected a variety of research fields and it has grown enormously since the late 1940s.^[88] With respect to biological issues, it supported to clarify the nature of respiratory and photosynthetic electron transfer (ET) chains and other redox enzymes.^[89] The first experiments regarding ET processes were on isotopic self-exchange reactions as illustrated in **Equation 1.1**.^[88]



Such self-exchange ET reactions have two key advantages: 1) reactants and reaction products are identical and thus the thermodynamic stability of the reactants and products is not influencing the rate of the ET reaction 2) during such simple ET reactions no bonds are broken or formed. Therefore, they are in contrast with the “transition state” theory, which describes chemical reactions in terms of the motion of the atoms of the reactants on a potential energy surface, whereby chemical bonds are broken and formed. Hence, to successfully describe the rates of ET reactions, a new type of theory was needed.^[88]

1.3.1 The Marcus Theory of Electron Transfer

In 1956, Rudolph A. Marcus made the first approach to quantitatively describe ET reactions and was awarded with the Nobel Prize in chemistry (1992) for his scientific work in the field of ET reactions.^[88,90,91]

He made the assumption, that chemical reactions can be best described via so-called “fluctuations” in the various nuclear coordinates on a potential energy surface as illustrated in **Figure 1.15**. The atoms included in this fluctuations are the reactants as well as the associated surrounding molecules.^[88,90]

The theory itself is based on two essential prerequisites: 1) while thermal electron transfer occurs (diabatic), the coordinates of the nuclei do not change, such as for an optical ET and therefore the Franck-Condon principle is satisfied and 2) an ET can only occur, if energy conservation is obeyed. Due to this energy conservation principle, ET can only arise on the saddle point of the energy surface, which is implemented by the aforementioned fluctuations of all nuclear coordinates.^[88,90]

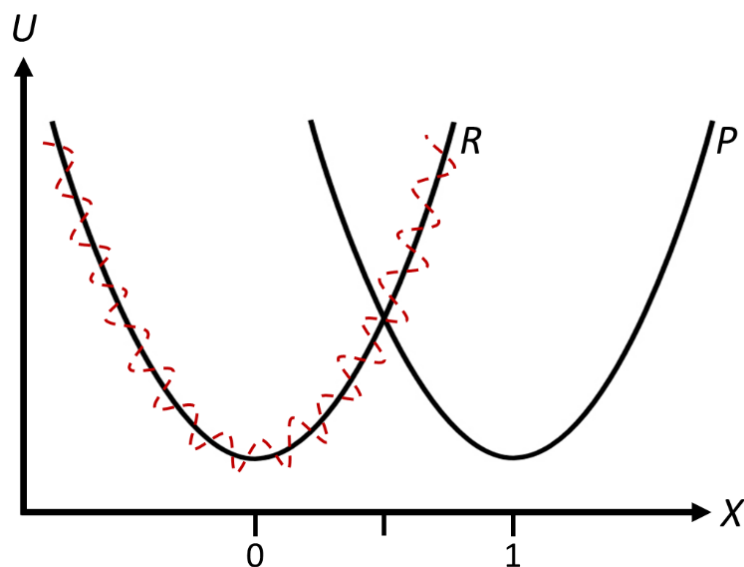


Figure 1.15 Profile of potential energy surface for reactants plus solvent environment (R) and for products plus solvent environment (P). Solid curves (black): simplified potential energy surfaces and dashed curve (red): realistic potential energy surface. X = nuclear coordinates.^[88]

Markus simplified this rather complex energy diagram (**Figure 1.15**), depending on fluctuations of many nuclear coordinates X , by two ingenious approximations: 1) the potential energies U of reactants and products in the many-dimensional coordinate space are simple functions of the vibrational coordinates and hence can be described via a harmonic oscillator potential and 2) a “linear response approximation”, in which any hypothetical change in charge of the reactants produces a proportional change in the dielectric polarization of the solvent. This linear approximation results in simple quadratic functions regarding the free energy curves for the reactant G_R and product G_P (see **Figure 1.16**; self-exchange ET reaction).^[88]

The resulting expression for the rate constant k_{ET} for the thermal ET is given by **Equation 1.2**. The term A depends on the nature of the ET reaction (e.g., bimolecular or intramolecular) whereas ΔG^* is the associated activation barrier and is represented with **Equation 1.3**.^[88]

$$k_{ET} = A \exp\left(\frac{-\Delta G^*}{k_B T}\right) \quad (1.2)$$

$$\Delta G^* = \frac{\lambda}{4} \left(1 + \frac{\Delta G^0}{\lambda}\right)^2 \quad (1.3)$$

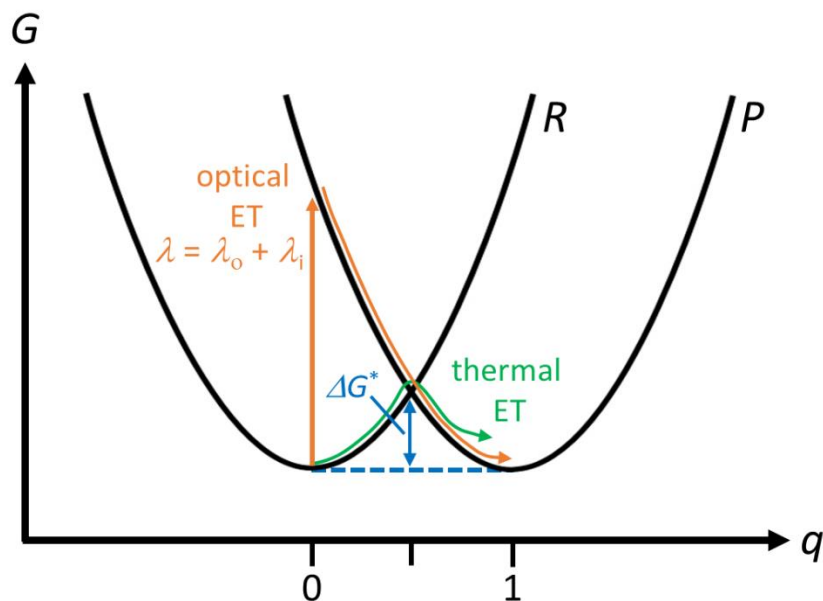


Figure 1.16 Plot of the diabatic free energy surface of reactants plus environment vs. the reaction coordinate q (R), the free energy surface of products plus environment vs. reaction coordinate q (P) and possible pathways for electron transfer (thermal and optical).^[88]

ΔG^0 is the standard free energy of the reaction (equals zero for a self-exchange reaction), and λ is the reorganisation energy of the system, assembled of solvational (λ_o) and vibrational (λ_i) components ($\lambda = \lambda_o + \lambda_i$). Hence, it considers the reorganisation of the solvent molecules outside the reactants as well as the inner structural changes. The rate constant for activation-free ET ($-\Delta G^0 = \lambda$) is given by **Equation 1.4**.^[88,89]

$$k_{\text{ET}} = A = \left(\frac{4\pi^3}{h^2 \lambda k_B T} \right)^{\frac{1}{2}} V_{\text{RP}}^2 \quad (1.4)$$

Equation 1.4 is considering Fermi's golden rule. The rule states that the ET rate is proportional to the square of the weak coupling of the reactant and product electronic states, V_{RP} . This is in turn proportional to the overlap of the donor and acceptor electronic wavefunctions across the space separating electron donor and acceptor molecules. Overall, this results in the semiclassical description for ET given by **Equation 1.5**.^[88,89]

$$k_{\text{ET}} = \left(\frac{4\pi^3}{h^2 \lambda k_B T} \right)^{\frac{1}{2}} V_{\text{RP}}^2 \exp\left(-\frac{(\Delta G^0 + \lambda)^2}{4\lambda k_B T} \right) \quad (1.5)$$

As illustrated in **Figure 1.16**, there are two possible ET pathways. The aforementioned thermal ET as well as the optical ET. For self-exchange reactions, ΔG^0 equals zero and therefore the optical excitation energy is identical with the reorganisation energy. In this case, the reorganisation energy equals the energy that is released by internal conversion of the system after an optical ET, to yield the novel relaxed geometry.^[92]

The quadratic dependence of k_{ET} regarding the sum $(\lambda + \Delta G^0)$ is directly correlated with the activation energy ΔG^* , and results in three different outcomes, as illustrated in **Figure 1.17**.

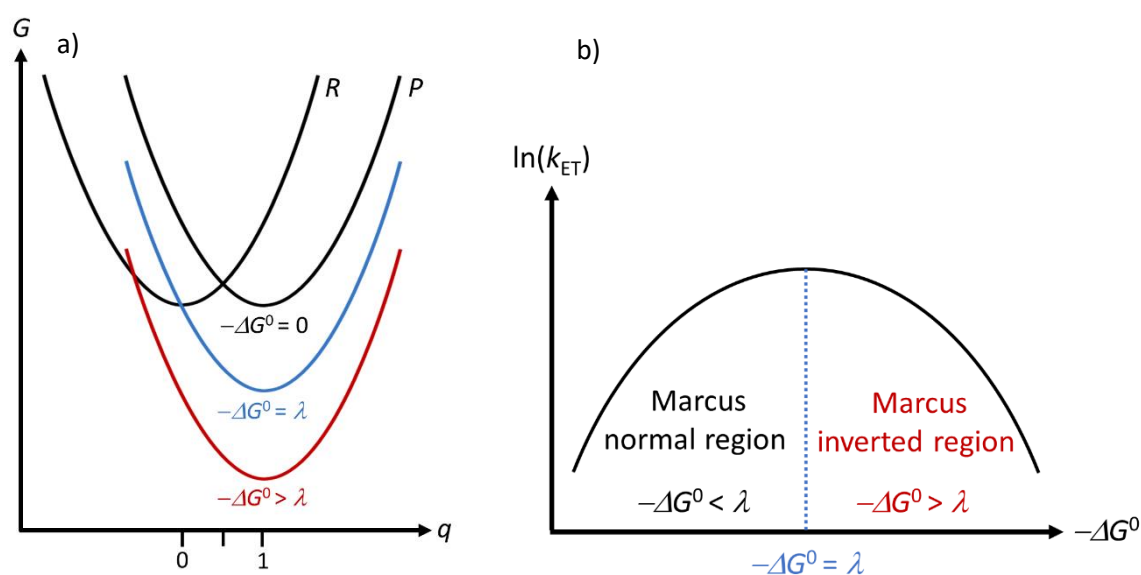


Figure 1.17 a) Plot of the free energy G vs. the reaction coordinate q for reactants (R) and products (P), for three different values of $-\Delta G^0$, b) Plot of $\ln(k_{\text{ET}})$ vs. $-\Delta G^0$.^[88,89]

The activation barrier ΔG^* is at its maximum for $-\Delta G^0 = 0$ (self-exchange reaction). The increase of $-\Delta G^0$ together with the condition $-\Delta G^0 < \lambda$, leads to a reduction of ΔG^* and consequently to an increase of k_{ET} (Marcus normal region). This is true until $-\Delta G^0 = \lambda$, where there is no activation barrier ($\Delta G^* = 0$) and therefore k_{ET} reaches its maximum value. In the highly exergonic region $-\Delta G^0 > \lambda$ the activation barrier rises again, together with a decrease of the ET transfer rate k_{ET} (Marcus inverted region).^[88]

1.3.2 The Marcus-Hush Theory of Electron Transfer

The aforementioned Marcus theory is only suitable for systems with very weak electronic interactions. Therefore, for systems with a significant electronic coupling, Hush extended the Marcus theory regarding strongly interacting systems (e.g. intramolecular ET reactions of bridged systems).^[93,94]

The Marcus-Hush theory is utilised when the electronic communication between two redox sites of a specific system is exceeding the thermal energy, which is given by $k_B T$. Consequently, the nuclear motion is coupled to the electron motion and the system remains on one adiabatic free energy surface, as illustrated in **Figure 1.18**. This is in contrast to the aforementioned diabatic ET, since the nuclei do not move during the diabatic ET between two redox sites (Franck-Condon principle). The electronic communication in this adiabatic approach is expressed by the electron coupling matrix element H_{AB} . Coupling of the two diabatic free energy curves for the reactants and products (which are known from the previously discussed Marcus theory) via H_{AB} yields the adiabatic free energy surfaces as shown in **Figure 1.18**.^[94]

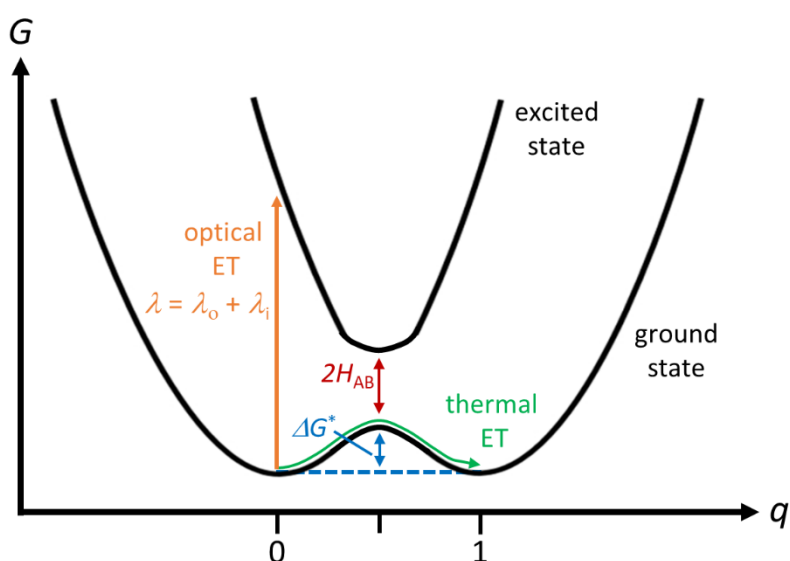


Figure 1.18 Plot of the adiabatic free energy surfaces (ground state, excited state) vs. the reaction coordinate q for reactants and products, possible pathways for electron transfer (thermal and optical) and the matrix element H_{AB} for electronic coupling.^[94]

The adiabatic ground state shows ET a double minimum, the excited state a single minimum and they are separated by an energy gap of $2 H_{AB}$. One may now assume, that the barrier lowering as a consequence of the electronic interaction of the reactants can be neglected. However, as H_{AB} increases, and the splitting between the ground state and excited state becomes larger and the reactants and products are stabilized. Altogether, this leads to a lowering of the reorganisation energy, which is expressed by a smaller activation barrier ΔG^* , and finally yields a fully delocalized system ($\Delta G^* = 0$). Consequently, in view of these energy changes, the activation barrier ΔG^* with appreciable coupling of the reactants is given by **Equation 1.6**.^[94]

$$\Delta G^* = \frac{(\lambda - 2H_{AB})^2}{4\lambda} \quad (1.6)$$

Depending on the magnitude of the electronic coupling between donor and acceptor sites, three classes of mixed-valence systems can be distinguished, as suggested by Robin and Day in the late 1960s (vide infra).^[95] In general, a mixed-valence system is based on two active redox sites in different oxidation states. One of the most remarkable compounds possessing this behaviour is the Creutz-Taube Ion, which is illustrated in **Figure 1.19**. It consists of two ruthenium redox centres bridged via a pyrazine unit and is fully saturated by five ammonia ligands per metal centre. Since the overall charge of the system is +5, one may assume either Ru^{II} and Ru^{III} centres or an averaged oxidation state of 2.5.^[96,97]

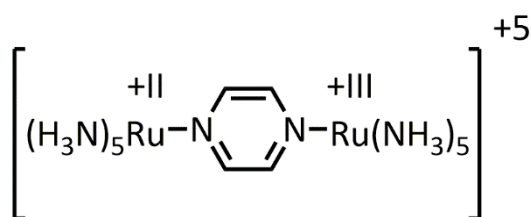


Figure 1.19 The mixed-valent Creutz-Taube Ion.^[96,97]

The class I type of mixed-valence systems demonstrates no electronic coupling between the donor and acceptor sites, and therefore the matrix element for electronic coupling H_{AB} equals zero, either because their interaction is spin or symmetry forbidden or because the sites are far apart. Indeed, the properties of class I type systems are essentially those of the separate reactants.^[94,95]

For class II systems, the electronic coupling is smaller than the reorganisation energy with $0 < 2 H_{AB} < \lambda$ and thermal or optical electron transfer is possible. They possess new electronic and optical properties in addition to those of the separate states. The optical transition is called intervalence charge transfer band (IVCT) and is often located in the near IR region regarding optical spectroscopy. The IVCT band allows the calculation of H_{AB} via band shape analysis. For class II systems H_{AB} is given by **Equation 1.7**.^[94,95]

$$H_{AB} = 0.0206 \frac{(\tilde{\nu}_{\max} \varepsilon_{\max} \Delta\tilde{\nu}_{\max})^{0.5}}{R_{AB}} \quad (1.7)$$

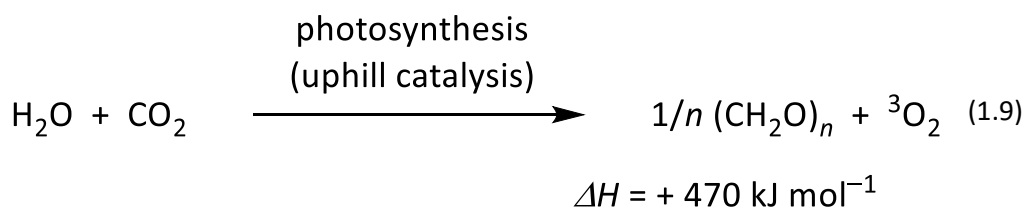
The value $\tilde{\nu}_{\max}$ is the energy of the maximum of the IVCT band in cm^{-1} , ε_{\max} is the extinction coefficient at the maximum, $\Delta\tilde{\nu}_{\max}$ resembles the bandwidth at half height in cm^{-1} and R_{AB} is the charge transfer distance in Å.

In class III systems, the interaction of the donor and acceptor sites has become very large and H_{AB} is at least as big as λ , $2 H_{AB} \geq \lambda$. Therefore, the two separate minima (**Figure 1.18**) are no longer noticeable and the ground state energy surface features a single well. This situation is describing the fully delocalised case, which readily results from the zero-activation barrier limit of **Equation 1.6** ($\Delta G^* = 0$).^[94,98] However, optical transitions are still possible, but do not involve charge transfer, since the excited state is delocalized over both redox centers, leading to no net dipole-moment change. These optical transitions are commonly described as IVCT bands as well, since they appear in the same near IR region of the optical spectrum regarding class II systems, but is technically incorrect because no electron is transferred. In this connection, H_{AB} for strongly coupled systems is given by half the energy of the maximum of the transition band (**Equation 1.8**).^[94,98]

$$H_{AB} = \frac{\tilde{\nu}_{\max}}{2} \quad (1.8)$$

1.4 Photosynthesis

During Photosynthesis, solar energy is absorbed and utilised to convert the low-energy starting materials water and carbon dioxide into high-energy organic compounds and oxygen, as illustrated with **Equation 1.9**. Therefore, this highly endergonic solar energy-consuming conversion process is crucial for the existence of higher organisms, providing them with food and oxygen to breathe.^[2]



Consequently, it is not surprising that Nobel Prizes in Chemistry have been awarded for the investigation of primary steps of photosynthesis, such as the structural elucidation of an isolated and crystallised cyanobacterial photosynthetic reaction centre by Deisenhofer, Huber and Michel in 1988 as well as for the theoretical portrayal of the underlying ET processes by Marcus in 1992.^[2,88,99] Besides the field of protein crystallisation, the design and preparation of artificial photosynthetic model compounds represents another possibility to gain a deeper understanding of the photosynthetic key reactions (vide infra).

1.4.1 Primary Processes in Photosynthesis

The primary processes start with the absorption of energy in form of photons via the so-called light harvesting complex (LHC) as exemplarily illustrated in **Figure 1.20** regarding the P700 photosystem (PS I), which is located in the thylakoid membranes of chloroplasts and cyanobacteria.^[100] The LHC consists of various organic pigments (embedded in polypeptide chains), such as chlorophylls or carotenoids, so that a broad absorption range is covered (see **Figure 1.20**; pigments indicated in green and orange).^[100] The absorption of solar energy requires less than 10^{-15} seconds and yields “excitons”, short-lived electronically excited states that would be able to produce charge-separation. However, the photon density in diffuse sunlight is rather low and it is more convenient, to use the major part of the chlorophyll molecules in the light harvesting process (>98 %).^[2] The collected energy is therefore effectively transferred by the Förster mechanism to the actual reaction centre (RC): the “special-pair” of photosynthesis (see **Figure 1.20**; RC indicated in magenta).^[2,100–102] For this purpose, the chlorophyll chromophores are arranged in spatial proximity to each other and a well-defined orientation. As a consequence, they are able to “funnel” the solar energy to the RC within a very short time frame (10–100 ps) and approximately 95 % efficiency.^[2]

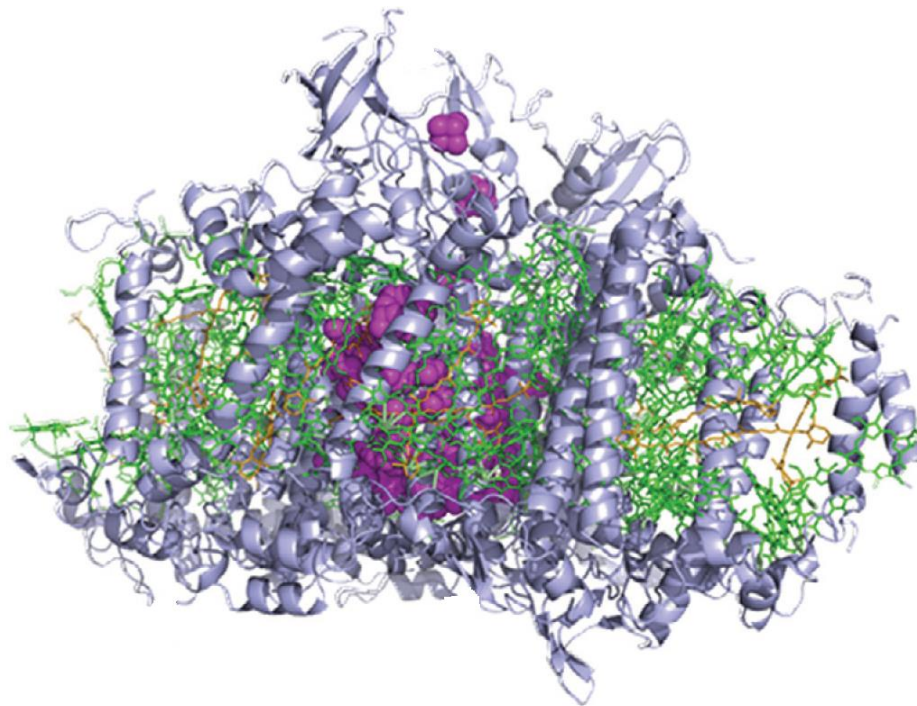


Figure 1.20 Molecular structure image of P700 (PS I) based on crystallographic data. P700 is composed of polypeptide chains (grey), chlorophyll and carotenoid pigments (green + orange) and the reaction centre (magenta), adapted from Ref. [100].

After excitation of the special pair to its first excited singlet state S_1 via photoexcitation or energy transfer, an electron is transferred to a monomeric chlorophyll (Chl) at ~ 1 ps, as illustrated in **Figure 1.21**. The excited electron is relaxing via two intermediate phylloquinones in 20 ps and is subsequently transferred to three iron-sulphur clusters in 15–150 ns. The final charge recombination (CR) requires 10 ms and is therefore significantly slower than the initial charge separation (CS) process.^[100] The success of photosynthesis is based on the extremely rapid CS and ET steps over a great distance, yielding a long-lived CS state. This is of great importance, since subsequent chemical reactions, such as the reduction of NADP^+ to NADPH , require a certain time.^[2]

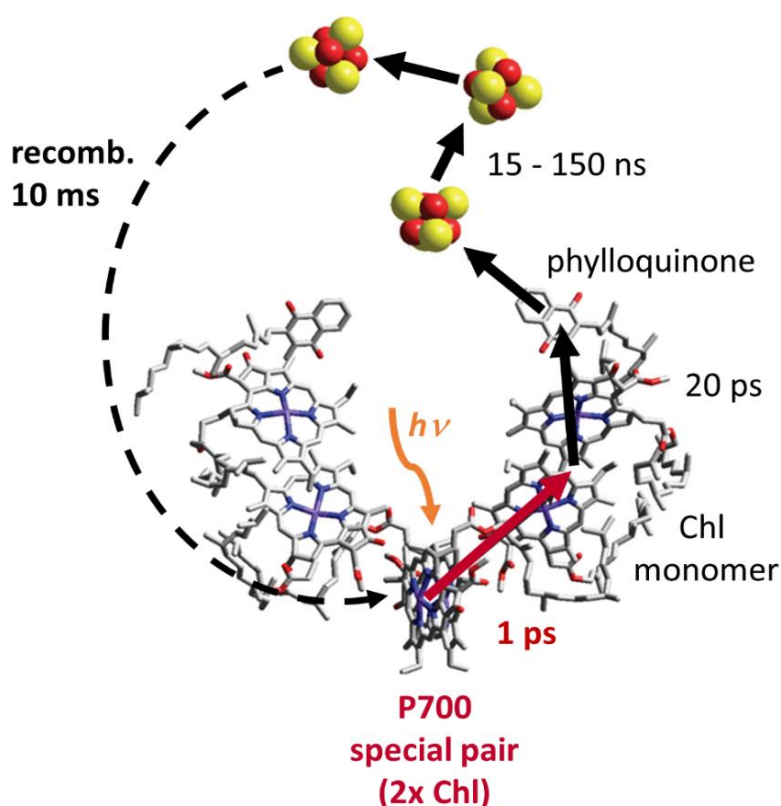
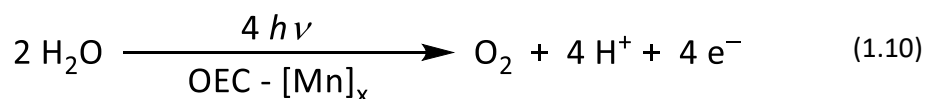


Figure 1.21 The P700 reaction centre electron transfer chain, showing electron transfer and recombination times, adapted from Ref. [100].

In photosynthetic reaction centres, the special arrangement of ET components results in a sizable reduction or even disappearance of the activation energies ΔG^* for the forward reaction process, placing it in the Marcus normal region ($-\Delta G^0 \leq \lambda$). The activation energy ΔG^* is small, if the reorganisation energy λ is small and indeed, the evolutionary process yielded a system with large reactants and a mainly unpolar immediate protein environment, both leading to a small λ . However, the CR process is rather slow, since it is highly exergonic ($-\Delta G^0 > \lambda$) and occurs in the Marcus inverted region of ET (vide supra).^[2,88,90,91]

The photosynthetic process of oxygen-evolving organisms (plants and cyanobacteria) differs significantly from the more simple anaerobic purple bacteria. Instead of one, they feature two separately excitable photochemical systems, namely photosystem II (P680) and photosystem I (P700), since the production of the universal hydride carrier NADPH and oxygen requires more potential difference than provided by only one photosystem (considering further energy losses, e. g. heat or radiation).^[2,103]

These two photochemical systems can be arranged in a redox potential diagram, the Z scheme of photosynthesis (see **Figure 1.22** for a simplified version), so that two sequentially captured photons drive electrons from the very weak reducing agent H₂O to the very weak oxidizing agent NADP⁺. The Z scheme contains several unique ET components, such as the cytochrome *b/f* complex (Cyt *b,f*) or the flavoprotein (Fp), utilised in the NADP⁺ reductase, as exemplarily shown in **Figure 1.22**. The electrons provided for the photoinduced ET processes are gathered via the “water-splitting” reaction, given by **Equation 1.10**.^[2,103]



After photoexcitation of P680, an electron hole remains, representing a very positive potential that is powerful enough to oxidize water to dioxygen in an overall four-electron process. This mechanistically challenging oxidation of H₂O to O₂ takes place at the so-called oxygen-evolving complex (OEC, see **Figure 1.22**), a polynuclear manganese complex, containing a distorted Mn₃CaO₄ heterocubane.^[2,103,104] The photoexcited P^{*₆₈₀} undergoes CS and ET to P700. Finally, after photoexcitation of P^{*₇₀₀}, subsequent CS and ET to the flavoprotein, the electron-rich NADPH is formed via reduction of NADP⁺, which is utilised for the CO₂ reduction during the “dark reaction” of photosynthesis (Calvin cycle).^[2,103]

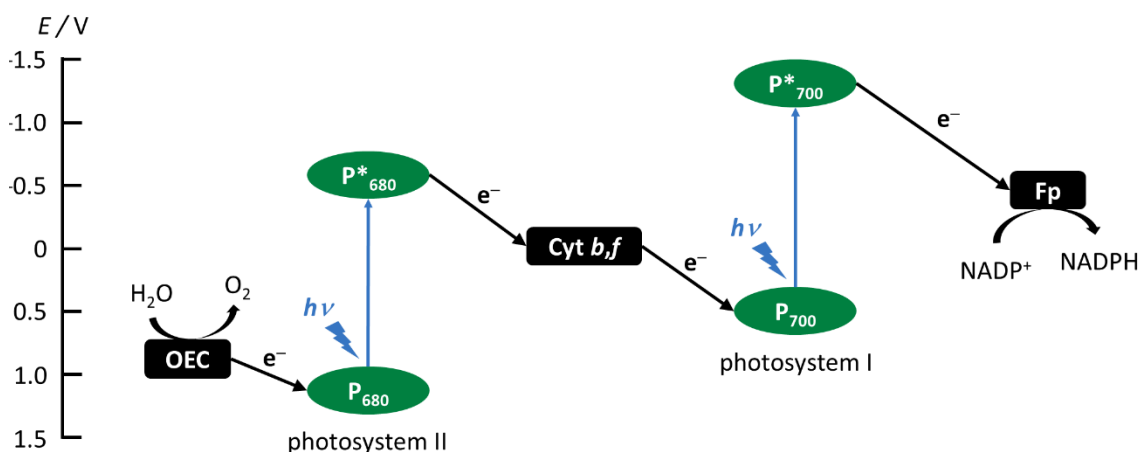


Figure 1.22 Simplified Z scheme of oxygenic photosynthesis (adapted from Ref. [103]).

1.4.2 From Natural to Artificial Photosynthesis

The artificial representation of LHCs and RCs with comparable rates and time scales of CS and ET found in nature is one of the substantial challenges of actual photosynthesis research. Especially the imitation of the aforementioned long-lived CS state characteristics is of great importance to successfully convert solar energy into chemical energy, since the exploitation of the latter during organic photoredox catalysis, e. g. for the production of solar fuels (hydrogen), requires a certain time frame.^[105,106]

The Marcus theory together with the insights gained so far regarding structure and orientation of the photosynthetic RC lead to the design of efficient synthetic photoinduced ET systems. Significant advances in the understanding of photoinduced CS and ET have been obtained via examination of artificial RCs consisting of covalently bridged donor–acceptor molecular units.^[105,106] Indeed, such bridge-mediated ET can significantly enhance ET transfer rates at long distances. One can imagine that the bridge acts either as an intermediate donor and acceptor by a step-wise hopping mechanism, or as a mediator of ET by enhancing the electronic coupling through its valence orbitals in the so-called super-exchange mechanism.^[107–110]

Furthermore, the careful choice of electron donors and acceptors with small reorganization energies λ is key to obtain a long-lived charge separation (*vide supra*). In these cases, the driving force of CR could be located in the Marcus inverted region, where the lifetime of the CS state increases, as the driving force of CR increases.^[105] Typical electron donor entities are represented by zinc(II) porphyrins, carotenoid polyenes or ferrocene whereas quinones (natural acceptors) and fullerenes act as potent electron acceptors in artificial photosynthetic systems.^[34,38,111–122]

The covalently bridged motive was thoroughly investigated by Heinze and co-workers, regarding amides as mediating bridges of ET in photosynthetic model systems together with free-base or zinc(II) porphyrin amino acid esters derivatives as the key building blocks for artificial photosynthesis.^[34,38,120,123] In this course, several free-base and mono/doubly metallated bis(porphyrins) P-P' with adjustable electron withdrawing power at each porphyrin were synthesised and characterised.^[38] Furthermore, linking of anthraquinone (Q) as electron acceptor and ferrocene (Fc) as suitable electron donor to free-base and metallated porphyrin amino acid esters derivatives yielded Q-P and Fc-P dyads, Fc-P-Q and P-Fc-P' triads and Fc-P-P'-Q tetrads with tunable electron density at the porphyrin chromophores.^[34,120] Recently, the cationic electron acceptor cobaltocenium (Cc⁺) was utilised in a Cc⁺-Zn(P) amide-bridged photosynthetic model dyad.^[123]

The ferrocene-*meso,meso*-linked porphyrin trimer-fullerene pentad: Fc-(Zn(P))₃-C₆₀

The Fc-(Zn(P))₃-C₆₀ pentad is one of the best performing molecules mimicking the multi-step ET processes in the photosynthetic reaction centre (see **Figure 1.22**).^[105,118] Ferrocene and fullerene are tethered at opposite ends of the zinc(II) porphyrin *meso-meso* linked triad with a large edge-to-edge distance of $R_{AB} = 46.9 \text{ \AA}$. The total efficiency of ET is $\Phi_{ET} = 83 \%$ and the lifetime of the final CS state $\text{Fc}^{\bullet+}\text{-(Zn(P))}_3\text{-C}_{60}^{\bullet-}$ in frozen DMF $\tau = 0.53 \text{ s}$ is one of the longest ever reported for intramolecular ET in an artificial photosynthetic system. The lifetime is comparable with that of the bacteriochlorophyll dimer radical cation ((BChl)₂^{•+})–secondary quinone radical anion (Q_B^{•-}) ion pair ($\approx 1 \text{ s}$) in natural bacterial photosynthetic reaction centres.^[118]

The organometallic ferrocene (Fc) is applied as a suitable electron donor for the imitation of photosynthetic reaction centres, due to well-defined Fc/Fc⁺ redox states and the ability to reduce the S₁ excited state of the porphyrin moiety.^[120]

Furthermore, fullerene (C₆₀) is utilized by Fukuzumi et al. as a potent 3D acceptor with small ET reorganization energy λ , since the uptake or release of electrons results in minimal structural (λ_i) or solvational (λ_o) changes. This derives from the large π -electron system together with the rigid and confined structure composed only of aromatic rings.^[105]

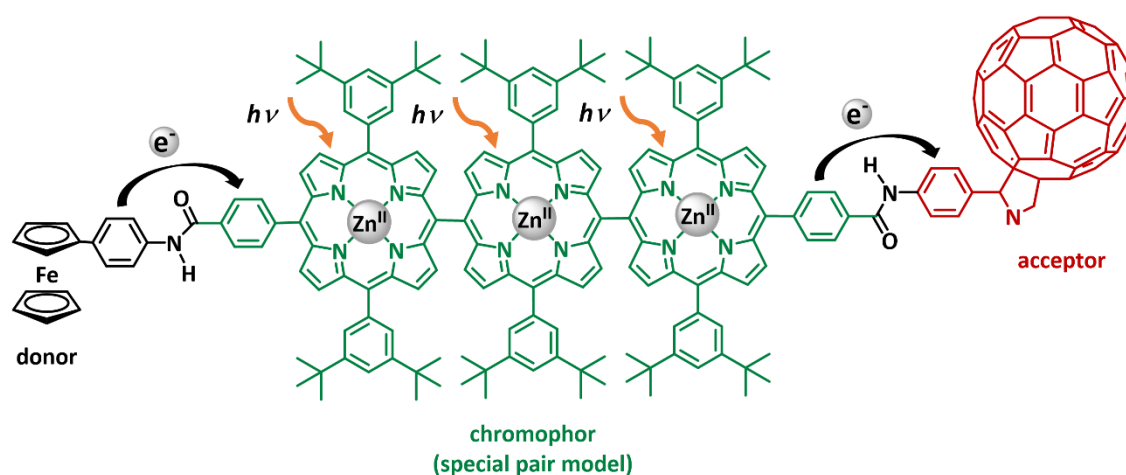


Figure 1.22 Structure of the Fc-(Zn(P))₃-C₆₀ pentad.^[105,118]

Suitable building blocks for artificial photoinduced ET are porphyrin derivatives, due to their important role in photosynthetic reaction centers.^[2,8,111,112,114,115,120,124,125] Herein, they are represented via a zinc(II) porphyrin triad acting as the chromophore/bridge unit. As outlined above, porphyrins have unique absorption features and highly delocalized π -systems ideal for

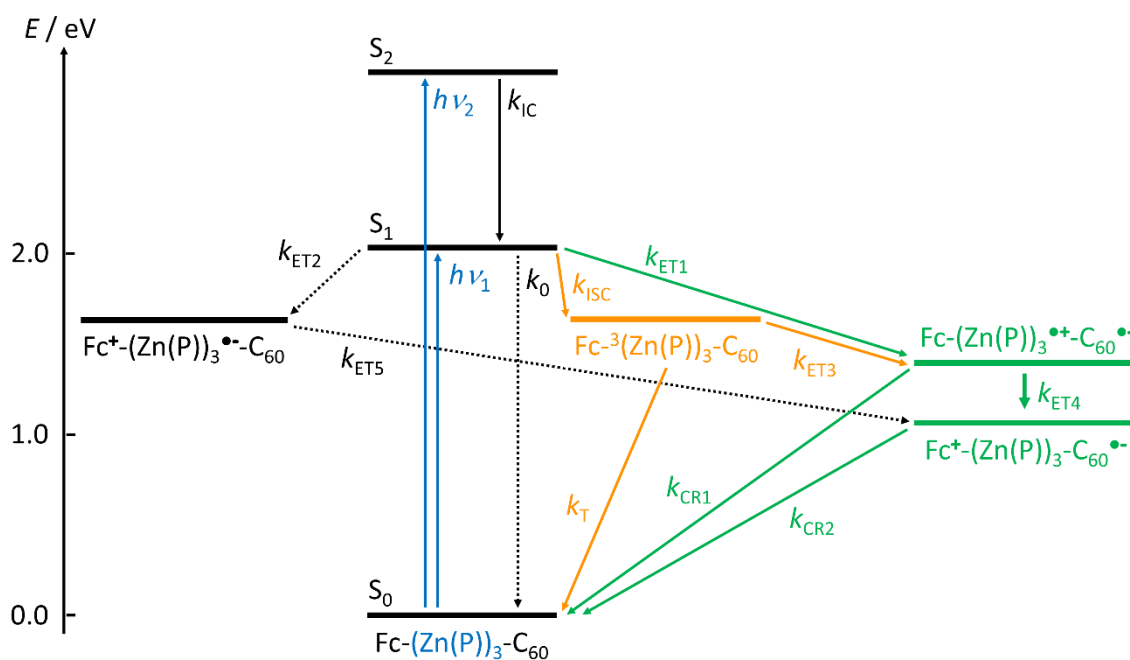


Figure 1.23 Energy level diagram of the Fc-(Zn(P))₃-C₆₀ pentad, including triplet and charge-separated states. Abbreviations: ET = electron transfer, CR = charge recombination, IC = internal conversion, ISC = intersystem crossing.^[105,118]

efficient ET, since the uptake or release of electrons is associated with a small reorganization energy λ with minimal structural and solvational changes upon ET.^[126] Therefore, porphyrins can serve as electron donors, acceptors, chromophores and bridges in photoinduced ET reactions.

A simplified and generalized energy level diagram describing the possible ET pathways towards the final CS state Fc^{•+}-(Zn(P))₃-C₆₀^{•-} is illustrated in **Figure 1.23**. Picosecond time-resolved transient absorption spectra in DMF after a 560 nm laser pulse revealed, that initial ET (k_{ET1}) occurs from Fc⁻¹(Zn(P))₃-C₆₀ to the C₆₀ moiety to generate Fc-(Zn(P))₃^{•+}-C₆₀^{•-} with a rate constant $k_{ET1} = 3.0 \times 10^9 \text{ s}^{-1}$ (determined from the fluorescence lifetime). The fluorescence lifetime measurement for the Fc-(Zn(P))₃ reference compound showed, that an initial ET (k_{ET2}) also takes place from the Fc to the ¹(Zn(P))₃ to produce Fc⁺-(Zn(P))₃^{•-}. However, the rate constant $k_{ET2} = 1.8 \times 10^8 \text{ s}^{-1}$ for this ET is significant smaller compared to k_{ET1} and therefore this deactivation pathway (via k_{ET5}) is negligible. EPR measurements were performed in frozen DMF under photoirradiation to determine the lifetime of the final CS state Fc^{•+}-(Zn(P))₃-C₆₀^{•-} via the slow decay of the characteristic broad organic signal attributable to C₆₀^{•-} ($g = 2.0004$), yielding $k_{CR2} = 1.9 \text{ s}^{-1}$.^[105,118]

The excellent performance of this system can be rationalized by the efficient charge separation and retarded charge recombination through the zinc(II) porphyrin triade. Nevertheless, such an extremely long lifetime of a charge-separated state could only be determined in frozen media,

since the dynamics of the intramolecular ET in model RCs in liquid media are dominated by the back ET. Furthermore, although C_{60} is a very potent electron acceptor, the received electrons are fully delocalized over the whole molecule and subsequent utilization of this reductive power is therefore strongly hindered.^[105,118]

Gold(III) porphyrins as efficient cationic electron acceptors for artificial photosynthesis

Porphyrin metalation with $KAuCl_4$ leads to a significant increase of the first reduction potential ($E[Au(TPP)]^+_{1/2}(\text{red}^1) = -0.97 \text{ V vs. Fc/Fc}^+$)^[127] compared with the corresponding zinc(II) porphyrins ($E[Zn(TPP)]_{1/2}(\text{red}^1) = -1.94 \text{ V vs. Fc/Fc}^+$)^[128] and consequently to an increase of the ET driving force ($-\Delta G^0$). Therefore, cationic gold(III) porphyrins are potent electron acceptors in porphyrin arrays. Indeed, the groups of Sauvage^[129–133], Crossley/Fukuzumi/Kadish^[65,134–139] and Hamarström/Odobel^[64,140–142] have shown that efficient and rapid ET ($k_{\text{ET}} = 10^{12} \text{ s}^{-1}$) occurs in artificial photosynthetic systems with cationic gold(III) porphyrins acting as electron acceptors together with a rather low back-electron transfer rate ($k_{\text{CR}} = 10^9 \text{ s}^{-1}$) both resulting in relatively long-lived charge-shifted states.^[64] Due to the π -conjugated bridges between the chromophore and the electron acceptor, the ET process is simplified and thus explains the high forward rates. The large driving force of the CR reaction leads to a hindered back-ET, since it is located in the Marcus inverted region ($-\Delta G^0 > \lambda$). Additionally, the group of Kadish assigned the slow CR rate to the trapping of the electron in the $5d_{x^2-y^2}$ orbital of gold, which is inhibiting the back ET.^[135,139]

An example for gold(III) porphyrins acting as potent electron acceptors is given by the zinc(II) phthalocyanine-oligo(phenylene-ethylene)-gold(III) porphyrine “donor-bridge-acceptor” dyad $[Zn(\text{Pc})\text{-Au}^{\text{III}}(\text{P})][\text{PF}_6]$ as illustrated in **Figure 1.24**.^[64]

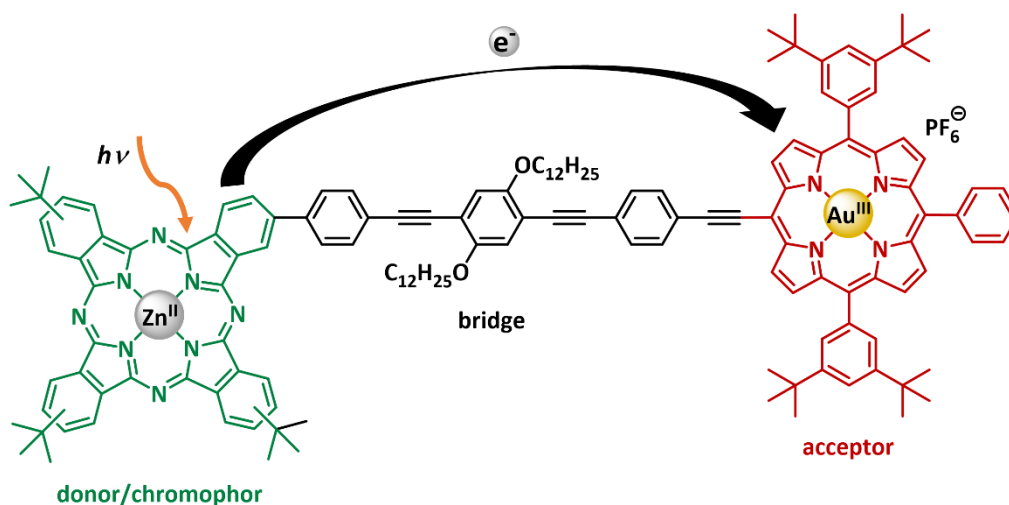


Figure 1.24 Structure of the zinc(II) phthalocyanine-oligo(phenylene-ethylene)-gold(III) porphyrine donor-bridge-acceptor dyad.^[64]

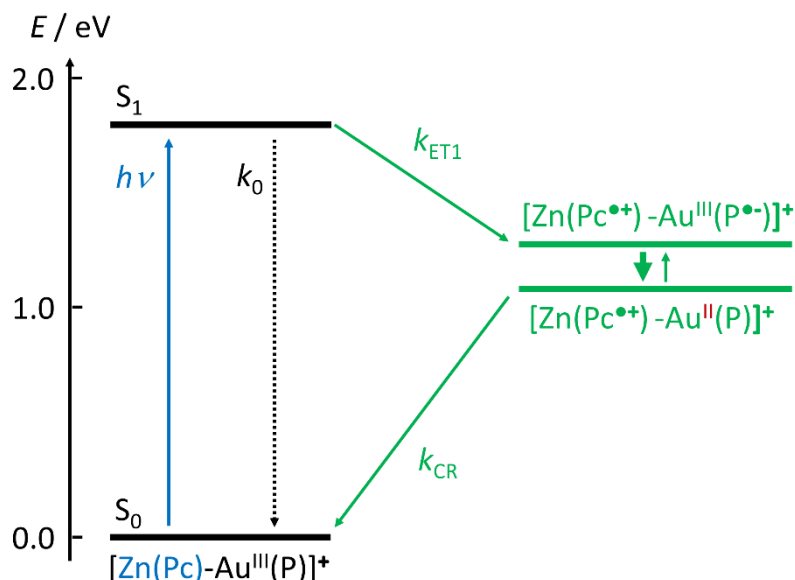


Figure 1.25 Energy level diagram of the $[\text{Zn}(\text{Pc})\text{-Au}^{\text{III}}(\text{P})][\text{PF}_6]$ dyad after photoexcitation with 680 nm (triplet state excluded). Abbreviations: ET = electron transfer, CR = charge recombination.^[64]

The system was designed to undergo long-range photoinduced ET using zinc(II) phthalocyanine as the chromophore and electron donor. Furthermore, an oligo(phenylene-ethylene) bridge was utilized to link the donor/chromophore Zn(Pc) with the electron acceptor $[\text{Au}^{\text{III}}(\text{P})]^+$, since this type of bridging unit has been shown to mediate ET over long distances and at very high rates.^[64]

A simplified and generalized energy level diagram describing the possible ET pathways towards the final charge-shifted state $[\text{Zn}(\text{Pc}^{\bullet+})\text{-Au}^{\text{II}}(\text{P})]^+$ is illustrated in **Figure 1.25** (triplet states excluded). Femtosecond time-resolved transient absorption spectra in benzonitrile after a 680 nm laser pulse revealed, that initial ET occurs from $^1\text{Zn}(\text{Pc})\text{-}$ to the $[\text{Au}^{\text{III}}(\text{P})]^+$ moiety with a very high rate constant $k_{\text{ET}} = 1.0 \times 10^{12} \text{ s}^{-1}$, whereas the CR rate $k_{\text{CR}} = 1.0 \times 10^9 \text{ s}^{-1}$ is significantly lower.^[64]

Hammarström, Odobel and co-workers attributed this retarded CR behavior to the aforementioned trapping of the electron on the gold center. Hence, the initial charge-shifted state $[\text{Zn}(\text{Pc}^{\bullet+})\text{-Au}^{\text{III}}(\text{P}^{\bullet-})]^+$ rapidly relaxes so that the gold ion is reduced instead of the porphyrin ring and therefore yielding the final charge-shifted state $[\text{Zn}(\text{Pc}^{\bullet+})\text{-Au}^{\text{II}}(\text{P})]^+$ with gold in the +II oxidation state. This valence-isomerization process has a significant effect regarding the electronic coupling, since the electron is mainly situated in metal-based orbitals and subsequent interaction with the bridge is far less compared to if it were situated on the porphyrin ring. However, no experimental proof was given that a gold(II) porphyrin species is involved during this photoinduced ET transfer process.^[64,139]

2 Aim of Work

The objective of this work is to investigate the key steps of photosynthesis, namely light harvesting, charge separation and electron transfer, via a biomimetic model compound. This artificial photosynthetic system should be composed of porphyrin derivatives, since they are similar to natural pigments within the light-harvesting complex and the photosynthetic reaction centre. The main focus of this work is on gold(III) porphyrins, which are suitable ingredients in photoinduced electron transfer chains with the gold(III) porphyrin acting as an electron acceptor.

The effort to achieve this goal can be categorised into three consecutive steps.

The first objective is the determination of the site of gold(III) porphyrin reduction, namely ligand or metal centred, which has been discussed controversially in literature and could not be unambiguously defined. For this purpose, a *meso*-tetraarylporphyrinato gold(III) cation reference system bearing different functional groups at the aryl substituents (COOMe, COOH, NO₂, NH₂, NHAc, H, O^tBu, CF₃) should be prepared and characterised to examine the potential influence on the site of reduction. After selective one-electron reduction with cobaltocene, the preferred location of spin density may be probed by EPR spectroscopy (Au^{II}: 5d⁹ metallo radical; (P^{•-}): organic π-radical anion).

The second objective deals with the synthesis, isolation and characterisation of a stable neutral gold(II) complex of a porphyrin derivative to obtain a deeper grasp of gold in the oxidation state +II. In this context, the porphyrin macrocycle should be applied as a potent stabilizing ligand by blocking the typical reactivity patterns of other labile gold(II) species, namely dimerization and disproportionation. After successful isolation, purification and characterisation, the reactivity of the gold(II) complex towards water, acids, oxygen and nitrosobenzene should be probed. Finally, the mode-of-action of gold(III) porphyrins (potent anti-cancer drug) inside tumor cells should be simulated by using BNAH as the reducing agent in the presence of a base (NADH model compound), since gold(II) porphyrin intermediates may play an important role in the induction of apoptosis.

The work is completed with the thorough analysis of three novel amide-bridged zinc(II)-gold(III) bis(porphyrin) dyads [Zn^{II}(P)-Au^{III}(P)]⁺ regarding gold(II) porphyrins as key intermediates in PET reactions. These artificial photosynthetic systems should be designed to undergo ultrafast PET using zinc(II) porphyrin amino acid derivatives as chromophores and electron donors and

gold(III) porphyrin amino acid derivatives as electron acceptors, which are connected by a π -conjugated amide bridge to establish a very efficient and directed electron transfer. After photoexcitation, the resulting charge-shifted states $[\text{Zn}(\text{P}^{\bullet+})\text{-Au}^{\text{II}}(\text{P})]^+$ are supposed to be probed by femtosecond transition absorption spectroscopy and should be employed in bimolecular reactions with amines as sacrificial electron donors to yield stable gold(II) dyads $\text{Zn}(\text{P})\text{-Au}^{\text{II}}(\text{P})$. Thus, spectroscopic evidence for gold(II) intermediates during photoredox catalysis should be accessible. The latter should be further confirmed by reducing aromatic azides with intermediary generated gold(II) species during a photoredox catalysis experiment.

3 Results and Discussion

The outcome of this dissertation has been published/submitted as scientific articles in/to peer-reviewed chemistry journals. These articles are reprinted here with the permission of the respective publishers.

The article in section 3.1 shows the successful synthesis and characterisation of *meso*-tetraarylporphyrinato gold(III) cations bearing different functional groups at the aryl substituents (COOMe, COOH, NO₂, NH₂, NHAc, H, O^tBu, CF₃). Their reversible one-electron reductions were studied by EPR spectroscopy as well as by density functional theory (DFT) calculations to clarify the influence of the aryl substituents on the preferred location of the spin density, namely gold centred or porphyrin centred (Au^{II}: 5d⁹ metallo radical; (P^{•-}): organic π-radical anion).

In section 3.2, the synthesis, isolation, characterization and reactivity of a mononuclear gold(II) complex is presented. The unprecedentedly stable neutral gold(II) complex of a porphyrin derivative, which adopts a second-order Jahn-Teller distorted 2+2 coordination mode, is studied in detail by using a combination of NMR, ultraviolet-visible (UV-vis), EPR and infrared (IR) absorption spectroscopy, as well as magnetic susceptibility, X-ray diffraction (XRD) analyses and theoretical methods. In addition, the role of gold(III) porphyrins in the induction of apoptosis is simulated by using BNAH (NADH model compound) as reducing agent in order to yield the presumably active gold(II) species. Furthermore, the reactivity of the gold(II) porphyrin towards water, acids, oxygen and nitrosobenzene is discussed.

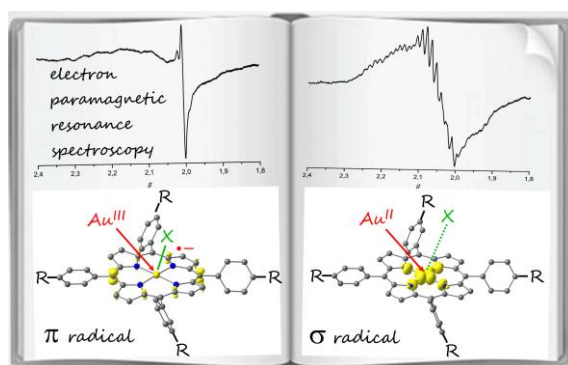
The role of gold(II) porphyrins as key intermediates in PET reactions is discussed in section 3.3. Therefore, the synthesis, characterization, electrochemical properties and photoinduced processes of three novel zinc(II)-gold(III) bis(porphyrin) dyads are presented in the context of solar to chemical energy transformation. The long-lived photoinduced CSh states [Zn(P)^{•+}-Au^{II}(P)]⁺ are examined via femtosecond transient absorption spectroscopy. Additionally, an attempt at understanding the electronic nature of the reduced (amine as sacrificial electron donor) and therefore stabilised CSh states Zn(P)-Au^{II}(P) is undertaken based on UV-Vis, EPR, gold L₃-edge X-ray absorption near edge structure (XANES) and paramagnetic ¹H NMR spectroscopy as well as by DFT calculations. Furthermore, the potential role of gold(II) intermediates during photoredox catalysis is investigated by the reduction of aromatic azides to anilines, since the gold(II) site in Zn(P)-Au^{II}(P) dyads is thermodynamically and kinetically competent to reduce azides.

Section 3.4 presents the intrinsic superoxide dismutase activity (SOD) of manganese oxide (MnO) nanoparticles. Gratifyingly, the magnetic resonance imaging contrast is simultaneously enhanced due to this SOD reaction. Therefore, MnO nanoparticles can be used for both, the imaging of tumor tissue and simultaneously for treating oxidative-stress-promoted tumor progression. The synthetic and spectroscopic work shown in this publication has been carried out by Ruben Ragg (group of Prof. Dr. W. Tremel, Johannes Gutenberg University Mainz), Sebastian Preiß assisted in the setup and evaluation of the EPR experiments regarding the superoxide treatment of MnO nanoparticles.

3.1 Gold(III) tetraarylporphyrin amino acid derivatives: ligand or metal centred redox chemistry?

Sebastian Preiß, Jasha Melomedov, Anica Wünsche von Leupoldt and Katja Heinze

Chem. Sci. **2016**, *7*, 596–610.



Chemical reduction of the gold(III) porphyrins via cobaltocene results in broad and characteristic EPR resonances in accordance with a gold centred radical displaying hyperfine coupling to ^{197}Au and ^{14}N . The reduction of the nitro derivative shows a further nitro π -radical anion valence isomeric species.

Author Contributions

The synthesis and characterisation of the gold(III) porphyrins as well as the spectroelectrochemical and EPR experiments were performed by Sebastian Preiß. [REDACTED] contributed to the experimental design and [REDACTED] helped with the EPR simulation. [REDACTED] performed the DFT calculations and wrote the manuscript.

Supporting Information

Supporting Information for this article (without Cartesian coordinates from DFT calculations) is found on pp. 91.

For full supporting information, refer to:

<http://www.rsc.org/suppdata/c5/sc/c5sc03429a/c5sc03429a1.pdf>

Reprinted with permission from:

S. Preiß, J. Melomedov, A. Wünsche von Leupoldt, K. Heinze, *Chem. Sci.* **2016**, *7*, 596–610.

Copyright 2016 the Royal Society of Chemistry.



CrossMark

click for updates

Cite this: *Chem. Sci.*, 2016, 7, 596

Gold(III) tetraarylporphyrin amino acid derivatives: ligand or metal centred redox chemistry?†

Sebastian Preiß, Jascha Melomedov, Anica Wünsche von Leupoldt and Katja Heinze*

Meso tetraarylporphyrinato gold(III) cations bearing different substituents at the aryl substituents (COOMe, COOH, NO₂, NH₂, NHAc, H, O^tBu, CF₃) were prepared and characterised. Their reversible one-electron reductions were studied by (spectro)electrochemical means as well as by selective chemical one-electron reduction using cobaltocene. The preferred location of the spin density, namely gold centred or porphyrin centred, was probed by electron paramagnetic resonance spectroscopy (*g* values, ¹⁹⁷Au hyperfine coupling) as well as by density functional theory calculations (spin densities). In all cases studied experimentally and theoretically, the gold(II) valence isomer (5d⁹ electron configuration) is preferred over the porphyrin π radical anion. In the hexafluorophosphate salt of the nitro derivative a further nitro π radical anion valence isomeric species is significantly populated. In the presence of chloride ions this nitro π radical anion/Au^{II} valence isomeric equilibrium evolves towards the porphyrin π radical anion. The electronic structures of the nitro π radical and the Au^{II} σ radical valence isomers (5d_{x²-y²} orbital) could be calculated by DFT methods. The electron transfer pathway between the nitro π radical anion and the Au^{II} valence isomer is well described by the location of the hexafluorophosphate counterion, the Au–N distances (corresponding to the totally symmetric stretching vibration), the symmetric stretching mode of the NO₂ substituent and a *meso*-nitrophenyl rotation. The specific geometric and electronic properties of the favoured gold(II) σ radical valence isomer, namely counterion dislocation and σ symmetry of the redox orbital, might stabilise charge-shifted states [(gold(II) porphyrin)-donor^{•+}] by retarding the back electron transfer to give the ground state (gold(III) porphyrin)-donor. This will guide the design of (photo-induced) electron transfer pathways with tetraarylporphyrinato gold(III) complexes as electron acceptors.

Received 11th September 2015

Accepted 16th October 2015

DOI: 10.1039/c5sc03429a

www.rsc.org/chemicalscience

Introduction

Synthetic metallo porphyrins are of increasing interest due to their suitability as chromophores, as well as electron and hole acceptors in artificial photosynthetic systems,¹ due to their catalytic and sensing properties,² due to their medical applications³ as well as due to their propensity to stabilise unusual metal oxidation states. Specifically, porphyrinato gold(III) complexes have evolved as efficient anticancer drugs.⁴ Furthermore, they are catalysts for the cycloisomerization of allenones.⁵ Recently, gold clusters with face-on coordinated free-base porphyrins have been reported.⁶ Finally, gold(III) porphyrins are suitable ingredients in photoinduced electron

transfer chains with the gold(III) porphyrin acting as electron acceptor.⁷

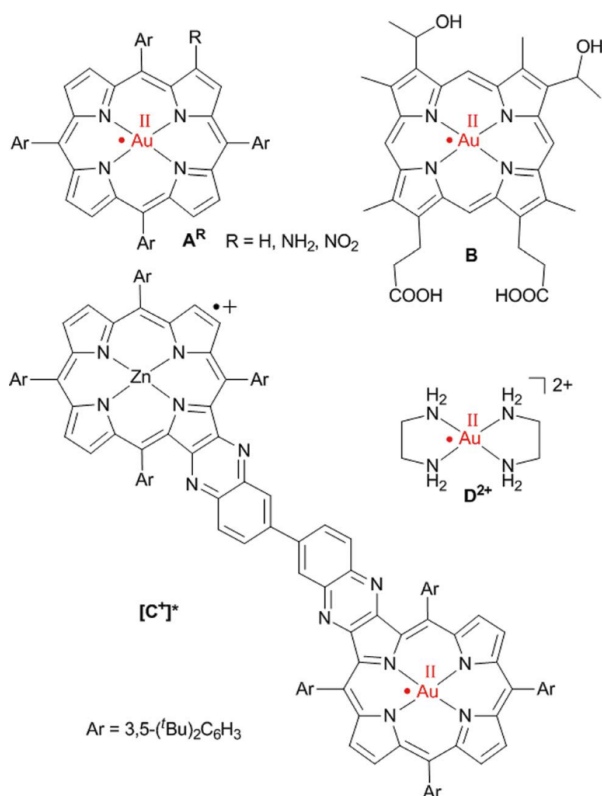
The site of gold(III) porphyrin reduction, namely ligand or metal centred, has been discussed controversially. Based on early UV/Vis spectroscopic and theoretical studies the products of the reduction of gold(III) porphyrins had been described as porphyrin-centred π radical anions.⁸ In a seminal paper, Kadish, Fukuzumi and Crossley provided compelling EPR spectroscopic evidence that the one-electron reduction of [A^{III}]⁺ to A^{II} is metal centred giving gold(II) porphyrins (Scheme 1).⁹ Only a few ligand types, such as thiolates or thioethers, are capable to stabilise mononuclear gold in the oxidation state +II.¹⁰ Further outstanding examples are the fluorosulfate¹¹ and xenon complexes¹² of Au^{II}. Nitrogen donor ligands such as porphyrinato ligands have been reported to stabilise Au^{II} with respect to disproportionation and dimerization^{9,13} to [Au₂^{II}] species¹⁴ as well (Scheme 1, **A**, **B**, [C⁺]*). Disproportionation and dimerisation of [Au^{II}(en)₂]²⁺ D²⁺ has been suppressed by encapsulation in the pores of a zeolite (en = ethylenediamine).¹⁵

The gold(II) porphyrin A^{II} (Scheme 1) prepared by reduction of the corresponding gold(III) porphyrin cation [AH]⁺ with the strongly reducing naphthalene radical anion yielded a broad

Institute of Inorganic Chemistry and Analytical Chemistry, Johannes Gutenberg-University of Mainz, Duesbergweg 10-14, 55128 Mainz, Germany. E-mail: katja.heinze@uni-mainz.de; Fax: +49-6131-39-27277; Tel: +49-6131-39-25886

† Electronic supplementary information (ESI) available: NMR and IR spectra, spectral changes upon reduction of [Au(TPP)]PF₆, [4a]PF₆, [4b]PF₆, [4c]PF₆, EPR spectra of **1a** in the absence and presence of chloride, DFT calculations of Au(TPP), Cu(TPP), **4a**, **4b** and **4c**, Cartesian coordinates of all optimised structures. See DOI: 10.1039/c5sc03429a





Scheme 1 Genuine mononuclear gold(II) complexes with planar N₄ coordination according to EPR spectroscopic results.^{9,13,15}

EPR resonance centred at $g_{av} = 2.06$.⁹ Hyperfine coupling to ^{197}Au has been reported for the central g line [$A(^{197}\text{Au}) = 27$ G at 113 K; $I(^{197}\text{Au}) = \frac{3}{2}$, natural abundance 100%].⁹ An EPR resonance with a significantly smaller peak-to-peak distance was observed for the gold(II) complex **B** of hematoporphyrin IX with $g_{\perp} = 2.035$, $g_{\parallel} = 1.970$ and $A_{\perp}(^{197}\text{Au}) = A_{\parallel}(^{197}\text{Au}) = 15$ G at 130 K suggesting a less pronounced metal character (Scheme 1).^{13b,e} The charge-shifted state $[\text{C}^*]^+$ of a Zn^{II}-Au^{III} bis(tetraarylporphyrin) C^+ yielded an EPR resonance with $g = 2.182, 2.043, 1.979$ and $A(^{197}\text{Au}) = 180, 14, \text{n.r.}$ G in frozen toluene solution at 143 K for the gold(II) centre (Scheme 1).^{13d} The gold complex $[\text{Au}(\text{en})_2]^{2+}$ D^{2+} with the pure σ -donor ligand ethylenediamine trapped in a zeolite shows $g_{\parallel} = 2.239$, $g_{\perp} = 2.051$, $A_{\parallel}(^{197}\text{Au}) = 188$ G and $A_{\perp}(^{197}\text{Au}) = 22$ G at room temperature (Scheme 1).¹³ Gold(III)-centred reductions have been associated with a significantly higher reorganization energy (*ca.* 1.25 eV) than porphyrin-based reductions (*ca.* 0.6 eV).^{13c} The large reorganization energy renders gold(III) porphyrins suitable electron acceptors in photoelectron transfer schemes.⁷ Moreover, gold(III)-associated counterions should dissociate upon Au^{III} to Au^{II} reduction further retarding the back-electron transfer. For instance, chloride is associated to the Au^{III} centre in solid **AuCl(TPP)** by electrostatic forces with a gold chloride distance of 3.01(1) Å.¹⁶ Unfortunately, no solid structures of porphyrinato gold(II) complexes have been reported so far and further experimental or theoretical studies are lacking.

We had previously reported synthetically versatile *meso*-substituted tetraaryl porphyrins with *trans*-AB₂C substitution pattern including A = nitrophenyl, aminophenyl or amido-phenyl, C = phenyl carboxylic acid or ester and B = EWG or EDG substituted aryl groups.¹⁷ These porphyrins can be metallated¹⁷ and assembled to multiporphyrin amides,^{17b,17c} electron donor substituted amide-linked dyads^{17a} as well as electron donor (ferrocene) and electron acceptor (quinone) substituted amide-linked triads and tetrads^{17b} with well defined sequences from the N-terminus to the C-terminus. The different *meso* substituents of the porphyrin amino acids at the B position can be used to modulate the solubilities and to fine-tune the redox potentials which allows to design redox gradients.¹⁷

With this family of porphyrins in hand, we disclose in this contribution the factors that control the relative stabilities of a gold(II) porphyrin and its valence isomeric gold(III) porphyrin radical anion. We report novel *meso*-substituted Au^{III} porphyrin amino acid derivatives with *trans*-AB₂C substitution pattern for potential incorporation into electron transfer chains *via* amide bonds. These gold(III) porphyrins were inspected by cyclic voltammetry, UV/Vis spectroelectrochemistry and by EPR spectroscopy upon selective one-electron reduction with cobaltocene. We provide strong EPR and UV/Vis spectroscopic evidence that all singly reduced gold(III) porphyrins are well described as gold(II) porphyrins essentially irrespective of the *meso*-substituents A, B and C and that the porphyrin radical anions are higher energy valence tautomers of the ground state Au^{II} valence isomers. Detailed EPR parameters of the gold(II) porphyrinato complexes were obtained by spectral simulations of the experimental spectra (g tensors, (super)hyperfine couplings, valence isomer ratios). The experimental data are corroborated and interpreted with the aid of density functional theory (DFT) calculations in the framework of electron transfer theory.

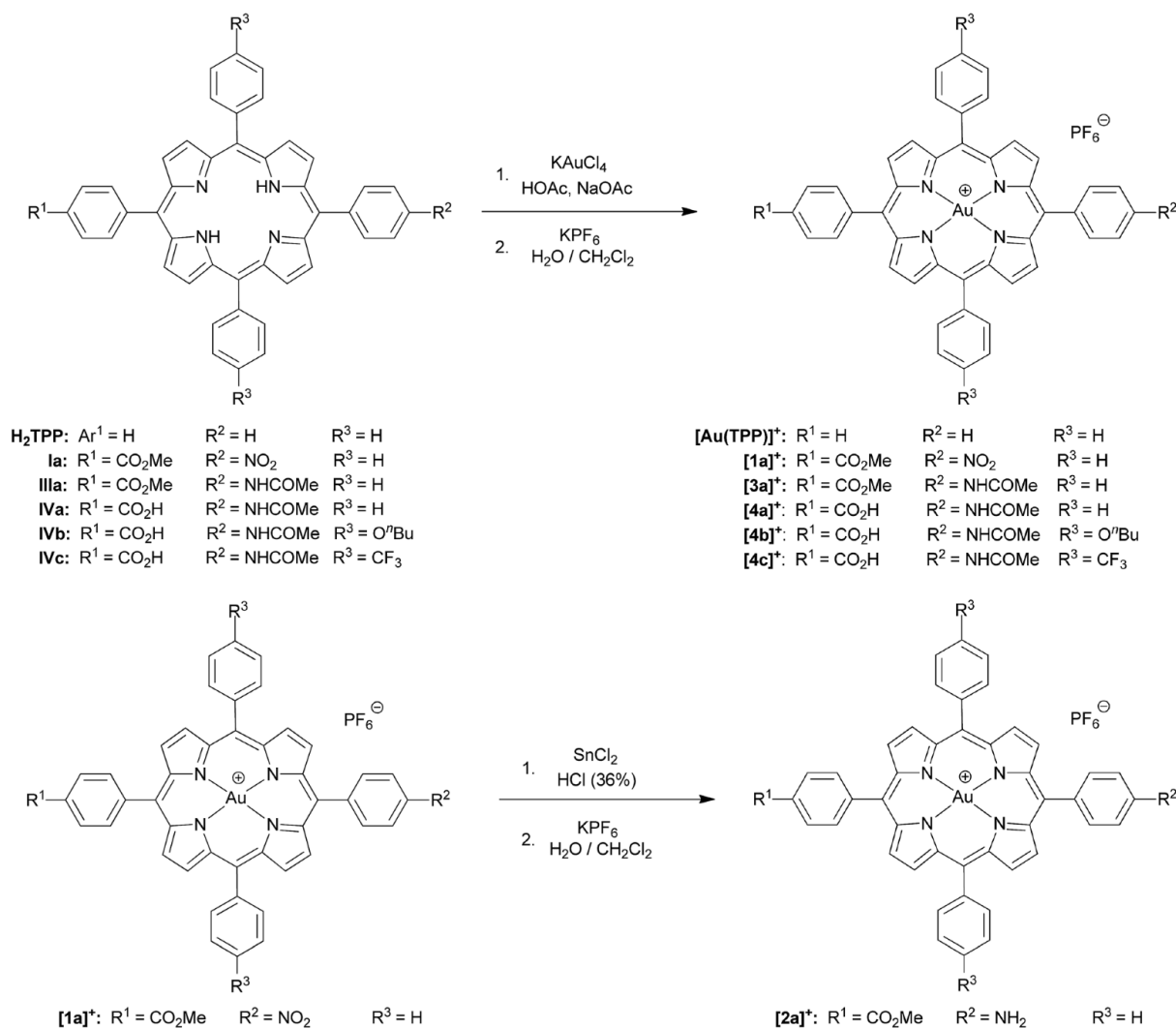
Results and discussion

Synthesis of free-base porphyrins and (porphyrinato)gold(III) complexes (series [1a]⁺-[3a]⁺ and series [4a]⁺-[4c]⁺)

The free-base porphyrins **Ia-IVc** were prepared according to literature procedures.¹⁷ Metallation of the free-base porphyrins was successful with potassium tetrachlorido aurate(III) in the presence of HOAc/NaOAc (Fleischer's route¹⁸), except for amino-substituted porphyrin **Ia** (Scheme 2). Best yields were obtained using four equivalents of KAuCl₄ giving the cationic aurated porphyrins as poorly soluble tetrachlorido aurate salts.

Auration of the amino-substituted porphyrin **Ia** with KAuCl₄/HOAc/NaOAc according to Fleischer's method resulted in acylation of the amino group. Auration of **Ia** according to Sauvage's protocol using $[\text{Au}^{\text{I}}(\text{tht})_2][\text{BF}_4]$ followed by disproportionation to Au^{III} and Au⁰ was unsuccessful as well (tht = tetrahydrothiophene).¹⁹ Thus, **[2a]⁺** was prepared *via* metallation and ion exchange of nitroporphyrin ester **Ia** to give **[1a]⁺** **[PF₆]**, followed by reduction of the nitro group of **[1a]⁺** with SnCl₂/HCl to give the aurated amino-substituted porphyrin **[2a]⁺** **Cl** (Scheme 2). During this procedure, the gold(III) ion was neither reduced nor removed. Hence, the Au^{III} porphyrins are



Scheme 2 Synthesis of (porphyrinato)gold(III) complexes ([Au(TPP)]⁺, series [1a]⁺, [2a]⁺, [3a]⁺ and series [4a]⁺, [4b]⁺, [4c]⁺).

stable under protic conditions. Counterion exchange of [Au(porph)][AuCl₄] or [2a]Cl with KPF₆ yielded the corresponding soluble hexafluorophosphate salts which are conveniently purified by column chromatography.

Characterization of (porphyrinato)gold(III) complexes (series [1a]⁺–[3a]⁺ and series [4a]⁺–[4c]⁺)

Ester-substituted complexes [1a][PF₆]–[3a][PF₆] are sufficiently soluble in dichloromethane. However, THF is required for acids [4b][PF₆] and [4c][PF₆] and even methanol is necessary for [4a][PF₆] in order to acquire NMR spectra with a satisfactory signal-to-noise ratio. This shows that the counterion and the *meso* substituents determine the solubility. All gold(III) complexes were characterised by ¹H NMR, ¹³C NMR, ³¹P NMR and 2D NMR spectroscopy, IR spectroscopy and high-resolution mass spectrometry. The proton NMR spectra display the expected number and intensities of resonances. The chemical shifts vary according to the substitution patterns paralleling the shifts of

the corresponding free-base porphyrins **Ia–IIIa** and **IVa–IVc**. The CH₃-ester, NH₂-amine and CH₃-amide substituents display characteristic resonances at δ = 4.1, 4.7, 2.2 ppm, respectively. The [PF₆][−] counterions show the characteristic septet at δ = −144 ppm in the ³¹P NMR spectra. Upon auration the characteristic high-field pyrrole NH resonances of the free-base porphyrin disappear. Furthermore, auration of the free-base porphyrins consistently shifts the pyrrole CH proton resonances to lower field by 0.5 ppm, in accordance with the positive charge of the metal centre. In the IR spectra, characteristic absorptions for group vibrations are found for the ester, amine, amide, nitro, trifluoromethyl and acid substituents at around 1719, 1618, 1690, 1520/1346, 1324 and 1716 cm^{−1}, respectively. The [PF₆][−] counterions display absorptions for the PF stretching and deformation modes at 835–843 and 556–558 cm^{−1}, respectively. ESI mass spectra fully confirm the integrity and stability of the complex cations displaying peaks at *m/z* values corresponding to the intact complex cation (see Exp. section).



With the exception of the electron-rich $R^3 = O^tBu$ -substituted complex **[4b]⁺** all gold(III) porphyrinato complexes **[1a]⁺**, **[2a]⁺**, **[3a]⁺**, **[4a]⁺** and **[4c]⁺** show hypsochromically shifted Soret bands as compared to their corresponding free-base porphyrins **Ia**, **IIa**, **IIIa**, **IVa** and **IVc** (*hypso* porphyrins^{8b}). In all cases, the number of Q bands is reduced from four to two (or even to one) as expected for metalloporphyrins with local D_{4h} symmetry of the porphyrin core. Expectedly, gold(III) porphyrinato complexes are non-emissive at room temperature in fluid solution as exemplarily checked for **[1a][PF₆]**, **[3a][PF₆]** and **[4c][PF₆]**.^{8b,20}

Redox chemistry of (porphyrinato)gold(III) complexes (series **[1a]⁺**–**[3a]⁺** and series **[4a]⁺**–**[4c]⁺**)

Several reversible reductions are observed for cations **[1a]⁺**, **[2a]⁺**, **[3a]⁺**, **[4b]⁺** and **[4c]⁺** 10^{-3} M in 0.1 M [^tBu₄N][PF₆]/THF solution (Fig. 1 and 2, Table 1). For solubility reasons complex **[4a]⁺** was measured in MeOH and the solvent window of MeOH allows for only a single reversible reduction wave to be observed (Fig. 2, Table 1). All potentials are given relative to the ferrocene/ferrocenium couple. As expected from substituent effects, **[1a]⁺** is more easily reduced to **1a** (−0.92 V) than **[Au(TPP)]⁺** to **Au(TPP)** (−0.97 V), while **[2a]⁺** (−0.99 V) is more difficult to reduce. Similarly, the potentials shift to more negative values in the series **[4c]⁺** (−1.00 V), **[4a]⁺** (−1.02 V) and **[4b]⁺** (−1.08 V), which is again explicable by the increasing electron donating

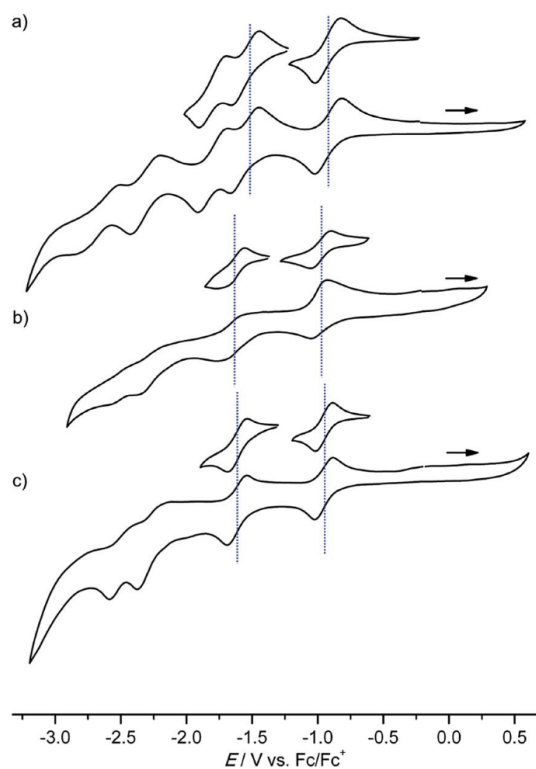


Fig. 1 Cyclic voltammograms of (a) **[1a]⁺**, (b) **[2a]⁺** and (c) **[3a]⁺** 10^{-3} M in 0.1 M [^tBu₄N][PF₆]/THF solution; potentials referenced against the ferrocene/ferrocenium couple.

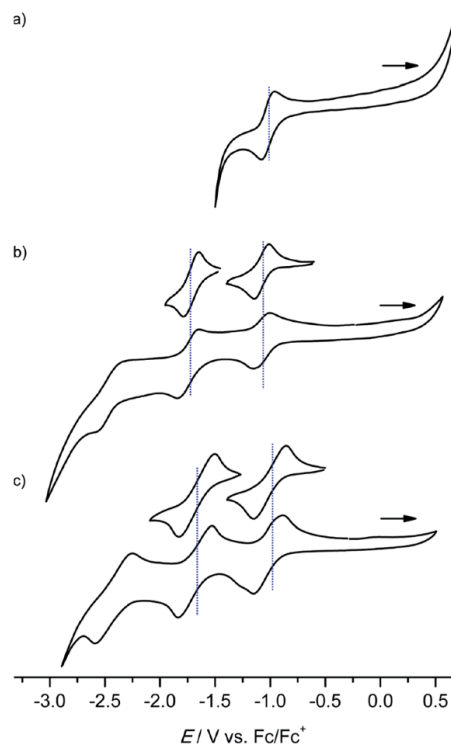


Fig. 2 Cyclic voltammograms of (a) **[4a]⁺** (MeOH), (b) **[4b]⁺** and (c) **[4c]⁺** 10^{-3} M in 0.1 M [^tBu₄N][PF₆]/THF solution; potentials referenced against the ferrocene/ferrocenium couple.

nature of the substituents (CF₃, H, O^tBu). Similar to the corresponding free-base porphyrins the shifts are only small.¹⁷ The second reduction is especially facile with the electron withdrawing NO₂ substituent (**1a**/**[1a][−]**; −1.55 V). The nitro derivative **[1a]⁺** shows even further reversible reductions. Hence, one of the **[1a]⁺** reductions might be associated to the nitro substituent itself (*vide infra*).

The differences between the first and second reduction potentials amount to 0.60–0.68 V which corresponds to very high comproportionation constants of $K_C > 10^{10}$ for the neutral complexes.²¹ Hence, disproportionation of the neutral complexes into the corresponding cations and anions can be safely neglected and spectral signatures after one-electron reduction will essentially be associated with the neutral complexes.

All gold(III) complexes were reduced electrochemically to the neutral species in an optically transparent thin layer electrochemical (OTTLE) cell using THF as solvent (MeOH for **[4a]⁺**). In all cases, isosbestic points were observed corroborating the reversible nature of the first reduction process (Fig. 3 and ESI[†]). The shifts of the Soret and Q bands as well as the observed isosbestic points closely resemble those found for the **[Au(TPP)]⁺**/**Au(TPP)** process in THF (ESI[†]) and in pyridine^{13c} or in PhCN.⁹ In all cases, except for the **[2a]⁺**/**2a** and **[4b]⁺**/**4b** redox couples with the strongly electron-donating NH₂ and O^tBu substituents, the intensity of the Soret band decreases while for **[2a]⁺**/**2a** and **[4b]⁺**/**4b** the intensity increases (Fig. 3b and ESI[†]). A



Table 1 Redox potentials (peak potentials in parentheses) of porphyrinato gold(III) complexes measured 10^{-3} M in 0.1 M [t Bu₄N][PF₆]/THF solution, potentials given relative to ferrocene/ferrocenium

	$E_{1/2}$ ([Au(P)] ⁺ /Au(P))	$E_{1/2}$ (Au(P)/[Au(P)] ⁻)	$E_{1/2}$ ([Au(P)] ⁻ /[Au(P)] ²⁻)	$E_{1/2}$ ([Au(P)] ²⁻ /[Au(P)] ³⁻)
[Au(TPP)][PF ₆]	-0.97 (-1.06/-0.88)	-1.65 (-1.73/-1.57)	-2.34 (-2.43/-2.25)	—
1a [PF ₆]	-0.92 (-1.02/-0.82)	-1.55 (-1.66/-1.44)	-1.80 (-1.90/-1.70)	-2.31 (-2.42/-2.20)
2a [PF ₆]	-0.99 (-1.06/-0.91)	-1.67 (-1.78/-1.56)	-2.27 (-2.38/-2.16)	-2.51 (-2.56/-2.45)
3a [PF ₆]	-0.96 (-1.02/-0.89)	-1.63 (-1.70/-1.55)	-2.28 (-2.37/-2.19)	-2.50 (-2.58/-2.41)
4a [PF ₆] ^a	-1.02 (-1.08/-0.96)	^b	^b	^b
4b [PF ₆]	-1.08 (-1.15/-1.01)	-1.72 (-1.79/-1.65)	-2.46 (-2.57/-2.34)	—
4c [PF ₆]	-1.00 (-1.15/-0.87)	-1.67 (-1.83/-1.50)	-2.42 (-2.58/-2.25)	—

^a In MeOH. ^b Outside solvent window.

similar hyperchromic effect has been observed for the [A^{NH2}]⁺/A^{NH2} couple with the amino group attached to a porphyrin *beta* position.^{13c}

For chemical reductions, the gold(III) porphyrin complexes were dissolved in CH₂Cl₂ (**1a**[PF₆]-**1c**[PF₆]), THF (**4b**[PF₆]/**4c**[PF₆]) or MeOH (**4a**[PF₆]) (ca. 5 mM). In order to definitely

prevent overreduction, these solutions were treated with slightly substoichiometric amounts of CoCp₂ ($E_{1/2} = -1.33$ V in CH₂Cl₂ vs. Fc/Fc⁺ (ref. 22)) in an EPR tube. The redox potential of CoCp₂ is perfectly in-between the first and second reduction of the gold porphyrins (Fig. 1 and 2) further avoiding over-reduction. The reaction mixture in the tube was immediately frozen by immersing into liquid nitrogen and subjected to X-band EPR spectroscopy. Hence, we obtained significantly better resolved EPR spectra than previously reported for neutral porphyrinato gold complexes prepared by reduction of [A^H]⁺ with the strongly reducing naphthalene radical anion in DMF (ca. -3 V vs. Fc/Fc⁺ (ref. 22)).⁹ In this case some over-reduction might have been occurred blurring the hyperfine couplings to gold and nitrogen nuclei.

Indeed, **Au(TPP)** as prepared by reduction of [Au(TPP)]⁺ by CoCp₂ in CH₂Cl₂ shows a well-resolved EPR pattern which could be reasonably simulated by a rhombic *g* tensor with hyperfine interaction to a single ¹⁹⁷Au nucleus ($I = \frac{3}{2}$; natural abundance 100%) and superhyperfine coupling to four ¹⁴N nuclei ($I = 1$, natural abundance 99.6%). The high resolution allows a very good estimation of the high-field parameters while the low-field parameters are less well-resolved (Table 2, Fig. 4). Compared to the isoelectronic **Cu(TPP)** complex (^{63/65}Cu; $I = \frac{3}{2}$; combined natural abundance 100%; $g_1 = 2.197$, $g_2 = g_3 = 2.054$)^{17d} the metal coupling constant A_1 [A_1 (¹⁹⁷Au) = 43 G; A_1 (^{63/65}Cu) = 197 G (ref. 17d)] is significantly reduced in **Au(TPP)**. This suggests a more covalent character of the Au^{II}-N bonds compared to the Cu^{II}-N bonds in their respective TPP²⁻ complexes. For [C⁺]* with strongly electron donating *meso* substituents at the gold porphyrin a much larger hfc to ¹⁹⁷Au has been reported [A_1 (¹⁹⁷Au) = 180 G].^{13d} In accordance with the stronger nephelauxetic effect of porphyrins, complex **D**²⁺ with the pure σ donor ligand ethylenediamine features a significantly larger hyperfine coupling to ¹⁹⁷Au than **Au(TPP)** as well.¹⁵

For complexes **1a-3a** the broad EPR resonance corresponding to the Au^{II} valence isomer is less well resolved due to the lower symmetry and hence different superhyperfine interactions (Fig. 5). Furthermore, the broad Au^{II} resonance is superimposed by a sharp slightly rhombic resonance around $g = 2.0$. For **2a** and **3a**, this sharp resonance accounts for approximately 5–6% of the total EPR intensity. The pattern can be satisfactorily simulated by $g_{1,2,3} = 2.018, 2.005, 1.994$ and hyperfine coupling to four nitrogen atoms ($A_{1,2,3} = 1, 12, 1$ G). These data fit to

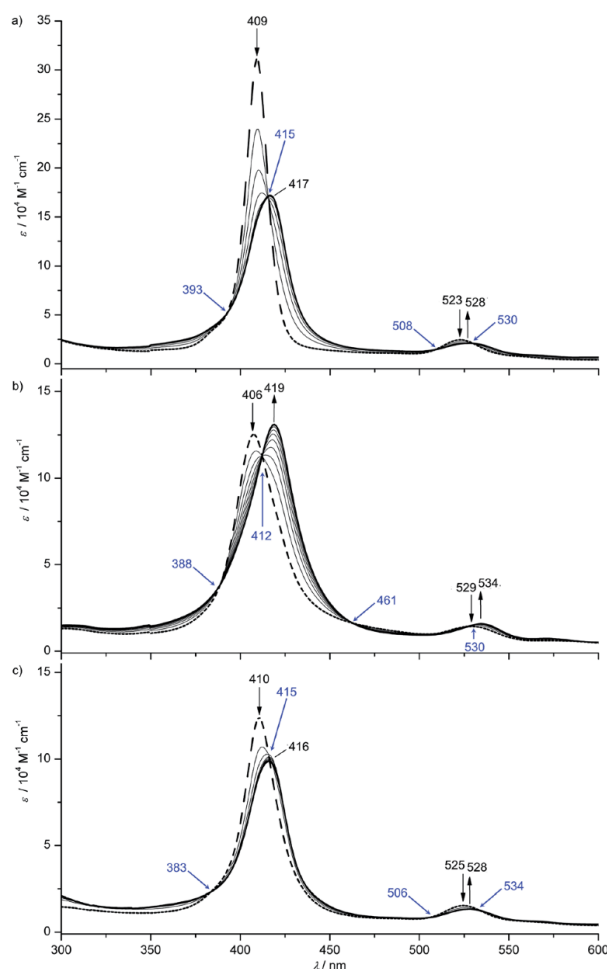


Fig. 3 UV/Vis spectral changes upon the first electroreduction of (a) **1a**⁺, (b) **2a**⁺ and (c) **3a**⁺ in 0.1 M [t Bu₄N][PF₆]/THF solution (isobestic points indicated in blue).



Table 2 X-band EPR data of one-electron reduced porphyrinato gold(III) complexes obtained from simulations of the experimental spectra

	Major species				Minor species			
	$g_{1,2,3}$	$A(^{197}\text{Au})_{1,2,3}/\text{G}$	$4 \times A(^{14}\text{N})_{1,2,3}/\text{G}$	Line width (Gauss/Lorentz)	Fraction/%	$g_{1,2,3}$	$4 \times A(^{14}\text{N})_{1,2,3}/\text{G}$	Line width (Gauss/Lorentz)
Au(TPP)	2.182, 2.056, 1.982	43, 20, 20	18, 22, 21	1.0/0.3	100	—	—	—
1a	2.190, 2.056, 1.974	44, 29, 29	18, 22, 21	1.7/0.3	78	2.016, 2.005, 1.995 ^a	1, 12, 1	0.75/0.1
1a/TBACl	2.190, 2.056, 1.974	44, 29, 29	18, 22, 21	1.7/0.3	65	2.016, 2.005, 1.994	1, 12, 1	0.9/0.3
2a	2.192, 2.062, 1.963	46, 25, 25	18, 22, 22	1.7/0.3	94	2.018, 2.005, 1.994	1, 12, 1	0.9/0.2
3a	2.192, 2.062, 1.968	44, 29, 29	18, 22, 21	1.7/0.3	95	2.016, 2.005, 1.994	1, 13, 1	0.9/0.3
4a	2.175, 2.057, 1.973	43, 29, 29	18, 22, 21	1.7/0.3	100	—	—	—
4b	2.175, 2.056, 1.972	42, 25, 25	18, 22, 21	3.0/0.3	100	—	—	—
4c	2.175, 2.055, 1.974	44, 29, 29	18, 22, 21	1.7/0.3	100	—	—	—

^a The nitro radical **1a''** (23%) shows $g_{1,2,3} = 2.031, 2.005, 1.948$ and $4 \times A(^{14}\text{N})_{1,2,3} = 2, 17, 2$ G.

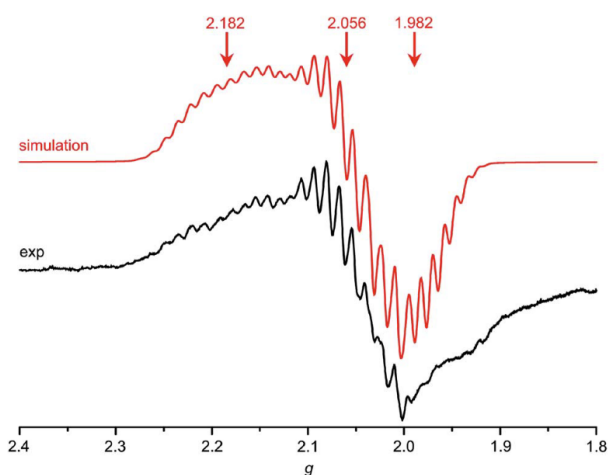


Fig. 4 X-band EPR spectrum of Au(TPP) in frozen CH_2Cl_2 solution (77 K, 9.4 GHz) and corresponding simulation.

gold(III) porphyrin radical anions **2a'** and **3a'**. For **4a–4c** prepared in THF or MeOH, the corresponding gold(III) porphyrin radical anions **4a'**, **4b'** and **4c'** are only present in negligible amounts (Fig. 6). Hence, in all these cases the equilibrium between the gold(II) valence isomers **2a–4c** and their corresponding porphyrin radical anions **2a'–4c'** is in favour of the gold(II) isomers. The very strong preference of **4a–4c** over **4a'–4c'** independent of the *meso* substituents might be due to a solvent effect overwhelming the substituent effects. Indeed, in THF or in MeOH solvent-separated ion-pairs $[\mathbf{4a–4c}]^+//[\text{PF}_6]^-$ should be present while in CH_2Cl_2 solution contact ion pairs of $[\mathbf{2a,3a}][\text{PF}_6]$ are formed. Indeed, reduction of $[\mathbf{2a}][\text{PF}_6]$ or $[\mathbf{3a}][\text{PF}_6]$ in THF resulted in EPR spectra mainly displaying the gold(II) valence isomers (ESI, Fig. S29 and S30[†]). The counterion location might affect the charge and spin distribution in the neutral species as well (*vide infra*).

The much more intense sharp EPR resonance present in the EPR spectrum of **1a** obtained from $[\mathbf{1a}][\text{PF}_6]$ in CH_2Cl_2 (Fig. 5a) differs from the sharp resonances assigned to the porphyrin π radical anions **2a'** and **3a'**. Indeed, simulations of the resonance suggests the presence of a further radical species with $g_{1,2,3} =$

2.031, 2.005, 1.948 and hyperfine coupling to a single nitrogen atom ($A_{1,2,3} = 2, 17, 2$ G). This is in good accordance with a nitroarene radical anion.²³ Hence, this distinct EPR resonance is assigned to a nitrophenyl radical anion valence isomer **1a''**. The radical distribution **1a** : **1a'** : **1a''** is estimated as 78 : 3 : 19. The decomposition into the component spectra is displayed in the ESI.[†] The effect of the type of counterions was probed by adding two equivalents of $[\text{Bu}_4\text{N}]\text{Cl}$ to the solution prior to reduction of the gold(III) porphyrin with CoCp_2 . No significant changes are observed for **Au(TPP)**, **3a** (CH_2Cl_2) or **4c** (THF) in the presence of chloride. However, the presence of chloride transforms the **1a** : **1a'** : **1a''** radical mixture almost completely into a **1a** : **1a'** mixture (65 : 35) as only the gold(II) resonance and the porphyrin radical anion resonance are observed under these conditions (ESI,[†] Table 2), similar to the **2a'** and **3a'** cases. Hence, for the nitro derivative **1a**, three possible valence isomers are possible: the gold(II) radical (**1a**), the porphyrin based π radical (**1a'**) and a further nitro group based π radical (**1a''**). Assuming, that rapid freezing does not strongly affect the equilibria of valence isomers, we can conclude that the environment, namely anions and the solvent, appears to influence these valence isomeric equilibria significantly. The substituents influence the equilibria as well, especially, when a strongly electron accepting nitro group is present. A conceivable inter-valence transition between **1a** and **1a'/1a''** is not detected in the UV/Vis spectrum by comparison with the spectra of **2a** and **3a** (Fig. 3). This might be associated with the different orbital symmetries of **1a** and **1a'/1a''**.

The electronic structure of the gold(II) radicals **1a–4c**, the valence isomeric equilibrium **1a/1a''** and the effect of counterions will be addressed by theoretical methods in the next section.

DFT studies of (porphyrinato)gold(III) complexes (series $[\mathbf{1a}]^+$ – $[\mathbf{3a}]^+$ and series $[\mathbf{4a}]^+$ – $[\mathbf{4c}]^+$) and the corresponding reduced species (series **1a–3a** and series **4a–4c**)

Both the geometries of the cationic gold(III) porphyrins $[\mathbf{Au}(\text{TPP})]^+$, $[\mathbf{1a}]^+$ – $[\mathbf{4c}]^+$ and the structures of all corresponding neutral species **Au(TPP)**, **1a–3a** and **4a–4c** were optimised by DFT methods (B3LYP, LANL2DZ, IEFPCM CH_2Cl_2 ; Table 3,



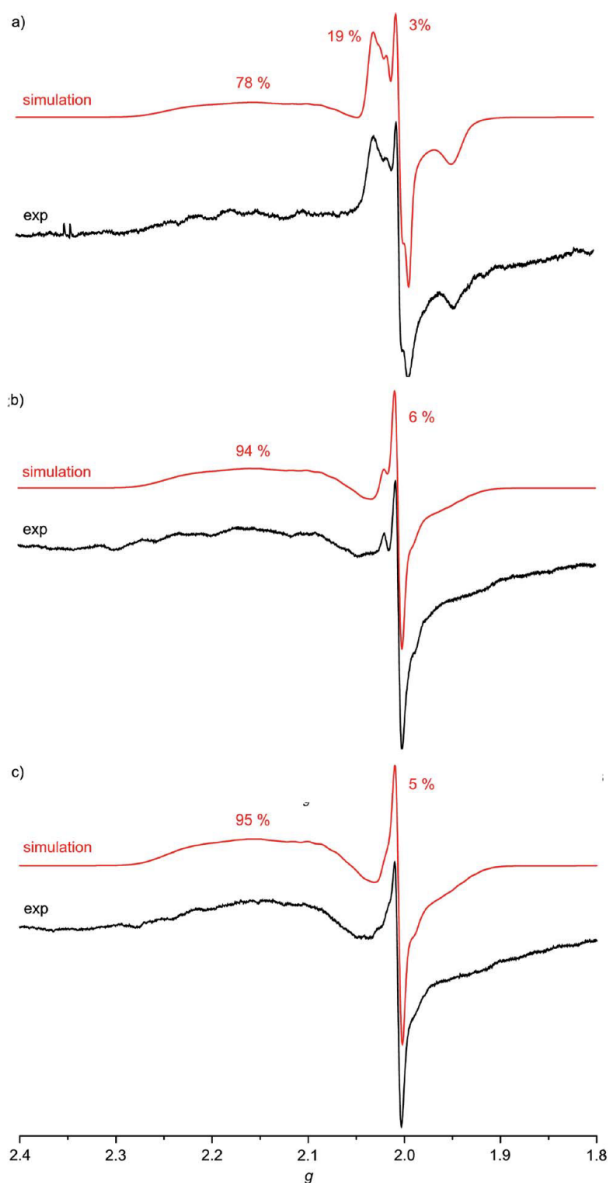


Fig. 5 X-band EPR spectra of (a) **1a/1a'/1a''** (78 : 3 : 19), (b) **2a/2a'** (94 : 6) and (c) **3a/3a'** (95 : 5) in frozen CH_2Cl_2 solution (77 K, 9.4 GHz) and corresponding simulations.

Fig. 7 and ESI†). The most significant differences between the cationic gold(III) complexes and their neutral congeners are found in the Au–N distances which increase by *ca.* 4% from 2.051 to 2.124 Å in all cases (Table 3). The large changes of the Au–N distances (Table 3) contribute to the reorganisation energy of the reduction process.^{13c} The gold ions are located nearly perfectly in the centre of the four pyrrolic nitrogen atoms in all complexes. The macrocycle itself displays only minor distortions both in the cations as well as in the neutral complexes. A minor increase of the saddling (B_{2u}) distortion is noted in the neutral complexes (Table 3). These metrical data of **1a–4c** strongly suggest that the reduction of the metal centre to Au^{II} is favoured in the electronic ground state. A reduction of

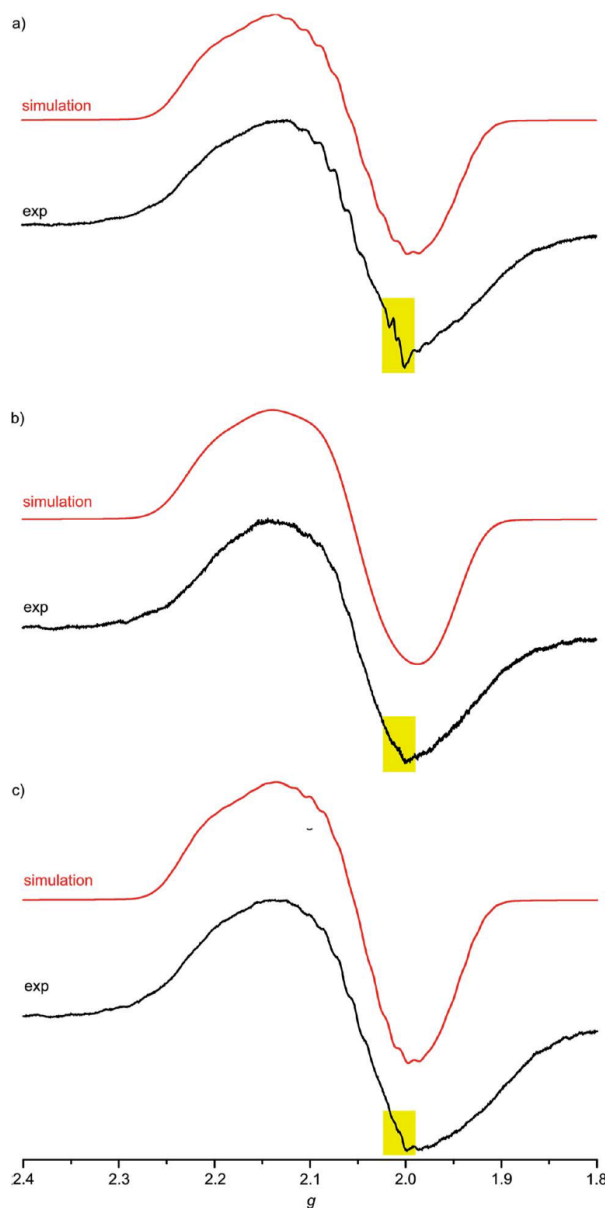


Fig. 6 X-band EPR spectra of (a) **4a** (MeOH), (b) **4b** (THF) and (c) **4c** (THF) in frozen solution (77 K, 9.4 GHz) and corresponding simulations; yellow squares highlight the presence of traces of porphyrin radical anions **4a'**, **4b'** and **4c'**, respectively.

the porphyrin to its radical anion **1a'–4c'** should result in pronounced macrocycle distortions as well as in small $\text{Au}^{\text{III}}\text{–N}$ (radical anion) bond distances which is not observed. The calculated Mulliken spin densities are in full accordance with these structural parameters. In all neutral complexes the majority of the spin density is located at the metal centre (Mulliken spin density at Au: 0.44), especially in the $5d_{x^2-y^2}$ orbital (Fig. 7 and ESI†). The remainder is distributed over the pyrrolic nitrogen atoms in the σ -orbitals pointing towards the metal centre (Mulliken spin density at N: 0.14). This clearly advocates a gold-centred radical localised in the σ -system of the



Table 3 Metrical data of DFT optimised porphyrinato gold(III) complexes and their one-electron reduced counterparts

	Au-N/Å	Centre-N/Å ^a	C _α -N-N'-C' _α (ruffling, B _{1u}) ^o	N-centre-N' (saddling, B _{2u}) ^{a/o}	N-O/Å	Torsion angle with respect to porphyrin plane C5-C12-C38-C43	Au...F/Å
[Au(TPP)] ⁺	2.051/2.051/2.051/2.051	2.051/2.051/2.051/2.051	-0.49 to +0.50	179.51/179.51			
Au(TPP)	2.124/2.124/2.124/2.124	2.124/2.124/2.124/2.124	-0.05 to +0.04	178.46/178.46			
[1a] ⁺	2.050/2.050/2.050/2.050	2.050/2.050/2.050/2.050	-2.23 to +1.95	179.57/179.57	1.281/1.281	66.1	
1a	2.124/2.124/2.124/2.124	2.124/2.124/2.124/2.124	-0.27 to -0.05	178.38/178.38	1.283/1.283	62.4	
1a''	2.057/2.058/2.058/2.057	2.057/2.058/2.058/2.057	-1.39 to +1.09	179.25/179.25	1.349/1.349 ^b	50.8	
[1a...PF ₆]	2.047/2.050/2.052/2.051	2.048/2.050/2.050/2.050	-2.71 to +1.47	179.82/179.83	1.282/1.282	68.3	3.146
[1a...PF ₆] ⁻	2.127/2.119/2.127/2.124	2.126/2.121/2.126/2.122	-1.54 to +1.78	178.75/178.75	1.284/1.285	61.4	4.076
[1a''...PF ₆] ⁻	2.057/2.057/2.056/2.055	2.056/2.056/2.057/2.056	-6.18 to +6.03	179.35/179.35	1.315/1.316	50.2	3.249
[2a] ⁺	2.051/2.052/2.051/2.052	2.052/2.052/2.052/2.051	-3.54 to +3.44	179.60/179.60			
2a	2.124/2.125/2.125/2.125	2.125/2.125/2.125/2.125	-2.26 to +2.35	178.28/178.28			
[3a] ⁺	2.051/2.051/2.051/2.051	2.051/2.051/2.051/2.051	-0.39 to +0.63	179.55/179.55			
3a	2.124/2.124/2.124/2.124	2.124/2.124/2.124/2.124	-0.85 to +0.69	178.43/178.43			
[4a] ⁺	2.051/2.051/2.051/2.051	2.051/2.051/2.051/2.051	-1.05 to +1.19	179.58/179.58			
4a	2.124/2.124/2.124/2.124	2.124/2.124/2.124/2.124	-0.76 to +0.74	178.42/178.42			
[4b] ⁺	2.052/2.052/2.052/2.052	2.052/2.052/2.052/2.052	-1.03 to +0.90	179.56/179.56			
4b	2.125/2.125/2.125/2.125	2.125/2.125/2.125/2.125	-0.77 to +0.69	178.35/178.35			
[4c] ⁺	2.051/2.051/2.051/2.051	2.051/2.051/2.051/2.051	-0.49 to +0.89	179.56/179.56			
4c	2.124/2.124/2.124/2.124	2.124/2.124/2.124/2.124	-0.92 to +1.10	178.53/178.53			

^a Centre denotes the geometric centre of the four pyrrole nitrogen atoms. ^b Constrained distances.

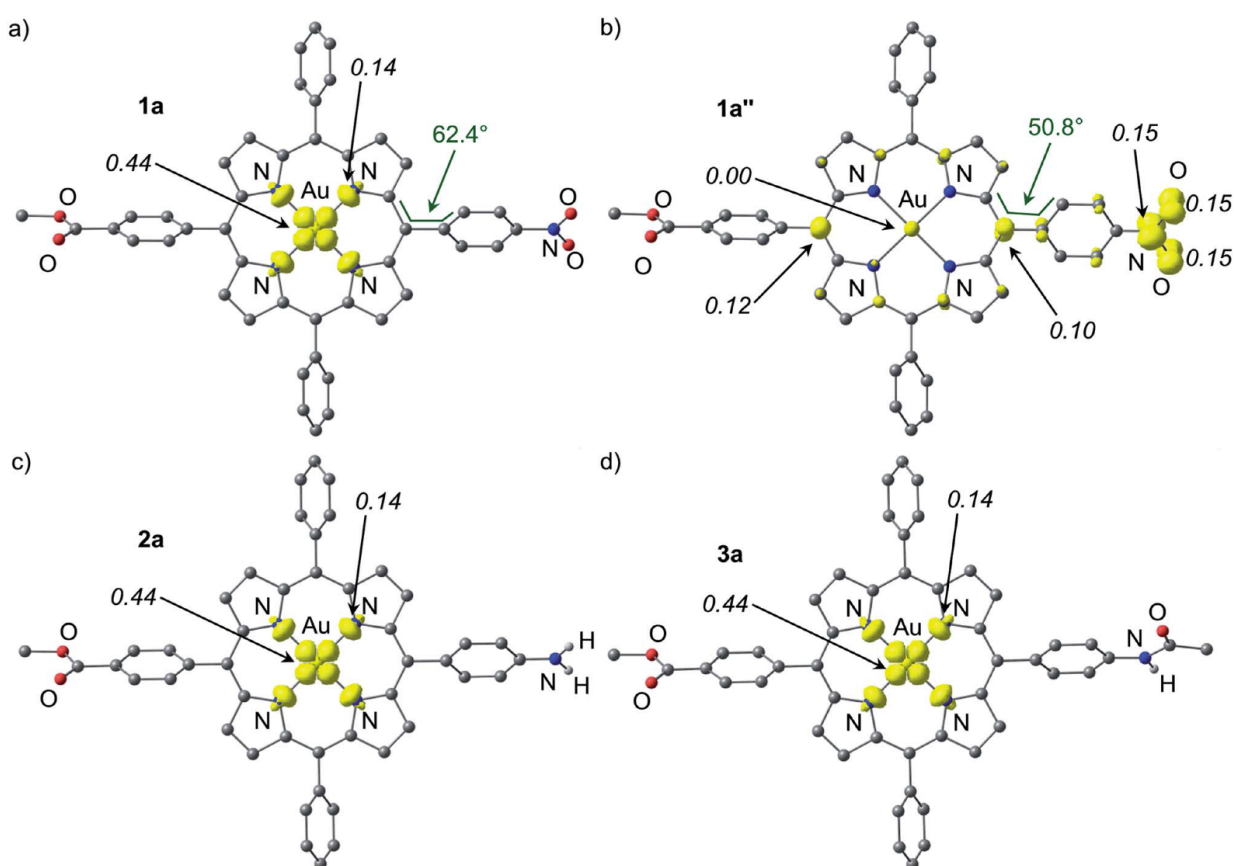


Fig. 7 Spin densities of DFT optimised geometries of (a) 1a, (b) 1a'' (constrained), (c) 2a and (d) 3a (isosurface value at 0.01 a.u. in yellow; 0.006 a.u. for 1a''; UB3LYP, LANL2DZ, IEFPCM CH₂Cl₂; CH hydrogen atoms omitted; Mulliken spin densities in italics).



almost planar molecule rather than a porphyrin radical anion with the spin delocalised in the π -system of the porphyrin. The DFT determined Au^{II} electronic ground states of **1a–4c** perfectly match the experimentally derived ground states. The spin densities are also in full agreement with experimentally determined EPR parameters (g values, ¹⁹⁷Au hyperfine coupling and ¹⁴N superhyperfine coupling). Compared with the isoelectronic Cu(TPP) [Mulliken spin density at Cu: 0.58; Mulliken spin density at N: 0.105] the spin densities are more delocalised onto the nitrogen atoms which is in agreement with the EPR results as well (ESI†).^{17d}

The special case of the nitro derivative **1a** which displays significant amounts of the nitrobenzene π radical anion valence isomer **1a''** in the EPR spectrum (Fig. 5a) was treated by DFT methods as well. However, all geometry optimisation attempts (with the employed functional, basis set and tight convergence criteria) converged to the stable Au^{II} valence isomer **1a**. In order to get an impression on the spin density distribution in valence isomer **1a''**, the nitrobenzene radical anion [C₆H₅NO₂]^{•-} was separately optimised by DFT methods giving NO distances of 1.349 Å. These NO distances were then constrained to 1.349 Å in geometry optimizations of **1a''** giving the (constrained) optimised structure of **1a''** as shown in Fig. 7. The Au–N bond lengths of **1a''** are fully consistent with a gold(III) oxidation state (Table 3). Compared to [1a]⁺ and **1a** the C₆H₄NO₂ torsion angle with respect to the porphyrin plane C5–C12–C38–C43 is significantly reduced from 66.1° and 62.4° to 50.8° suggesting

a conjugative electron withdrawing effect of the gold(III) porphyrin as expected for a π -centred radical. The spin density is mainly located at the NO₂ substituent and partially delocalised over the π -system of the porphyrin. The Mulliken spin density at the gold atom in **1a''** is essentially zero (Fig. 7).

As an unconstrained optimization of **1a''** was unsuccessful, we investigated the effect of the counterion [PF₆]⁻ on the charge and spin distribution in [1a^{•-}PF₆]⁻ and [1a''^{•-}PF₆]⁻, respectively. Indeed, we succeeded in optimising both valence isomers [1a^{•-}PF₆]⁻ and [1a''^{•-}PF₆]⁻ without any constraints (Fig. 8). The Au^{II} valence isomer [1a^{•-}PF₆]⁻ is preferred by 12 kJ mol⁻¹. In this Au^{II} isomer [1a^{•-}PF₆]⁻ the [PF₆]⁻ ion is not coordinated to the metal (Au^{•-}F 4.076 Å) but only hydrogen-bonded to two CH groups of the aryl substituents (Fig. 8a). The spin density is again localised at the metal centre (Mulliken spin density at Au: 0.44) and the pyrrolic nitrogen atoms (Mulliken spin density at N: 0.14). In the nitro-based π radical [1a''^{•-}PF₆]⁻ the [PF₆]⁻ ion is much closer to the gold centre (Au^{•-}F 3.249 Å, Fig. 8b). The presence of the negative charge close to the metal centre stabilises the Au^{III} oxidation state and indeed the gold ion carries no spin density. Au–N distances (2.057 Å; [1a''^{•-}PF₆]⁻) fully agree with a gold(III) porphyrin but not with a gold(II) porphyrin

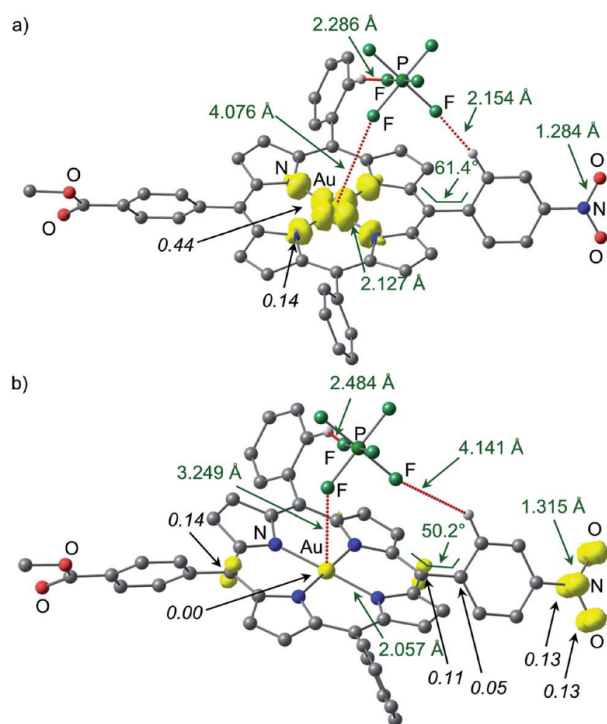
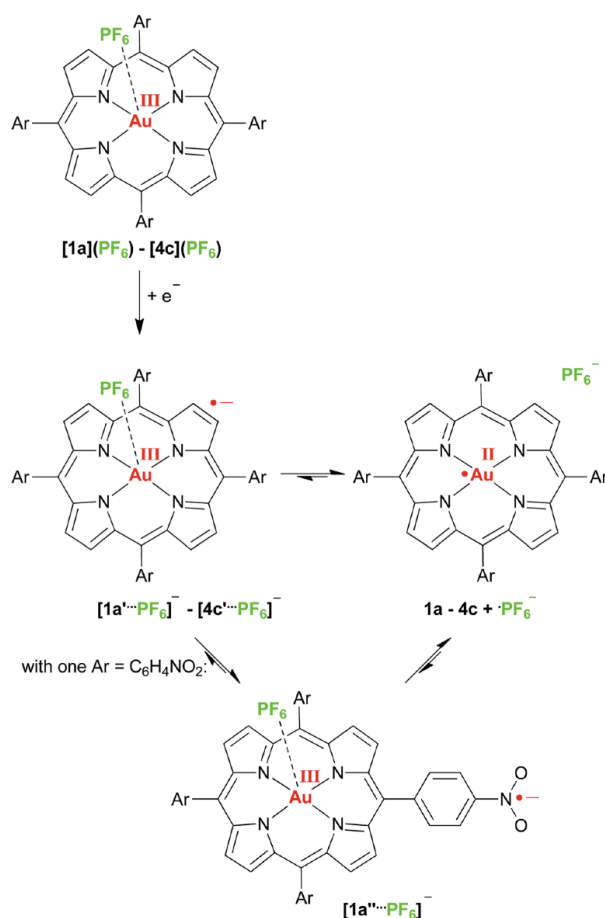


Fig. 8 Spin densities of DFT optimised geometries of (a) [1a^{•-}PF₆]⁻ and (b) [1a''^{•-}PF₆]⁻ (isosurface value at 0.01 a.u. in yellow; UB3LYP, LANL2DZ, IEFPCM CH₂Cl₂; hydrogen atoms which are not involved in hydrogen bonds are omitted; Mulliken spin densities in italics).



Scheme 3 Valence tautomeric equilibria of gold(II) porphyrins and gold(III) porphyrin radical anions.



(2.127 Å; $[\mathbf{1a}\cdots\text{PF}_6]^-$). The N–O distances have increased from 1.284 Å in $[\mathbf{1a}\cdots\text{PF}_6]^-$ to 1.315 Å in $[\mathbf{1a}''\cdots\text{PF}_6]^-$ as expected for population of N–O antibonding orbitals. The spin density is largely confined to the NO₂ substituent and partially delocalized to the π -system of the porphyrin. The C5–C12–C38–C43 torsion angle of the nitrophenyl substituent decreases from 61.4° ($[\mathbf{1a}\cdots\text{PF}_6]^-$) to 50.2° ($[\mathbf{1a}''\cdots\text{PF}_6]^-$) similar to the $\mathbf{1a}/\mathbf{1a}''$ (constrained) pair. In essence, the intramolecular electron transfer pathway between $[\mathbf{1a}\cdots\text{PF}_6]^-$ and $[\mathbf{1a}''\cdots\text{PF}_6]^-$ encompasses the Au–N and Au⋯F distances (totally symmetric stretching vibration of the gold coordination sphere), the symmetric NO₂ stretching mode and a phenyl torsional motion (Fig. 8).

With respect to photoinduced electron transfer reactions using porphyrinato gold(III) complexes as electron acceptors we suggest that the initial kinetic reduction product of a porphyrinato gold(III) complex should be a gold(III) porphyrin π radical anion (such as $\mathbf{1a}'\text{-4c}'$) due to the smaller activation barrier and the better electronic coupling to electron donors (Scheme 3). In a following intramolecular valence isomerisation the electron shifts to the central gold ion (σ -system) with concomitant dissociation of the counterion giving the thermodynamic Au^{II} product (such as $\mathbf{1a}\text{-4c}$) (Scheme 3). The latter chemical reaction will render the whole photoinduced ET process irreversible, which is advantageous for further reactivity of the redox sites. In the case of nitro substituted porphyrins a further valence isomer $[\mathbf{1a}''\cdots\text{PF}_6]^-$ with a nitrophenyl π radical anion is existent as well. Both the solvent, the present ions and the substituents determine the final charge and spin distribution.

Experimental

Porphyrins $\mathbf{H}_2\text{TPP}$, \mathbf{Ia} , \mathbf{IIa} , \mathbf{IIIa} , \mathbf{IVa} , \mathbf{IVb} and \mathbf{IVc} were prepared according to published procedures.¹⁷ Solvents were dried by standard methods. Other reagents were used as received from commercial suppliers (Acros, Sigma-Aldrich). NMR spectra were recorded on a Bruker Avance DRX 400 spectrometer at 400.31 MHz (¹H), 100.05 MHz (¹³C{¹H}), 162.05 MHz (³¹P{¹H}). Resonances are reported in ppm *versus* the solvent signal as an internal standard. CD₂Cl₂ (¹H: δ = 5.32 ppm; ¹³C: δ = 53.8 ppm), d₈-THF (¹H: δ = 1.73, 3.58 ppm; ¹³C: δ = 25.5, 67.7 ppm) MeOD (¹H: δ = 3.31, 4.87 ppm; ¹³C: δ = 49.0 ppm) and *versus* external H₃PO₄ (85%) (³¹P: δ = 0 ppm); (s) = singlet, (pt) = pseudo triplet (unresolved doublet of doublets), (br, s) = broad singlet, septet (sept). IR spectra were recorded with a BioRad Excalibur FTS 3100 spectrometer as KBr disks; (vs) = very strong, (s) = strong, (m) = medium, (w) = weak. ESI mass spectra were recorded on a Micromass Q-TOF-Ultima spectrometer. Electrochemical experiments were carried out on a BioLogic SP-50 voltammetric analyzer using a glassy carbon working electrode, a platinum wire as the counter electrode and a 0.01 M Ag/AgNO₃ electrode as the reference electrode. The measurements were carried out at a scan rate of 100 mV s⁻¹ for cyclic voltammetry experiments and for square wave voltammetry experiments using a concentration of 10⁻³ M in 0.1 M [ⁿBu₄N][PF₆] as the supporting electrolyte in THF (MeOH). Potentials are given relative to the ferrocene/ferrocenium couple. Spectroelectrochemical experiments were performed using a thin layer quartz glass (path

length 1 mm) cell kit (GAMEC Analysentechnik, Illingen, Germany) equipped with a Pt gauze working electrode, a Pt counter electrode and a Ag/AgNO₃ reference electrode (10⁻⁵ M solutions in THF or in MeOH, containing 0.1 M [ⁿBu₄N][PF₆]). X-band CW EPR spectra were measured on a Miniscope MS 300 (Magnettech GmbH, Germany). *g*-Values are referenced to external Mn²⁺ in ZnS (*g* = 2.118, 2.066, 2.027, 1.986, 1.946, 1.906). Simulations were performed with the program package EasySpin.²⁴ UV/Vis/NIR spectra were recorded on a Varian Cary 5000 spectrometer using 1.0 cm cells (Hellma, suprasil).

DFT calculations

Density functional calculations were carried out with the Gaussian09/DFT series²⁵ of programs. The B3LYP formulation of density functional theory was used employing the LANL2DZ basis set. To include solvent effects the integral equation formalism polarisable continuum model (IEFPCM CH₂Cl₂) was employed. No (symmetry) constraints were imposed on the molecules, except for the NO distance constraint for $\mathbf{1a}'$. The presence of energy minima of the ground states was checked by analytical frequency calculations.

EPR measurements of radical anions

Under an inert atmosphere a solution of the respective gold(III) porphyrin complex (*c* = 5 × 10⁻³ M) in CH₂Cl₂ ($[\mathbf{Au}(\text{TPP})][\text{PF}_6]$, $[\mathbf{1a}][\text{PF}_6]$, $[\mathbf{2a}][\text{PF}_6]$, $[\mathbf{3a}][\text{PF}_6]$), MeOH ($[\mathbf{4a}][\text{PF}_6]$) or THF ($[\mathbf{4b}][\text{PF}_6]$, $[\mathbf{4c}][\text{PF}_6]$) was treated with 0.95 equivalents of cobaltocene CoCp₂. The X-band EPR spectrum of the sample was measured immediately after freezing the solution to 77 K. The effect of chloride was measured by addition of 2.0 equivalents of [ⁿBu₄N]Cl prior to the reduction.

[5,10,15,20-Tetraphenylporphyrinato]gold(III) hexafluorophosphate $[\mathbf{Au}(\text{TPP})][\text{PF}_6]$

5,10,15,20-Tetraphenylporphyrin (50 mg, 0.08 mmol), potassium tetrachloridoaurate(III) (121 mg, 0.32 mmol) and sodium acetate (302 mg, 3.68 mmol) were dissolved in glacial acetic acid (20 mL). The reaction mixture was heated to reflux for 20 h, allowed to cool to room temperature, and diluted with dichloromethane (100 mL). The mixture was washed with water (2 × 50 mL), saturated sodium carbonate solution (2 × 50 mL) and water (1 × 50 mL), dried over anhydrous magnesium sulfate and filtered. The filtrate was evaporated to dryness and the residue dissolved in dichloromethane (50 mL). The organic phase was stirred with a saturated aqueous solution of potassium hexafluorophosphate (10 mL) for 72 h. The mixture was diluted with dichloromethane (100 mL) and washed with water (2 × 50 mL), dried over anhydrous magnesium sulfate, and filtered. The filtrate was removed under reduced pressure and the residue purified by chromatography over silica [dichloromethane : methanol (20 : 1); *R_f* = 0.40] to yield $[\mathbf{Au}(\text{TPP})][\text{PF}_6]$ (66 mg, 0.09 mmol, 88%) as a purple crystalline solid. C₄₄H₂₈AuF₆N₄P (954.7). UV/Vis: $\lambda_{\text{max}}(\text{THF})/\text{nm}$ 409 ($\epsilon/\text{M}^{-1}\text{cm}^{-1}$ 258 000), 523 (12 400). IR: $\nu_{\text{max}}/\text{cm}^{-1}$ 1638 (m), 1617 (s), 839 (vs, PF), 556 (m, PF_{6,def}). NMR: δ_{H} (400 MHz, CD₂Cl₂) 7.93 (12H, m, H^{5/5/10/10/15/15/20/20}_{3/4/3/4/3/4/3/4}), 8.24 (8H, m, H^{5/10/15/20}_{2/2/2/2}),



9.36 (8H, s, $H^{2,3,7,8,12,13,17,18}$); δ_C (100 MHz, CD_2Cl_2) 124.1 (s, $C^{5/10/15/20}$), 128.1 (s, $C^{5/10/15/20}_{3/3/3/3}$), 129.8 (s, $C^{5/10/15/20}_{4/4/4/4}$), 132.7 (s, $C^{2/3/7/8/12/13/17/18}$), 134.5 (s, $C^{5/10/15/20}_{2/2/2/2}$), 137.3 (s, $C^{1/4/6/9/11/14/16/19}$), 138.7 (s, $C^{5/10/15/20}_{1/1/1/1}$). δ_P (162 MHz, CD_2Cl_2) -143.8 (sept, $^1J_{PF} = 710$ Hz). MS (ESI): m/z 809.99 (100%) $[M]^+$. HR-MS (ESI): m/z 809.1993 (calcd for $C_{44}H_{28}AuN_4$: 809.1980). CV (Fc/Fc⁺, THF): $E_{1/2}^V - 2.350, -1.650, -0.975$.

[10,20-Di(phenyl)-15-(4-(methoxycarbonylphenyl))-5-(4-nitrophenyl)porphyrinato]gold(III) hexafluorophosphate [1a][PF₆]

10,20-Di(phenyl)-15-(4-(methoxycarbonylphenyl))-5-(4-nitrophenyl)porphyrin **1a** (100 mg, 0.14 mmol), potassium tetrachloridoaurate(III) (212 mg, 0.56 mmol) and sodium acetate (529 mg, 6.44 mmol) were dissolved in glacial acetic acid (40 mL). The reaction mixture was heated to reflux for 22 h, allowed to cool to room temperature, and diluted with dichloromethane (200 mL). The mixture was washed with water (2 × 100 mL), saturated aqueous sodium carbonate solution (2 × 100 mL) and water (1 × 100 mL), dried over anhydrous magnesium sulfate and filtered. The filtrate was evaporated to dryness and the residue dissolved in dichloromethane (100 mL). The organic phase was stirred with a saturated aqueous solution of potassium hexafluorophosphate (20 mL) for 72 h. The mixture was diluted with dichloromethane (100 mL) and washed with water (2 × 50 mL), dried over anhydrous magnesium sulfate, and filtered. The filtrate was removed under reduced pressure and the residue purified by chromatography over silica [dichloromethane : methanol (10 : 1); $R_f = 0.35$] to yield **[1a][PF₆]** (64 mg, 0.06 mmol, 43%) as a purple crystalline solid. $C_{46}H_{29}AuF_6N_5O_4P$ (1057.7). UV/Vis: λ_{max} (THF)/nm 410 ($\epsilon/M^{-1} cm^{-1}$ 329 000), 523 (17 600). IR: ν_{max}/cm^{-1} 1717 (s, CO_{ester}), 1597 (m), 1520 (s, NO_{asym}), 1439 (m), 1346 (s, NO_{sym}), 1277 (s, OCO_{def}), 1106 (m), 1034 (s), 1018 (s), 837 (vs, PF), 556 (s, PF_{6,def}). NMR: δ_H (400 MHz, CD_2Cl_2) 4.12 (3H, s, H^{15}_6), 7.95 (6H, m, $H^{10/10/20/20}_{3/3/4/4}$), 8.29 (4H, d, $H_{2/2}$), 8.39 (2H, d, $^3J_{HH} = 8.2$ Hz, H^{15}_2), 8.50 (2H, d, $^3J_{HH} = 8.5$ Hz, H^5_2), 8.57 (2H, d, $^3J_{HH} = 8.1$ Hz, H^{15}_3), 8.75 (2H, d, $^3J_{HH} = 8.5$ Hz, H^5_3), 9.35 (8H, m, $H^{2,3,7,8,12,13,17,18}$); δ_C (100 MHz, CD_2Cl_2) 52.5 (s, C^{15}_6), 121.4 (s, C^{15}), 123.4 (s, C^5_3), 124.8 (s, $C^{10/20}$), 128.4 (s, $C^{10/20}_{3/3}$), 129.4 (s, C^{15}_3), 130.0 (s, $C^{10/20}_{4/4}$), 132.2 (s, C^{15}_4), 132.8–133.7 (multiple s, $C^{2/3/7/8/12/13/17/18}$), 134.8 (s, $C^{10/20/15}_{2/2/2}$), 136.5 (s, C^5_2), 136.9–138.0 (multiple s, $C^{1/4/6/9/11/14/16/19}$), 138.9 (s, $C^{10/20}_{1/1}$), 143.3 (s, C^{15}_1), 145.4 (s, C^5_1), 149.4 (s, C^5_4), 167.1 (s, C^{15}_5). δ_P (162 MHz, CD_2Cl_2) -144.1 (sept, $^1J_{PF} = 711$ Hz). MS (ESI): m/z 912.11 (100%) $[M]^+$. HR-MS (ESI): m/z 912.1905 (calcd for $C_{46}H_{29}AuN_5O_4$: 912.1885). CV (Fc/Fc⁺, THF): $E_{1/2}^V - 2.300, -1.795, -1.560, -0.920$.

[5-(4-Aminophenyl)-10,20-di(phenyl)-15-(4-(methoxycarbonylphenyl))porphyrinato]gold(III) hexafluorophosphate [2a][PF₆]

[10,20-Di(phenyl)-15-(4-(methoxycarbonylphenyl))-5-(4-nitrophenyl)porphyrinato]gold(III) hexafluorophosphate **[1a][PF₆]** (100 mg, 0.09 mmol) and tin(II) chloride dihydrate were suspended in concentrated hydrochloric acid (36%, 50 mL). The reaction mixture was stirred in the dark under argon for 20 h.

The mixture was diluted with dichloromethane (200 mL), washed with water (2 × 100 mL), saturated sodium carbonate solution (2 × 100 mL), and water (1 × 100 mL), dried over anhydrous magnesium sulfate and filtered. The filtrate was evaporated to dryness and the residue dissolved in dichloromethane (100 mL). The organic phase was stirred with a saturated aqueous solution of potassium hexafluorophosphate (20 mL) for 72 h. The mixture was diluted with dichloromethane (100 mL) and washed with water (2 × 50 mL), dried over anhydrous magnesium sulfate and filtered. The filtrate was removed under reduced pressure and the residue purified by chromatography over silica [dichloromethane : methanol (25 : 1); $R_f = 0.22$] to yield **[2a][PF₆]** (31 mg, 0.03 mmol, 34%) as a reddish-brown solid. $C_{46}H_{31}AuF_6N_5O_2P$ (1027.7). UV/Vis: λ_{max} (THF)/nm 406 ($\epsilon/M^{-1} cm^{-1}$ 126 000), 529 (10 800), 589 (4800). IR: ν_{max}/cm^{-1} 1723 (s, CO_{ester}), 1638 (s), 1618 (vs, NH_{2,def}), 1277 (s, OCO_{def}), 966 (s), 835 (vs, PF), 567 (vs), 557 (s, PF_{6,def}). NMR: δ_H (400 MHz, CD_2Cl_2) 4.14 (3H, s, H^{15}_6), 4.7 (2H, br s, NH₂), 7.25 (2H, d, $^3J_{HH} = 8.3$ Hz, H^5_3), 7.95 (6H, m, $H^{10/10/20/20}_{3/4/3/4}$), 8.03 (2H, d, $^3J_{HH} = 8.4$ Hz, H^5_2), 8.27 (4H, m, $H^{10/20}_{2/2}$), 8.37 (2H, d, $^3J_{HH} = 8.3$ Hz, H^{15}_2), 8.57 (2H, d, $^3J_{HH} = 8.3$ Hz, H^{15}_3), 9.40 (8H, m, $H^{2,3,7,8,12,13,17,18}$); δ_C (100 MHz, CD_2Cl_2) 52.2 (s, C^{15}_6), 114.6 (s, C^5_3), 122.6 (s, C^{15}), 124.4 (s, $C^{10/20}$), 127.5 (s, C^5), 128.4 (s, $C^{10/20}_{3/3}$), 129.4 (s, C^{15}_3), 130.2 (s, $C^{10/20}_{4/4}$), 132.3 (s, C^{15}_4), 132.8–133.6 (multiple s, $C^{2/3/7/8/12/13/17/18}$), 134.8 (s, $C^{10/20/15}_{2/2/2}$), 135.6 (s, C^5_1), 136.5 (s, C^5_2), 137.1–137.7 (multiple s, $C^{1/4/6/9/11/14/16/19}$), 139.0 (s, $C^{10/20}_{1/1}$), 143.5 (s, C^{15}_1), 149.5 (s, C^5_4), 167.2 (s, C^{15}_5). δ_P (162 MHz, CD_2Cl_2) -143.5 (sept, $^1J_{PF} = 710$ Hz). MS (ESI): m/z 882.09 (100%) $[M]^+$. HR-MS (ESI): m/z 882.2163 (calcd for $C_{46}H_{31}AuN_5O_2$: 882.2143). CV (Fc/Fc⁺, THF): $E_{1/2}^V - 2.500$ (irrev.), $-2.280, -1.645, -0.990$.

[5-(4-(N-Acetylaminophenyl))-10,20-di(phenyl)-15-(4-(methoxycarbonylphenyl))porphyrinato]gold(III) hexafluorophosphate [3a][PF₆]

5-(4-(N-Acetylaminophenyl))-10,20-di(phenyl)-15-(4-(methoxycarbonylphenyl))porphyrin **IIIa** (50 mg, 0.07 mmol), potassium tetrachloridoaurate(III) (104 mg, 0.28 mmol) and sodium acetate (258 mg, 3.15 mmol) were dissolved in glacial acetic acid (20 mL). The reaction mixture was heated to reflux for 24 h, allowed to cool to room temperature, and diluted with dichloromethane (100 mL). The mixture was washed with water (2 × 50 mL), saturated aqueous sodium carbonate solution (2 × 50 mL) and water (1 × 50 mL), dried over anhydrous magnesium sulfate and filtered. The filtrate was evaporated to dryness and the residue dissolved in dichloromethane (50 mL). The organic phase was stirred with a saturated aqueous solution of potassium hexafluorophosphate (10 mL) for 72 h. The mixture was diluted with dichloromethane (50 mL) and washed with water (2 × 50 mL), dried over anhydrous magnesium sulfate, and filtered. The filtrate was removed under reduced pressure and the residue purified by chromatography over silica [dichloromethane : methanol (10 : 1); $R_f = 0.43$] to yield **[3a][PF₆]** (32 mg, 0.03 mmol, 49%) as a purple crystalline solid. $C_{48}H_{33}AuF_6N_5O_3P$ (1069.7). UV/Vis: λ_{max} (THF)/nm 410 ($\epsilon/M^{-1} cm^{-1}$ 124 000), 525 (10 500). IR: ν_{max}/cm^{-1} 2964 (m, NH), 1717 (s,



CO_{ester}), 1677 (s, CO_{amide}), 1616 (m), 1262 (s, OCO_{def}), 1096 (s), 1020 (s), 839 (s), 803 (vs, PF), 708 (m), 557 (m, PF_{6,def}). NMR: δ_{H} (400 MHz, CD₂Cl₂) 2.33 (3H, s, H⁵₆), 4.11 (3H, s, H¹⁵₆), 7.93 (6H, m, H^{10/20/20}_{3/4/3/4}), 8.04 (1H, s, NH), 8.12 (2H, d, ³J_{HH} = 8.3 Hz, H⁵₃), 8.19 (2H, d, ³J_{HH} = 8.4 Hz, H⁵₂), 8.24 (4H, m, H^{10/20}_{2/2}), 8.34 (2H, d, ³J_{HH} = 8.3 Hz, H¹⁵₂), 8.55 (2H, d, ³J_{HH} = 8.3 Hz, H¹⁵₃), 9.37 (8H, m, H^{2,3,7,8,12,13,17,18}); δ_{C} (100 MHz, CD₂Cl₂) 24.9 (s, C⁵₆), 53.2 (s, C¹⁵₆), 119.2 (s, C⁵₃), 122.6 (s, C¹⁵₃), 124.5 (s, C^{10/20}_{4/4}), 124.8 (s, C⁵₃), 128.4 (s, C^{10/20}_{3/3}), 129.3 (s, C¹⁵₃), 130.2 (s, C^{10/20}_{4/4}), 132.0 (s, C¹⁵₄), 132.5–133.3 (multiple s, C^{2/3/7/8/12/13/17/18}), 134.8 (s, C^{10/20/15}_{2/2/2}), 135.4 (s, C⁵₂), 137.0–137.9 (multiple s, C^{1/4/6/9/11/14/16/19}), 139.0 (s, C^{10/20}_{1/1}), 140.4 (s, C⁵₁), 141.5 (s, C⁵₄), 143.4 (s, C¹⁵₁), 169.9 (s, C¹⁵₅). δ_{P} (162 MHz, CD₂Cl₂) –143.5 (sept, ¹J_{PF} = 711 Hz). MS (ESI): *m/z* 924.01 (100%) [M]⁺. HR-MS (ESI): *m/z* 924.2229 (calcd for C₄₈H₃₃AuN₅O₃: 924.2249). CV (Fc/Fc⁺, THF): E₂/V –2.490 (irrev.), –2.300, –1.630, –0.990.

[5-(4-(*N*-Acetylamino-phenyl))-10,20-di(phenyl)-15-(4-(carboxyphenyl))porphyrinato]gold(III) hexafluorophosphate [4a][PF₆]

5-(4-(*N*-Acetylamino-phenyl))-10,20-di(phenyl)-15-(4-(carboxyphenyl))porphyrin **IVa** (50 mg, 0.07 mmol), potassium tetrachloridoaurate(III) (104 mg, 0.28 mmol) and sodium acetate (258 mg, 3.15 mmol) were dissolved in glacial acetic acid (20 mL). The reaction mixture was heated to reflux for 24 h, allowed to cool to room temperature and diluted with dichloromethane (100 mL). The mixture was washed with water (2 × 50 mL), saturated aqueous sodium carbonate solution (2 × 50 mL) and water (1 × 50 mL), dried over anhydrous magnesium sulfate and filtered. The filtrate was evaporated to dryness and the residue dissolved in dichloromethane (50 mL). The organic phase was stirred with a saturated aqueous solution of potassium hexafluorophosphate (10 mL) for 72 h. The mixture was diluted with dichloromethane (50 mL) and washed with water (2 × 50 mL), dried over anhydrous magnesium sulfate, and filtered. The filtrate was removed under reduced pressure and the residue purified by chromatography over silica [dichloromethane : methanol (10 : 1); R_f = 0.41] to yield **[4a][PF₆]** (24 mg, 0.02 mmol, 28%) as a reddish-brown solid. C₄₇H₃₁AuF₆N₅O₃P (1055.7). UV/Vis: λ_{max} (MeOH)/nm 408 ($\epsilon/\text{M}^{-1} \text{cm}^{-1}$ 204 000), 522 (12 300). IR: $\nu_{\text{max}}/\text{cm}^{-1}$ 2955, 2914, 2872 (m, OH), 1712 (m, CO_{acid}), 1695 (m, CO_{amide}), 1638 (s), 1618 (s), 1432 (s), 1385 (s), 1363 (s), 1232 (s, COC_{def}), 1155 (s), 1121 (m), 839 (vs, PF), 775 (s), 770 (s), 558 (s, PF_{6,def}). NMR: δ_{H} (400 MHz, CD₃OD) 2.33 (3H, s, H⁵₆), 7.95 (6H, m, H^{10/20/20}_{3/4/3/4}), 8.12 (2H, d, ³J_{HH} = 8.3 Hz, H⁵₃), 8.20 (2H, d, ³J_{HH} = 8.4 Hz, H⁵₂), 8.24 (2H, d, ³J_{HH} = 8.3 Hz, H¹⁵₂), 8.26 (4H, m, H^{10/20}_{2/2}), 8.45 (2H, d, ³J_{HH} = 8.3 Hz, H¹⁵₃), 9.36 (8H, m, H^{2,3,7,8,12,13,17,18}); δ_{C} (100 MHz, CD₃OD) 24.0 (s, C⁵₆), 120.1 (s, C⁵₃), 124.8 (s, C¹⁵₃), 125.0 (s, C^{10/20}_{4/4}), 127.1 (s, C⁵₃), 127.4 (s, C^{10/20}_{3/3}), 128.1 (s, C¹⁵₃), 129.1 (s, C^{10/20}_{4/4}), 131.4 (s, C¹⁵₄), 131.9 (br s, C^{2/3/7/8/12/13/17/18}), 133.5 (s, C⁵₂), 134.8 (s, C^{10/20/15}_{2/2/2}), 136.9 (br s, C^{1/4/6/9/11/14/16/19}), 138.7 (s, C^{10/20}_{1/1}), 140.0 (s, C⁵₁), 140.2 (s, C¹⁵₁), 141.4 (s, C⁵₄), 165.9 (s, C¹⁵₅), 170.9 (s, C⁵₅). δ_{P} (162 MHz, CD₃OD) –143.5 (sept, ¹J_{PF} = 710 Hz). MS (ESI): *m/z* 910.18 (100%) [M]⁺. HR-MS (ESI): *m/z* 910.2115 (calcd for C₄₇H₃₁AuN₅O₃: 910.2093). CV (Fc/Fc⁺, MeOH): E₂/V –1.030.

[5-(4-(*N*-Acetylamino-phenyl))-10,20-di((4-butoxy)phenyl)-15-(4-(carboxyphenyl))porphyrinato]gold(III) hexafluorophosphate [4b][PF₆]

5-(4-(*N*-Acetylamino-phenyl))-10,20-di((4-butoxy)phenyl)-15-(4-(carboxyphenyl))porphyrin **IVb** (75 mg, 0.09 mmol), potassium tetrachloridoaurate(III) (133 mg, 0.36 mmol) and sodium acetate (328 mg, 4.00 mmol) were dissolved in glacial acetic acid (40 mL). The reaction mixture was heated to reflux for 24 h, allowed to cool to room temperature, and diluted with dichloromethane (200 mL). The mixture was washed with water (2 × 100 mL), saturated aqueous sodium carbonate solution (2 × 100 mL) and water (1 × 100 mL), dried over anhydrous magnesium sulfate and filtered. The filtrate was evaporated to dryness and the residue dissolved in dichloromethane (100 mL). The organic phase was stirred with a saturated aqueous solution of potassium hexafluorophosphate (20 mL) for 72 h. The mixture was diluted with dichloromethane (100 mL) and washed with water (2 × 50 mL), dried over anhydrous magnesium sulfate and filtered. The filtrate was removed under reduced pressure and the residue purified by chromatography over silica [dichloromethane : methanol (10 : 1); R_f = 0.40] to yield **[4b][PF₆]** (72 mg, 0.06 mmol, 66%) as a purple solid. C₅₅H₄₇AuF₆N₅O₅P (1199.9). UV/Vis: λ_{max} (THF)/nm 422 ($\epsilon/\text{M}^{-1} \text{cm}^{-1}$ 86 000), 527 (9100), 571 (3200). IR: $\nu_{\text{max}}/\text{cm}^{-1}$ 2957, 2924, 2870, 2855 (m, OH), 1716 (sh, CO_{acid}), 1699 (s, CO_{amide}), 1605 (s), 1505 (m), 1247 (s, COC_{def}), 843 (vs, PF), 804 (s), 558 (s, PF_{6,def}). NMR: δ_{H} (400 MHz, d₈-THF) 1.10 (6H, t, ³J_{HH} = 7.3 Hz, H^{10/20}_{8/8}), 1.66 (4H, m, H^{10/20}_{7/7}), 1.96 (4H, m, H^{10/20}_{6/6}), 2.14 (3H, s, H⁵₆), 4.30 (2H, t, ³J_{HH} = 6.4 Hz, H^{10/20}_{5/5}), 7.44 (2H, d, ³J_{HH} = 7.4 Hz, H^{10/20}_{3/3}), 8.12 (4H, m, H^{5/5}_{2/3}), 8.17 (2H, d, ³J_{HH} = 7.3 Hz, H^{10/20}_{2/2}), 8.37 (2H, d, ³J_{HH} = 7.1 Hz, H¹⁵₂), 8.53 (2H, d, ³J_{HH} = 7.0 Hz, H¹⁵₃), 9.36 (8H, m, H^{2,3,7,8,12,13,17,18}), 9.48 (1H, s, NH); δ_{C} (100 MHz, d₈-THF) 14.3 (s, C^{10/20}_{8/8}), 20.4 (s, C^{10/20}_{7/7}), 24.4 (s, C⁵₆), 32.5 (s, C^{10/20}_{6/6}), 67.6 (s, C^{10/20}_{5/5}), 114.7 (s, C^{10/20}_{3/3}), 118.8 (s, C⁵₃), 122.9 (s, C¹⁵₃), 124.7 (s, C^{10/20}_{2/2}), 125.1 (s, C⁵₃), 129.8 (s, C¹⁵₃), 131.7 (s, C^{10/20}_{1/1}), 132.5 (s, C¹⁵₄), 133.1–133.8 (br s, C^{2/3/7/8/12/13/17/18}), 135.2 (s, C¹⁵₂), 135.7 (s, C⁵₂), 136.6 (s, C^{10/20}_{2/2}), 137.6 (s, C⁵₁), 138.5 (br s, C^{1/4/6/9/11/14/16/19}), 141.3 (s, C⁵₄), 143.9 (s, C¹⁵₁), 161.5 (s, C^{10/20}_{4/4}), 167.5 (s, C¹⁵₅), 169.3 (s, C⁵₅). δ_{P} (162 MHz, d₈-THF) –143.5 (sept, ¹J_{PF} = 710 Hz). MS (ESI): *m/z* 1054.26 (100%) [M]⁺. HR-MS (ESI): *m/z* 1054.3218 (calcd for C₅₅H₄₇AuN₅O₅: 1054.3243). CV (Fc/Fc⁺, THF): E₂/V –2.450, –1.745, –1.070.

[5-(4-(*N*-Acetylamino-phenyl))-10,20-bis(4-(trifluoromethylphenyl))-15-(4-(carboxyphenyl))porphyrinato]gold(III) hexafluorophosphate [4c][PF₆]

5-(4-(*N*-Acetylamino-phenyl))-10,20-bis(4-(tri-fluoromethylphenyl))-15-(4-(carboxyphenyl))porphyrin **IVc** (63 mg, 0.07 mmol), potassium tetrachlorido aurate(III) (104 mg, 0.28 mmol), and sodium acetate (258 mg, 3.15 mmol) were dissolved in glacial acetic acid (20 mL). The reaction mixture was heated to reflux for 24 h, allowed to cool to room temperature and diluted with dichloromethane (100 mL). The mixture was washed with water (2 × 50 mL), saturated aqueous sodium carbonate solution (2 × 50 mL) and water (1 × 50 mL), dried over anhydrous magnesium sulfate and filtered. The filtrate was



evaporated to dryness and the residue dissolved in dichloromethane (50 mL). The organic phase was stirred with a saturated aqueous solution of potassium hexafluorophosphate (10 mL) for 72 h. The mixture was diluted with dichloromethane (50 mL) and washed with water (2 × 50 mL), dried over anhydrous magnesium sulfate and filtered. The filtrate was removed under reduced pressure and the residue purified by chromatography over silica [dichloromethane : methanol (10 : 1); $R_f = 0.30$] to yield [4c][PF₆] (71 mg, 0.06 mmol, 85%) as a purple, crystalline solid. C₄₉H₂₉AuF₁₂N₅O₃P (1191.7). UV/Vis: λ_{\max} (THF)/nm 409 ($\epsilon/M^{-1} \text{ cm}^{-1}$ 170 000), 525 (15 100), 571 (3200). IR: $\nu_{\max}/\text{cm}^{-1}$ 2959, 2922, 2851 (w, OH), 1721 (s, CO_{acid}), 1689 (s, CO_{amide}), 1616 (m), 1591 (m), 1515 (m), 1406 (m), 1324 (vs, CF), 1168 (m), 1126 (m), 1109 (m), 1069 (s), 1034 (m), 1017 (s), 842 (vs, PF), 820 (s), 800 (s), 706 (m), 556 (s, PF_{6,def}). NMR: δ_{H} (400 MHz, d₈-THF) 2.21 (3H, s, H⁵₆), 8.08 (2H, d, ³ $J_{\text{HH}} = 8.2$ Hz, H⁵₃), 8.14 (2H, d, ³ $J_{\text{HH}} = 8.2$ Hz, H⁵₂), 8.25 (2H, d, ³ $J_{\text{HH}} = 7.5$ Hz, H^{10/20}_{2/2}), 8.39 (2H, d, ³ $J_{\text{HH}} = 7.1$ Hz, H¹⁵₂), 8.53 (2H, d, ³ $J_{\text{HH}} = 7.5$ Hz, H^{10/20}_{3/3}), 8.53 (2H, d, ³ $J_{\text{HH}} = 7.5$ Hz, H¹⁵₃), 9.40 (8H, m, H^{2,3,7,8,12,13,17,18}), 9.41 (1H, s, NH); δ_{C} (100 MHz, d₈-THF) 24.3 (s, C⁵₆), 118.8 (s, C⁵₃), 122.9 (s, C⁵), 123.5 (s, C¹⁵), 124.3 (s, C^{10/20}), 125.6 (s, C^{10/20}_{2/2}), 127.0 (s, C^{10/20}_{4/4}), 129.8 (s, C¹⁵₃), 132.4 (s, C¹⁵₄), 133.1–133.8 (multiple s, C^{2/3/7/8/12/13/17/18}), 135.3 (s, C¹⁵₂), 135.7 (s, C^{5/5/10/10}_{2/3/2/3}), 137.7 (s, C⁵₁), 137.9–138.7 (multiple s, C^{1/4/6/9/11/14/16/19}), 142.2 (s, C⁵₄), 143.9 (s, C^{10/15/20}_{1/1/1}), 161.5 (s, C^{10/20}_{4/4}), 167.5 (s, C¹⁵₅), 169.2 (s, C⁵₅). δ_{p} (162 MHz, d₈-THF) –143.3 (sept, ¹ $J_{\text{PF}} = 711$ Hz). MS (ESI): m/z 1045.97 (100%) [M]⁺. HR-MS (ESI): m/z 1046.1863 (calcd for C₄₉H₂₉AuF₆N₅O₃: 1046.1840). CV (Fc/Fc⁺, THF): $E_{1/2}/\text{V}$ –2.300, –1.590, –0.990.

Conclusions

Auration of *meso*-tetraaryl substituted AB₂C porphyrins with KAUCl₄ in the presence of HOAc/NaOAc cleanly gives the corresponding gold(III) porphyrinato complex cations. Amino-substituted porphyrins are *N*-acetylated under these conditions and have to be prepared from the corresponding nitro-substituted gold(III) porphyrins by reduction with SnCl₂/HCl. The gold(III) complexes can be reduced at least three times. The potentials slightly depend on the electron withdrawing and donating nature of the substituents. The first reduction is addressed by UV/Vis spectroelectrochemistry and by EPR spectroscopy. Upon one-electron reduction, the Soret band experiences a small bathochromic shift. The intensity of the Soret band of the electron rich complexes [2a]⁺ (R² = NH₂) and [4b]⁺ (R³ = O^{*n*}Bu) slightly increases upon reduction while all other neutral complexes feature less intense Soret bands as compared to their parent Au^{III} complexes. These spectral data clearly suggest the presence of an unreduced porphyrinato ligand in all cases under these conditions. Chemical one-electron reduction of the porphyrinato gold(III) hexafluorophosphate salts by cobaltocene yields the corresponding Au^{II} porphyrin complexes with a characteristic EPR pattern displaying hyperfine coupling to ¹⁹⁷Au and ¹⁴N. The degree of ¹⁹⁷Au hfc and *g* anisotropy places the gold contribution to the spin density in (tetraphenylporphyrinato)gold(II) complexes in between that of [Au(en)₂]²⁺ (ref. 15) and the neutral gold hematoporphyrin IX

complex.^{13c} DFT calculations fully support the metal centred reduction in all cases, essentially irrespective of the substituent at the *meso* aryl groups. Only, the nitro substituent reduction competes significantly with the Au^{III} reduction and a valence isomeric equilibrium between the Au^{II} valence isomer and the nitro π radical anion valence isomer is established. DFT calculations suggest that the position of the counterion triggers the position of the equilibria between the different valence isomers that interconvert by an intramolecular electron transfer process. These findings allows the usage of *meso*-substituted Au^{III} porphyrins as electron acceptors and electron storage materials in photo-induced redox processes, almost irrespective of the substitution pattern. Hence, the substituents fine-tune the redox potential or other properties such as solubility without compromising the thermodynamically preferred metal site of one-electron reduction. Combination of electron-accepting gold(III) porphyrins bearing carboxylic acid, amine and amide substituents, as introduced in this report, with light-harvesting porphyrins and electron donating porphyrins *via* amide connectivity¹⁷ are currently explored in our laboratory and will be reported in due course.

Acknowledgements

The authors S. P., A. W. v. L. and K. H. thank the Center of Innovative and Emerging Materials (CINEMA) for financial support. We thank the students Katrin Limberg and Heike Pfaff for preparative assistance.

Notes and references

- (a) D. Gust and T. A. Moore, in *The Porphyrin Handbook*, ed. K. M. Kadish, K. M. Smith and R. Guilard, Academic Press, San Diego, CA, 2000, vol. 8, p. 153; (b) D. Gust, T. A. Moore and A. L. Moore, in *Electron Transfer in Chemistry*, ed. V. Balzani, Wiley-VCH, Weinheim, 2001, vol. 3, p. 272; (c) S. Fukuzumi and H. Imahori, in *Electron Transfer in Chemistry*, ed. V. Balzani, Wiley-VCH, Weinheim, 2001, vol. 2, p. 927; (d) S. Fukuzumi and D. M. Guldi, in *Electron Transfer in Chemistry*, ed. V. Balzani, Wiley-VCH, Weinheim, 2001, vol. 2, p. 270.
- (a) S. Ishihara, J. Labuta, W. Van Rossom, D. Ishikawa, K. Minami, J. P. Hill and K. Ariga, *Phys. Chem. Chem. Phys.*, 2014, **16**, 9713; (b) N. A. Rakow and K. S. Suslick, *Nature*, 2000, **406**, 710; (c) N. A. Rakow, A. Sen, M. C. Janzen, J. B. Ponder and K. S. Suslick, *Angew. Chem., Int. Ed.*, 2005, **44**, 4528; (d) S. H. Lim, L. Feng, J. W. Kemling, C. J. Musto and K. S. Suslick, *Nat. Chem.*, 2009, **1**, 562; (e) P. Heier, N. D. Boscher, P. Choquet and K. Heinze, *Inorg. Chem.*, 2014, **53**, 11086; (f) P. Heier, T. Bohn, P. Choquet, N. D. Boscher and K. Heinze, *J. Mater. Chem. A*, 2014, **2**, 1560; (g) N. D. Boscher, T. Bohn, P. Heier, F. Moisy, B. Untereiner, K. Heinze and P. Choquet, *Sens. Actuators, B*, 2014, **191**, 553; (h) P. Heier, C. Förster, D. Schollmeyer, N. Boscher, P. Choquet and K. Heinze, *Dalton Trans.*, 2013, **42**, 906.



- 3 (a) M. Ethirajan, Y. Chen, P. Joshia and R. K. Pandey, *Chem. Soc. Rev.*, 2011, **40**, 340; (b) E. D. Sternberg, D. Dolphin and C. Brücker, *Tetrahedron*, 1998, **54**, 4151.
- 4 (a) L. He, T. Chen, Y. You, H. Hu, W. Zheng, W.-L. Kwong, T. Zou and C.-M. Che, *Angew. Chem., Int. Ed.*, 2014, **53**, 12532; (b) C. T. Lum, R. W.-Y. Sun, T. Zou and C.-M. Che, *Chem. Sci.*, 2014, **5**, 1579; (c) C.-M. Che and R. W.-Y. Sun, *Chem. Commun.*, 2011, **47**, 9554; (d) R. W.-Y. Sun, C. K.-L. Li, D.-L. Ma, J. J. Yan, C.-N. Lok, C.-H. Leung, N. Zhu and C.-M. Che, *Chem.–Eur. J.*, 2010, **16**, 3097; (e) R. W.-Y. Sun and C.-M. Che, *Coord. Chem. Rev.*, 2009, **253**, 1682; (f) C.-M. Che, R. W.-Y. Sun, W.-Y. Yu, C.-B. Ko, N. Zhu and H. Sun, *Chem. Commun.*, 2003, 1718.
- 5 (a) C.-Y. Zhou, P. W. H. Chan and C.-M. Che, *Org. Lett.*, 2006, **8**, 325; (b) A. Nijamudheen, D. Jose and A. Datta, *J. Phys. Chem. C*, 2011, **115**, 2187.
- 6 D. Tanaka, Y. Inuta, M. Sakamoto, A. Furube, M. Haruta, Y.-G. So, K. Kimoto, I. Hamada and T. Teranishi, *Chem. Sci.*, 2014, **5**, 2007.
- 7 (a) E. Göransson, J. Boixel, J. Fortage, D. Jacquemin, H.-C. Becker, E. Blart, L. Hammarström and F. Odobel, *Inorg. Chem.*, 2012, **51**, 11500; (b) K. Ohkubo, R. Garcia, P. J. Santic, T. Khoury, M. J. Crossley, K. M. Kadish and S. Fukuzumi, *Chem.–Eur. J.*, 2009, **15**, 10493; (c) J. Fortage, A. Scarpaci, L. Viau, Y. Pellegrin, E. Blart, M. Falkenström, L. Hammarström, I. Asselberghs, R. Kellens, W. Libaers, K. Clays, M. P. Eng and F. Odobel, *Chem.–Eur. J.*, 2009, **15**, 9058; (d) J. Fortage, J. Boixel, E. Blart, H. C. Becker and F. Odobel, *Inorg. Chem.*, 2009, **48**, 518; (e) J. Fortage, J. Boixel, E. Blart, L. Hammarström, H. C. Becker and F. Odobel, *Chem.–Eur. J.*, 2008, **14**, 3467; (f) K. Ohkubo, P. J. Santic, N. V. Tkachenko, H. Lemmetyinen, W. E. Z. Ou, J. Shao, K. M. Kadish, M. J. Crossley and S. Fukuzumi, *Chem. Phys.*, 2006, **326**, 3; (g) S. Fukuzumi, K. Ohkubo, W. E. Z. Ou, J. Shao, K. M. Kadish, J. A. Hutchison, K. P. Ghiggino, P. J. Santic and M. J. Crossley, *J. Am. Chem. Soc.*, 2003, **125**, 14984; (h) K. Kilså, J. Kajanus, A. N. Macpherson, J. Mårtensson and B. Albinsson, *J. Am. Chem. Soc.*, 2001, **123**, 3069; (i) E. K. L. Yeow, P. J. Santic, N. M. Cabral, J. N. H. Reek, M. J. Crossley and K. P. Ghiggino, *Phys. Chem. Chem. Phys.*, 2000, **2**, 4281; (j) I. M. Dixon, J.-P. Collin, J.-P. Sauvage, F. Barigelletti and L. Flamigni, *Angew. Chem., Int. Ed.*, 2000, **39**, 1292; (k) D. B. Amabilino and J.-P. Sauvage, *New J. Chem.*, 1998, 395; (l) A. Harriman, F. Odobel and J.-P. Sauvage, *J. Am. Chem. Soc.*, 1995, **117**, 9461; (m) V. Heitz, S. Chardon-Noblat and J.-P. Sauvage, *Tetrahedron Lett.*, 1991, **32**, 197; (n) A. M. Brun, A. Harriman, V. Heitz and J.-P. Sauvage, *J. Am. Chem. Soc.*, 1991, **113**, 8657.
- 8 (a) Z. Abou-Gamra, A. Harriman and P. Neta, *J. Chem. Soc., Faraday Trans. 2*, 1986, 2337; (b) A. Antipas, D. Dolphin, M. Gouterman and E. C. Johnson, *J. Am. Chem. Soc.*, 1978, **100**, 7705; (c) M. E. Jamin and R. T. Iwamoto, *Inorg. Chim. Acta*, 1978, **27**, 135.
- 9 K. M. Kadish, W. E. Z. Ou, J. Shao, P. J. Santic, K. Ohkubo, S. Fukuzumi and M. J. Crossley, *Chem. Commun.*, 2002, 356.
- 10 (a) J. H. Waters and H. B. Gray, *J. Am. Chem. Soc.*, 1965, **87**, 3534; (b) R. L. Schlupp and A. H. Maki, *Inorg. Chem.*, 1974, **13**, 44; (c) A. J. Blake, J. A. Greig, A. J. Holder, T. I. Hyde, A. Taylor and M. Schröder, *Angew. Chem., Int. Ed. Engl.*, 1990, **29**, 197; (d) A. P. Koley, S. Purohit, S. Ghosh, L. S. Prasad and P. T. Manoharan, *J. Chem. Soc., Dalton Trans.*, 1988, 2607; (e) A. P. Koley, S. Purohit, L. S. Prasad, S. Ghosh and P. T. Manoharan, *Inorg. Chem.*, 1992, **31**, 305; (f) A. P. Koley, L. S. Prasad, P. T. Manoharan and S. Ghosh, *Inorg. Chim. Acta*, 1992, **194**, 219; (g) L. Ihlo, M. Kampf, R. Böttcher and R. Kirmse, *Z. Naturforsch., B: J. Chem. Sci.*, 2002, **57**, 171; (h) M. Kampf, J. Griebel and R. Kirmse, *Z. Anorg. Allg. Chem.*, 2004, **630**, 2669; (i) M. Kampf, R.-M. Olk and R. Kirmse, *Z. Anorg. Allg. Chem.*, 2002, **628**, 34.
- 11 F. G. Herring, G. Hwang, K. C. Lee, F. Mistry, P. S. Phillips, H. Willner and F. Aubke, *J. Am. Chem. Soc.*, 1992, **114**, 1271.
- 12 S. Seidel and K. Seppelt, *Science*, 2000, **290**, 117.
- 13 (a) Z. Ou, W. Zhu, Y. Fang, P. J. Santic, T. Khoury, M. J. Crossley and K. M. Kadish, *Inorg. Chem.*, 2011, **50**, 12802; (b) A. Klein, in *Spectroelectrochemistry*, ed. W. Kaim and A. Klein, RSC publishing, 2008, p. 91; (c) Z. Ou, K. M. Kadish, W. E. J. Shao, P. J. Santic, K. Ohkubo, S. Fukuzumi and M. J. Crossley, *Inorg. Chem.*, 2004, **43**, 2078; (d) S. Fukuzumi, K. Ohkubo, W. E. Z. Ou, J. Shao, K. M. Kadish, J. A. Hutchison, K. P. Ghiggino, P. J. Santic and M. J. Crossley, *J. Am. Chem. Soc.*, 2003, **125**, 14984; (e) G. Gencheva, D. Tsekova, G. Gochev, D. Mehandjiev and P. R. Bontchev, *Inorg. Chem. Commun.*, 2003, **6**, 325.
- 14 (a) F. Mohr, S. Sanz, E. Vergara, E. Cerrada and M. Laguna, *Gold Bull.*, 2006, **39**, 212; (b) F. Mohr, S. Sanz, E. R. T. Tiekink and M. Laguna, *Organometallics*, 2006, **25**, 3084; (c) E. Cerrada, M. Laguna, L. A. Mendez and F. Mohr, *J. Am. Chem. Soc.*, 2005, **127**, 852.
- 15 Z. Qu, L. Giurgiub and E. Roduner, *Chem. Commun.*, 2006, 2507.
- 16 R. Timkovich and A. Tulinsky, *Inorg. Chem.*, 1977, **4**, 962.
- 17 (a) J. Melomedov, J. R. Ochsmann, M. Meister, F. Laquai and K. Heinze, *Eur. J. Inorg. Chem.*, 2014, 2902; (b) J. Melomedov, J. R. Ochsmann, M. Meister, F. Laquai and K. Heinze, *Eur. J. Inorg. Chem.*, 2014, 1984; (c) J. Melomedov, A. Wünsche von Leupoldt, M. Meister, F. Laquai and K. Heinze, *Dalton Trans.*, 2013, **42**, 9272; (d) K. Heinze and A. Reinhart, *Dalton Trans.*, 2008, 469.
- 18 E. B. Fleischer and A. Laszlo, *Inorg. Nucl. Chem. Lett.*, 1969, **5**, 373.
- 19 (a) J.-C. Chambron, V. Heitz and J.-P. Sauvage, *New J. Chem.*, 1997, **21**, 237; (b) N. Solladié, J.-C. Chambron and J.-P. Sauvage, *J. Am. Chem. Soc.*, 1999, **121**, 3684.
- 20 (a) V. W.-W. Yam and E. C.-C. Cheng, *Top. Curr. Chem.*, 2007, **281**, 269–309; (b) M. P. Eng, T. Ljungdahl, J. Andréasson, J. Mårtensson and B. Albinsson, *J. Phys. Chem. A*, 2005, **109**, 1776–1784.
- 21 J. Heinze, *Angew. Chem., Int. Ed.*, 1984, **23**, 831.
- 22 N. G. Connelly and W. E. Geiger, *Chem. Rev.*, 1996, **96**, 877.



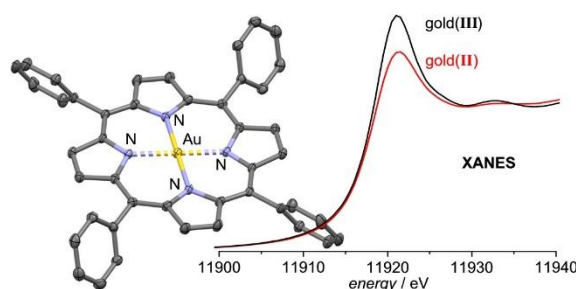
- 23 (a) D. H. Geske and A. H. Maki, *J. Am. Chem. Soc.*, 1969, **82**, 2671; (b) D. H. Geske, J. L. Ragle, M. A. Bambenek and A. L. Balch, *J. Am. Chem. Soc.*, 1964, **86**, 987.
- 24 S. Stoll and A. Schweiger, *J. Magn. Reson.*, 2006, **178**, 42.
- 25 M. J. Frisch, G. W. Trucks, H. B. Schlegel, G. E. Scuseria, M. A. Robb, J. R. Cheeseman, G. Scalmani, V. Barone, B. Mennucci, G. A. Petersson, H. Nakatsuji, M. Caricato, X. Li, H. P. Hratchian, A. F. Izmaylov, J. Bloino, G. Zheng, J. L. Sonnenberg, M. Hada, M. Ehara, K. Toyota, R. Fukuda, J. Hasegawa, M. Ishida, T. Nakajima, Y. Honda, O. Kitao, H. Nakai, T. Vreven, J. A. Montgomery Jr, J. E. Peralta, F. Ogliaro, M. Bearpark, J. J. Heyd, E. Brothers, K. N. Kudin, V. N. Staroverov, R. Kobayashi, J. Normand, K. Raghavachari, A. Rendell, J. C. Burant, S. S. Iyengar, J. Tomasi, M. Cossi, N. Rega, J. M. Millam, M. Klene, J. E. Knox, J. B. Cross, V. Bakken, C. Adamo, J. Jaramillo, R. Gomperts, R. E. Stratmann, O. Yazyev, A. J. Austin, R. Cammi, C. Pomelli, J. W. Ochterski, R. L. Martin, K. Morokuma, V. G. Zakrzewski, G. A. Voth, P. Salvador, J. J. Dannenberg, S. Dapprich, A. D. Daniels, O. Farkas, J. B. Foresman, J. V. Ortiz, J. Cioslowski and D. J. Fox, *Gaussian 09 (Revision A.02)*, Gaussian, Inc., Wallingford CT, 2009.



3.2 Structure and reactivity of a mononuclear gold(II) complex

Sebastian Prei, Christoph Frster, Sven Otto, Matthias Bauer, Patrick Mller, Dariush Hinderberger, Haleh Hashemi Haeri, Luca Carella and Katja Heinze

Nat. Chem. **2017**, *9*, 1249–1255.



The porphyrin macrocycle confers exceptional stability towards the gold(II) core in the mononuclear gold(II) complex Au^{II}(TPP). Typical reactivity patterns of other labile gold(II) species, namely dimerization and disproportionation, become high-energy pathways. The

gold(II) core prefers a 2+2 coordination mode, in between that of gold(I) and gold(III) due to a second-order Jahn-Teller distortion due to the the relativistically lowered 6s orbital of gold.

Author Contribution

Sebastian Prei synthesized and characterised [Au^{III}(TPP)][PF₆] and Au^{II}(TPP), measured the X-band EPR, NMR, infrared, UV-vis and mass spectra and studied the reactivity behaviour of Au^{II}(TPP). [REDACTED] performed the quantum chemical calculations. [REDACTED] performed the single-crystal XRD analysis. [REDACTED] and [REDACTED] measured and interpreted the Q-band EPR spectra at the Martin Luther University Halle-Wittenberg, Germany. [REDACTED] and [REDACTED] measured and interpreted the X-ray absorption spectra at the University of Paderborn, Germany. [REDACTED] performed the magnetic susceptibility measurements. [REDACTED] wrote the manuscript and designed the experiments.

Supporting Information

Supporting Information for this article is found on pp. 107. For full S. I. refer to:

<https://media.nature.com/original/nature-assets/nchem/journal/v9/n12/extref/nchem.2836-s1.pdf>

Reprinted with permission from:

S. Prei, C. Frster, S. Otto, M. Bauer, P. Mller, D. Hinderberger, H. H. Haeri, L. Carella, K. Heinze, *Nat. Chem.* **2017**, *9*, 1249–1255. Copyright 2017 Springer Nature.

Structure and reactivity of a mononuclear gold(II) complex

Sebastian Preiß¹, Christoph Förster¹, Sven Otto^{1,2}, Matthias Bauer³, Patrick Müller³, Dariush Hinderberger⁴, Haleh Hashemi Haeri⁴, Luca Carella¹ and Katja Heinze^{1*}

Mononuclear gold(II) complexes are very rare labile species. Transient gold(II) species have been suggested in homogeneous catalysis and in medical applications, but their geometric and electronic structures have remained essentially unexplored: even fundamental data, such as the ionic radius of gold(II), are unknown. Now, an unprecedentedly stable neutral gold(II) complex of a porphyrin derivative has been isolated, and its structural and spectroscopic features determined. The gold atom adopts a 2+2 coordination mode in between those of gold(III) (four-coordinate square planar) and gold(I) (two-coordinate linear), owing to a second-order Jahn–Teller distortion enabled by the relativistically lowered 6s orbital of gold. The reactivity of this gold(II) complex towards dioxygen, nitrosobenzene and acids is discussed. This study provides insight on the ionic radius of gold(II), and allows it to be placed within the homologous series of nd^9 Cu/Ag/Au divalent ions and the $5d^{8/9/10}$ Pt/Au/Hg ‘relativistic’ triad in the periodic table.

Over the past two decades, gold complexes have attracted a great deal of attention for their role in homogeneous catalysis^{1–3}. Most of the homogeneous gold (pre-)catalysts and intermediates have featured gold in the +I and +III oxidation states^{4–7}, but gold(II) species have also recently been proposed as transient intermediates in photocatalysis, for example by Toste, Glorius and Hashmi and their co-workers^{8–14}. Yet, currently there is a lack of spectroscopic and/or structural evidence for mononuclear gold(II) intermediates in homogeneous catalysis.

In mononuclear species, gold is well known in its favoured oxidation states +I and +III, whereas the +II oxidation state is only very rarely realized¹⁵. Typically, mononuclear Au(II) species dimerize into $[\text{Au(II)}-\text{Au(II)}]^{4+}$ dumbbell complexes or disproportionate into Au(I) and Au(III) (refs 15,16). Only six genuine mononuclear Au(II) complexes have been characterized structurally so far^{17–20}. All of them are ionic compounds and most have been trapped only at low temperature in HF/SbF₅ matrices^{17,19,20}. Apart from a room-temperature X-band electron paramagnetic resonance (EPR) spectrum¹⁸, neither further spectroscopic data nor reactivity or stability studies have been reported so far. The formation of a gold(II) phthalocyanine complex has been reported based on an EPR spectrum²¹, but its preparation could not be reproduced and consequently further characterization is lacking²².

Here we describe the preparation, isolation and characterization of a stable mononuclear gold(II) complex. Gold(III) porphyrin cations have been used as electron acceptors in artificial photosynthetic charge-separation systems^{23–25}. It has also been shown that, after a photoinduced one-electron transfer to a gold(III) porphyrin cation, a gold(II) oxidation state prevails over the gold(III) porphyrin radical anion valence isomer. Indeed, this gold(II) oxidation state had been assigned unambiguously by EPR evidence on species generated *in situ* by the chemical reduction of gold(III) porphyrins^{26–28}. Isolation or further characterization of this material has, however, not yet been reported. Gold(III) porphyrins are used as potent drugs for cancer treatment^{29–32}, but their

biological mode-of-action has not yet been identified fully, and redox reactions, such as those discussed below, might play a role.

For the starting point of this synthesis, we chose a gold(III) porphyrin that was chemically reduced to gold(II) by stoichiometric amounts of cobaltocene or KC₈ and by excess 1-benzyl-1,4-dihydro-nicotinamide. Isolation and purification was then achieved by sublimation or recrystallization. The gold(II) complex was characterized by EPR, NMR, X-ray, ultraviolet–visible (UV–vis) and infrared absorption spectroscopy, as well as by magnetic susceptibility and X-ray diffraction (XRD) analyses. Its reactivity towards oxygen, nitrosobenzene, water and acids is disclosed.

Results and discussion

Synthesis and spectroscopy. $[\text{Au(III)}(\text{TPP})][\text{PF}_6]$ was prepared according to a literature method (in which H₂TPP is meso-tetraphenylporphyrin)²⁸. Reduction of this Au(III) porphyrin at room temperature ($E_{1/2} = -0.97, -1.65, -2.34$ V versus (vs) ferrocene) with 1 equiv. cobaltocene $\text{Co}(\eta^5\text{-C}_5\text{H}_5)_2$, which features a matching redox potential for the first reduction ($E_{1/2} = -1.3$ V vs ferrocene) and hence avoids overreduction, yields a solution of Au(TPP) (Fig. 1)²⁸.

The X-band EPR spectrum of this solution frozen to 77 K has been reported, and displays a rhombic EPR pattern ($g_{zz} = 2.182$, $g_{yy} = 2.056$ and $g_{xx} = 1.982$) with ¹⁹⁷Au and ¹⁴N hyperfine couplings²⁸. The *g* factor deviating from the free-electron value (2.0023) and the hyperfine coupling to gold are only consistent with a metal-centred radical and exclude the formulation of a porphyrin π radical anion²⁸. This electronic description is also consistent with the spin-density plot obtained by density functional theory (DFT) calculations (Fig. 2a). The EPR pattern of the isoelectronic $3d^9$ and $4d^9$ complexes Cu(TPP) and Ag(TPP) are axial, as expected (Cu(TPP), $g_{zz} = 2.187$ and $g_{yy} = g_{xx} = 2.032$; Ag(TPP), $g_{zz} = 2.109$ and $g_{yy} = g_{xx} = 2.038$) (ref. 33). The rhombicity of the X-band EPR spectrum of Au(TPP) was thus unexpected and remained unexplained. Yet, the Q-band EPR spectrum at 50 K of Au(TPP)

¹Institute of Inorganic Chemistry and Analytical Chemistry, Johannes Gutenberg-University, Duesbergweg 10-14, D-55128 Mainz, Germany. ²Graduate School Materials Science in Mainz, Staudingerweg 9, D-55128 Mainz, Germany. ³Department Chemie, University of Paderborn, Warburger Straße 100, D-33098 Paderborn, Germany. ⁴Institute of Chemistry, Martin-Luther-Universität Halle-Wittenberg, von-Danckelmann-Platz 4, D-06120 Halle (Saale), Germany. *e-mail: katja.heinze@uni-mainz.de

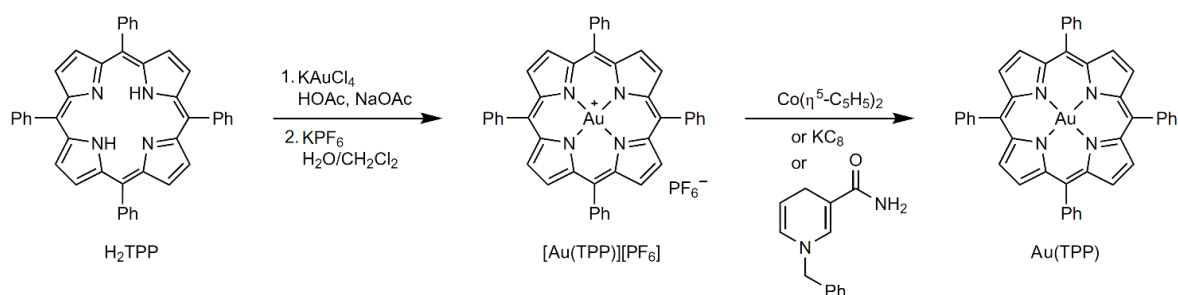


Figure 1 | Preparation of $[\text{Au}(\text{TPP})][\text{PF}_6]$ and chemical reduction to the Au(II) complex $\text{Au}(\text{TPP})$ by cobaltocene, KC_8 or 1-benzyl-1,4-dihydropyridinamide.

prepared *in situ* in CH_2Cl_2 fully confirms the rhombicity of the X-band EPR spectra (Fig. 2b; $g_{zz} = 2.123$, $g_{yy} = 2.057$ and $g_{xx} = 1.968$). Both $\text{Cu}(\text{TPP})$ and $\text{Ag}(\text{TPP})$ display EPR resonances at room temperature³³, whereas $\text{Au}(\text{TPP})$ is EPR silent at room temperature. Hence, the observed EPR spectra at low temperatures are not ascribable to traces of copper(II) or silver(II) species.

Encouraged by the stability of $\text{Au}(\text{TPP})$ even at room temperature, we attempted to isolate $\text{Au}(\text{TPP})$ from the $[\text{Au}(\text{TPP})][\text{PF}_6]/\text{Co}(\eta^5\text{-C}_5\text{H}_5)_2$ reaction mixture by sublimation. At approximately 573 K and 5×10^{-3} mbar, a dark purple-red material sublimed (Supplementary Fig. 1). This material showed the same X-band EPR spectra in frozen CH_2Cl_2 solution as the *in situ* prepared species. Reduction using stoichiometric amounts of KC_8 was also successful (Fig. 1). A liquid-injection field-desorption ionization (LIFDI) mass spectrum in THF under an inert atmosphere confirmed the composition of $\text{Au}(\text{TPP})$ ($\text{C}_{44}\text{H}_{28}\text{N}_4\text{Au}$), and displayed the expected peak at a mass-to-charge ratio of 809.4 (Supplementary Fig. 2). The UV-vis spectrum of $\text{Au}(\text{TPP})$ shows—apart from the expected Soret and Q bands of the porphyrin at 409 and 520 nm—conspicuous bands between 550 and 1,100 nm with extinction coefficients up to $6,500 \text{ M}^{-1} \text{ cm}^{-1}$ (Fig. 3 inset (in $\text{CH}_2\text{Cl}_2:\text{THF}$ 4:1 at 77 K)). Such absorption bands in the visible spectral region are absent in the spectra of $\text{Cu}(\text{TPP})$ and $\text{Ag}(\text{TPP})$ (Supplementary Fig. 3).

$\text{Au}(\text{TPP})$ features an infrared absorption band at 595 cm^{-1} that has no counterpart in the infrared spectra of either $\text{Cu}(\text{TPP})$ or $[\text{Au}(\text{TPP})][\text{PF}_6]$ (Supplementary Figs 4 and 5), which is discussed below. The magnetic susceptibility of $\text{Au}(\text{TPP})$ in the solid state at room temperature, $\chi_{\text{M}}T = 0.40 \text{ cm}^3 \text{ K mol}^{-1}$, is consistent with a $S = 1/2$ ground state of the bulk material with an isotropic g factor of $g_{\text{iso}} = 2.073$ (excellently matching the EPR spectral data), which rules out a disproportionation to diamagnetic ‘ $\text{Au}(\text{I})(\text{TPP})\text{Au}(\text{III})(\text{TPP})$ ’ or a dimerization of the radicals to diamagnetic ‘ $(\text{TPP})\text{Au}-\text{Au}(\text{TPP})$ ’ in the solid state. At low temperatures, only a very weak intermolecular antiferromagnetic interaction between the radicals is present in the solid state, which precludes a strong metal–metal interaction (Supplementary Fig. 6). The room-temperature ^1H and $^{13}\text{C}\{^1\text{H}\}$ NMR spectra of $\text{Au}(\text{TPP})$ in solution show paramagnetically shifted, yet reasonably sharp, NMR resonances. The chemical shifts depend slightly on the solvent (Supplementary Figs 7–14). All the observed ^1H resonances are successfully assigned based on ^1H NMR integrals and cross-peaks in the ^1H correlation spectra. Clearly, the pyrrole β -hydrogen nuclei are strongly shifted, whereas the phenyl nuclei (*ortho*, *meta* and *para*) are less affected. This is consistent with a gold-centred radical with $(5d_{x^2-y^2})^1$ electron configuration, which supports the EPR and susceptibility data.

To corroborate further the +II oxidation state of gold, we employed X-ray absorption near-edge structure (XANES) spectroscopy at the gold L_3 edge. Indeed, the first resonance of $\text{Au}(\text{TPP})$ after the edge step with a medium intensity caused by the $2p \rightarrow 5d^9$ transition is perfectly in between that of the gold(I) reference $\text{Au}_2\text{Cl}_2(\text{xantphos})$ ($5d^{10}$ electron configuration, zero

intensity for the $2p \rightarrow 5d^{10}$ transition) (xantphos, 4,5-bis(diphenylphosphano)-9,9-dimethylxanthene) and the gold(III) porphyrin $[\text{Au}(\text{TPP})][\text{PF}_6]$ ($5d^8$ electron configuration, high intensity for the $2p \rightarrow 5d^8$ transition) according to deconvolution and difference spectra (Fig. 4 and Supplementary Fig. 15). All the accumulated data are consistent with a mononuclear gold(II) species with essentially negligible intermolecular magnetic interactions in the solid state. Yet, the rhombicity of the EPR resonance and the extra

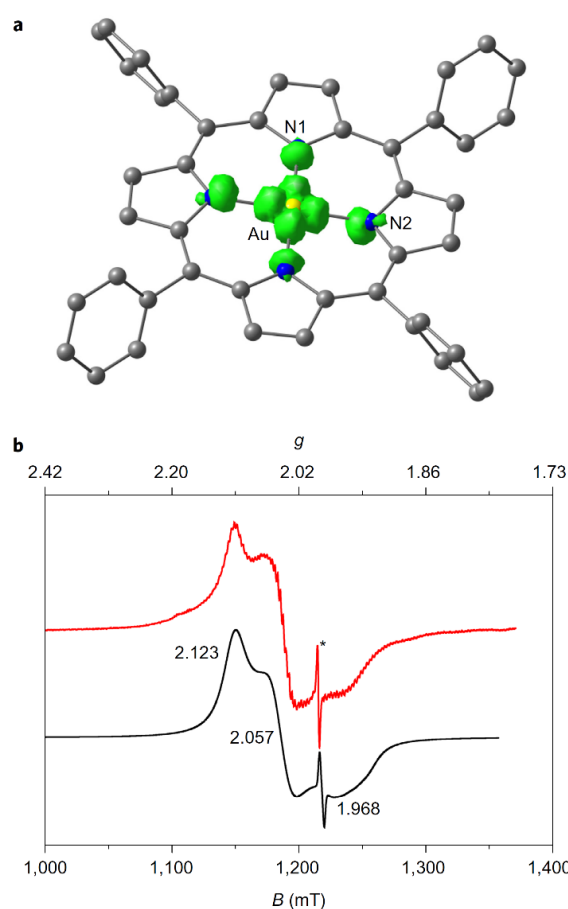


Figure 2 | Electronic structure of $\text{Au}(\text{TPP})$. **a**, The spin-density plot of $\text{Au}(\text{TPP})$ calculated by DFT (B3LYP, def2-TZVPP, ZORA, D3(BJ), COSMO CH_2Cl_2 ; isosurface value in green at 0.01 atomic units; H atoms omitted) illustrates the Au-centred radical. **b**, The Q-band EPR spectrum (red) of $\text{Au}(\text{TPP})$ in CH_2Cl_2 at 50 K (34 GHz) and the simulated spectrum (black) confirms the Au-centred spin density (the asterisk denotes the presence of a porphyrin radical, <30%).

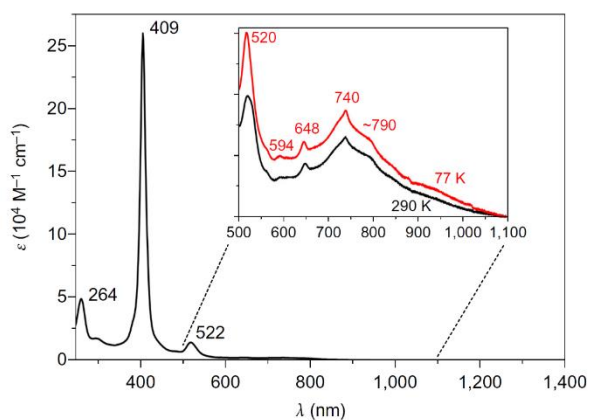


Figure 3 | Absorption spectrum of sublimed **Au(TPP)** in CH_2Cl_2 at 295 K. The inset shows the zoomed absorption spectrum in CH_2Cl_2 :THF (4:1) at 290 K (black) and at 77 K (red), and demonstrates the low-energy charge-transfer bands of **Au(TPP)** in addition to the expected Soret and Q bands.

bands in the visible and infrared regions remain to be explained (*vide infra*).

Solid-state structure. Extended X-ray absorption fine structure (EXAFS) spectroscopy confirms that gold is coordinated by four nitrogen atoms both in $[\text{Au}(\text{TPP})][\text{PF}_6]$ and in **Au(TPP)**, as expected, with Au–N distances of 2.010(20) Å and 2.031(20) Å, respectively. Distinct metrical differences of the different oxidation states could not be extracted from the EXAFS data (Supplementary Fig. 16 and Supplementary Table 1).

In the reported solid-state structure of $[\text{Au}(\text{III})(\text{TPP})][\text{ClO}_4]$ (ref. 29), the coordination geometry of gold is square planar, as expected for a d^8 -M(TPP) complex³⁴. Gold–nitrogen distances amount to 2.032(5)–2.033(5) Å and N–Au–N angles to 89.8–90.1(2)°. The porphyrin core is slightly ruffled with the nitrogen atoms alternately 0.047 Å above and below the N_4 plane. The pyrrole rings are bent with Au–N–X angles $\tau = 170.6$ – 172.0° (X, centre of the β carbon atoms of the respective pyrrole).

Single-crystals of **Au(TPP)**, suitable for single-crystal XRD analysis, were obtained by recrystallization from THF at room temperature (Fig. 5a,b). **Au(TPP)** crystallizes in the triclinic space group $P\bar{1}$, isomorphous with the triclinic modifications of **H₂TPP** (ref. 35) and **Ag(TPP)** (ref. 36). The molecules of **Au(TPP)** are isolated with Au...Au distances of 6.17 Å, which substantiates the very weak intermolecular magnetic interactions. No further solvent co-crystallized, as deduced already from the NMR data. The AuN_4 geometry is planar, similar to isoelectronic M(II)(TPP) complexes (M = Cu, Ag)^{36,37}. However, the Au–N bond lengths are significantly distinct, with Au1–N1 = 2.0586(24) and Au1–N2 = 2.0970(23) Å ($\Delta d = 0.038$ Å), whereas **Cu(TPP)** and **Ag(TPP)** exhibit essentially equal M–N distances ($\Delta d = 0.000$ and 0.019 Å, respectively)^{36,37}. This bond-length alternation of the AuN_4 core is achieved by bending two of the *trans*-positioned pyrrole rings (N2) with $\tau_2 = 165.2^\circ$, whereas the two other pyrrole rings (N1) are essentially coplanar ($\tau_1 = 178.1^\circ$). A similar bending is observed in **H₂TPP**, with $\tau_1 = 178.3^\circ$ and $\tau_2 = 169.1^\circ$ with the two NH groups pointing above and below the plane³⁵. The average M–N bond distance in **Au(TPP)** (2.078(2) Å) is smaller than that in **Ag(TPP)** (2.092(3) Å) (ref. 36), which suggests that gold(II) is slightly smaller than silver(II), similar to observations made by Schmidbauer and co-workers for the Ag(I)/Au(I) pair³⁸.

Electronic structure and quantum-chemical calculations. The nd^9 electron configuration (in D_{4h} symmetry) can invoke a second-order

Jahn–Teller distortion³⁹ by including an excited state with an $nd^8(n+1)s^1$ electron configuration. In the D_{4h} point group, the nd^9 ground state possesses B_{1g} symmetry, whereas the excited state with the electron configuration $nd^8(n+1)s^1$ belongs to the A_{1g} irreducible representation. The direct product $B_{1g} \times A_{1g}$ gives B_{1g} , which corresponds to a symmetry-lowering mode $D_{4h} \rightarrow D_{2h}$, that is, the elongation/contraction of two *trans*-positioned Au–N distances. Within the constrained macrocyclic porphyrin ring, this bond-length differentiation is achieved by bending two *trans*-positioned pyrrole rings. In the series Cu–Ag–Au, the second-order Jahn–Teller distortion should increase because of the amplified relativistic lowering of the $(n+1)s$ orbitals in that series^{40,41}. Indeed, the bond-length differences ($\Delta d = 0.000$ and 0.019–0.039 Å) and the increased bending ($\tau = 175.6^\circ$ and 169.7–165.2°) reflect this trend in the homologous Cu–Ag–Au series. Consequently, the symmetry lowering in **Au(TPP)** is ascribed to a second-order Jahn–Teller effect promoted by the relativistically lowered 6s orbital of gold. The observed distortion in the crystalline state also accounts for the rhombic EPR pattern observed for **Au(TPP)** in frozen solution (Fig. 2b). Vice versa, the EPR spectrum in frozen solution confirms that this distortion is an intrinsic property of four-coordinate gold(II) and should not be ascribed to packing effects in the crystal. Second-order Jahn–Teller distortions using the 6s orbital of gold have been invoked previously for the electronically excited triplet states of Au(I) ($\text{GeCl}_3(\text{PR}_3)_3$), but experimental evidence had been lacking⁴².

In the series of gold oxidation states, d^8 -Au(III) prefers a square-planar geometry and d^{10} -Au(I) a linear coordination mode. Gold in the intermediate oxidation state d^9 -Au(II) appears to prefer a 2+2 coordination geometry in between four and two coordination (Fig. 5a,b). As the solid-state structure of a $[\text{Au}(\text{TPP})]^-$ anion is not available (and probably would not correspond to Au(I) but to a Au(II) porphyrin radical anion species), a comparison with $5d^{10}$ **Hg(TPP)** is more appropriate. The solid-state structure of meso-tetra-(*p*-cyanophenyl)porphyrin mercury(II) has been reported in which the mercury(II) ion sits 0.56 Å above the N_4 mean plane and features alternating short and long Hg–N distances (2.177(6), 2.255(6), 2.169(6) and 2.212(6) Å), and alternating τ angles (176.6°, 154.6°, 177.7° and 163.9°)⁴³. Hence, the increasing ionic radius of M(II) in the relativistic triad⁴⁰ with average M–N distances of 2.005, 2.078 and 2.204 Å (M = Pt, Au and Hg, respectively), might also add to the appreciable M(TPP) distortion. However,

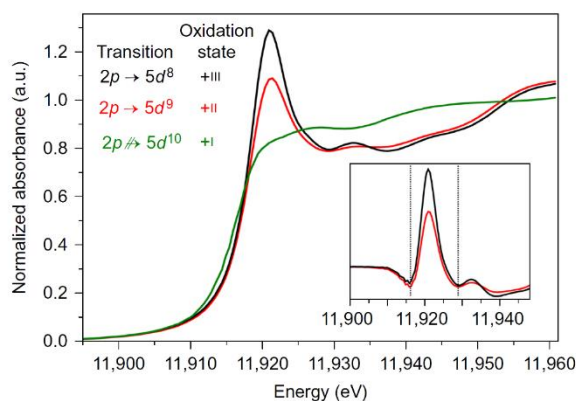


Figure 4 | Experimental normalized XANES spectra of $[\text{Au}(\text{TPP})][\text{PF}_6]$ (black), **Au(TPP)** (red) and $\text{Au}_2\text{Cl}_2(\text{xantphos})$ (green). The inset shows the difference spectra of **Au(TPP)** (red) and $[\text{Au}(\text{TPP})][\text{PF}_6]$ (black) with respect to the Au(I) reference $\text{Au}_2\text{Cl}_2(\text{xantphos})$; the grey dotted lines indicate the region in which analysis was carried out. These confirm the intermediate +II oxidation state of **Au(TPP)** (see Supplementary Information for the details). a.u., arbitrary units.

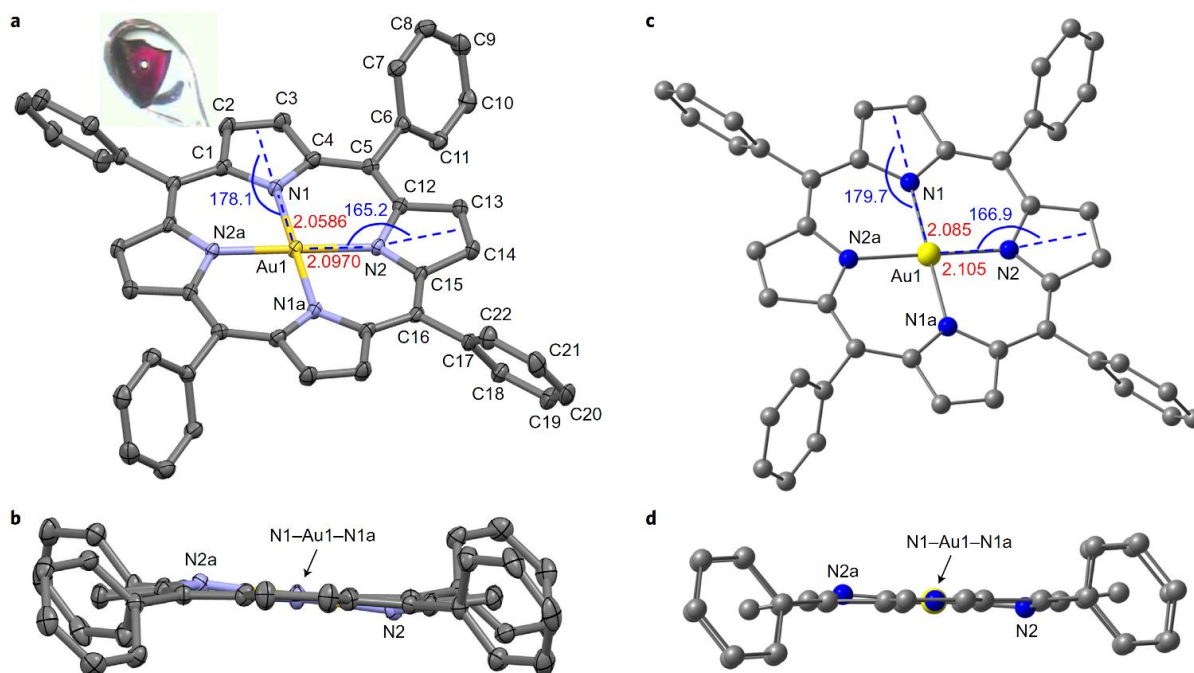


Figure 5 | Molecular structure of the neutral Au(II) complex Au(TPP). **a,b**, Top (**a**) and side (**b**) views along the N1–Au1–N1a axis of the structure obtained by XRD analysis (thermal ellipsoids at 50% probability, hydrogen atoms omitted). Inset: photograph of the examined crystal. **c,d**, Top (**c**) and side (**d**) views along the N1–Au1–N1a axis of the structure obtained by DFT calculation (B3LYP, def2-TZVPP, ZORA, D3(BJ), COSMO (CH₂Cl₂)). The side views illustrate the distorted geometry because of the second-order Jahn–Teller effect. Relevant distances are given in ångströms, and relevant angles are given in degrees.

the average M–N distances are smaller for gold(II) than for silver(II) because of the lanthanide contraction and the relativistic contraction, which suggests that the major part of the distortion arises from the second-order Jahn–Teller distortion and not from the ionic radius.

DFT calculations locate the spin density at the Au centre ($5d_{x^2-y^2}$) and reproduce the second-order Jahn–Teller distortion of Au(TPP) with $\Delta d = 0.020$ Å and $\tau = 166.9^\circ$ (Fig. 5c,d and Supplementary Figs 17 and 18). The distortion is also reflected in the calculated g factor ($g_{zz} = 2.3461$, $g_{yy} = 2.1102$ and $g_{xx} = 1.9625$), which reasonably fits to the experimental data. It is tempting to identify the extra infrared band at 595 cm^{-1} (Supplementary Figs 4 and 5) as the Jahn–Teller modes of Au(TPP) that involve the bending of two *trans* pyrroles. Bending modes of two *trans*-positioned pyrroles are calculated at 574 and 577 cm^{-1} (unscaled), which we tentatively assign to the experimentally observed extra infrared band of Au(TPP). DFT calculations find a transition state between two degenerate Jahn–Teller isomers at 15 kJ mol^{-1} (Supplementary Fig. 19). This low barrier is consistent with the observed averaged ^1H NMR signal set, which suggests an averaged fourfold symmetry of Au(TPP) at room temperature in solution. On cooling to -25°C , only the paramagnetic temperature-dependent Curie shift (*vide supra*, $\delta(\text{H}^{\beta}) \approx T^{-1}$) (Supplementary Figs 20 and 21) is detected and the ^1H NMR resonances neither broaden nor split. This demonstrates a rapid interconversion between the Jahn–Teller isomers on the ^1H NMR timescale.

The extra absorption bands of Au(TPP) observed in the visible/near-infrared (NIR) spectral region are assigned to metal-to-ligand charge transfer (MLCT) bands from the gold $5d_{x^2-y^2}$ orbital to porphyrin π^* orbitals and to ligand-to-metal charge transfer bands from the porphyrin's π orbitals to the half-filled $5d_{x^2-y^2}$ orbital according to time-dependent DFT calculations (Supplementary Fig. 22). This interpretation is in accordance with the gold(II) oxidation state that features a singly occupied $5d_{x^2-y^2}$ orbital. In contrast to Cu(TPP) and similar to Ag(TPP) (ref. 44), Au(TPP) is non-emissive

both at room temperature and at 77 K in a CH_2Cl_2 :THF (4:1) glass. The non-emissive behaviour of Ag(TPP) has been ascribed to the presence of the low-energy, symmetry-forbidden MLCT state⁴⁴ and the same argument applies to Au(TPP), which also features such low-energy MLCT states.

Stability and reactivity. The inertness of Au(TPP) towards disproportionation (Fig. 6a), an otherwise common reactivity pattern of Au(II) complexes, is reflected in the electrochemical data with $\Delta E = 680\text{ mV}$ (THF, [*n*Bu₄N][PF₆]) for the oxidation and reduction of Au(TPP) to [Au(TPP)]⁺ and [Au(TPP)][−], respectively²⁸. The equilibrium constant for disproportionation is estimated as $K_D = \exp(-\Delta E/25.69) = 3 \times 10^{-12}$ at 298 K . Though the Au(III) porphyrin [Au(TPP)]⁺ is stable and easily accessible, the anion [Au(TPP)][−] appears not particularly favourable, either as a Au(I) valence isomer or, more likely, as a Au(II) porphyrin radical anion.

Thanks to the favourable NMR properties of both [Au(TPP)]⁺ and Au(TPP), the self-exchange reaction (Fig. 6b) between [Au(TPP)]⁺ and Au(TPP) is easily probed by ^1H NMR spectroscopy. The addition of Au(TPP) to a [Au(TPP)]⁺ solution in CD_2Cl_2 shifts the ^1H NMR resonances according to the amount of paramagnetic Au(TPP) added. No distinct resonances for Au(TPP) appear (Supplementary Fig. 23). Hence, electron transfer between [Au(TPP)]⁺ and Au(TPP) is rapid on the ^1H NMR timescale, which suggests small inner- and outer-sphere reorganizations.

The porphyrin macrocycle prohibits the typical dimerization^{15,16} of Au(II) complexes to dumbbell shaped [Au–Au]⁴⁺ dimers by blocking in-plane binding sites (Fig. 6c). According to DFT calculations, the spin density of the 17-valence-electron complex Au(TPP) is distributed in the σ system within the porphyrin AuN₄ plane (xy plane (Supplementary Fig. 18)) and not perpendicular to the ligand plane (z axis), which would be required for dimerization along the z axis. Hence, the formation of Au₂(TPP)₂ dimers is unfavourable for steric reasons.

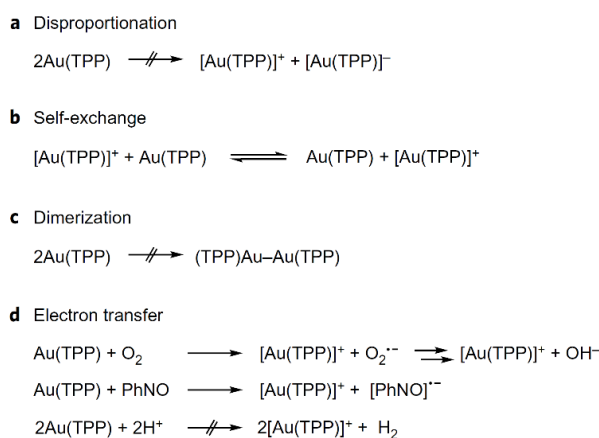


Figure 6 | Studies of the reactivity of Au(TPP). **a**, Towards disproportionation into $[\text{Au(TPP)}]^+$ and $[\text{Au(TPP)}]^-$. **b**, Towards electron self-exchange between $[\text{Au(TPP)}]^+$ and Au(TPP) . **c**, Towards dimerization to a metal-metal bonded dimer $\text{Au}_2(\text{TPP})_2$. **d**, Towards electron transfer to substrates O_2 , PhNO or H^+ .

The porphyrin macrocycle stabilizes the gold(II) oxidation state with respect to disproportionation and dimerization. This also accounts for the exceptional thermal stability of Au(TPP) (vide supra). Yet, redox reactions are feasible. Au(TPP) ($E_{1/2} = -0.96$ V vs ferrocene²⁸) is thermodynamically competent to reduce dioxygen to superoxide ($E_{1/2}(\text{O}_2(\text{dissolved})/\text{O}_2^{\cdot-}) = -0.18$ V vs the normal hydrogen electrode; -0.81 V vs ferrocene⁴⁵). ^1H NMR spectroscopy shows the appearance of $[\text{Au(TPP)}]^+$ after allowing Au(TPP) to stand under a non-inert atmosphere (air, humidity) in d_8 -THF, which confirms the electron transfer (Fig. 6d (Supplementary Fig. 24)). The infrared spectrum of the product shows an absorption band at $3,487\text{ cm}^{-1}$, characteristic for an OH stretching vibration. This infrared spectrum is fully congruent with the infrared spectrum of $[\text{Au(TPP)}][\text{OH}]$ obtained from the anion exchange of $[\text{Au(TPP)}][\text{PF}_6]$ with KOH (Supplementary Fig. 25). Peaks at m/z 825 are observed in the positive electrospray ionization mass spectra of both products and correspond to $[\text{Au(TPP)}(\text{OH})-\text{H}]^+$ (Supplementary Fig. 26). Hence, the final product of Au(TPP) and O_2 is $[\text{Au(TPP)}][\text{OH}]$, which confirms the further reduction of superoxide into hydroxide. Gold(III) hydroxido species are of fundamental importance for the water-splitting reaction and oxygen-reduction reaction (ORR), as has been elegantly demonstrated by Bochmann and co-workers using gold complexes of tridentate C–N–C pincer ligands⁴⁶. Yet, with tridentate ligands, mononuclear Au(II) complexes are not accessible because the dumbbell dimer (C–N–C)Au–Au(C–N–C) forms⁴⁷. In contrast to mononuclear Au(TPP) , this (C–N–C)Au(II)–Au(II)(C–N–C) dimer is kinetically incompetent in the ORR because of its strong Au–Au bond^{46,47}.

To demonstrate further the redox reactivity of Au(TPP) , the spin-trapping agent nitrosobenzene^{48,49} was added to Au(TPP) as an O_2 surrogate (Fig. 6d). The EPR resonance changes from the broad gold(II) resonance (Fig. 2b and Preiß *et al.*²⁸) to a narrow resonance around $g = 2.0$ (Supplementary Fig. 27). This is consistent with a nitroxyl radical anion without the participation of the metal centre^{49,50}. Obviously, electron transfer from Au(TPP) to PhNO without a strong coordination of the resulting $[\text{PhNO}]^{\cdot-}$ radical anion to gold(III)⁵⁰ has occurred. The reduction of PhNO to $[\text{PhNO}]^{\cdot-}$ resembles the initial step of the ORR by Au(TPP) , that is, the formation of reactive oxygen species (ROS) (Fig. 6d). The formation of ROS by $[\text{Au(TPP)}]^+$ drugs has been suggested as one of the pathways that leads to apoptosis^{29,30} and we present direct evidence for ROS formation from Au(TPP) and O_2 . Several natural redox mediators, such as glutathione, thioredoxins or NADH feature redox potentials close

to the Au(III)/Au(II) redox couple and hence the $[\text{Au(TPP)}]^{+/0}$ pair might play a role in, the biological mode of action of Au(III) porphyrin-based anticancer drugs, namely the reduction of $[\text{Au(TPP)}]^+$ to Au(TPP) followed by ROS formation with O_2 and $[\text{Au(TPP)}]^+$ regeneration (Fig. 6d). Indeed, excess 1-benzyl-1,4-dihydronicotinamide (as the NADH model⁵⁰) reduces $[\text{Au(TPP)}]^+$ to Au(TPP) in the presence of a base (Supplementary Fig. 28).

In the absence of O_2 , Au(TPP) is stable in the presence of water (Supplementary Fig. 29). The coordination of water, protodemetalation to give H_2TPP and the formation of H_2 and $[\text{Au(TPP)}]^+$ do not occur. Even with excess trifluoroacetic acid, Au(TPP) does not reduce protons (Fig. 6d and Supplementary Fig. 30). Hence, Au(TPP) catalyses the ORR, but not the proton reduction reaction. Neither oxygen donor ligands (water and THF) nor nitrogen donor ligands (pyridine) coordinate to Au(TPP) , as shown by ^1H NMR spectroscopy, because of the first-order Jahn–Teller effect that operates in the d^9 electron configuration³⁹.

Conclusion

In the mononuclear Au(II) complex Au(TPP) , the porphyrin macrocycle confers exceptional stability towards Au(II) by blocking the typical reactivity patterns (dimerization and disproportionation) of Au(II). In the planar N_4 coordination environment of Au(TPP) , Au(II) prefers a 2+2 coordination mode, in between that of Au(III) (four-coordinate square planar) and that of Au(I) (two-coordinate linear), because of a second-order Jahn–Teller distortion enabled by the relativistically lowered $6s$ orbital of Au. The degenerate Jahn–Teller distortion in the xy plane of the macrocycle is dynamic on the ^1H NMR timescale but is frozen in solid matrices.

Electron transfer between Au(TPP) and $[\text{Au(TPP)}]^+$ is fast on the ^1H NMR timescale. Electronic coupling is sufficiently large, although the electron formally transfers between the σ systems of Au ($5d_{x^2-y^2}$ orbitals) and not the π systems of the porphyrins. Electron transfer from Au(TPP) to O_2 gives $[\text{Au(TPP)}]^+$ and superoxide (ROS), and finally hydroxide. Similarly, Au(TPP) reduces PhNO to $[\text{PhNO}]^{\cdot-}$. In oxygen-free water and in the presence of acids, Au(TPP) is stable. The reduction of $[\text{Au(TPP)}]^+$ by an NADH model even produces Au(TPP) . The combined data suggest a decisive role of the $[\text{Au(TPP)}]^{+/0}$ redox couple capable of ROS generation in the presence of reductant and O_2 in Au-based anticancer drugs.

We anticipate that the ease of synthesis and exceptional stability of Au(TPP) will allow future studies of the reactivity of this first isolable Au(II) complex, for example, towards main-group elements, radicals and Lewis acids and bases. Furthermore, clever coordination-geometry design will allow the preparation and isolation of further mononuclear Au(II) complexes and will allow the exploration of this novel class of mononuclear Au(II) coordination compounds in the areas of catalysis, electron transfer and medicinal chemistry.

Methods

Full details of the employed methods are given in Supplementary Information.

Preparation of Au(TPP) by reduction with cobaltocene. Under an inert atmosphere, $[\text{Au(TPP)}][\text{PF}_6]$ (239 mg, 0.250 mmol) was dissolved in CH_2Cl_2 (20 ml). Cobaltocene ($\text{Co}(\eta^3\text{-C}_5\text{H}_5)_2$) (47 mg, 0.250 mmol) was added as a solid. After stirring for 1 h at room temperature, the solvent was removed under reduced pressure. The dark residue was sublimed at approximately 573 K and 5×10^{-3} mbar to give a dark purple material, yield 87 mg (0.107 mmol, 43%). Under these conditions, variable amounts of cobaltocene sublime concomitantly. The presence of some cobaltocene is only seen by NMR spectroscopy after re-oxidation to $[\text{Au(TPP)}]^+$ and cobaltocenium ions. Single crystals of Au(TPP) were obtained by recrystallization from THF at room temperature.

Preparation of Au(TPP) by reduction with KC_8 . Under an inert atmosphere, $[\text{Au(TPP)}][\text{PF}_6]$ (10.0 mg, 0.010 mmol) was dissolved in THF (10 ml). KC_8 (1.5 mg, 0.011 mmol) was added as a solid. After stirring for 12 h at room temperature, solid materials were removed by filtration and the solvent was removed under reduced

pressure. The dark residue was dissolved in CH_2Cl_2 (5 ml) and the brown solution was filtered to remove KPF_6 (the ^{31}P NMR spectrum of the material confirms the successful removal of KPF_6). The solvent was removed under reduced pressure to give the dark purple product in essentially quantitative yield, 7.9 mg (0.0098 mmol, 98%). ^1H NMR (CD_2Cl_2) δ (ppm) = 4.15 (H^a), 5.78 (H^b), 9.05 (H^m), 25.38 (H^p). ^1H NMR (d_8 -toluene) δ (ppm) = 2.45 (H^a), 4.65 (H^b), 9.22 (H^m), n.o. (H^p). ^1H NMR (d_6 -THF) δ (ppm) = 4.34 (H^a), 5.89 (H^b), 8.95 (H^m), 27.5 (H^p). $^{13}\text{C}\{^1\text{H}\}$ NMR (d_6 -THF) δ (ppm) = 133.8 (C^a), 137.4 (C^m), 230.4 (C^p), n.o. (C^b). FD^+ (LIFDI, THF) m/z (%) = 809.4 (100, M^+). Infrared (KBr) (cm^{-1}) 1,072(m), 1,015(s), 595(m). UV-vis-NIR (THF): λ (nm) (ϵ ($\text{M}^{-1}\text{cm}^{-1}$)) = 410 (158,480), 523 (10,685), 596 (2,380), 654 (3,865), 741 (5,150). Magnetism (298 K) $\chi_{\text{M}}T = 0.40\text{ cm}^3\text{ K mol}^{-1}$. Elemental analysis calculated (found) for $\text{C}_{44}\text{H}_{28}\text{AuN}_4$: C, 65.27 (65.06); H 3.49 (5.80); N 6.92 (5.13). The consistently low N values might point to nitride formation during combustion analysis.

Data availability. Atomic coordinates and structure factors for the crystal structure of $\text{Au}(\text{TPP})$ are deposited at the Cambridge Crystallographic Data Centre (CCDC) under the accession code CCDC 1520924; copies of the data can be obtained free of charge from www.ccdc.cam.ac.uk/data_request/cif. All the other data that support the findings of this study are available within Supplementary Information files, and are also available from the corresponding author on reasonable request.

Received 24 January 2017; accepted 27 June 2017;
published online 7 August 2017

References

- Fürstner, A. Gold and platinum catalysis—a convenient tool for generating molecular complexity. *Chem. Soc. Rev.* **38**, 3208–3221 (2009).
- Hashmi, A. S. K. Dual gold catalysis. *Acc. Chem. Res.* **47**, 864–876 (2014).
- Dorel, R. & Echavarren, A. M. Gold(I)-catalyzed activation of alkynes for the construction of molecular complexity. *Chem. Rev.* **115**, 9028–9072 (2015).
- Hashmi, A. K. S. Homogeneous gold catalysis beyond assumptions and proposals—characterized intermediates. *Angew. Chem. Int. Ed.* **49**, 5232–5241 (2010).
- Liu, L. P. & Hammond, G. B. Recent advances in the isolation and reactivity of organogold complexes. *Chem. Soc. Rev.* **41**, 3129–3139 (2012).
- Echavarren, A. M. & Obradors, C. Intriguing mechanistic labyrinths in gold(I) catalysis. *Chem. Commun.* **50**, 16–28 (2014).
- Joost, M., Amgoune, A. & Bourissou, D. Reactivity of gold complexes towards elementary organometallic reactions. *Angew. Chem. Int. Ed.* **54**, 15022–15045 (2015).
- Sahoo, B., Hopkinson, M. N. & Glorius, F. Combining gold and photoredox catalysis: visible light-mediated oxy- and aminoarylation of alkenes. *J. Am. Chem. Soc.* **135**, 5505–5508 (2013).
- Winston, M. S., Wolf, W. J. & Toste, F. D. Photoinitiated oxidative addition of CF_3I to gold(I) and facile aryl- CF_3 reductive elimination. *J. Am. Chem. Soc.* **136**, 7777–7782 (2014).
- Shu, X., Zhang, M., He, Y., Frei, H. & Toste, F. D. Dual visible light photoredox and gold-catalyzed arylate ring expansion. *J. Am. Chem. Soc.* **136**, 5844–5847 (2014).
- Tlahuext-Aca, A., Hopkinson, M. N., Sahooab, B. & Glorius, F. Dual gold/photoredox-catalyzed C(sp)-H arylation of terminal alkynes with diazonium salts. *Chem. Sci.* **7**, 89–93 (2016).
- Hopkinson, M. N., Tlahuext-Aca, A. & Glorius, F. Merging visible light photoredox and gold catalysis. *Acc. Chem. Res.* **49**, 2261–2272 (2016).
- Huang, L., Rudolph, M., Rominger, F. & Hashmi, A. S. K. Photosensitizer-free visible-light-mediated gold-catalyzed 1,2-difunctionalization of alkynes. *Angew. Chem. Int. Ed.* **55**, 4808–4813 (2016).
- Kim, S., Rojas-Martin, J. & Toste, F. D. Visible light-mediated gold-catalysed carbon(sp²)-carbon(sp) cross-coupling. *Chem. Sci.* **7**, 85–88 (2016).
- Gimeno, M. C. & Laguna, A. in *Comprehensive Coordination Chemistry II* Vol. 6 (eds McCleverty, J. A. & Meyer, T. J.) 999–1145 (Elsevier, 2005).
- Mohamed, A. A., Abdou, H. E. & Fackler, J. P. Jr. Coordination chemistry of gold(II) with amidinate, thiolate and ylide ligands. *Coord. Chem. Rev.* **254**, 1253–1259 (2010).
- Elder, S. H., Lucier, G. M., Hollander, F. J. & Bartlett, N. Synthesis of Au(II) fluoro complexes and their structural and magnetic properties. *J. Am. Chem. Soc.* **119**, 1020–1026 (1997).
- Blake, A. J. *et al.* Bis(1,4,7-trithiacyclononane)gold dication: a paramagnetic, mononuclear Au^{II} complex. *Angew. Chem. Int. Ed.* **29**, 197–198 (1990).
- Seidel, S. & Seppelt, K. Xenon as a complex ligand: the tetra xenon gold(II) cation in $\text{AuXe}_4^{2+}(\text{Sb}_2\text{F}_{11}^-)$. *Science* **290**, 117–118 (2000).
- Drews, T., Seidel, S. & Seppelt, K. Gold-xenon complexes. *Angew. Chem. Int. Ed.* **41**, 454–456 (2002).
- MacCragh, A. & Koski, W. S. The phthalocyanine of gold. *J. Am. Chem. Soc.* **87**, 2496–2497 (1965).
- Wong, E. W. Y. *et al.* Gold(II) phthalocyanine revisited: synthesis and spectroscopic properties of gold(III) phthalocyanine and an unprecedented ring-contracted phthalocyanine analogue. *Chem. Eur. J.* **18**, 12404–12410 (2012).
- Brun, A. M., Harriman, A., Heitz, V. & Sauvage, J. P. Charge transfer across oblique bisporphyrins: two-center photoactive molecules. *J. Am. Chem. Soc.* **113**, 8657–8663 (1991).
- Fukuzumi, S. *et al.* Metal-centered photoinduced electron transfer reduction of a gold(III) porphyrin cation linked with a zinc porphyrin to produce a long-lived charge-separated state in nonpolar solvents. *J. Am. Chem. Soc.* **125**, 14984–14985 (2003).
- Fortage, J. *et al.* Single-step electron transfer on the nanometer scale: ultra-fast charge shift in strongly coupled zinc porphyrin-gold porphyrin dyads. *Chem. Eur. J.* **14**, 3467–3480 (2008).
- Kadish, K. M. *et al.* Evidence that gold(III) porphyrins are not electrochemically inert: facile generation of gold(II) 5,10,15,20-tetrakis(3,5-di-*tert*-butylphenyl)porphyrin. *Chem. Commun.* 356–357 (2002).
- Ou, Z. *et al.* Substituent effects on the site of electron transfer during the first reduction for gold(III) porphyrins. *Inorg. Chem.* **43**, 2078–2086 (2004).
- Preiß, S., Melomedov, J., Wünsche von Leupoldt, A. & Heinze, K. Gold(III) tetraarylporphyrin amino acid derivatives: ligand or metal centred redox chemistry? *Chem. Sci.* **7**, 596–610 (2016).
- Che, C.-M. *et al.* Gold(III) porphyrins as a new class of anticancer drugs: cytotoxicity, DNA binding and induction of apoptosis in human cervix epithelioid cancer cells. *Chem. Commun.* 1718–1719 (2003).
- Wang, Y., He, Q. Y., Sun, R. W., Che, C. M. & Chiu, J. F. Gold(III) porphyrin Ia induced apoptosis by mitochondrial death pathways related to reactive oxygen species. *Cancer Res.* **65**, 11553–11564 (2005).
- Lum, C. T., Sun, R. W.-Y., Zou, T. & Che, C.-M. Gold(III) complexes inhibit growth of cisplatin-resistant ovarian cancer in association with upregulation of proapoptotic *PMS2* gene. *Chem. Sci.* **5**, 1579–1584 (2014).
- Hu, D. *et al.* Anticancer gold(III) porphyrins target mitochondrial chaperone Hsp60. *Angew. Chem. Int. Ed.* **55**, 1387–1391 (2016).
- Manoharan, P. T. & Rogers, M. T. in *Electron Spin Resonance of Metal Complexes* (ed. Yen, T. F.) 143–173 (Plenum, 1969).
- Hazell, A. Structure of (5,10,15,20-tetraphenyl-21H,23H-porphinato)platinum(II), $\text{C}_{44}\text{H}_{28}\text{N}_4\text{Pt}$. *Acta Cryst. C* **40**, 751–753 (1984).
- Silvers, S. J. & Tulinsky, A. The crystal and molecular structure of tris(4-tetraphenylporphyrin). *J. Am. Chem. Soc.* **89**, 3331–3337 (1967).
- Scheidt, W. R. *et al.* Crystal and molecular structure of the silver(II) and zinc(II) derivatives of meso-tetraphenylporphyrin. An exploration of crystal-packing effects on bond distance. *Inorg. Chem.* **25**, 795–799 (1986).
- Plaza, L. A. & Chojnacki, J. Influence of chloroform on crystalline products yielded in reactions of 5,10,15,20-tetraphenylporphyrin with HCl and copper(II) salts. *Acta Cryst. C* **86**, m24–m28 (2012).
- Bayler, A., Schier, A., Bowmaker, G. A. & Schmidbaur, H. Gold is smaller than silver. Crystal structures of [bis(trimesitylphosphine)gold(I)] and [bis(trimesitylphosphine)silver(I)] tetrafluoroborate. *J. Am. Chem. Soc.* **118**, 7006–7007 (1996).
- Pearson, R. G. Concerning Jahn-Teller effects. *Proc. Natl Acad. Sci. USA* **72**, 2104–2106 (1975).
- Leyva-Pérez, A. & Corma, A. Similarities and differences between the ‘relativistic’ triad gold, platinum, and mercury in catalysis. *Angew. Chem. Int. Ed.* **51**, 614–635 (2012).
- Pyykkö, P. Theoretical chemistry of gold. III. *Chem. Soc. Rev.* **37**, 1967–1997 (2008).
- Bojan, R. V. *et al.* Double Jahn-Teller distortion in AuGe complexes leading to a dual blue-orange emission. *ChemPlusChem* **81**, 176–186 (2016).
- Wang, M. C. *et al.* Mercury complexes of meso-tetra-(*p*-cyanophenyl)porphyrin and *N*-methylporphyrin: meso-tetra-(*p*-cyanophenyl)porphyrinatomercury(II) and chloro(*N*-methyl-meso-tetraphenylporphyrinato) mercury(II). *Inorg. Chem.* **40**, 6064–6068 (2001).
- Antipas, A., Dolphin, D., Gouterman, M. & Johnson, E. C. Porphyrins. 38. Redox potentials, charge transfer transitions, and emission of copper, silver, and gold complexes. *J. Am. Chem. Soc.* **100**, 7705–7709 (1978).
- Koppenol, W. H., Stanbury, D. M. & Bounds, P. L. Electrode potentials of partially reduced oxygen species, from dioxygen to water. *Free Radic. Biol. Med.* **49**, 317–322 (2010).
- Roşca, D.-A., Wright, J. A., Hughes, D. L. & Bochmann, M. Gold peroxide complexes and the conversion of hydroperoxides into gold hydrides by successive oxygen-transfer reactions. *Nat. Commun.* **4**, 2167 (2013).
- Dann, T. *et al.* Electrochemistry of Au^I and Au^{III} pincer complexes: determination of the Au^I-Au^{III} bond energy. *Chem. Commun.* **49**, 10169–10171 (2013).
- Neidinger, A., Kienz, T. & Heinze, K. Spin trapping of carbon-centered ferrocenyl radicals with nitrosobenzene. *Organometallics* **34**, 5310–5320 (2015).
- Núñez-Vergara, L. J. *et al.* Nitrosobenzene: electrochemical, UV-visible and EPR spectroscopic studies on the nitrosobenzene free radical generation and its interaction with glutathione. *Electrochim. Acta* **45**, 3555–3561 (2000).
- Zhu, X.-Q. *et al.* Hydride, hydrogen atom, proton, and electron transfer driving forces of various five-membered heterocyclic organic hydrides and their reaction intermediates in acetonitrile. *J. Am. Chem. Soc.* **130**, 2501–2516 (2008).

Acknowledgements

Parts of this research were conducted using the supercomputer Mogon and advisory services offered by Johannes Gutenberg University Mainz (www.hpc.uni-mainz.de), which is a member of the AHRP and the Gauss Alliance. We thank P. Auerbach and M. Mondeshki for collecting the LIFDI mass spectra and assistance with the paramagnetic NMR spectra and R. Jung-Pothmann for collection of the diffraction data. This work was financially supported by the Deutsche Forschungsgemeinschaft (GSC 266, Materials Science in Mainz, scholarship for S.O.). PETRA III is acknowledged for the provision of beamtime at beamline P64. This article is dedicated to G. Huttner on the occasion of his 80th birthday.

Author contributions

S.P. synthesized $[\text{Au}(\text{TPP})][\text{PF}_6]$ and $\text{Au}(\text{TPP})$, measured the X-band EPR, NMR, infrared, UV-Vis and mass spectra and studied the reactivity, S.O. made the quantum chemical calculations, C.F. performed the single-crystal XRD analysis, D.H. and H.H.H. measured

and interpreted the Q-band EPR spectra, P.M. and M.B. measured and interpreted the X-ray absorption spectra and L.C. measured the magnetic susceptibility data. K.H. conceived and designed the experiments and wrote the paper. All of the authors discussed the results and commented on the manuscript.

Additional information

Supplementary information and chemical compound information are available in the [online version of the paper](#). Reprints and permissions information is available online at www.nature.com/reprints. Publisher's note: Springer Nature remains neutral with regard to jurisdictional claims in published maps and institutional affiliations. Correspondence and requests for materials should be addressed to K.H.

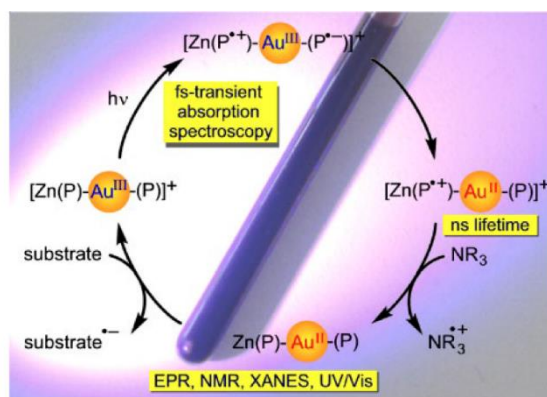
Competing financial interests

The authors declare no competing financial interests.

3.3 Gold(II) porphyrins in photoinduced electron transfer reactions

Sebastian Preiß, Ayla Pöpcke, Lukas Burkhardt, Luca Großmann, Stefan Lochbrunner, Matthias Bauer, Till Opatz and Katja Heinze

Chemistry a European Journal, 2019, accepted.



The light irradiation of zinc(II)-gold(III) bis(porphyrin) dyads $[Zn(P)-Au^{III}(P)]^+$ yields long-lived gold(II) intermediates. These gold(II) intermediates are confirmed by using a combination of spectroscopic and theoretical techniques. The dyads are competent enough to be utilised as photoredox catalysts.

Author Contributions

The synthesis and characterisation of the zinc(II)-gold(III) bis(porphyrin) dyads as well as the PET experiments and DFT calculations were performed by Sebastian Preiß. The time-resolved photoluminescence and transient absorption spectroscopy experiments were performed and analysed by [REDACTED] and [REDACTED] at the University of Rostock, Germany. The XANES experiments were performed and analysed by [REDACTED] and [REDACTED] at the University of Paderborn, Germany. [REDACTED] and [REDACTED] contributed to the PET experiments and the catalytic test reactions. [REDACTED] designed the experiments and supervised the project. The manuscript was written by [REDACTED] (80 %) and [REDACTED] (20 %).

Supporting Information

Supporting Information for this article is found on pp. 141. For full S. I. refer to:

<https://doi.org/10.1002/chem.201900050>

“Preiß, S.; Pöpcke, A.; Burkhardt, L.; Großmann, L.; Lochbrunner, S.; Bauer, M.; Opatz, T.; Heinze, K. *Chem. Eur. J.* 2019, accepted. Copyright Wiley-VCH Verlag GmbH & Co. KGaA. Reproduced with permission.”

Gold(II) Porphyrins in Photoinduced Electron Transfer Reactions

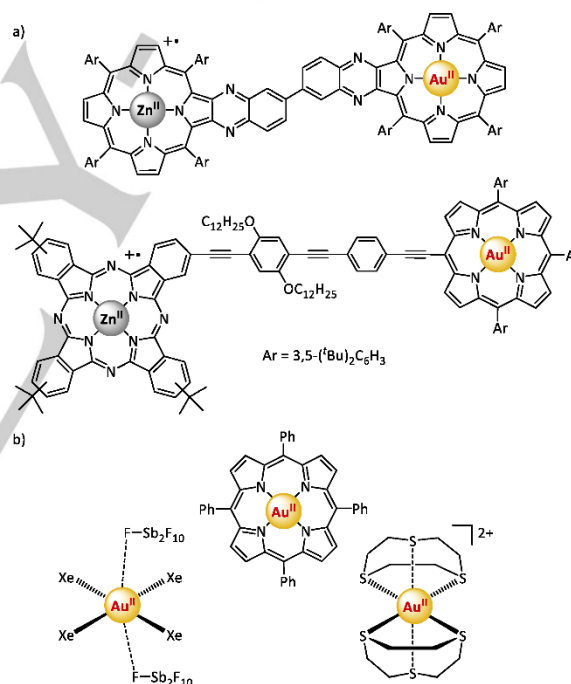
Sebastian Preiß^[a], Ayla Pöpcke^[b], Lukas Burkhardt^[c], Luca Großmann^[d], Stefan Lochbrunner^[b], Matthias Bauer^[c], Till Opatz^[d], and Katja Heinze^{[a]*}

Abstract: In the context of solar to chemical energy conversion inspired by natural photosynthesis, we present the synthesis, electrochemical properties and photoinduced electron transfer processes of three novel zinc(II)-gold(III) bis(porphyrin) dyads $[\text{Zn}^{\text{II}}(\text{P})-\text{Au}^{\text{III}}(\text{P})]^+$. Time-resolved spectroscopic studies indicate ultrafast dynamics ($k_{\text{ET1}} > 10^{10} \text{ s}^{-1}$) after visible light excitation finally yielding a charge-shifted state $[\text{Zn}^{\text{II}}(\text{P}^{++})-\text{Au}^{\text{II}}(\text{P})]^+$ featuring a gold(II) centre. The lifetime of this excited state is quite long thanks to a comparably slow charge recombination ($k_{\text{BET2}} \approx 3 \times 10^9 \text{ s}^{-1}$). The $[\text{Zn}^{\text{II}}(\text{P}^{++})-\text{Au}^{\text{II}}(\text{P})]^+$ charge-shifted state is reductively quenched by amines in bimolecular reactions yielding the neutral zinc(II)-gold(II) bis(porphyrin) $\text{Zn}^{\text{II}}(\text{P})-\text{Au}^{\text{II}}(\text{P})$. The electronic nature of this key gold(II) intermediate, prepared by chemical or photochemical reduction, is elucidated by UV/Vis, X-band EPR, gold L_3 -edge XANES and paramagnetic ^1H NMR spectroscopy as well as by quantum chemical calculations. Finally, the gold(II) site in $\text{Zn}^{\text{II}}(\text{P})-\text{Au}^{\text{II}}(\text{P})$ is thermodynamically and kinetically competent to reduce an aryl azide to the corresponding amine paving the way to catalytic applications of gold(III) porphyrins in photoredox catalysis involving the gold(III/II) redox couple.

Introduction

Photoinduced electron transfer (PET) can be considered as the most important chemical reaction with enormous relevance to life.^[1] It constitutes the fundamental step in natural photosynthesis as well as in many artificial devices to convert solar energy into chemical energy.^[2] Significant advances in the understanding of photoinduced charge separation have been obtained via examination of artificial reaction centres consisting of covalently linked donor and acceptor molecular units.^[3] Ferrocene^[4], carotenoid polyenes^[5] and zinc(II) porphyrins^[6] represent typical electron donor entities whereas quinones^[4c,4h] (natural acceptors) or fullerenes^[4a,4b,4d,4e,4f] act as electron acceptors. Cobaltocenium ions^[7] or gold(III) porphyrins^[8,9,10] (Scheme 1a) constitute a class of cationic electron acceptors.

Pioneering studies by Sauvage^[8], and more recently by the groups of Crossley/Fukuzumi/Kadish^[9] and Hammarström/Odobel^[10] have shown that efficient and even ultrafast electron transfer ($k_{\text{ET}} = 10^{12} \text{ s}^{-1}$) occurs in porphyrin arrays composed of zinc(II) porphyrin chromophores and gold(III) porphyrins along with a rather low back-electron transfer rate ($k_{\text{BET}} = 10^9 \text{ s}^{-1}$) resulting in comparably long-lived charge-shifted states.^[10d]



Scheme 1. a) Suggested transient charge-shifted states in zinc-gold dyads including gold(II)^{9e,10d} and b) selection of structurally characterised genuine mononuclear gold(II) complexes.^{11,12,13}

The high forward rate is due to π -conjugated bridges between the chromophore and the electron acceptor facilitating the electron transfer.^[12] The recombination reaction has a large driving force and hence the back-electron transfer occurs in the Marcus inverted region. Furthermore, the slow recombination has been attributed to the trapping of the electron on the gold centre retarding the back electron transfer.^[12]

- [a] S. Preiß, Prof. Dr. K. Heinze
Institute of Inorganic Chemistry and Analytical Chemistry
Johannes Gutenberg University of Mainz
Duesbergweg 10-14, 55128 Mainz, Germany
E-mail: katja.heinze@uni-mainz.de
- [b] A. Pöpcke, Prof. Dr. S. Lochbrunner
Institute of Physics and Department of Life, Light, and Matter,
University of Rostock, 18051 Rostock, Germany
- [c] L. Burkhardt, M. Bauer,
Department Chemie and Center for Sustainable Systems Design
(CSSD), University of Paderborn, Warburger Straße 100, D-33098
Paderborn, Germany
- [d] L. Großmann, T. Opatz
Institute of Organic Chemistry, Johannes Gutenberg University of
Mainz, Duesbergweg 10-14, 55128 Mainz, Germany

Supporting information for this article is given via a link at the end of the document.

FULL PAPER

The localisation of the unpaired electron at the gold centre has been unambiguously demonstrated for the paramagnetic prototype d^9 complex $Au^I(PPP)$ ($H_2PPP = meso$ -tetraphenylporphyrin) by EPR and XANES spectroscopy as well as by single crystal X-ray diffraction.^[13] Apart from gold(II) porphyrins $Au^I(P)$, further genuine mononuclear gold(II) complexes with d^9 electron configuration are still quite rare species (Scheme 1b) due to the favoured disproportionation or dimerisation.^[11,13c] The valence isomerisation process of $[Au^{III}(P^{•-})]$ to $Au^I(P)$ depends on thermodynamic and kinetic aspects, especially changes in Au-N bond lengths and macrocycle deformation,^[13] and is a further key to the long lifetime of charge-shifted states involving gold(III) porphyrins (Scheme 1a).

Homogeneous gold catalysis is dominated by reactions which retain the +1 oxidation state of gold(I) in the catalytic cycle.^[14] A single report deals with the cycloisomerisation of allenones employing $[Au^I(PPP)]^+$.^[15] Yet, low-coordinate gold(II) intermediates have been repeatedly suggested as transient intermediates in the context of photochemical gold-catalysed reactions, for instance by Glorius, Hashmi and Toste.^[16] However, spectroscopic or structural evidence for low-coordinate gold(II) species in photoredox catalysis is still lacking. The isolable tetracoordinate gold(III/II) porphyrins, however, are well suited for further studies involving the $Au^{III/II}$ redox couple in redox and photoredox processes.

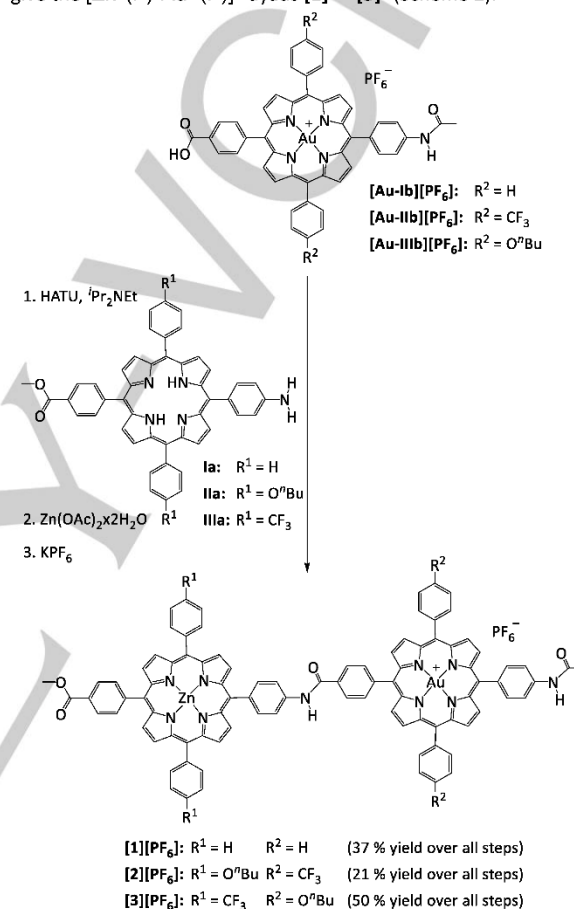
Herein we present the synthesis and properties of three novel donor-bridge-acceptor dyads $[Zn^II(P)-Au^III(P)][PF_6]$ **[1][PF₆]** – **[3][PF₆]**, designed to undergo rapid photoinduced electron transfer using zinc(II) porphyrin amino acid derivatives as chromophores and electron donors and gold(III) porphyrin amino acid derivatives as electron acceptors connected by a π -conjugated amide bridge with porphyrin-aryl torsion angles around 50 – 80° in the solid state.^[4a] In order to tune the driving forces of the forward PET and recombination reactions, the individual building blocks bear electron-donating and electron-withdrawing *meso*-aryl groups (Ar = 4- $C_6H_4O^tBu$, 4- $C_6H_4CF_3$). The light-induced charge-shifted states are probed by femtosecond transient absorption spectroscopy and are employed in bimolecular reactions with amines as sacrificial electron donors. The electronic structure of the resulting reduced dyads $Zn^II(P)-Au^I(P)$ is elucidated by X-band EPR, gold L_3 -edge X-ray absorption near edge structure (XANES) and paramagnetic 1H NMR spectroscopy in combination with Density Functional Theory calculations. Finally, $[Zn^II(P)-Au^III(P)]^+$ is employed in a visible-light induced catalytic process.

Results and Discussion

Syntheses of building blocks, reference compounds and dyads.

The free-base and aurated building blocks **la** – **IIla** and **[Au-Ib][PF₆]** – **[Au-IIIb][PF₆]**, as well as the *N*-acetyl or ester protected zinc(II) and gold(III) reference compounds **Zn-Ac-Ia** – **Zn-Ac-IIIa** and **[Au-Ac-Ib][PF₆]** – **[Au-Ac-IIIb][PF₆]** were

prepared according to literature procedures.^[4a,13b,17] The cationic gold(III) porphyrin acids were easily prepared by metalation of the free-base porphyrins **lb** – **IIIb** with potassium tetrachloridoaurate(III) in the presence of HOAc/NaOAc according to “Fleischer’s route”.^[18] The synthetic strategy is based on coupling a substitutionally inert, cationic gold(III) porphyrin acid **[Au-Ib]⁺** – **[Au-IIIb]⁺** with a free-base amine-substituted porphyrin **la** – **IIIa** to give the $[Zn^II(P)-Au^III(P)]^+$ dyads **[1]⁺** – **[3]⁺** (Scheme 2).



Scheme 2. Synthesis of dyads **[1][PF₆]** – **[3][PF₆]**.

Amide formation between the porphyrins is enabled by the coupling reagent HATU (1-[bis(dimethylamino)methylene]-1*H*-1,2,3-triazolo[4,5-*b*]pyridinium 3-oxide hexafluorophosphate) and DIPEA (*N,N*-diisopropylethylamine) in DMF. The dyads **[1][PF₆]** – **[3][PF₆]** were obtained from the free base dyads via metalation with zinc(II) acetate dihydrate and subsequent counterion exchange with KPF₆ (Scheme 2).

Characterisation of dyads **[1][PF₆]** – **[3][PF₆]**.

The constitution of dyads **[1][PF₆]** – **[3][PF₆]** was established via 1H NMR, ^{13}C NMR, ^{31}P NMR and 2D NMR spectroscopy

FULL PAPER

(Supporting Information, Fig. S1 – S8), IR spectroscopy (Supporting Information, Fig. S9 – S11), UV/Vis spectroscopy (Supporting Information, Fig. S12 – S13) and high-resolution mass spectrometry (Supporting Information, Fig. S14 – S16). For solubility reasons, DMF is employed in the NMR studies.

The successful amide formation is clearly substantiated by the appearance of the NH amide proton resonances at $\delta = 11.25 - 11.29$ ppm in the ^1H NMR spectra. The terminal $\text{CH}_3(\text{ester})$ and $\text{CH}_2(\text{amide})$ substituents exhibit characteristic resonances at $\delta = 4.11 - 4.14$ and $2.32 - 2.34$ ppm, respectively, in a correct integral ratio. A consequence of the successful metalation with zinc(II) acetate dihydrate is the expected disappearance of the inner pyrrole NH resonances. The $[\text{PF}_6]^-$ counterions feature the characteristic septet at $\delta = -144$ ppm in the ^{31}P NMR spectra. IR absorption bands for group vibrations appear for the ester and amide substituents at around 1715 and 1668 cm^{-1} , respectively. Absorptions of PF stretching and deformation modes of $[\text{PF}_6]^-$ counterions appear at $839 - 841$ and $556 - 557$ cm^{-1} , respectively. ESI⁺ mass spectra show the expected signals of the **[1]⁺**, **[2]⁺** and **[3]⁺** cations at $m/z = 1641.3703$, 1921.4610 , 1921.4605 , respectively, confirming the stability and integrity of the complex cations.

Photophysical properties.

The electronic absorption spectra of the dyads **[1][PF₆]** – **[3][PF₆]** are in good agreement with those of the constituent monoporphyrins displaying similar band maxima and no splitting of Soret or Q bands. The absorption spectra of **[1][PF₆]** – **[3][PF₆]** are essentially a superposition of the unperturbed monoporphyrin spectra,^[19] as exemplarily shown for dyad **[1][PF₆]** in Fig. 1 (Supporting Information, Fig. S12 – S13 for **[2][PF₆]** and **[3][PF₆]**). This indicates a very weak ground-state electronic interaction between the individual building blocks of the amide-bridged dyads.

The gold(III) porphyrinato reference complexes **[Au-Ac-Ib][PF₆]** and **[Au-Ac-Ilb][PF₆]** show hypsochromically shifted and weaker Soret bands as compared to the reference zinc porphyrins **Zn-Ac-Ia** – **Zn-Ac-Ila** representing the Au and Zn constituents of dyads **[1]⁺** and **[2]⁺**. This furnishes the characteristic high-energy shoulder on the Soret bands of **[1]⁺** and **[2]⁺** (Fig. 1; Supporting Information, Fig. S12). The gold(III) porphyrin **[Au-Ac-Ilb]** with electron-donating *O^tBu* substituents, however, displays a similar Soret energy as the zinc(II) porphyrin **Zn-Ac-Ila** with electron-withdrawing CF_3 substituents, resulting in a Soret band of **[3]⁺** without a shoulder (Supporting Information, Fig. S13).^[20] As expected for metalloporphyrins with local D_{4h} symmetry, a reduction of the number of Q bands from four to two is observed in all cases compared to their free-base ancestors with local D_{2h} symmetry. In all cases, the Q bands of the gold(III) porphyrin are at higher energy than those of the corresponding zinc(II) porphyrin (Fig. 1; Supporting Information, Fig. S12 – S13).

The fluorescence maxima, fluorescence quantum yields and the excited state lifetimes of the dyads **[1][PF₆]** – **[3][PF₆]** and the associated reference zinc porphyrins **Zn-Ac-Ia** – **Zn-Ac-Ila** are summarised in Table 1. Gold(III) porphyrins are non-emissive in fluid solution at room temperature.^[20b,21] This also holds for the

reference compounds **[Au-Ac-Ib][PF₆]** – **[Au-Ac-Ilb][PF₆]** (Fig. 1; Supporting Information, Fig. S12 – S13). Emission energies (S_1 state) of the zinc reference compounds **Zn-Ac-Ia** – **Zn-Ac-Ila** and the respective dyads **[1][PF₆]** – **[3][PF₆]** are very similar (Fig. 1; Supporting Information, Fig. S12 – S13), confirming that only the zinc porphyrins are emissive. However, the zinc(II) porphyrin S_1 fluorescence is nearly completely quenched in all dyads irrespective of the *meso*-substituents R^1 and R^2 ($> 97\%$). Similar to comparable dyads^[10], depopulation of the fluorescent S_1 state of Zn(P) occurs by photoinduced electron transfer towards the appended gold(III) porphyrin resulting in a charge-shifted singlet state ^1CSh (and the triplet state ^3CSh after intersystem crossing) $^{1,3}[\text{Zn}^{\text{II}}(\text{P}^{\text{+}})-\text{Au}^{\text{III}}(\text{P})]^{\text{+}}$ (*vide infra*). The residual weak fluorescence is associated with a small fraction of unquenched dyads. The driving force for the light-induced electron transfer is estimated from electrochemical data.

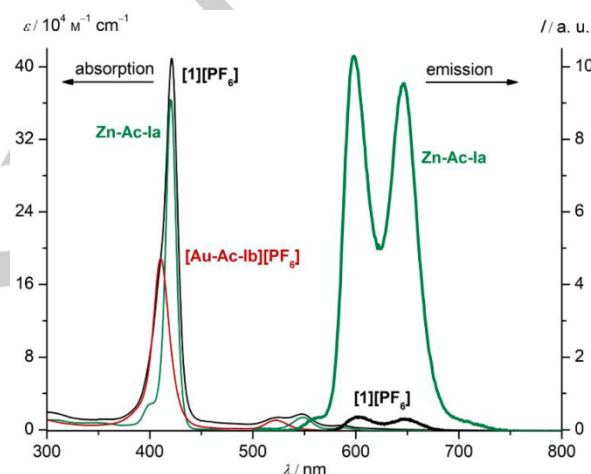


Figure 1. Absorption and emission spectra of **[1][PF₆]** and constituent monoporphyrins in CH_2Cl_2 . Excitation wavelength was 421 nm.

Table 1. Fluorescence data of porphyrins in CH_2Cl_2 at room temperature.

	R^1	R^2	$\lambda_{\text{em}}/\text{nm}^{[a]}$	ϕ_{f}	$\tau/\text{ns}^{[b]}$	quenching [%]
Zn-Ac-Ia	H	–	598, 648	0.1037	1.7	
[1][PF₆]	H	H	599, 646	0.0029	1.6	97
Zn-Ac-Ila	<i>O^tBu</i>	–	602, 649	0.0770	1.5	
[2][PF₆]	<i>O^tBu</i>	CF_3	601, 649	0.0017	1.3	98
Zn-Ac-Illa	CF_3	–	599, 644	0.1003	1.8	
[3][PF₆]	CF_3	<i>O^tBu</i>	599, 647	0.0011	1.7	99

^[a] Excitation wavelength was 421 nm, except for **Zn-Ac-Ila** and **[3][PF₆]** (418 nm). ^[b] All decays are monoexponential.

Electrochemical investigations.

During sequential one-electron redox reactions, porphyrin macrocycles generally exhibit two reversible oxidations, which lead to the π cation radical and the porphyrin dication, whereas reversible reductions yield the π anion radical and the porphyrin dianion. This also includes metalloporphyrins with coordinated

FULL PAPER

redox-inert metal ions, such as Mg^{2+} (d^0) or Zn^{2+} (d^{10}). The situation can change in the presence of a "non-innocent" metal ion like Au^{3+} (d^8) with an empty $d_{x^2-y^2}$ orbital. In gold(III) porphyrins, the initial gold-based reduction is followed by a porphyrin-based reduction.^[10,12,13] The individual redox potentials of the dyads **[1][PF₆]** – **[3][PF₆]** are close to those of the respective reference zinc and gold porphyrins **Zn-Ac-Ia** – **Zn-Ac-IIIa** and **[Au-Ac-Ib][PF₆]** – **[Au-Ac-IIIb][PF₆]** (Fig. 2; Supporting Information, Fig. S17 – S19) indicating the absence of ground state interactions between the zinc(II) porphyrin chromophores and the attached gold(III) porphyrin acceptors (Table 2).^[49] Furthermore, the negligible shift of the first reduction of the mononuclear gold(III) porphyrins and the corresponding dyads is in agreement with a metal-based mechanism that is only weakly affected by the appended chromophore.^[9e,10c] This behaviour is exemplarily illustrated in Fig. 2 displaying the cyclic voltammograms of dyad **[2][PF₆]** and associated "building-blocks" **Zn-Ac-Ila** and **[Au-Ac-IIIb][PF₆]**.

Table 2. Redox potentials of reference compounds **Zn-Ac-Ia** – **Zn-Ac-IIIa**, **[Au-Ac-Ib][PF₆]** – **[Au-Ac-IIIb][PF₆]** and dyads **[1][PF₆]** – **[3][PF₆]** in 0.1 M [ⁿBu₄N][PF₆]/THF solution, potentials given in V relative to the ferrocene/ferrocenium couple.

	$E_{1/2}(\text{P/Zn})$ (ox ²)	$E_{1/2}(\text{P/Zn})$ (ox ¹)	$E_{1/2}(\text{Au}^{\text{III/II}})$ (red ⁰)	$E_{1/2}(\text{P/Au})$ (red ¹)	$E_{1/2}(\text{P/Zn})$ (red ²)
Zn-Ac-Ia	^[b]	0.40	–	–	–1.78
[Au-Ac-Ib][PF₆] ^[a]	–	–	–0.96	–1.44	–
[1][PF₆]	^[b]	0.42	–0.95	–1.44	–1.77
Zn-Ac-IIa	0.71	0.35	–	–	–1.93
[Au-Ac-IIIb][PF₆]	–	–	–0.91	–1.55	–
[2][PF₆]	0.68	0.33	–0.92	–1.53	–1.93
Zn-Ac-IIIa	^[b]	0.49	–	–	–1.85
[Au-Ac-IIIb][PF₆]	–	–	–0.98	–1.64	–
[3][PF₆]	^[b]	0.49	–0.99	–1.63	–1.83

^[a] In DMF. ^[b] Outside solvent window.

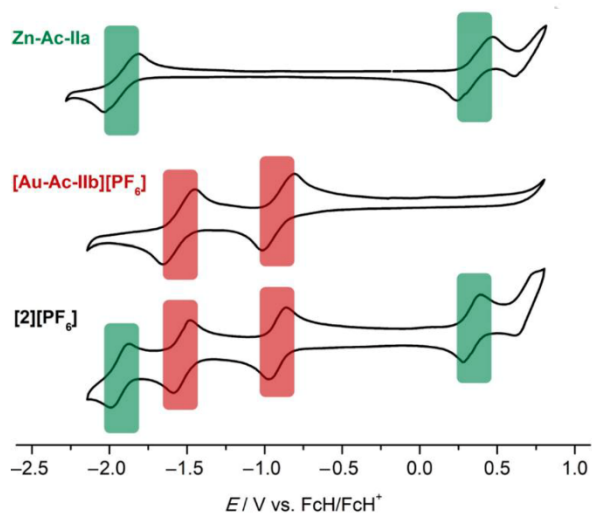


Figure 2. Cyclic voltammograms of **Zn-Ac-Ila**, **[Au-Ac-IIIb][PF₆]** and dyad **[2][PF₆]** in 0.1 M [ⁿBu₄N][PF₆]/THF solution.

The *meso*-aryl substituents generally induce an anodic shift of the first oxidation and reduction potentials in the series $\text{R} = \text{O}^t\text{Bu} > \text{H} > \text{CF}_3$.^[19] The shifts amount up to 0.14 V for the first ligand-centred oxidation (ox¹) from **Zn-Ac-Ila** ($\text{R}^1 = \text{O}^t\text{Bu}$) to **Zn-Ac-IIIa** ($\text{R}^1 = \text{CF}_3$) and 0.07 V for the first metal-centred reduction (red⁰) from **[Au-Ac-IIIb][PF₆]** ($\text{R} = \text{O}^t\text{Bu}$) to **[Au-Ac-Ib][PF₆]** ($\text{R} = \text{CF}_3$). The differences between the gold-centred and subsequent ligand-centred reduction of the respective dyads amount to 0.49 – 0.64 V. This translates to high comproportionation constants of $K_c > 10^{10}$ for the neutral gold(II) complexes.^[13,22] Therefore, disproportionation of neutral dyads $\text{Zn}^{\text{II}}(\text{P})\text{-Au}^{\text{II}}(\text{P})$ (prepared electrochemically, chemically or photochemically) can be ruled out and all spectral signatures after one-electron reduction will be associated with the neutral $\text{Zn}^{\text{II}}(\text{P})\text{-Au}^{\text{II}}(\text{P})$ dyads.^[13b]

Table 3. Energies of the porphyrin $\text{S}_1(\text{Zn})$ and ${}^1,{}^3\text{CSh}$ states, as well as rate constants and driving forces for the three dyads.

	$E(\text{S}_0 \rightarrow \text{S}_1)$ (Zn) [eV]	$E({}^1,{}^3\text{CSh})$ [eV]	$k_{\text{ET1/HT1}}$ [s ⁻¹]	ΔG_{ET1}^0 [eV]	k_{BET1} [s ⁻¹]	k_{BET2} [s ⁻¹]
[1][PF₆]	2.07	1.37	4.8×10^{10}	–0.70	8.3×10^9	3.3×10^8
[2][PF₆]	2.06	1.25	8.3×10^{10}	–0.81	12.2×10^9	3.3×10^8
[3][PF₆]	2.07	1.48	–	–0.59	3.4×10^8	2.9×10^8

Energy diagrams of the dyads.

The fluorescence data (Table 1) along with the electrochemical data (Table 2) enable assessing the free energy changes of the photoinduced electron transfer from the zinc(II) porphyrin's first singlet excited state (S_1) to the corresponding gold(III) porphyrin (ΔG_{ET}^0) and of the subsequent back electron transfer to restore the ground state ($-E({}^1,{}^3\text{CSh})$; Table 3).

As these are merely charge-shift reactions (CSh) without charge separation, the simplified Rehm-Weller equation^[23] is used neglecting a Coulomb interaction term to estimate the energy of the CSh state(s). As illustrated in Table 3, the driving force for photoinduced electron transfer (ΔG_{ET}^0) increases in the series **[2]⁺** > **[1]⁺** > **[3]⁺** in accordance with the electron donating and withdrawing effects of the *meso*-aryl substituents. Concomitantly, the driving force for the back electron transfer ($-E({}^1,{}^3\text{CSh})$) increases in the series **[3]⁺** > **[1]⁺** > **[2]⁺**. With the free Gibbs energies between –1.25 and –1.48 eV, the BET processes are likely to be in the Marcus inverted region.^[10d,24]

A simplified and generalised energy level diagram of $[\text{Zn}^{\text{II}}(\text{P})\text{-Au}^{\text{III}}(\text{P})]^+$ dyads upon photoexcitation is illustrated in Fig. 3. The zinc(II) porphyrin and gold(III) porphyrin excited singlet states $\text{S}_1(\text{Zn/Au})$ and $\text{S}_2(\text{Zn/Au})$ are determined from emission and absorption spectroscopic data (Table 3, Supporting Information, Exp. Section). The zinc and gold porphyrin triplet state energies $\text{T}_1(\text{Zn})$ and $\text{T}_1(\text{Au})$ are estimated from literature data. The triplet energies of zinc(II) porphyrins range from 1.41 eV to 1.81 eV,^[25] those of gold(III) porphyrins from 1.75 eV to 1.82 eV.^[8e,21b,26] Both depend slightly on the substitution pattern and the solvent. The final charge shifted states ${}^1,{}^3[\text{Zn}^{\text{II}}(\text{P}^{*+})\text{-Au}^{\text{II}}(\text{P})]^+$ (${}^1,{}^3\text{CSh}$) are calculated from the electrochemical data (Table 3). A significant energy difference between singlet and triplet charge-shifted

FULL PAPER

states ^1CSh and ^3CSh is not expected considering the large distance of the spin centres. In fact, the unpaired electrons should be essentially uncoupled in the CSh states. The energies of the intermediate charge shifted states $^{1,3}[\text{Zn}^{\text{II}}(\text{P}^{**})-\text{Au}^{\text{III}}(\text{P}^{*})]^+$, populated directly after the electron transfer from the π -HOMO of the Zn(P) to the π -LUMO of the Au^{III}(P) moiety, are not experimentally accessible. However, quantum chemical calculations place these states above the $^{1,3}[\text{Zn}^{\text{II}}(\text{P}^{**})-\text{Au}^{\text{II}}(\text{P})]^+$ valence isomeric state in agreement with the gold(II) nature of the final $^{1,3}\text{CSh}$ states (see below; ESI).^[13] Irradiating at the Soret band energies, in principle both sites of the dyad can be excited as seen in Fig. 1. Starting with excitation of the Zn(P) site, the $\text{S}_2(\text{Zn})$ state of Zn(P) is populated. The driving force of PET from the $\text{S}_2(\text{Zn})$ state to yield the charge-shifted states is very high, placing these reactions in the Marcus inverted region.²⁴ Consequently, internal conversion (IC) from the $\text{S}_2(\text{Zn})$ to the $\text{S}_1(\text{Zn})$ state should dominate ($k_{\text{IC}(\text{Zn})}$). In principle, energy transfer from the $\text{S}_1(\text{Zn})$ to the $\text{S}_1(\text{Au})$ state can occur but this is slightly uphill and therefore excluded from Fig. 3. The $\text{S}_1(\text{Zn})$ state can undergo ISC to the zinc porphyrin triplet state $^3[\text{Zn}^{\text{II}}(\text{P})-\text{Au}^{\text{III}}(\text{P})]^+$ ($\text{T}_1(\text{Zn})$; $k_{\text{ISC}(\text{Zn})}$) or give the CSh state(s) by electron transfer ($k_{\text{ET}1}$). The $\text{T}_1(\text{Zn})$ state is also above the CSh state(s) and hence, electron transfer yielding ^3CSh states from $\text{T}_1(\text{Zn})$ is conceivable as well ($k_{\text{ET}2}$).

Excitation of the gold porphyrin site at the Soret band should yield the $\text{S}_2(\text{Au})$ state of the gold porphyrin. This $\text{S}_2(\text{Au})$ state should undergo efficient internal conversion to the $\text{S}_1(\text{Au})$ state ($k_{\text{IC}(\text{Au})}$) similar to the zinc site. Based on the efficient spin-orbit coupling enabled by the gold atom, rapid ISC to the gold porphyrin triplet state $\text{T}_1(\text{Au})$ occurs in a few hundred femtoseconds ($k_{\text{ISC}(\text{Au})}$).^[21b,26] Triplet-triplet energy transfer from the $\text{T}_1(\text{Au})$ to the $\text{T}_1(\text{Zn})$ state is slightly downhill by ca. 0.2 eV^[9e,26] and therefore conceivable (not shown in Fig. 3 for clarity).^[27] Hole-transfer from $\text{S}_1(\text{Au})$ and $\text{T}_1(\text{Au})$ states to give the CSh state(s) is thermodynamically feasible as well ($k_{\text{HT}1}$, $k_{\text{HT}2}$). In any case, the CSh states are well below the S_1 and T_1 states of both metalloporphyrins and are in principle accessible via diverse pathways.

(Figure 3 see end of manuscript)

Figure 3. Energy level diagram of dyads **[1][PF₆]**–**[3][PF₆]** including triplet and charge-shifted states. Abbreviations: CSh = charge-shift, ET = electron transfer, HT = hole transfer, BET = back electron transfer, IC = internal conversion, ISC = intersystem crossing.

Time-resolved emission and transient absorption spectroscopy.

Excitation of **[1][PF₆]** – **[3][PF₆]** at 410 nm in THF results in weak fluorescence from the $\text{S}_1(\text{Zn})$ state (Fig. 1, Table 1). Applying time-resolved photoluminescence reveals that the emission follows a monoexponential decay law in all cases. The corresponding emission lifetimes are similar to the lifetimes of the respective zinc(II) porphyrin references **Zn-Ac-Ia** – **Zn-Ac-IIIa** (Table 1, Supporting Information, Figure S20). However, the much lower fluorescence quantum yield of **[1][PF₆]** – **[3][PF₆]** indicates that only a minority of the excited population ends up in

the minimum of the S_1 state while the majority is quenched by an ultrafast decay to a non-emissive state. This decay is faster than the time resolution of the instrument of 50 ps. We assign this ultrafast decay to the electron transfer yielding the CSh state(s) ($k_{\text{ET}1/\text{HT}1} > 10^{10} \text{ s}^{-1}$, in the Marcus normal region).^[24] Consequently, most of the observed residual steady-state emission of the dyads arises from a small, unquenched fraction of the S_1 state population.

In order to track the evolution of the non-emissive states ($\text{S}_1(\text{Au})$, $\text{T}_1(\text{Zn})$; $\text{T}_1(\text{Au})$ and $^{1,3}\text{CSh}$), pump-probe transient absorption (TA) spectroscopy was employed in the fs-ns time regime. The TA spectra of **[1][PF₆]** in THF 0.3 – 1400 ps after excitation with a 400 nm pulse are depicted in Fig. 4a. The TA spectra of the dyads **[2][PF₆]** and **[3][PF₆]** and their dynamics are basically similar to that of **[1][PF₆]** (Supporting Information, Fig. S21).

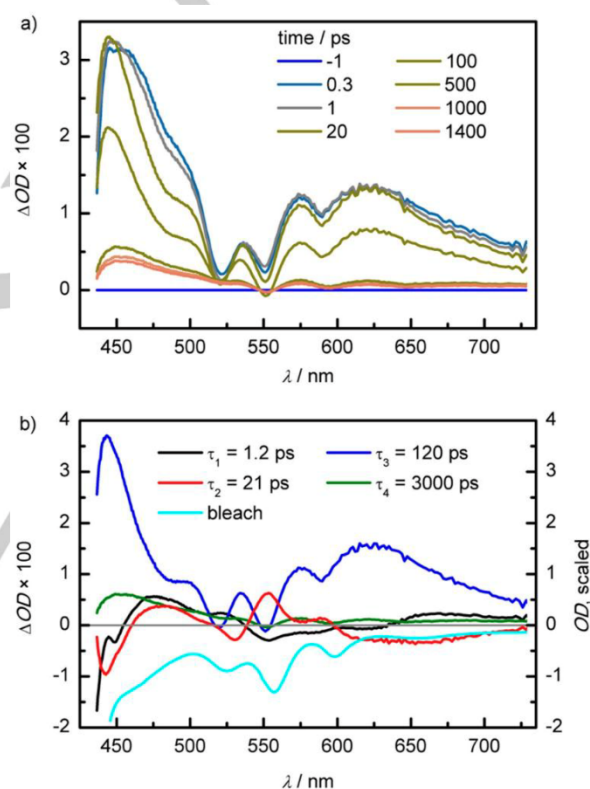


Figure 4. a) fs-TA spectra of **[1][PF₆]** in THF at room temperature at different time points after excitation with 400 nm and b) amplitude spectra of the components labelled with the respective time constants.

The TA spectra of **[1]⁺** show three characteristic local minima at 522, 551 and 591 nm. These are assigned to the combined Q band ground state bleaches of the zinc(II) and gold(III) porphyrin (Fig. 1). Obviously, the 400 nm pulse excites both the zinc and the gold site as discussed above ($\text{S}_2(\text{Zn})$, $\text{S}_1(\text{Zn})$, $\text{S}_2(\text{Au})$, $\text{S}_1(\text{Au})$) and excited states from both sites are likely observable. Indeed, the excited state absorption (ESA) at 575 nm can be assigned to

FULL PAPER

the $T_1(\text{Zn})$ state^[26], whereas the broad ESA between 590 – 650 nm is a feature of the $T_1(\text{Au})$ state.^[29] With this assignment, the local triplet states $T_1(\text{Zn})$ and $T_1(\text{Au})$ are populated in the sub-picosecond time scale. After 1 ns, features of a long-lived state ($\tau = 3.0$ ns) reminiscent of those of the cation radical $[\text{Zn}(\text{TPP}^{**})]^+$ remain.^[30] As the $\text{Au}^{\text{II}}(\text{P})^+$ absorption spectra are similar to the $[\text{Au}^{\text{III}}(\text{P})]^+$ spectra,^{13b} the $^1,^3\text{CSh}$ state is essentially manifested by the $[\text{Zn}(\text{P}^{**})]^+$ characteristics. Hence, the long-lived excited state is assigned to the $^1,^3\text{CSh}$ state(s). Typical lifetimes of $^3\text{Zn}(\text{P})$ and $^3\text{Au}^{\text{III}}(\text{P})^+$ triplet states are in the millisecond range.^[21b,28] The significantly reduced lifetimes of these triplet states in the dyad (< 1 ns) suggest an efficient decay path for both the $T_1(\text{Zn})$ and $T_1(\text{Au})$ states, namely the final population of the lower lying $^1,^3\text{CSh}$ state(s). Consequently, all excitation pathways can converge to the same final charge-shifted state $^1,^3[\text{Zn}^{\text{II}}(\text{P}^{**})-\text{Au}^{\text{II}}(\text{P})]^+$.

To analyse the TA data more quantitatively, a multiexponential global fit was applied. Four exponential components had to be included in order to reproduce the measured data. Figure 4b shows the obtained amplitude spectra of these components labelled by the respective time constants resulting from the fit. The fastest component has a time constant of 1.2 ps and its amplitude spectrum (black line) is not very strong and unspecific. The time scale is slightly faster than the internal conversion from the S_2 , which is originally populated by excitation at the Soret band, to the S_1 state in Zn and Au porphyrins. In the dyad this process can be accelerated by the higher density of states or energy redistribution processes contribute to the observed dynamics. The amplitude spectrum of the second exponential component (red line), which has a time constant of 21 ps, exhibits characteristic features in the spectral region of the Q bands of the ground state absorption. In particular, the positive feature at about 555 nm indicates that the bleach of the zinc porphyrin site becomes stronger. The applied pump pulses at 400 nm preferentially excite the gold porphyrin site (Fig. 1) but the population of the CSh state changes also the electronic configuration on the zinc side. We therefore assign the 21 ps time constant to the formation of the CSh state(s) ($k_{\text{ET1/HT1}}$, Table 3, Fig. 3) and a corresponding depopulation of the ground state of the zinc porphyrin. The component with a time constant of 120 ps (blue line) corresponds to a strong decrease of the excited state absorption and shows in addition the bleach features of the Q bands. It reflects relaxation of the excited states back to the electronic ground state (k_{BET1} , Table 3, Fig. 3). Its strength indicates that the majority of the excited molecules takes part. However, a significant fraction of the excited dyads remains in a longer living excited state which is responsible for the fourth component (green line) and which relaxes with a time constant of 3 ns. It is assigned to a CSh state, namely the $[\text{Zn}^{\text{II}}(\text{P}^{**})-\text{Au}^{\text{II}}(\text{P})]^+$ state, probably with triplet character or featuring essentially uncorrelated paramagnetic centres. Back electron transfer from this state is rather slow with $k_{\text{BET2}} = 3.3 \times 10^8 \text{ s}^{-1}$ (Table 3).

In dyad **[2][PF₆]**, the time for the formation of the CSh state was determined to 12 ps following the same line of arguments (Table 3, Supporting Information, Fig. S21). The driving force for the electron transfer increases from **[1]*** to **[2]*** (Table 3) which is in line with the faster formation rate of the CSh state in **[2][PF₆]** compared to **[1][PF₆]**. Recombination of the initial CSh state

yielding the ground state is faster than for **[1][PF₆]** due to the smaller driving force (Marcus inverted region; Table 3). For dyad **[3][PF₆]**, it is difficult to extract the $k_{\text{ET1/HT1}}$ rate since both porphyrin sites are about equally strongly excited due to the overlapping Soret bands and the feature associated with a delayed excitation of the zinc porphyrin is missing (Supporting Information, Fig. S21).

In all cases, back-electron transfer from the CSh state $^1,^3[\text{Zn}^{\text{II}}(\text{P}^{**})-\text{Au}^{\text{II}}(\text{P})]^+$ is significantly slower than the forward electron transfer ($k_{\text{BET2}} \ll k_{\text{ET1/HT1}}$) and the recombination from the initial CSh state $^1,^3[\text{Zn}^{\text{II}}(\text{P}^{**})-\text{Au}^{\text{III}}(\text{P}^{*})]^+$ ($k_{\text{BET2}} < k_{\text{BET1}}$) (Table 3). The decreasing recombination rate k_{BET2} correlates with the increasing driving force for BET in the series **[2]*** > **[1]*** > **[3]*** (Table 3) in accordance with the BET occurring in the Marcus inverted region. In addition, the weak electronic coupling due to the mismatched symmetry of the wavefunctions hampers the recombination.^[10d,12b,24] In fact, the electron is located in a gold-based σ -type $5d_{x^2-y^2}$ orbital in the final CSh state, but in a π -orbital of the zinc porphyrin in the ground state. This molecular orbital point of view will be discussed next.

Quantum chemical calculations.

To confirm the excited state ordering in Fig. 3 and to pin down the electronic nature of the intermediate triplet and charge-shifted states, Density Functional Theory (DFT) calculations have been conducted on the ground state, the $T_1(\text{Zn})$ state, the intermediate charge shifted state $^3[\text{Zn}^{\text{II}}(\text{P}^{**})-\text{Au}^{\text{III}}(\text{P}^{*})]^+$ and the final ^3CSh state $^3[\text{Zn}^{\text{II}}(\text{P}^{**})-\text{Au}^{\text{II}}(\text{P})]^+$ of **[1]*** (Fig. 5). Gratifyingly, all calculations converged to local minima on the respective potential energy surface.

FULL PAPER

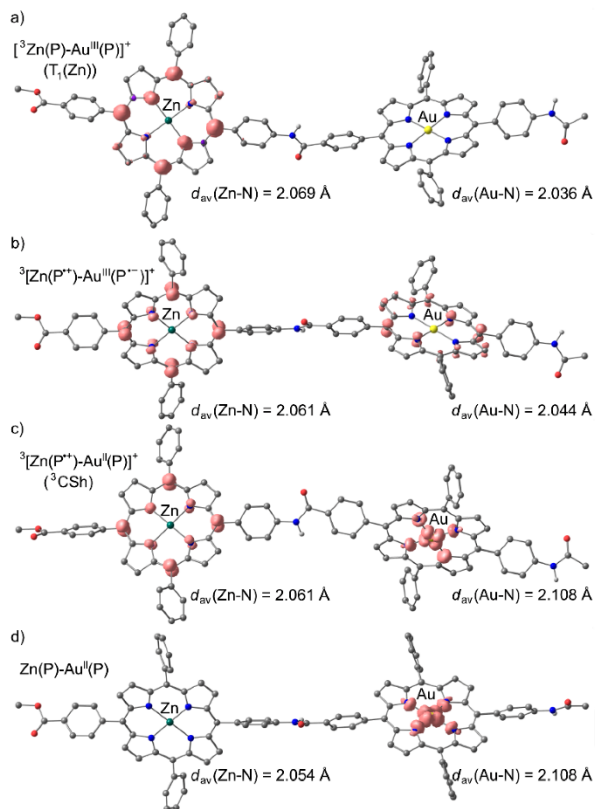


Figure 5. DFT optimised geometries and calculated spin densities of a) the local triplet state of the zinc porphyrin $[\text{}^3\text{Zn}(\text{P})\text{-Au}^{\text{III}}(\text{P})]^+$, b) the intermediate charge-shifted state $[\text{}^3\text{Zn}(\text{P}^{**})\text{-Au}^{\text{III}}(\text{P}^{*-})]^+$, c) the final ${}^3\text{CSh}$ state $[\text{}^3\text{Zn}(\text{P}^{**})\text{-Au}^{\text{I}}(\text{P})]^+$ of **[1]**⁺ and d) $\text{Zn}(\text{P})\text{-Au}^{\text{I}}(\text{P})$. Isosurfaces in pale red at a value of 0.008 a.u.; CH hydrogen atoms omitted.

The energies of the triplets are comparably close and we refrain from discussing these energy differences. However, we note, that the $[\text{}^3\text{Zn}^{\text{II}}(\text{P}^{**})\text{-Au}^{\text{I}}(\text{P})]^+$ state is lower in energy than the $[\text{}^3\text{Zn}^{\text{II}}(\text{P}^{**})\text{-Au}^{\text{III}}(\text{P}^{*-})]^+$ state which fits to the observed stability of $\text{Au}^{\text{I}}(\text{P})$ over $\text{Au}^{\text{III}}(\text{P}^{*-})$.^[13a] Additionally, the DFT calculations reproduce the second-order Jahn-Teller distortion of the gold(II) tetraphenylporphyrin with $\Delta d(\text{Au-N}) = 0.016$ Å and a bending of two *trans* positioned pyrrole rings of $\tau = 168.7^\circ$ similar to the reported parent $\text{Au}^{\text{II}}(\text{TPP})$ complex.^[13a]

Population of the $T_1(\text{Zn})$ state increases the Zn-N bond lengths from 2.054 Å (ground state) to 2.069 Å but leaves the Au-N distances unaffected ($d_{av}(\text{Au-N}) = 2.032/2.036$ Å; ground state/ $T_1(\text{Zn})$). After electron transfer to the gold porphyrin site, the Zn-N bond lengths are slightly reduced and the Au-N distances slightly elongated (Fig. 5b). Valence isomerisation from $[\text{}^3\text{Zn}^{\text{II}}(\text{P}^{**})\text{-Au}^{\text{III}}(\text{P}^{*-})]^+$ to $[\text{}^3\text{Zn}^{\text{II}}(\text{P}^{**})\text{-Au}^{\text{I}}(\text{P})]^+$ merely affects the gold porphyrin site significantly elongating the Au-N distances as expected for a gold(II) ion (Fig. 5c).^[13a] These geometrical changes contribute to the reorganisation energy of the valence isomerisation. Basically,

the Au-N distances increase during the reaction cascade from $\text{Au}^{\text{III}}(\text{P})$ over $\text{Au}^{\text{III}}(\text{P}^{*-})$ to $\text{Au}^{\text{I}}(\text{P})$ (Fig. 5a – 5c).

The local spin density of the Zn porphyrin subunits in both charge-shifted states $[\text{}^3\text{Zn}^{\text{II}}(\text{P}^{**})\text{-Au}^{\text{III}}(\text{P}^{*-})]^+$ and $[\text{}^3\text{Zn}^{\text{II}}(\text{P}^{**})\text{-Au}^{\text{I}}(\text{P})]^+$ is located in the π system (Fig. 5b, 5c). The local symmetry is of a_{2u} character (in the standard Gouterman's orbital model^[20]) featuring large coefficients at the *meso* positions. On the gold porphyrin site, the accepting orbital is one of the e_g LUMOs (in the standard Gouterman's orbital model) featuring large coefficients at the *meso* positions as well (Fig. 5b). This orbital symmetry is certainly beneficial for the forward electron transfer (k_{ET1}) via the bridging unit. After the internal redox reaction generating the gold(II) porphyrin, the spin density is located in the $5d_{z^2}$ orbital of gold (with some spin delocalisation onto the coordinating nitrogen atoms), and hence in a σ -type orbital relative to the porphyrin planes (Fig. 5c). This will certainly retard the direct back-electron transfer to the a_{2u} SOMO of the zinc porphyrin site. Back-electron transfer will consequently occur via the higher energy charge-shifted state $[\text{}^3\text{Zn}^{\text{II}}(\text{P}^{**})\text{-Au}^{\text{III}}(\text{P}^{*-})]^+$. This will contribute to the large lifetime of the charge-shifted state.

Reduction of the long-lived charge-shifted state $[\text{}^3\text{Zn}^{\text{II}}(\text{P}^{**})\text{-Au}^{\text{I}}(\text{P})]^+$ will give the neutral dyad $\text{Zn}^{\text{II}}(\text{P})\text{-Au}^{\text{I}}(\text{P})$ (Fig. 5d). The Zn-N distances in $\text{Zn}^{\text{II}}(\text{P})\text{-Au}^{\text{I}}(\text{P})$ correspond to those of the initial ground state, yet the Au-N bond lengths and the spin-density still fit to a gold(II) description. The next section discusses electron transfer processes giving the neutral dyad $\text{Zn}^{\text{II}}(\text{P})\text{-Au}^{\text{I}}(\text{P})$.

Visible light-induced electron transfer processes.

As the lifetimes of the visible light-induced charge-shifted states $[\text{}^3\text{Zn}^{\text{II}}(\text{P}^{**})\text{-Au}^{\text{I}}(\text{P})]^+$ ($\tau = 3.0 - 3.4$ ns for **[1]**⁺ – **[3]**⁺) are long enough to enable subsequent bimolecular reactions and the charge-shifted state is quite oxidising ($E_{1/2}(\text{Zn}^{\text{II}}(\text{P}^{**})) = 0.42$ V and 0.49 V vs. ferrocene for **[1]**⁺ and **[3]**⁺; Table 2), the charge-shifted states were reductively quenched by NEt_3 ($E_p = 0.47$ vs. ferrocene in CH_3CN ^[31]). The resulting neutral species $\text{Zn}^{\text{II}}(\text{P})\text{-Au}^{\text{I}}(\text{P})$ should display the characteristic spectroscopic features of a gold(II) complex.^[13] For comparison of the spectral data, $\text{Zn}^{\text{II}}(\text{P})\text{-Au}^{\text{I}}(\text{P})$ was also prepared by chemical reduction of the cationic dyads with one equivalent of potassium graphite.

Gratifyingly, photochemical (10 eq NEt_3 , 420±5 nm) and chemical reduction (1 eq KC_8) yield species displaying the same electronic (Supporting Information, Fig. S22 – S23) and X-band EPR spectra (at 77 K) (Supporting Information, Fig. S24). In addition, XANES spectra of **[3][PF₆]** at the gold L_3 -edge confirm the formation of gold(II) in the presence of NEt_3 under irradiation (420±5 nm) (Supporting Information, Fig. S25) with results fully analogous to the prototype $\text{Au}^{\text{II}}(\text{TPP})$.^[13] Furthermore, dioxygen re-oxidises the neutral species $\text{Zn}^{\text{II}}(\text{P})\text{-Au}^{\text{I}}(\text{P})$ **3** back to the starting material **[3]**⁺ according to XANES (Supporting Information, Fig. S25). The EXAFS region of the XANES remains essentially identical for the Au^{II} and Au^{III} species suggesting full structural integrity of the $[\text{AuN}_4]$ moiety during the redox processes (Supporting Information, Fig. S25).

FULL PAPER

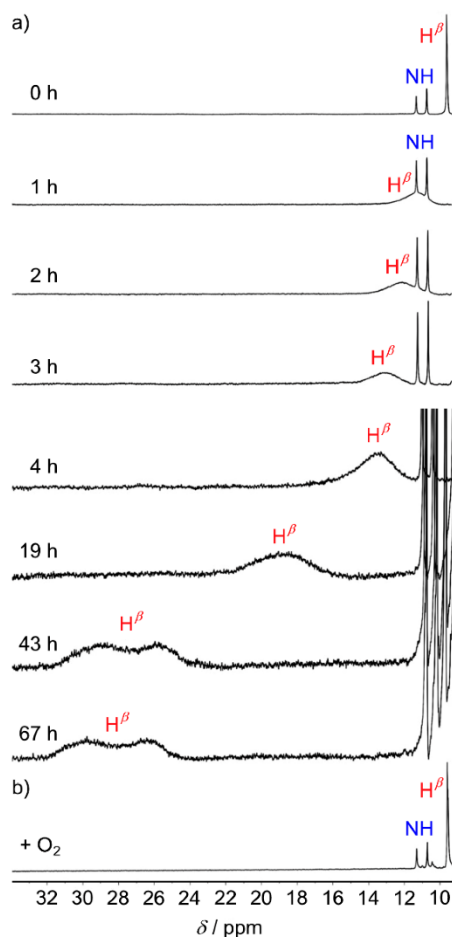


Figure 6. ^1H NMR spectra of $[3][\text{PF}_6]$ in the presence of 10 eq NEt_3 under irradiation with 420 ± 5 nm over time in d_7 -DMF and b) ^1H NMR spectrum of the resulting solution after reaction with O_2 .

Similar to $\text{Au}(\text{TPP})^{13a}$, the neutral dyads **1** and **3** display paramagnetically shifted ^1H NMR resonances^[32] for the gold(II) porphyrin subunit at room temperature. This is especially pronounced for the β protons of the gold(II) porphyrin with $\delta = 26 - 33$ ppm (Fig. 6, Supporting Information, Fig. S26).^[13] The $\text{Au}^{\text{II/III}}$ self-exchange between gold porphyrins is rapid on the ^1H NMR timescale (fast exchange regime) yielding averaged resonances with the chemical shifts weighted with the Au^{II} molar fraction.^[13] Consequently, ^1H NMR spectroscopy allows monitoring the visible-light induced reductive quenching of the dyads in the presence of NEt_3 and the formation of the gold(II) species over time (Fig. 6). Although the reaction is rather slow, almost quantitative reduction of $[3]^+$ to **3** by NEt_3 is achieved in 67 h under irradiation at 420 ± 5 nm. The quite low reaction rate is probably due to the competition between valence isomerisation of $^{1,3}[\text{Zn}^{\text{II}}(\text{P}^{**})-\text{Au}^{\text{III}}(\text{P}^*)]^+$ to the long-lived, productive $^{1,3}[\text{Zn}^{\text{II}}(\text{P}^{**})-\text{Au}^{\text{II}}(\text{P})]^+$ state and the recombination of $^{1,3}[\text{Zn}^{\text{II}}(\text{P}^{**})-\text{Au}^{\text{III}}(\text{P}^*)]^+$ to

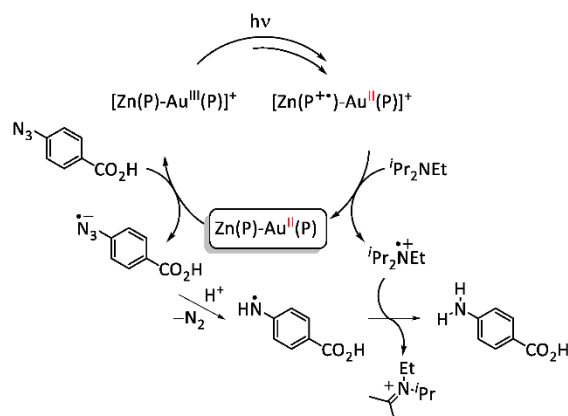
the ground state (k_{BET1} ; Fig. 3, Table 3), so that only a fraction of the excited dyads is competent to react with amines. In addition, at increasing conversion to gold(II) the inner filter effect of the gold(II) product (Supporting Information, Fig. S26 – S27) captures most of the incident light further slowing down the reaction. Under the same conditions, $[1]^+$ is only converted to $\sim 34\%$ according to ^1H NMR monitoring (Supporting Information, Fig. S26 – S27). This might be due to the lower oxidation potential of $[1]^+$ (Table 2) and the very unfavourable bathochromic shift of the Soret band of the gold(II) unit^[13b,33] capturing more of the incident light as the reaction proceeds (Supporting Information, Fig. S23b).

We further confirmed, that both irradiation into the Soret (420 ± 5 nm) and the Q band (560 ± 5 nm) trigger the reduction by NEt_3 (Supporting Information, Fig. S26) confirming our mechanistic picture, that IC from S_2 to S_1 precedes the electron transfer steps and that the S_1 state is competent to evolve to the charge-shifted states (Fig. 3). In the absence of NEt_3 , the dyads are photostable (Supporting Information, Figure S27b), substantiating the bimolecular electron transfer between the dyad and the amine. Vice versa, NEt_3 is unable to reduce the dyads in the dark.

To the best of our knowledge, the possibility to monitor photoinduced electron transfer by conventional NMR spectroscopy is a very rare situation due to the paramagnetic nature of intermediates in one-electron transfer reactions, which often hampers observation of NMR resonances.^[32] Re-oxidation of the gold(II) species to the starting material by dioxygen is also successfully confirmed by ^1H NMR spectroscopy (Fig. 6). In the absence of O_2 as oxidant, the neutral gold(II)-containing dyads should be able to reduce substrates with redox potentials above -1.0 V (Table 2).

As an initial test reaction, we employed the reduction of aromatic azides to anilines.^[34] Azides are irreversibly reduced around potentials of $E_p = -0.88$ V to -1.22 V vs. ferrocene.^[35] Hence, gold(II) should be competent to reduce azides (Table 2). In analogy to the procedure developed by Liu et al. using $^1\text{Pr}_2\text{NEt}$ as sacrificial reductant (10 eq; $E_p = 0.34$ V vs. ferrocene^[36]), acetic acid as proton donor (10 eq), 4-azidobenzoic acid as substrate and $[\text{Ru}(\text{bpy})_3]^{2+}$ (5 mol-%) as the classical photosensitizer (bpy = 2,2'-bipyridine),^[37] we employed the same conditions, yet replacing $[\text{Ru}(\text{bpy})_3]^{2+}$ by $[3][\text{PF}_6]$ (1 mol-%). Gratifyingly, 4-azidobenzoic acid is converted to 4-aminobenzoic acid under these conditions after 72 h irradiation with 420 nm in d_7 -DMF (Scheme 3; 50 % unoptimised spectroscopic yield; Supporting Information, Fig. S28).

FULL PAPER



Scheme 3. Proposed mechanism of the $[Zn(P)Au^{II}(P)]^+$ -mediated azide-reduction induced by visible light (420 ± 5 nm, d_7 -DMF).

Scheme 3 illustrates the proposed mechanism including the mechanistic results from the previous sections. The sensitizer $[Zn(P)-Au^{II}(P)]^+$ is excited by visible light (420 ± 5 nm) to initially yield S_2 state(s). A fraction evolves to the long-lived 1,3 CSh states with gold(II) centres. These long-lived CSh state are reduced by the amine generating the neutral $Zn(P)-Au^{II}(P)$ species and the amine radical cation. The gold(II) complex $Zn(P)-Au^{II}(P)$ is oxidised by the azide re-generating $[Zn(P)-Au^{III}(P)]^+$. The azide radical anion finally eliminates dinitrogen, adds a proton (from acetic acid) and a hydrogen atom (from the amine radical cation) furnishing the aniline as suggested in the literature.^[35]

Conclusions

In summary, $[Zn^{II}(P)-Au^{II}(P)]^+$ dyads **[1][PF₆]** – **[3][PF₆]** undergo ultrafast photoinduced electron transfer. A fraction of these excited states decays to a long-lived charge-shifted state $^1,3[Zn^{II}(P^{++})-Au^{II}(P)]^+$ (lifetime ~ 3 ns). The redox potentials of zinc(II) porphyrins and gold(III) porphyrins place the respective charge-shifted states 1.25 eV – 1.48 eV relative to the ground state and well below the individual singlet and triplet excited states of the zinc and gold porphyrins ($S_1(Zn)$, $S_1(Au)$, $T_1(Zn)$, $T_1(Au)$). Consequently, the charge-shifted states can be populated from the local $S_1(M)$ and $T_1(M)$ states via an intermediate charge-shifted state $^1,3[Zn^{II}(P^{++})-Au^{III}(P^-)]^+$ with π radical character at the gold site. After valence isomerisation to the long-lived charge-shifted states $^1,3[Zn^{II}(P^{++})-Au^{II}(P)]^+$ with metal radical character at the gold site, bimolecular reduction of the $Zn^{II}(P^{++})$ site with amines yields a stable gold(II) species $Zn(P)-Au^{II}(P)$ as confirmed by UV/Vis, EPR, XANES and NMR spectroscopy. This gold(II) dyad $Zn(P)-Au^{II}(P)$ reduces aromatic azides regenerating the initial gold(III) dyad $[Zn^{II}(P)-Au^{III}(P)]^+$ and hence closing a catalytic cycle. This study identifies the most important light-induced steps and key intermediates of dyads containing gold(III) porphyrins as electron acceptors after excitation with visible light. Furthermore, this study delivers the first UV/Vis, EPR, XANES and NMR

spectroscopic evidences for the involvement of tetracoordinate gold(II) species during photoredox catalysis.^[8,9,10,12,13] This also paves the way for further studies of photoinduced gold-catalysed reactions with low-coordinate gold(II) species proposed as transient intermediates.^[16]

Author contributions

S.P. prepared and characterised the compounds (NMR, UV/Vis, EPR, MS, CV) and performed the PET experiments and DFT calculations. A.P. and S.L. performed and analysed the time-resolved photoluminescence and transient absorption spectroscopy experiments. L.B. and M.B. performed and analysed the XANES experiments. L.G. and T.O. contributed to the PET experiments and the catalytic test reactions. K.H. designed the experiments and supervised the project.

Acknowledgements

Financial support from the Center for INnovative and Emerging MATerials (CINEMA), the Forschungsinitiative Rheinland-Pfalz (LESSING) and the Deutsche Forschungsgemeinschaft [DFG, Priority Program SPP 2102 "Light-controlled reactivity of metal complexes" (LO 714/11-1)] is gratefully acknowledged. Parts of this research were conducted using the supercomputer Mogon and advisory services offered by Johannes Gutenberg University Mainz (www.hpc.uni-mainz.de), which is a member of the AHRP and the Gauss Alliance e.V.. PETRA III is acknowledged for provision of beamtime, Dr. Aleksandr Kalinko for help during XANES measurements.

References

- [1] a) M. Natali, S. Campagna, F. Scandola, *Chem. Soc. Rev.* **2014**, *43*, 4005–4018; b) R. A. Marcus, N. Sutin, *Biochim. Biophys. Acta* **1985**, *811*, 265–322.
- [2] a) B. O'Regan, M. Grätzel, *Nature* **1991**, *353*, 737–740; b) D. Gust, T. A. Moore, A. L. Moore, *Acc. Chem. Res.* **1993**, *26*, 198–205; c) L. Peter, *Acc. Chem. Res.* **2009**, *42*, 1839–1847; d) A. Magnuson, M. Anderlund, O. Johansson, P. Lindblad, R. Lomoth, T. Polivka, S. Ott, K. Stensjö, S. Styring, V. Sundström, L. Hammarström, *Acc. Chem. Res.* **2009**, *42*, 1899–1909; e) T. Cardona, A. Sedoud, N. Cox, A. W. Rutherford, *Biochim. Biophys. Acta* **2012**, *1817*, 26–43; f) J. Deisenhofer, O. Epp, K. Miki, R. Huber, H. Michel, *Nature* **1985**, *318*, 618–624; g) S. Niwa, L. J. Yu, K. Takeda, Y. Hirano, T. Kawakami, Z. Y. Wang-Otomo, K. Miki, *Nature* **2014**, *508*, 228–232.
- [3] B. Albinsson, J. Mårtensson, *J. Photochem. Photobiol. C* **2008**, *9*, 138–155.
- [4] a) H. Imahori, D. M. Guldi, K. Tamaki, Y. Yoshida, C. Luo, Y. Sakata, S. Fukuzumi, *J. Am. Chem. Soc.* **2001**, *123*, 6617–6628; b) H. Imahori, K. Tamaki, Y. Araki, Y. Sekiguchi, O. Ito, Y. Sakata, S. Fukuzumi, *J. Am. Chem. Soc.* **2002**, *124*, 5165–5174; c) S. Fukuzumi, K. Okamoto, H. Imahori, *Angew. Chem.* **2002**, *114*, 642–644; *Angew. Chem. Int. Ed.* **2002**, *41*, 620–622; d) H. Imahori, Y. Sekiguchi, Y. Kashiwagi, T. Sato, Y. Araki, O. Ito, H. Yamada, S. Fukuzumi, *Chem. Eur. J.* **2004**, *10*, 3184–3196; e) M. U. Winters, E. Dahlstedt, H. E. Blades, C. J. Wilson, M. J. Frampton, H. L. Anderson, B. Albinsson, *J. Am. Chem. Soc.* **2007**, *129*, 4291–4297; f) C. A. Wijesinghe, M. E. El-Khouly, M. E. Zandler, S. Fukuzumi, F. D'Souza, *Chem. Eur. J.* **2013**, *19*, 9629–9638; g) J. Melomedov, J. R. Ochsmann, M. Meister, F. Laquai, K. Heinze, *Eur. J. Inorg. Chem.* **2014**, 1984–2001; h) S. Fukuzumi, K. Okamoto, Y. Yoshida, H. Imahori, Y. Araki, O. Ito, *J. Am. Chem. Soc.* **2003**, *125*, 1007–1013.

FULL PAPER

- [5] a) S. L. Gould, G. Kodis, R. E. Palacios, L. de La Garza, A. Brune, D. Gust, T. A. Moore, A. L. Moore, *J. Phys. Chem. B* **2004**, *108*, 10566–10580; b) D. Gust, T. A. Moore, A. L. Moore, A. N. Macpherson, A. Lopez, J. M. DeGraziano, I. Gouni, E. Bittersmann, G. R. Seely, F. Gao, R. A. Nieman, X. C. Ma, L. J. Demanche, S.-C. Hung, D. K. Luttrull, S.-J. Lee, P. K. Kerrigan, *J. Am. Chem. Soc.* **1993**, *115*, 11141–11152.
- [6] a) D. Gust, T. A. Moore, A. L. Moore, L. Leggett, S. Lin, J. M. DeGraziano, R. M. Hermant, D. Nicodem, P. Craig, G. R. Seely, R. A. Nieman, *J. Phys. Chem.* **1993**, *97*, 7926–7931; b) S. K. Das, B. Song, A. Mahler, V. N. Nesterov, A. K. Wilson, O. Ito, F. D'Souza, *J. Phys. Chem. C* **2014**, *118*, 3994–4006; c) T. H. Ngo, D. Zieba, W. A. Webre, G. N. Lim, P. A. Karr, S. Kord, S. Jin, K. Ariga, M. Galli, S. Goldup, J. P. Hill, F. D'Souza, *Chem. Eur. J.* **2016**, *22*, 1301–1312.
- [7] M. Lauck, C. Förster, D. Gehrig, K. Heinze, *J. Organomet. Chem.* **2017**, *847*, 33–40.
- [8] a) I. M. Dixon, J.-P. Collin, J.-P. Sauvage, F. Barigelletti, L. Flamigni, *Angew. Chem.* **2000**, *112*, 1348–1351; *Angew. Chem. Int. Ed.* **2000**, *39*, 1292–1295; b) D. B. Amabilino, J.-P. Sauvage, *New J. Chem.* **1998**, *22*, 395–409; c) V. Heitz, S. Chardon-Noblat, J.-P. Sauvage, *Tetrahedron Lett.* **1991**, *32*, 197–198; d) A. Harriman, F. Odobel, J.-P. Sauvage, *J. Am. Chem. Soc.* **1995**, *117*, 9461–9472; e) A. M. Brun, A. Harriman, V. Heitz, J. P. Sauvage, *J. Am. Chem. Soc.* **1991**, *113*, 8657–8663.
- [9] a) E. K. L. Yeow, P. J. Santic, N. M. Cabral, J. N. H. Reek, M. J. Crossley, K. P. Ghiggino, *Phys. Chem. Chem. Phys.* **2000**, *2*, 4281–4291; b) K. Ohkubo, P. J. Santic, N. V. Tkachenko, H. Lemmetyinen, E. Wenbo, Z. Ou, J. Shao, K. M. Kadish, M. J. Crossley, S. Fukuzumi, *Chem. Phys.* **2006**, *326*, 3–14; c) K. Ohkubo, R. Garcia, P. J. Santic, T. Khoury, M. J. Crossley, K. M. Kadish, S. Fukuzumi, *Chem. Eur. J.* **2009**, *15*, 10493–10503; d) M. E. El-Khouly, S. Fukuzumi, *Photochem. Photobiol.* **2016**, *15*, 1340–1346; e) S. Fukuzumi, K. Ohkubo, E. Wenbo, Z. Ou, J. Shao, K. M. Kadish, J. A. Hutchison, K. P. Ghiggino, P. J. Santic, M. J. Crossley, *J. Am. Chem. Soc.* **2003**, *125*, 14984–14985.
- [10] a) J. Fortage, A. Scarpa, L. Viau, Y. Pellegrin, E. Blart, M. Falkenström, L. Hammarström, I. Asselberghs, R. Kellens, W. Libaers, K. Clays, M. P. Eng, F. Odobel, *Chem. Eur. J.* **2009**, *15*, 9058–9067; b) J. Fortage, J. Boixel, E. Blart, H. C. Becker, F. Odobel, *Inorg. Chem.* **2009**, *48*, 518–526; c) J. Fortage, J. Boixel, E. Blart, L. Hammarström, H. C. Becker, F. Odobel, *Chem. Eur. J.* **2008**, *14*, 3467–3480; d) E. Göransson, J. Boixel, J. Fortage, D. Jacquemin, H.-C. Becker, E. Blart, L. Hammarström, F. Odobel, *Inorg. Chem.* **2012**, *51*, 11500–11512.
- [11] a) D. Huang, X. Zhang, E. J. L. McInnes, J. McMaster, A. J. Blake, E. S. Davies, J. Wolowska, C. Wilson, M. Schröder, *Inorg. Chem.* **2008**, *47*, 9919–9929; b) S. Seidel, K. Seppelt, *Science* **2000**, *290*, 117–118.
- [12] a) Z. Ou, K. M. Kadish, W. E. J. Shao, P. J. Santic, K. Ohkubo, S. Fukuzumi, M. J. Crossley, *Inorg. Chem.* **2004**, *43*, 2078–2086; b) K. M. Kadish, W. E. Z. Ou, J. Shao, P. J. Santic, K. Ohkubo, S. Fukuzumi, M. J. Crossley, *Chem. Commun.* **2002**, 356–357.
- [13] a) S. Preiß, C. Förster, S. Otto, M. Bauer, P. Müller, D. Hinderberger, H. Hashemi Haeri, L. Carella, K. Heinze, *Nat. Chem.* **2017**, *9*, 1249–1255; b) S. Preiß, J. Melomedov, A. Wünsche von Leupoldt, K. Heinze, *Chem. Sci.* **2016**, *7*, 598–610; c) K. Heinze, *Angew. Chem.* **2017**, *129*, 16342–16350; *Angew. Chem. Int. Ed.* **2017**, *56*, 16126–16134.
- [14] a) D. Pflästerer, A. S. K. Hashmi, *Chem. Soc. Rev.* **2016**, *45*, 1331–1367; b) A. M. Asiri, A. S. K. Hashmi, *Chem. Soc. Rev.* **2016**, *45*, 4471–4503; c) R. Dorel, A. M. Echavarren, *Chem. Rev.* **2015**, *115*, 9028–9072.
- [15] C.-Y. Zhou, P. W. H. Chan, C.-M. Che, *Org. Lett.* **2006**, *8*, 325–328.
- [16] a) B. Sahoo, M. N. Hopkinson, F. Glorius, *J. Am. Chem. Soc.* **2013**, *135*, 5505–5508; b) M. N. Hopkinson, A. Tlahuext-Aca, F. Glorius, *Acc. Chem. Res.* **2016**, *49*, 2261–2272; c) J. Xie, S. Shi, T. Zhang, N. Mehrkens, M. Rudolph, A. S. K. Hashmi, *Angew. Chem. Int. Ed.* **2015**, *54*, 6046–6050; *Angew. Chem.* **2015**, *127*, 6144–6148; d) J. Xie, J. Yu, M. Rudolph, F. Rominger, A. S. K. Hashmi, *Angew. Chem. Int. Ed.* **2016**, *55*, 9416–9421; *Angew. Chem.* **2016**, *128*, 9563–9568; e) J. Xie, J. Li, V. Weingand, M. Rudolph, A. S. K. Hashmi, *Chem. Eur. J.* **2016**, *22*, 12646–12650; f) L. Huang, M. Rudolph, F. Rominger, A. S. K. Hashmi, *Angew. Chem.* **2016**, *128*, 4888–4893; *Angew. Chem. Int. Ed.* **2016**, *55*, 4808–4813; g) S. Witzel, J. Xie, M. Rudolph, A. S. K. Hashmi, *Adv. Synth. Catal.* **2017**, *359*, 1522–1528; h) S. Witzel, K. Sekine, M. Rudolph, A. S. K. Hashmi, *Chem. Commun.* **2018**, *54*, 13802–13804; i) M. S. Winston, W. J. Wolf, F. D. Toste, *J. Am. Chem. Soc.* **2014**, *136*, 7777–7782; j) X.-Z. Shu, M. Zhang, Y. He, H. Frei, F. D. Toste, *J. Am. Chem. Soc.* **2014**, *136*, 5844–5847; k) S. Kim, J. Rojas-Martin, F. D. Toste, *Chem. Sci.* **2016**, *7*, 85–88.
- [17] a) J. Melomedov, J. R. Ochsmann, M. Meister, F. Laquai, K. Heinze, *Eur. J. Inorg. Chem.* **2014**, 2902–2915; b) M. O. Senge, *Chem. Commun.* **2011**, *47*, 1943–1960; c) J. S. Lindsey, *Acc. Chem. Res.* **2010**, *43*, 300–311; d) K. Heinze, A. Reinhardt, *Dalton Trans.* **2008**, 469–480.
- [18] E. B. Fleischer, A. Laszlo, *Inorg. Nucl. Chem. Lett.* **1969**, *5*, 373–376.
- [19] J. Melomedov, A. Wünsche von Leupoldt, M. Meister, F. Laquai, K. Heinze, *Dalton Trans.* **2013**, *42*, 9727–9739.
- [20] a) A. Antipas, J. W. Buchler, M. Gouterman, P. D. Smith, *J. Am. Chem. Soc.* **1978**, *100*, 3015–3024; b) A. Antipas, D. Dolphin, M. Gouterman, E. C. Johnson, *J. Am. Chem. Soc.* **1978**, *100*, 7705–7709.
- [21] a) V. W.-W. Yam, E. C.-C. Cheng, *Top. Curr. Chem.* **2007**, *281*, 269–309; b) M. P. Eng, T. Ljungdahl, J. Andréasson, J. Mårtensson, B. Albinsson, *J. Phys. Chem. A* **2005**, *109*, 1776–1784.
- [22] J. Heinze, *Angew. Chem.* **1984**, *96*, 823–840; *Angew. Chem. Int. Ed.* **1984**, *23*, 831–847.
- [23] a) D. Rehm, A. Weller, *Isr. J. Chem.* **1970**, *8*, 259–271; b) A. Weller, *Z. Phys. Chem.* **1982**, *133*, 93–98.
- [24] a) R. A. Marcus, *J. Chem. Phys.* **1956**, *24*, 966–978; b) R. A. Marcus, *Annu. Rev. Phys. Chem.* **1964**, *15*, 155–196; c) R. A. Marcus, *Angew. Chem.* **1993**, *105*, 1161–1172; *Angew. Chem. Int. Ed.* **1993**, *32*, 1111–1121.
- [25] J. Andréasson, G. Kodis, S. Lin, A. L. Moore, T. A. Moore, D. Gust, J. Mårtensson, B. Albinsson, *Photochem. Photobiol.* **2002**, *76*, 47–50.
- [26] N. J. Turro, *Modern Molecular Photochemistry*, University Science Books, **1991**.
- [27] a) G. N. Lim, C. O. Obondi, F. D'Souza, *Angew. Chem.* **2016**, *128*, 11689–11693; *Angew. Chem. Int. Ed.* **2016**, *55*, 11517–11521; b) V. A. Walters, J. C. de Paula, B. Jackson, C. Nutaitis, K. Hall, J. Lind, K. Cardozo, K. Chandran, D. Raible, C. M. Phillips, *J. Phys. Chem.* **1995**, *99*, 1166–1171.
- [28] R. L. Brookfield, H. Ellul, A. Harriman, *J. Chem. Soc., Faraday Trans.* **1985**, *81*, 1837–1848.
- [29] P. K. Poddutoori, G. N. Lim, S. Vassiliev, F. D'Souza, *Phys. Chem. Chem. Phys.* **2015**, *17*, 26346–26358.
- [30] Y. Kobayashi, T. Katayama, T. Yamane, K. Setoura, S. Ito, H. Miyasaka, J. Abe, *J. Am. Chem. Soc.* **2016**, *138*, 5930–5938.
- [31] N. G. Connelly, W. E. Geiger, *Chem. Rev.* **1996**, *96*, 877–910.
- [32] *Solution NMR of Paramagnetic Molecules* (Eds. I. Bertini, C. Luchinat, G. Parigi), *Curr. Methods Inorg. Chem.* **2001**, vol. 2, Elsevier.
- [33] Z. Ou, W. Zhu, Y. Fang, P. J. Santic, T. Khoury, M. J. Crossley, K. M. Kadish, *Inorg. Chem.* **2011**, *50*, 12802–12809.
- [34] E. F. V. Scriven, K. Turnbull, *Chem. Rev.* **1988**, *88*, 298–368.
- [35] a) D. E. Herbranson, M. D. Hawley, *J. Org. Chem.* **1990**, *55*, 4297–4303; b) J. Moutet, A. Ourari, A. Zouaoui, *Electrochim. Acta* **1992**, *37*, 1261–1263; c) M. Warrier, M. K. F. Lo, H. Monbouquette, M. A. Garcia-Garbay, *Photochem. Photobiol. Sci.* **2004**, *3*, 859–862.
- [36] G. J. Barbante, N. Kebede, C. M. Hindson, E. H. Doeven, E. M. Zammit, G. R. Hanson, C. F. Hogan, P. S. Francis, *Chem. Eur. J.* **2014**, *20*, 14028–14031.
- [37] Y. Chen, A. S. Kamlet, J. B. Steinman, D. R. Liu, *Nat. Chem.* **2011**, *3*, 146–153.

Keywords: electron transfer • gold • paramagnetic NMR spectroscopy • photoinduced electron transfer • porphyrins

FULL PAPER

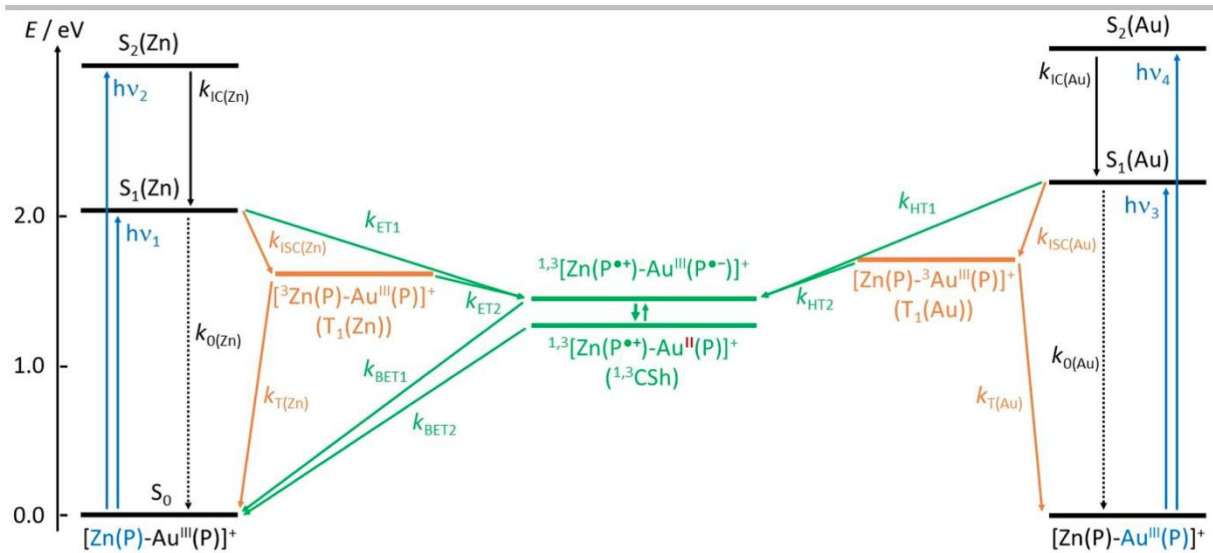
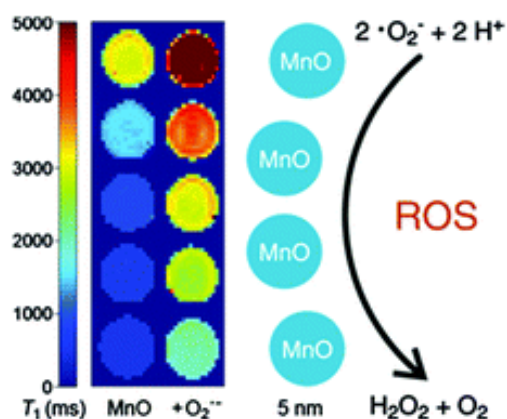


Figure 3.

3.4 Intrinsic superoxide dismutase activity of MnO nanoparticles enhances the magnetic resonance imaging contrast

Ruben Ragg, Anna Maria Schilman, Karsten Korschelt, Christian Wieseotte, Martin Kluncker, Melanie Viel, Lara Völker, Sebastian Preiß, Jana Herzberger, Holger Frey, Katja Heinze, Peter Blümmler, Muhammad Nazir Tahir, Filipe Natalio and Wolfgang Tremel

J. Mater. Chem. B. **2016**, *4*, 7423–7428.



Superoxide radicals are removed fast and catalytically by means of manganese oxide nanoparticles via a disproportionation mechanism resembling the natural enzyme superoxide dismutase. Exposition of the nanoparticles to superoxide radicals enhances the magnetic resonance imaging contrast based on extended relaxation times of the latter.

Author Contributions

The synthesis, characterisation and application of the MnO nanoparticles was performed by Dr.

██████████, ██████████, ██████████, ██████████, ██████████, ██████████, ██████████, ██████████, ██████████, ██████████ and ██████████ assisted with the synthesis, characterisation and validation. Sebastian Preiß performed and analysed the EPR experiments. ██████████, ██████████ and ██████████ reviewed and supervised the project. The manuscript was written by ██████████ (50 %) and ██████████ (50 %).

Supporting Information

Supporting Information for this article is found at pp. 173. For full supporting information refer to: <http://www.rsc.org/suppdata/c6/tb/c6tb02078j/c6tb02078j1.pdf>

Reprinted with permission from:

R. Ragg, A. M. Schilman, K. Korschelt, C. Wieseotte, M. Kluncker, M. Viel, L. Völker, S. Preiß, J. Herzberger, H. Frey, K. Heinze, P. Blümmler, M. N. Tahir, F. Natalio, W. *J. Mater. Chem. B.* **2016**, *4*, 7423–7428; Copyright 2016 the Royal Society of Chemistry.



Cite this: *J. Mater. Chem. B*, 2016, 4, 7423

Intrinsic superoxide dismutase activity of MnO nanoparticles enhances the magnetic resonance imaging contrast†

R. Ragg,^a A. M. Schilmann,^a K. Korschelt,^a C. Wieseotte,^b M. Kluncker,^a M. Viel,^a L. Völker,^a S. Preiß,^a J. Herzberger,^{cd} H. Frey,^c K. Heinze,^a P. Blümler,^e M. N. Tahir,^{*a} F. Natalio^f and W. Tremel^{*a}

Superoxide radicals are associated with the development of many severe diseases, such as cancer. Under nonpathogenic conditions, the natural enzyme superoxide dismutase (SOD) regulates the intracellular superoxide concentrations, but nearly all tumor tissues show reduced SOD levels. Selective imaging in early progression stages remains a key requirement for efficient cancer diagnosis and treatment. Magnetic resonance imaging (MRI) as a noninvasive tool with high spatial resolution may offer advantages here, but MRI contrast agents exhibiting a redox-triggered change in the image contrast towards superoxide radicals have not been reported so far. Here we show that manganese oxide (MnO) nanoparticles (NPs) exhibit an intrinsic SOD-like activity, which is higher than that of the native Mn-dependent SOD. In addition, MnO NPs significantly enhance the MRI contrast when exposed to superoxide radicals, making them responsive MRI contrast agents for the treatment and imaging of cancer cells with reduced SOD levels.

Received 16th August 2016,
Accepted 20th October 2016

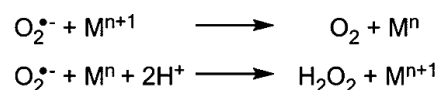
DOI: 10.1039/c6tb02078j

www.rsc.org/MaterialsB

Introduction

The origin of many severe diseases can be attributed to elevated cellular superoxide radical ($O_2^{\bullet-}$) concentrations.^{1,2} Superoxide is one of the main constituents of reactive oxygen species (ROS) and shows elevated concentrations in nearly all tumor tissues.^{3,4} Since tumor progression and metastasis are driven by oxidative stress based on high superoxide concentrations, antioxidants can be key components in cancer treatment.^{5,6} Besides medical therapy, tumor visualization in early stages has always been a demanding need for cancer prevention. Magnetic resonance imaging (MRI) as a noninvasive and highly sensitive technique

has proven to be valuable in modern cancer diagnostics. Therefore, in recent years, the research interest has shifted towards the development of MRI contrast agents that change the image contrast based on specific biochemical stimuli.⁷ Still, contrast agents demonstrating a redox-triggered contrast change are rare, and the selective response towards superoxide radicals has not been observed so far.⁷ In addition to classical MRI contrast agents based on lanthanide complexes, nonlanthanide inorganic nanomaterials, especially manganese oxide (MnO), were successfully used for the imaging of tumor tissue.^{8–12} Just recently, the pH-responsive MRI contrast of Mn²⁺-containing calcium phosphate nanoparticles was reported.⁸ Manganese is encountered in the ubiquitous enzyme superoxide dismutase (SOD), which regulates the intracellular superoxide radical concentration as part of the cellular protection machinery by decomposing superoxide into dioxygen (O_2) and hydrogen peroxide (H_2O_2) (Scheme 1).^{13–15} Besides Mn other transition



Scheme 1 SOD-catalyzed dismutation of superoxide radicals ($O_2^{\bullet-}$). The first part of the reaction leads to a release of dioxygen (O_2) and a reduction of the metal M^{n+1} to M^n ($M = Fe, Mn, Cu, Ni$). In the second step the metal M^n is reoxidized (regeneration) in a pH-dependent reaction in which hydrogen peroxide (H_2O_2) is formed.¹⁷

^a Institute of Inorganic and Analytical Chemistry, Johannes Gutenberg University Mainz, Duesbergweg 10-14, 55128 Mainz, Germany. E-mail: tremel@uni-mainz.de, tahir@uni-mainz.de

^b Section of Medical Physics, University Medical Center, Johannes Gutenberg University Mainz, Langenbeckstr. 1, 55131 Mainz, Germany

^c Institute of Organic Chemistry, Johannes Gutenberg University Mainz, Duesbergweg 10-14, 55128 Mainz, Germany

^d Graduate School Materials Science in Mainz, Staudinger Weg 9, 55128 Mainz, Germany

^e Institute of Physics, Johannes Gutenberg University Mainz, Staudingerweg 7, 55128 Mainz, Germany

^f Institute of Chemistry – Inorganic Chemistry, Martin Luther University Halle-Wittenberg, Kurt Mothes Straße 2, 06120 Halle, Germany

† Electronic supplementary information (ESI) available: TEM of the MnO NP size distribution, P-XRD, TEM of the NP functionalization, O_2 and H_2O_2 evolution, catalase assay, and EPR. See DOI: 10.1039/c6tb02078j

metal ions, such as Cu, Fe, and Ni, can occur in the active site of natural SODs.¹⁶

Mn-containing model complexes have already been used to mimic the enzymatic SOD activity, but their use is limited due to their low stability and sensitivity towards temperature/pH changes; this holds as well for native SOD, whose synthesis is in addition highly cost intensive.^{13,18–22} In comparison, inorganic nanoparticles (NPs) are readily available by cost-efficient synthesis up to the industrial scale and they easily tolerate changes in the reaction conditions, while having at the same time a huge number of active sites per unit volume due to their large surface area.²³ In recent years, some nanomaterials have been used to mimic enzymatic activities. A few have shown SOD-like reactions.^{18,24} Cerium dioxide (CeO₂) NPs are the most promising example, and they may find medical use both *in vitro* and *in vivo* because of their antioxidant properties combined with low toxicity.^{25,26} However, an inorganic NP mimic that combines an SOD-like activity with an MRI contrast, let alone a redox-triggered MRI response, has not been reported.

Based on the knowledge on Mn-SODs and model complexes, we investigated the potential of Mn-containing nanoparticles as SOD mimics. Here we report the intrinsic SOD-like activity of C-PEG (catechol-polyethylene glycol)-functionalized water-dispersible MnO NPs that exhibit a strongly enhanced MRI contrast based on extended T_1 and T_2 times when exposed to superoxide radicals (Fig. 1). Additionally, MnO NPs decompose H₂O₂, one of the SOD reaction products, in a catalase-like reaction. The formation of dioxygen (O₂), the second reaction product, was demonstrated with an oxygen sensitive electrode. Since MnO NPs decompose superoxide radicals and H₂O₂, both leading to tumor progression, MnO NPs with an enhanced MRI contrast may be used as a combination therapeutic for cancer treatment and imaging.

Experimental

Chemicals

Cytochrome *c* from equine heart (cyt *c*, ≥95%, Sigma), manganese(II) chloride tetrahydrate (≥98%, Sigma-Aldrich), nitrosyl tetrafluoroborate (NOBF₄, 95%, Sigma-Aldrich), oleic acid (≥99%, Sigma-Aldrich), phosphate buffered saline (PBS, tablets, Sigma), potassium hydroxide (KOH, 85%, Sigma-Aldrich), 1-octadecene (≥95%, Aldrich), sodium dithionite (85%, Sigma),

sodium hydroxide (NaOH, ≥98%, Sigma-Aldrich), trimethylamine *N*-oxide (98%, Aldrich), xanthine (≥99%, Sigma), and xanthine oxidase from bovine milk (grade IV, ammonium sulfate suspension, 0.1–0.4 units per mg, Sigma) were used without further purification.

Physical characterization

Transmission electron microscopy (TEM) images were obtained on a Philips EM-420 instrument with an acceleration voltage of 120 kV. Powdered X-ray diffraction (P-XRD) was carried out on a Bruker AXS D8 Advance diffractometer using Mo K α radiation and analyzed using the EVA software. UV/Vis kinetics were recorded on a Cary 5G UV/Vis-NIR spectrophotometer (Varian Inc., Palo Alto, CA, USA). Atomic absorption spectroscopy (AAS) measurements were carried out on a Perkin-Elmer 5100 ZL.

MnO nanoparticles (1)

MnO NPs were synthesized based on a previously reported procedure with some modifications.²⁷ In brief, manganese(II) chloride tetrahydrate (7.92 g, 40 mmol) and oleic acid (22.60 g, 80 mmol) were dissolved in 200 mL of methanol under constant stirring at RT. KOH (5.16 g, 80 mmol) was separately dissolved in 200 mL of methanol and slowly added to the first solution. The mixed solutions were stirred for 1 h at RT to yield the reddish-brown waxy solid manganese(II) oleate, which was separated by decantation and washed several times with water, ethanol, and acetone. Afterwards the oleate was dissolved in hexane and again washed with water, ethanol, and acetone. Finally hexane was removed by rotary evaporation and the precursor was dried under high vacuum.

1.23 g of the manganese(II) oleate were dissolved in 10 mL of 1-octadecene under argon, heated to 593 K with 2 K min⁻¹, and stirred for 30 min. The brown product was precipitated by addition of acetone or ethanol, separated by centrifugation, washed several times with acetone or ethanol, dried under high vacuum, and characterized by P-XRD and TEM. Yield: ≈100 mg.

Mn₃O₄ nanoparticles (2)

100 mg of **1** and trimethylamine *N*-oxide (100 mg, 1.33 mmol) were dissolved in 10 mL of 1-octadecene and stirred at 573 K (3 K min⁻¹) for 4 h. Afterwards the dark brown product was precipitated by addition of acetone or ethanol, separated by centrifugation, washed several times with acetone or ethanol, dried under high vacuum, and characterized by P-XRD and TEM. Yield: ≈100 mg.

Nanoparticle functionalization

The catechol-PEG polymer (C-PEG₆₇, $M_w \approx 2900$ g mol⁻¹, PDI = 1.07) was synthesized as described elsewhere.^{28,29} The surface of the hydrophobic oleate-capped manganese oxide nanoparticles was modified by a ligand-exchange reaction as previously reported with some modifications.³⁰ 5 mg of Mn_xO_y-NPs were dissolved in 1.25 mL of hexane and quickly added to a solution of 1.45 mg (0.01 mol) of NOBF₄ in 1.25 mL of DMF. The mixture was inverted, the NPs were precipitated by addition of 1.25 mL of ethanol and 0.5 mL of DCM,

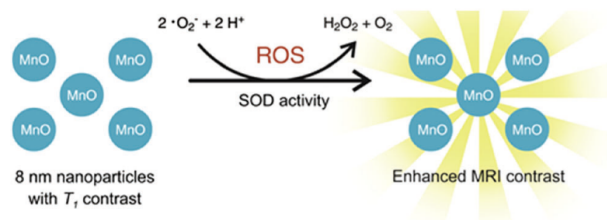


Fig. 1 MnO NPs with intrinsic SOD-like activity. Water-dispersible manganese oxide nanoparticles functionalized with catechol-PEG show an intrinsic SOD activity. MRI relaxation times of MnO increase due to the SOD reaction and lead to a significant enhancement in the MRI image contrast.

and separated by centrifugation. Afterwards the NPs were dispersed in 2.5 mL of DMF, mixed with a solution of 5 mg of C-PEG in 2.5 mL of DMF, and stirred for 3 h at RT. Finally, the nanoparticles were separated by centrifugation, redispersed and stored in milli Q water, and the final Mn concentration was estimated by AAS.

Superoxide dismutase assay

The SOD assay was based on a classical method monitoring the inhibition of the cytochrome *c* reduction at 550 nm caused by superoxide.³¹ Superoxide ions were generated *in situ* by the enzyme xanthine oxidase in PBS buffer (50 mM, pH 7.4) supplemented with 10 μM cyt *c* and 500 μM xanthine (solution in 0.01 M NaOH) and the final concentrations of 0, 0.2, 0.7, 1.1, and 2.2 $\mu\text{g mL}^{-1}$ of MnO/Mn₃O₄ nanoparticles and 0, 0.01, 0.03, 0.05, 0.1, and 0.2 $\mu\text{g mL}^{-1}$ MnCl₂, respectively. Afterwards, xanthine oxidase was added to start the reaction. The total amount of xanthine oxidase needed to exhibit an absorbance change of 0.025 A min⁻¹ at 550 nm (in our case 0.2 U mL⁻¹) was determined before starting the actual measurement. The slopes of the reactions of the nanoparticle with cyt *c* without the addition of XO (*e.g.*, possible cross-reaction of MnO/Mn₃O₄ with Fe in cyt *c*) were close to zero, and were subtracted from the final reaction rates.

Determination of the kinetic parameters

The cyt *c* reduction by superoxide was monitored at 505 nm for 3 min at RT while varying the Mn_xO_y/Mn²⁺ concentrations and compared with the reaction that did not contain Mn_xO_y or Mn²⁺ (100% value). Mean values of the initial cytochrome *c* reduction rates of three traces were used in the calculations. The initial rate values plotted against the catalyst concentration were adjusted to first order exponential decay kinetics to determine the catalyst concentration needed to inhibit 50% of the cyt *c* reduction (IC₅₀).³² The catalytic rate constant of the superoxide turnover with SOD k_{SOD} was determined using the known rate constant for the reduction of cyt *c* by superoxide at pH 7.2 ($1.1 \times 10^5 \text{ M}^{-1} \text{ s}^{-1}$)³¹ at 50% inhibition, in which the velocities of the reaction of superoxide with cyt *c* and SOD are equal: $v_{\text{cyt}} = v_{\text{SOD}}$ which can be written as $k_{\text{cyt}} \times c_{\text{cyt}} = k_{\text{SOD}} \times c_{\text{SOD}}$ finally leading to $k_{\text{SOD}} = (k_{\text{cyt}} \times c_{\text{cyt}}) / c_{\text{SOD}}$. Molar nanoparticle concentrations were determined using the average nanoparticle diameter (TEM) as previously described.^{23,26} The average NP diameter was converted to the spherical NP volume and the mass $m(\text{Mn}_x\text{O}_y)$ of a single particle attained by multiplication with the density of bulk MnO/Mn₃O₄. Afterwards, $[\text{Mn}_x\text{O}_y]$ was determined as follows: $[\text{Mn}_x\text{O}_y] = \text{IC}_{50} / m(\text{Mn}_x\text{O}_y) \times N_{\text{A}}$, in which N_{A} is the Avogadro constant. Errors of the kinetic values were calculated using the Gaussian error propagation.

Measurement of O₂ formation

The rate of the dioxygen (O₂) formation was measured by using a Mettler Toledo oxygen electrode in a microchamber at RT under continuous stirring. This method was carried out similar to the SOD assay without the addition of cyt *c* and with final MnO concentrations of 2 $\mu\text{g mL}^{-1}$.

Measurement of H₂O₂ formation

The formation of hydrogen peroxide (H₂O₂) was measured by using a classical HRP/ABTS assay.³³ This method was carried out similar to the SOD assay without the addition of cyt *c*. Final concentrations of MnO 8 $\mu\text{g mL}^{-1}$, ABTS 10 μM , HRP 5 mg mL^{-1} , xanthine 500 μM , and xanthine oxidase 2 U mL⁻¹ were used in PBS-buffer (50 mM, pH 7.4). As a positive control, 10 μM H₂O₂ were added to HRP/ABTS (without MnO) in PBS-buffer (50 mM, pH 7.4) without further addition.

Catalase assay

The catalase activity of the MnO nanoparticles was measured by following the disappearance of peroxide at 240 nm for 3 min at RT by UV/Vis, based on a reported procedure.³⁴ Concentrations of 10 mM H₂O₂ and 50 mM PBS pH 7.4 were used, while varying the amounts of the MnO nanoparticles (0.2, 0.7, 1.1, 2.2 $\mu\text{g mL}^{-1}$). The slope of the reaction without the addition of MnO (*e.g.*, background reaction of H₂O₂ in buffer) was subtracted from the final reaction rates.

EPR measurements

All EPR measurements were carried out with a Miniscope MS300 (Magnetech GmbH, 9.4 GHz) under liquid nitrogen at 77 K in water containing 50% glycerin.³⁵ For catalytic tests, standard SOD assay conditions were used without the addition of cyt *c* and an equilibration time of roughly 30 min.

MRI measurements

All MnO samples were measured using a 3.0 T Magnetom Prisma MRI System (Siemens, Erlangen, Germany) together with a custom-built 60 channel ¹H receive-coil array for best volume coverage. For measurements of T_1 , an inversion-recovery pulse sequence was used with $T_1 = 24, 50, 100, 200, 500, 750, 1000,$ and 2000 ms (TR = 2500 ms, image matrix = 192 × 120, field of view (FOV) = 62 × 99 mm, flip angle (FA) = 150°, acquisition time = 6:20 min). T_2 was measured using a spin echo pulse sequence with 12 echoes at TE = 16.6, 33.2, ..., 199.2 ms (TR = 3000 ms, image matrix = 192 × 120, field of view (FOV) = 62 × 99 mm, flip angle (FA) = 180°, acquisition time = 5:57 min). Standard SOD assay conditions were used without the addition of cyt *c* and an equilibration time of roughly 60 min.

Comparative MRI measurements with Mn²⁺ ions were carried out with a Bruker/Oxford Instrument 7T/150 mm Super wide bore system operated at 4.7 T with a DRX spectrometer from Resonance Instruments and a Bruker Microimaging 200 MHz ¹H-frequency probe head. A Bruker BLAH und BLAX 1 kW high frequency amplifier together with a Copley gradient amplifier were used.

Results and discussion

Monodisperse and phase-pure spherical MnO NPs (Mn²⁺) with an average diameter of 7.6 ± 0.7 nm (size distribution in Fig. S1, ESI†) were synthesized by thermolysis of Mn-oleate in 1-octadecene as described previously (Fig. 2a).²⁷ Phase purity of

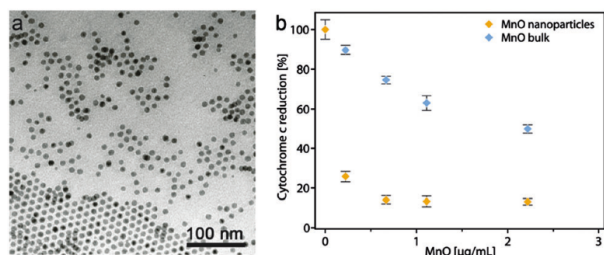


Fig. 2 (a) TEM image of monodisperse 7.6 ± 0.7 nm MnO NPs. Scale bar: 100 nm. (b) Catalytic SOD activity of varying MnO concentrations (NPs and bulk, 0.2 – $2.2 \mu\text{g mL}^{-1}$) towards the superoxide radical dismutation, generated by xanthine/xanthine oxidase (XO) and colorimetric determination by the cytochrome *c* reduction (550 nm, $10 \mu\text{M}$ cyt *c*, PBS buffer 50 mM pH 7.4). The inhibition of the cytochrome *c* reduction was determined compared to 100% of the control reaction rate (no MnO).

the MnO NPs was confirmed by powder X-ray diffraction (P-XRD, Fig. S2, ESI[†]). Since the as-synthesized MnO NPs are covered with a hydrophobic oleate layer and therefore are insoluble in water, the NPs were refunctionalized with the hydrophilic polymer ligand C-PEG ($M_w \approx 2900 \text{ g mol}^{-1}$; PDI = 1.07), leading to a pronounced water solubility of the MnO NPs while retaining size (hydrodynamic radius increased to about 10 nm due to the hydrophilic polymer shell)³⁶ and morphology (Fig. S3, ESI[†]).^{28–30} It is worth mentioning that these aqueous dispersions are stable for several months.^{10,29,36} The catechol anchor group of the ligand strongly binds to the Mn surface atoms,¹⁰ while C-PEG enhances the solubility of the nanoparticles in aqueous media and allows for *in vitro* applications of the material.^{10,28,37,38}

The C-PEG-functionalized MnO NPs were assessed for their ability to decompose superoxide in a SOD-like reaction using a routine UV/Vis assay utilizing xanthine oxidase (XO) for the generation of superoxide that reduces cytochrome *c* ($10 \mu\text{M}$).³¹ The rate of reduction can be monitored spectrophotometrically at 550 nm; the SOD-activity is equivalent to the inhibition of this reduction. The catalytic SOD rate constant k_{SOD} was calculated by using the molar MnO NP concentration in solution that was determined based on the NP diameter (a typical approach for NP enzyme mimics).^{18,23,24,26,39} MnO NPs exhibit an intrinsic SOD-like activity with a k_{SOD} of $2.4 \pm 0.1 \times 10^9 \text{ M}^{-1} \text{ s}^{-1}$ that is higher than that of bulk MnO (Fig. 2b), native Mn-SOD ($1.8 \times 10^9 \text{ M}^{-1} \text{ s}^{-1}$),³¹ and Mn-containing SOD model complexes (ranging from values just slightly above the autodismutation of $\text{O}_2^{\bullet-}$ $5 \times 10^5 \text{ M}^{-1} \text{ s}^{-1}$ up to $1.2 \times 10^9 \text{ M}^{-1} \text{ s}^{-1}$),^{19,40} when molar nanoparticle concentrations based on the NP radius were used for the calculations (Table 1). Mixed-valent Mn_3O_4 ($\text{Mn}^{2+}/\text{Mn}^{3+}$) NPs, with a size and morphology (Fig. S4, ESI[†]) comparable to those of MnO (Mn^{2+}) NPs, catalyze the decomposition of superoxide with a similar k_{SOD} of $1.5 \pm 0.2 \times 10^9 \text{ M}^{-1} \text{ s}^{-1}$ (Fig. 3a). These findings and the observed exchange bias (EB) effect due to exchange interaction between the antiferromagnetic MnO core and a ferrimagnetic shell in the hysteresis loops for MnO particles⁴¹ are compatible with the presence of a thin surface layer of Mn_3O_4 (or Mn_2O_3)^{42,43} caused by an oxidation of the Mn^{2+} surface species. Due to the exchange interaction between the antiferromagnetic MnO core and the ferrimagnetic shell, an EB effect can occur.^{42–44}

Table 1 Catalytic/relaxation properties of MnO NPs, Mn^{2+} , and Mn-SOD

Material	k_{SOD}^a [$\text{M}^{-1} \text{ s}^{-1}$]	r_1^b [$\text{mM}^{-1} \text{ s}^{-1}$]	r_2^b [$\text{mM}^{-1} \text{ s}^{-1}$]	$r_1^b + \text{O}_2^{\bullet-}$ [$\text{mM}^{-1} \text{ s}^{-1}$]	$r_2^b + \text{O}_2^{\bullet-}$ [$\text{mM}^{-1} \text{ s}^{-1}$]
MnO^c	2.4×10^9	0.35	4.94	0.06	1.90
Mn^{2+}	6.1×10^7	7.95	62.07	6.81	36.95
Mn-SOD ^d	1.8×10^9	—	—	—	—

^a Catalytic SOD rate constant in 50 mM PBS buffer pH 7.4. ^b T_1/T_2 weighted specific relaxivities. ^c Average particle size 8 nm. ^d Kinetic value by Fridovich *et al.*³¹

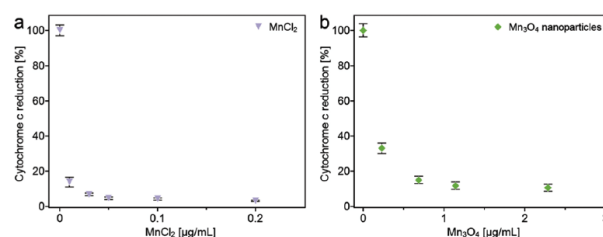


Fig. 3 SOD-activity of Mn_3O_4 NPs and Mn^{2+} cations. Catalytic SOD activity of varying (a) Mn_3O_4 (0 , 0.2 , 0.7 , 1.1 , $2.2 \mu\text{g mL}^{-1}$) and (b) MnCl_2 concentrations (0 , 0.01 , 0.03 , 0.05 , 0.1 , $0.2 \mu\text{g mL}^{-1}$) towards the superoxide radical dismutation, generated by XO and colorimetric determination by cytochrome *c* reduction (550 nm, $10 \mu\text{M}$ cyt *c*, PBS buffer 50 mM pH 7.4). The inhibition of cytochrome *c* reduction was determined compared to 100% of the control reaction rate (no Mn_3O_4 or Mn^{2+} , respectively).

Therefore, in contrast to Mn-containing complexes (whose activity is influenced by the $\text{Mn}^{2+}/\text{Mn}^{3+}$ ratio),¹³ the SOD-like activity of MnO is independent of the $\text{Mn}^{2+}/\text{Mn}^{3+}$ ratio, and a simple oxidation of the MnO NP surface from Mn^{2+} to Mn^{3+} is very unlikely. However, an exact determination of the $\text{Mn}^{2+}/\text{Mn}^{3+}$ ratio on the NP surface is difficult due to the heterogeneous nature of the reaction. Recent studies from Barnese *et al.* showed that even free Mn^{2+} ions display an SOD-like activity.⁴⁵ Therefore, as a control we measured the SOD activity of free Mn^{2+} ions (dissolved MnCl_2). Compared to MnO NPs, the SOD-like activity of Mn^{2+} with a k_{SOD} of $6.1 \pm 0.3 \times 10^7 \text{ M}^{-1} \text{ s}^{-1}$ (Table 1, original values from Barnese *et al.* $2.8 \times 10^7 \text{ M}^{-1} \text{ s}^{-1}$ for $\text{Mn}_3(\text{PO}_4)_2$) was two orders of magnitude lower than that for the MnO NPs (Fig. 3b).

As illustrated in Scheme 1, natural SODs decompose superoxide to molecular O_2 and H_2O_2 . By using an oxygen-sensitive electrode together with the xanthine/xanthine oxidase system for $\text{O}_2^{\bullet-}$ formation, the O_2 evolution was demonstrated triggered by the addition of MnO NPs to the reaction mixture (Fig. S5, ESI[†]). In contrast, the formation of H_2O_2 could not be shown using a classical H_2O_2 sensitive horseradish peroxidase/2,2'-azino-bis(3-ethylbenzothiazole-6-sulfonic acid) (HRP/ABTS, Fig. S6, ESI[†]).³³ Therefore, we probed a possible catalase-like activity of the manganese oxide NPs, which is associated with the consumption of H_2O_2 resulting from the SOD reaction. The decomposition of H_2O_2 was monitored by its absorbance at 240 nm indicating also a catalase-like activity of the MnO NPs (Fig. S7, ESI[†]).³⁴ This dual SOD- and catalase-like activity is very rare and has been reported only for selected metal complexes and CeO_2 NPs so far.^{46,47}

Finally, the T_1 and T_2 weighted MRI contrast of the MnO NPs was investigated (Fig. 4). MnO NPs show a T_1 of 501 ms and a T_2 of

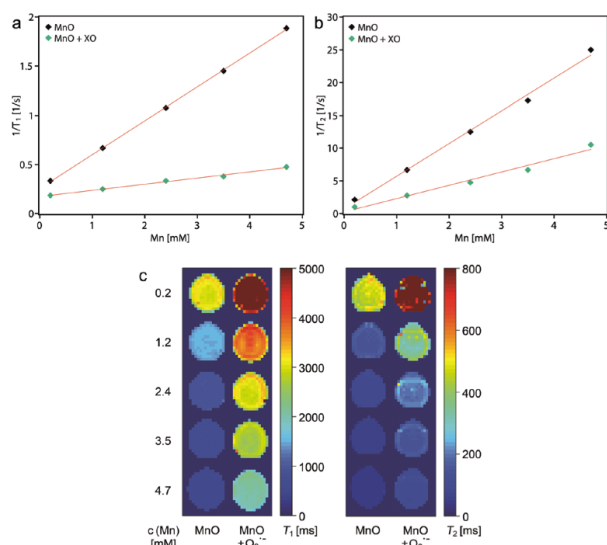


Fig. 4 Specific relaxivities (a) r_1 and (b) r_2 of MnO NPs without and with the addition of superoxide generated by XO. Relaxivities were determined by linear regression and showed values for MnO NPs without XO of $r_1 = 0.35 \pm 0.01 \text{ mM}^{-1} \text{ s}^{-1}$ and $r_2 = 4.94 \pm 0.11 \text{ mM}^{-1} \text{ s}^{-1}$, and for MnO NPs with XO of $r_1 = 0.06 \pm 0.01 \text{ mM}^{-1} \text{ s}^{-1}$ and $r_2 = 1.90 \pm 0.14 \text{ mM}^{-1} \text{ s}^{-1}$. (c) MRI imaging of varying MnO concentrations (0.2–4.7 mM) showing T_1 - (MnO, left) and T_2 -weighted images (MnO, right) with relaxation times (T_1 , T_2) measured on a standard clinical MRI instrument using a 96 well-plate with an equilibration time of roughly 60 min. Upon generation of superoxide radicals *in situ* by adding xanthine oxidase, T_1 and T_2 substantially increase, resulting in significant changes in the MRI contrast.

39 ms (at 5 mM Mn), and specific relaxivities r_1 and r_2 of $0.35 \pm 0.01 \text{ mM}^{-1} \text{ s}^{-1}$ and $4.94 \pm 0.11 \text{ mM}^{-1} \text{ s}^{-1}$, respectively (Table 1, Fig. 4a and b), which are in good agreement with the values reported by Hyeon and coworkers ($T_1 = 481 \text{ ms}$ and $T_2 = 85 \text{ ms}$ at 5 mM Mn; $r_1 = 0.37 \text{ mM}^{-1} \text{ s}^{-1}$ and $r_2 = 1.74 \text{ mM}^{-1} \text{ s}^{-1}$).⁴⁸ Most interestingly, when MnO NPs were exposed to superoxide radicals, the T_1 and T_2 relaxation times increased significantly with r_1 and r_2 values of $0.06 \pm 0.01 \text{ mM}^{-1} \text{ s}^{-1}$ and $1.90 \pm 0.14 \text{ mM}^{-1} \text{ s}^{-1}$, respectively (Fig. 4a and b). This remarkable effect was observed as well for free Mn^{2+} ions in the presence of equal superoxide radical concentrations (Table 1 and Fig. S8, ESI†). An increase of the relaxation times can possibly be explained by a temporary change of the oxidation states of manganese ions during the SOD reaction, leading to alterations in the paramagnetic field. This effect could also be observed by electron paramagnetic resonance (EPR),^{32,49} in which MnO NPs showed the typical anisotropic six line pattern for Mn^{2+} (^{55}Mn ; $I = 5/2$; 100%),⁵⁰ with a clear reduction in the signal intensity due to the treatment with superoxide (Fig. S9, ESI†). Since MRI and EPR measurements were performed after an equilibration time of 60 and 30 min, respectively, a simple and permanent oxidation of Mn^{2+} to Mn^{3+} is unlikely.

Conclusions

Manganese oxide nanoparticles were demonstrated to have the ability to remove superoxide radicals rapidly and catalytically

via a disproportionation mechanism resembling that of SOD enzymes. MnO NPs catalyze the SOD-mimetic decomposition of $\text{O}_2^{\bullet-}$ with a catalytic rate constant exceeding that of native SOD, while being a potent T_1 -weighted contrast agent for magnetic resonance imaging (MRI). When exposed to superoxide radicals, MnO NPs show significantly prolonged T_1 and T_2 times, which lead to an enhanced MRI contrast. This effect could also be observed to a lower extent for free Mn^{2+} ions. Due to the unique combination of SOD-like activity with enhanced MRI contrast, MnO NPs could be used simultaneously for treating oxidative-stress-promoted tumor progression and metastases or as a selective clinical MRI imaging tool.

Acknowledgements

This work was supported through the SFB 1066 “Nano-dimensionale polymere Therapeutika für die Tumorthherapie”. R. R. and M. K. were supported by a fellowship from the Max Planck Graduate Center Mainz (MPGC). J. H. acknowledges a fellowship through the Excellence Initiative (DFG/GSC 266) in the context of MAINZ “Materials Science in Mainz”.

Notes and references

- 1 T. Fukai and M. Ushio-Fukai, *Antioxid. Redox Signaling*, 2011, **15**, 1583–1606.
- 2 T. Finkel and N. J. Holbrook, *Nature*, 2000, **408**, 239–247.
- 3 L. W. Oberley and G. R. Buettner, *Cancer Res.*, 1979, **39**, 1141–1149.
- 4 S. K. Dhar and D. K. St. Clair, *Free Radical Biol. Med.*, 2012, **52**, 2209–2222.
- 5 M. O. Laukkanen, *Oxid. Med. Cell. Longevity*, 2016, **2016**, 9.
- 6 P. Huang, L. Feng, E. A. Oldham, M. J. Keating and W. Plunkett, *Nature*, 2000, **407**, 390–395.
- 7 G.-L. Davies, I. Kramberger and J. J. Davis, *Chem. Commun.*, 2013, **49**, 9704–9721.
- 8 P. Mi, D. Kokuryo, H. Cabral, H. Wu, Y. Terada, T. Saga, I. Aoki, N. Nishiyama and K. Kataoka, *Nat. Nanotechnol.*, 2016, **11**, 724–730.
- 9 K. An, M. Park, J. H. Yu, H. B. Na, N. Lee, J. Park, S. H. Choi, I. C. Song, W. K. Moon and T. Hyeon, *Eur. J. Inorg. Chem.*, 2012, 2148–2155.
- 10 T. D. Schladt, K. Schneider, M. I. Shukoor, F. Natalio, H. Bauer, M. N. Tahir, S. Weber, L. M. Schreiber, H. C. Schroder, W. E. G. Muller and W. Tremel, *J. Mater. Chem.*, 2010, **20**, 8297–8304.
- 11 H. B. Na, I. C. Song and T. Hyeon, *Adv. Mater.*, 2009, **21**, 2133–2148.
- 12 H. B. Na, J. H. Lee, K. An, Y. I. Park, M. Park, I. S. Lee, D.-H. Nam, S. T. Kim, S.-H. Kim, S.-W. Kim, K.-H. Lim, K.-S. Kim, S.-O. Kim and T. Hyeon, *Angew. Chem., Int. Ed.*, 2007, **46**, 5397–5401.
- 13 S. Miriyala, I. Spasojevic, A. Tovmasyan, D. Salvemini, Z. Vujaskovic, D. St. Clair and I. Batinic-Haberle, *Biochim. Biophys. Acta*, 2012, **1822**, 794–814.

- 14 V. L. Pecoraro, M. J. Baldwin and A. Gelasco, *Chem. Rev.*, 1994, **94**, 807–826.
- 15 V. L. Pecoraro, *Manganese redox enzymes*, Wiley-VCH, Weinheim, 1992.
- 16 Y. Sheng, I. A. Abreu, D. E. Cabelli, M. J. Maroney, A.-F. Miller, M. Teixeira and J. S. Valentine, *Chem. Rev.*, 2014, **114**, 3854–3918.
- 17 R. H. Holm, P. Kennepohl and E. I. Solomon, *Chem. Rev.*, 1996, **96**, 2239–2314.
- 18 H. Wei and E. Wang, *Chem. Soc. Rev.*, 2013, **42**, 6060–6093.
- 19 O. Iranzo, *Bioorg. Chem.*, 2011, **39**, 73–87.
- 20 R. van Eldik and J. Reedijk, *Advances in Inorganic Chemistry: Homogeneous Biomimetic Oxidation Catalysis*, Academic Press, London, 2006.
- 21 D. Pursche, M. U. Triller, C. Slinn, N. Reddig, A. Rempel and B. Krebs, *Inorg. Chim. Acta*, 2004, **357**, 1695–1702.
- 22 J. Reedijk and E. Bouwman, *Bioinorganic catalysis*, Marcel Dekker, Inc., New York, 1999.
- 23 R. Ragg, F. Natalio, M. N. Tahir, H. Janssen, A. Kashyap, D. Strand, S. Strand and W. Tremel, *ACS Nano*, 2014, **8**, 5182–5189.
- 24 R. Ragg, M. N. Tahir and W. Tremel, *Eur. J. Inorg. Chem.*, 2016, 1906–1915.
- 25 C. Xu and X. Qu, *NPG Asia Mater.*, 2014, **6**, e90.
- 26 C. Korsvik, S. Patil, S. Seal and W. T. Self, *Chem. Commun.*, 2007, 1056–1058.
- 27 T. D. Schladt, T. Graf and W. Tremel, *Chem. Mater.*, 2009, **21**, 3183–3190.
- 28 M. N. Tahir, J. Herzberger, F. Natalio, O. Kohler, R. Branscheid, E. Mugnaioli, V. Ksenofontov, M. Panthofer, U. Kolb, H. Frey and W. Tremel, *Nanoscale*, 2016, **8**, 9548–9555.
- 29 V. S. Wilms, H. Bauer, C. Tonhauser, A.-M. Schilman, M.-C. Müller, W. Tremel and H. Frey, *Biomacromolecules*, 2013, **14**, 193–199.
- 30 A. Dong, X. Ye, J. Chen, Y. Kang, T. Gordon, J. M. Kikkawa and C. B. Murray, *J. Am. Chem. Soc.*, 2011, **133**, 998–1006.
- 31 H. J. Forman and I. Fridovich, *Arch. Biochem. Biophys.*, 1973, **158**, 396–400.
- 32 C. Yung-Chi and W. H. Prusoff, *Biochem. Pharmacol.*, 1973, **22**, 3099–3108.
- 33 R. E. Childs and W. G. Bardsley, *Biochem. J.*, 1975, **145**, 93–103.
- 34 R. F. Beers and I. W. Sizer, *J. Biol. Chem.*, 1952, **195**, 133–140.
- 35 K. A. Campbell, E. Yikilmaz, C. V. Grant, W. Gregor, A.-F. Miller and R. D. Britt, *J. Am. Chem. Soc.*, 1999, **121**, 4714–4715.
- 36 T. D. Schladt, K. Koll, S. Prufer, H. Bauer, F. Natalio, O. Dumele, R. Raidoo, S. Weber, U. Wolfrum, L. M. Schreiber, M. P. Radsak, H. Schild and W. Tremel, *J. Mater. Chem.*, 2012, **22**, 9253–9262.
- 37 J. Kim, H. S. Kim, N. Lee, T. Kim, H. Kim, T. Yu, I. C. Song, W. K. Moon and T. Hyeon, *Angew. Chem., Int. Ed.*, 2008, **47**, 8438–8441.
- 38 M. I. Shukoor, F. Natalio, M. N. Tahir, M. Wiens, M. Tarantola, H. A. Therese, M. Barz, S. Weber, M. Terekhov, H. C. Schröder, W. E. G. Müller, A. Janshoff, P. Theato, R. Zentel, L. M. Schreiber and W. Tremel, *Adv. Funct. Mater.*, 2009, **19**, 3717–3725.
- 39 L. Gao, J. Zhuang, L. Nie, J. Zhang, Y. Zhang, N. Gu, T. Wang, J. Feng, D. Yang, S. Perrett and X. Yan, *Nat. Nanotechnol.*, 2007, **2**, 577–583.
- 40 S. Cuzzocrea, E. Mazzon, L. Dugo, A. P. Caputi, K. Aston, D. P. Riley and D. Salvemini, *Br. J. Pharmacol.*, 2001, **132**, 19–29.
- 41 A. K. X. Sun, Y. Su, K. Nemkovski, A. Wildes, H. Bauer, O. Köhler, A.-M. Schilman, W. Tremel, O. Petravic and T. Brückel, submitted for publication.
- 42 A. E. Berkowitz, G. F. Rodriguez, J. I. Hong, K. An, T. Hyeon, N. Agarwal, D. J. Smith and E. E. Fullerton, *Phys. Rev. B: Condens. Matter Mater. Phys.*, 2008, **77**, 024403.
- 43 I. V. Golosovsky, G. Salazar-Alvarez, A. López-Ortega, M. A. González, J. Sort, M. Estrader, S. Suriñach, M. D. Baró and J. Nogués, *Phys. Rev. Lett.*, 2009, **102**, 247201.
- 44 J. Nogués, J. Sort, V. Langlais, V. Skumryev, S. Suriñach, J. S. Muñoz and M. D. Baró, *Phys. Rep.*, 2005, **422**, 65–117.
- 45 K. Barnese, E. B. Gralla, D. E. Cabelli and J. Selverstone Valentine, *J. Am. Chem. Soc.*, 2008, **130**, 4604–4606.
- 46 G. N. Ledesma, H. Eury, E. Anxolabéhère-Mallart, C. Hureau and S. R. Signorella, *J. Inorg. Biochem.*, 2015, **146**, 69–76.
- 47 T. Pirmohamed, J. M. Dowding, S. Singh, B. Wasserman, E. Heckert, A. S. Karakoti, J. E. S. King, S. Seal and W. T. Self, *Chem. Commun.*, 2010, **46**, 2736–2738.
- 48 H. B. Na, J. H. Lee, K. An, Y. I. Park, M. Park, I. S. Lee, D.-H. Nam, S. T. Kim, S.-H. Kim, S.-W. Kim, K.-H. Lim, K.-S. Kim, S.-O. Kim and T. Hyeon, *Angew. Chem.*, 2007, **119**, 5493–5497.
- 49 G. Jeschke, *Curr. Opin. Solid State Mater. Sci.*, 2003, **7**, 181–188.
- 50 K. A. P. Payne, M. D. White, K. Fisher, B. Khara, S. S. Bailey, D. Parker, N. J. W. Rattray, D. K. Trivedi, R. Goodacre, R. Beveridge, P. Barran, S. E. J. Rigby, N. S. Scrutton, S. Hay and D. Leys, *Nature*, 2015, **522**, 497–501.

4 Summary and Outlook

In this work, the site of one-electron reduction could be mainly assigned to the gold centre regarding gold(III) porphyrin derivatives as the electron acceptors (section 3.1). Indeed, the chemical reduction of the gold(III) porphyrins with cobaltocene gives broad EPR resonances in accordance with a gold centred radical displaying hyperfine splitting due to the ^{197}Au and ^{14}N nuclei. This behaviour is independent of the nature of the *meso*-aryl group. The broad Au^{II} resonances were superimposed by a sharp resonance, which could be assigned to a porphyrin π -radical anion. Only in the case of the nitro derivative reduction an additional radical species is formed and has been assigned to a nitro- π radical anion. These findings enable the application of *meso*-substituted gold(III) porphyrins as potent electron acceptors in artificial photosynthetic systems, almost unaffected of the substitution pattern. The substituents can thus be used to fine-tune the redox potential or to control other properties such as solubility. In addition, gold(III) porphyrins are excellently suited for photoinduced electron transfer processes with retarded BET, since the BET from the gold centred σ -radical ($5d_{x^2-y^2}$ orbital) is strongly hindered by the inappropriate orbital symmetry concerning the π -system of the porphyrin macrocycle.

Furthermore, an isolable and exceptionally stable mononuclear gold(II) porphyrin complex was synthesised and characterised (section 3.2). This was possible, since the porphyrin macrocycle blocks the typical reactivity pathways such as dimerisation (via the single occupied $5d_{x^2-y^2}$ orbital) and disproportionation of other labile gold(II) species. Indeed, the unpaired electron is trapped in the σ -system of the metal centre. The EPR experiments together with XRD studies and supporting quantum chemical calculations revealed that the gold(II) ion adopts a [2+2] coordination geometry with alternating Au-N bond distances. This is triggered by a second-order Jahn-Teller distortion due to the relativistically reduced energy gap between the $5d_{x^2-y^2}$ orbital and the 6s orbital of Au. This second-order Jahn-Teller distortion of the porphyrin ligand is dynamic regarding the ^1H NMR time scale at room temperature (one $\text{Au}^{\text{II}}(\text{TPP})$ signal set) but is frozen in solid matrices as demonstrated via EPR spectroscopy at 77 K. It could be shown, that $[\text{Au}^{\text{III}}(\text{TPP})]^+$ is reduced to $\text{Au}^{\text{II}}(\text{TPP})$ with an excess of BNAH (NADH model compound) in the presence of a base suggesting a significant role of the $[\text{Au}^{\text{III}}(\text{TPP})]^{+/0}$ redox couple during the reactive oxygen species formation in Au-based anticancer drugs. This was further underscored, since $\text{Au}^{\text{II}}(\text{TPP})$ is able to reduce O_2 yielding superoxide $\text{O}_2^{\bullet-}$ as ROS species. In the absence from oxidants, $\text{Au}^{\text{II}}(\text{TPP})$ is remarkably stable, for example in water or even in the presence of acids. Since

the porphyrin macrocycle confers unmatched stability towards the Au^{II} core, this will allow future studies concerning the reactivity of Au^{II}(TPP) towards other radicals or main-group elements. The data obtained so far, in combination with clever ligand design (four donor atoms in the xy plane) points to the possibility to isolate further compounds of this novel class of mononuclear gold(II) complexes and hence will allow the exploration of the latter regarding visible-light-mediated gold-catalysed reactions, photoinduced electron transfer processes or medicinal applications.

Finally, three novel zinc(II)-gold(III) bis(porphyrin) dyads [Zn^{II}(P)-Au^{III}(P)]⁺ to mimic solar to chemical energy conversion were synthesised and characterised (section 3.3). Their suitability with respect to PET was successfully tested via time-resolved spectroscopic techniques revealing an ultrafast forward PET ($k_{\text{ET}} = 8.3 \times 10^{10} \text{ s}^{-1}$ for [Zn^{II}(P^{OnBu})-Au^{III}(P^{CF3})]⁺ (**[2]**⁺)) due to the π -conjugated bridge between the zinc(II) porphyrin chromophore and the gold(III) porphyrin acceptor. A part of the resulting excited states decays to a rather long-lived CSh state [Zn(P^{•+})-Au^{II}(P)]⁺ (lifetime $\approx 3 \text{ ns}$) with gold in the oxidation state +II. This can be attributed to the trapping of the electron in the gold σ -system, which leads to unsuitable orbital overlap for the BET process. Furthermore, the recombination reaction possesses a large driving force and thus the BET occurs in the Marcus inverted region. Interestingly, the role of the *meso*-aryl substituents regarding the PET/BET rate constants is negligible, but they should still play an important role with respect to solubility and fine-tuning of the redox potentials as well as Soret- and Q bands. The latter is of great importance, since it has been shown that at increasing conversion to gold(II) (during the photoinduced ET process in [Zn^{II}(P^H)-Au^{III}(P^H)]⁺ (**[1]**⁺)) the inner filter effect of the gold(II) product captures most of the incident light and thus significantly retards the reaction (unfavourable bathochromic shift of the Au^{II}(P) Soret band). Gratifyingly, it was possible to reductively quench the long-lived CSh state in a bimolecular reaction by using triethylamine as the sacrificial electron donor agent and yielded the neutral and stable zinc(II)-gold(II) species Zn(P)-Au^{II}(P). This enabled the very rare opportunity to illustrate the photoinduced electron transfer process by means of classical methods such as NMR spectroscopy, since the [Au^{III}(TPP)]⁺/Au^{II}(TPP) redox couple possesses unique paramagnetic NMR properties as shown in section 3.2. The formation of gold(II) was underscored by XANES spectra at the gold L₃-edge, EPR measurements at 77 K and quantum chemical calculations. Furthermore, this bimolecular reaction is fully reversible as shown with the reoxidation of the gold(II) species by dioxygen regenerating the starting material. Encouraged by the reversible nature of the PET reactions and due to the long lifetime of the CSh states it was possible to employ the dyads as photoredox catalysts for the reduction of aromatic azides

to anilines during a visible-light-induced photoredox catalysis experiment. This first test reaction provided 50 % spectroscopic yield without any reaction optimisation.

In summary, gold(III) porphyrins are excellently suited electron acceptors in multiporphyrin arrays. On one hand, they possess a low first reduction potential in comparison to other metalloporphyrins and on the other hand the lifetime of the final CSh states is long enough to be involved in bimolecular reactions. This will allow access to further studies of photoinduced gold-catalysed reactions with gold(II) species as key transient intermediates.

Merging the gold(III) porphyrin accepting properties with directional, amide bridged porphyrin chromophores and the highly suitable electron donating features of ferrocene derivatives one should be able to obtain a potent artificial photosynthetic reaction centre. Furthermore, it should be possible to extend the lifetime of the final CSh state by increasing the distance between electron acceptor and electron donor entities by means of additional porphyrin chromophore units, as illustrated in **Figure 4.1**.

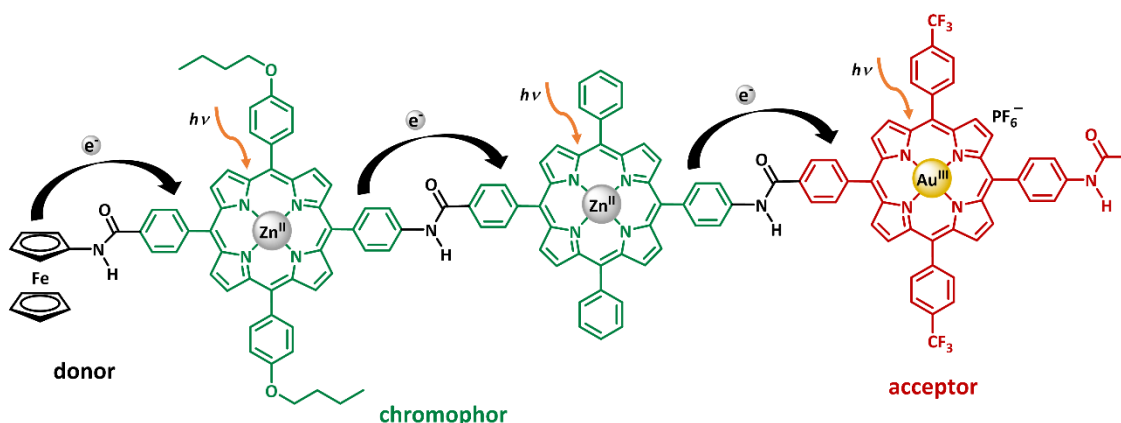


Figure 4.1 Structure of a proposed second generation artificial photosynthetic RC.

To increase the future applicabilities of zinc(II)-gold(III) bis(porphyrin) dyads with respect to organic photoredox catalysis, a larger potential difference between the first oxidation ($\text{Zn(P)}/\text{Zn(P}^{\bullet+})$) and the first reduction ($[\text{Au}^{\text{III}}(\text{P})]^+/\text{Au}^{\text{II}}(\text{P})$) of the system is desirable, leading to higher oxidative and reductive power, respectively. This should be achieved by means of amide-bridged *meso*- A_3B -type porphyrins, thus increasing the number of functional groups with major electron-donating and electron-withdrawing power, as shown in **Figure 4.2**. If compared to dyad $[\text{Zn}^{\text{II}}(\text{P}^{\text{CF}_3})-\text{Au}^{\text{III}}(\text{P}^{\text{O}^n\text{Bu}})]^+$ (**[3]**⁺, section 3.3) the functional group arrangement in **Figure 4.2** should be also beneficial regarding the aforementioned undesired inner filter effect of the gold(II) species, since the excitation wavelengths of Zn(P) and $\text{Au}^{\text{II}}(\text{P})$ should be separated during the course of photoinduced ET.

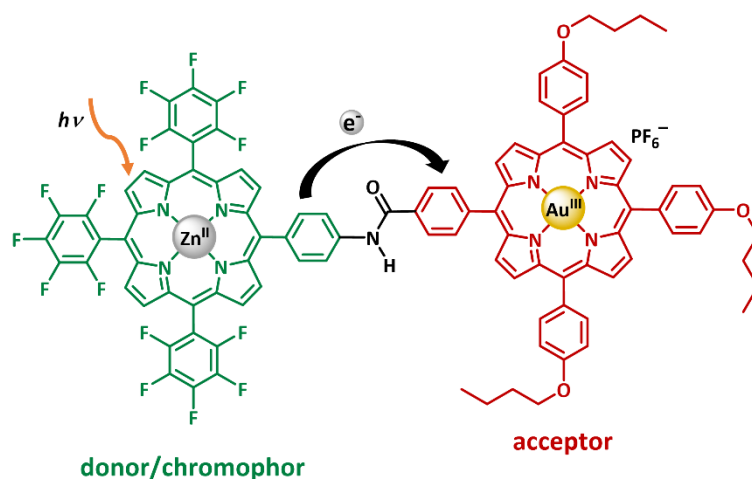


Figure 4.2 Structure of a proposed second generation artificial photosynthetic RC, designed for organic photoredox catalysis.

Another practical aim of artificial photosynthesis is to convert solar energy to chemical energy in the form of fuels, such as methanol or hydrogen. However, water oxidation, hydrogen production or reduction of carbon dioxide involves multi-electron catalysis at high reduction potentials (e. g. -1.90 V for $\text{CO}_2/\text{CO}_2^{\bullet-}$ vs. NHE).^[143] Therefore, it is necessary to couple the single-electron event of photoinduced ET with the multi-electron reactions of water splitting and fuel formation.^[144]

The gold(III) porphyrin acceptor unit is probably competent enough to achieve this goal, regarding two photons \rightarrow two electrons processes. The electrochemical investigations of the gold(III) porphyrin system revealed, that it should be capable to reversible accept two electrons, yielding the doubly reduced $[\text{Au}^{\text{I}}(\text{P}^{\bullet-})]^-$ species. This could be achieved by increasing the number of electron donor/chromophore units $\text{Zn}(\text{P})$, which are arranged in a dendritic manner around the gold(III) porphyrin $[(\text{Zn}(\text{P}))_4\text{-Au}(\text{P})][\text{PF}_6]$ to simulate the light-harvesting environment of natural photosynthesis (see **Figure 4.3**). A proposed energy level diagram describing the second photoinduced ET process of the dendritic artificial light-harvesting complex $[(\text{Zn}(\text{P}))_4\text{-Au}(\text{P})][\text{PF}_6]$ is illustrated in **Figure 4.4**. After photoexcitation of a $\text{Zn}(\text{P})$ unit, the $\text{Au}^{\text{III}}(\text{P})$ site could be reduced via oxidative quenching (k_{ET1}) to yield the doubly reduced $[\text{Au}^{\text{I}}(\text{P}^{\bullet-})]^-$ species, which may be exploited for the aforementioned multi-electron processes as a potent two-electron reducing agent. Certainly, it would be desirable that the k_{ET1} route is faster than the reductive quenching via k_{ET2} yielding a $\text{Zn}(\text{P}^{\bullet-})$ π -radical anion. However, since the latter should have a very large driving force ($\Delta G^{\circ}_{\text{ET2}} \approx -1.25$ eV) it is readily located in the Marcus-inverted region and thus rather slow. But even in the case of $\text{Zn}(\text{P}^{\bullet-})$ π -radical anion formation, $\text{Zn}(\text{P}^{\bullet-})$ could be utilised as a potent one-electron reducing agent during photoredox catalysis ($E_{1/2} \text{Zn}(\text{P})/\text{Zn}(\text{P}^{\bullet-}) = -1.77$ V).

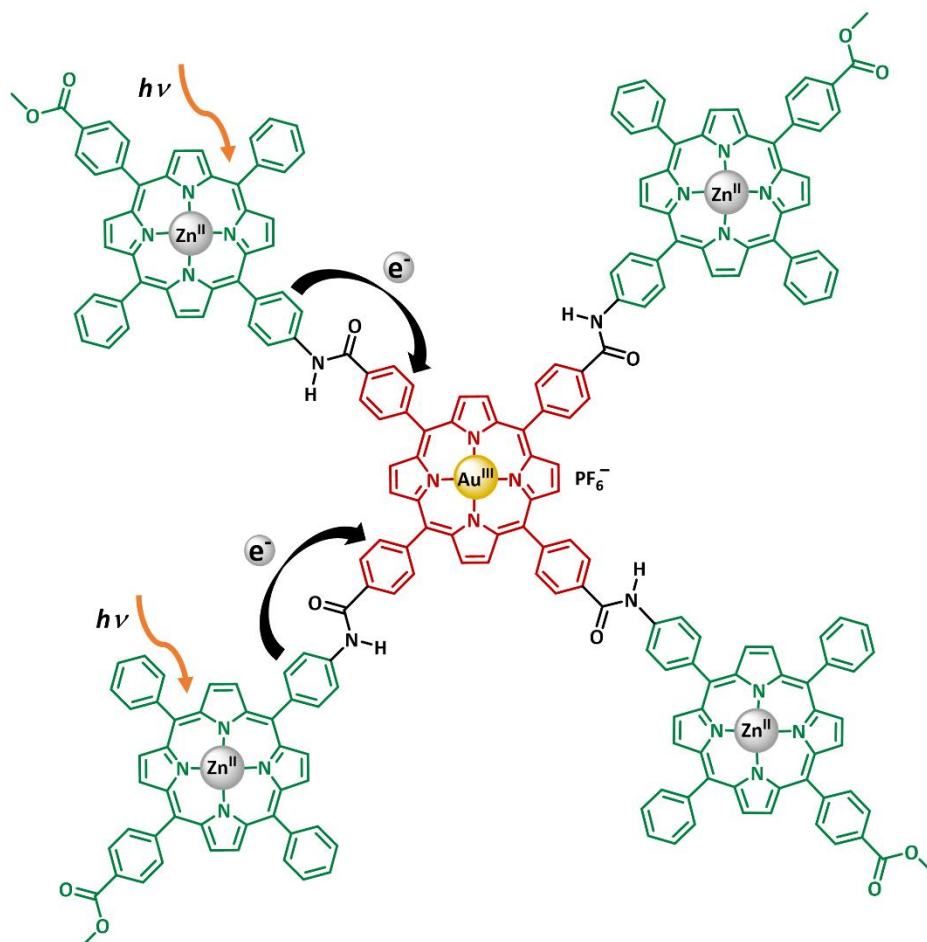


Figure 4.3 Proposed dendritic artificial light-harvesting system $[(\text{Zn}(\text{P}))_4\text{-Au}(\text{P})][\text{PF}_6]$.

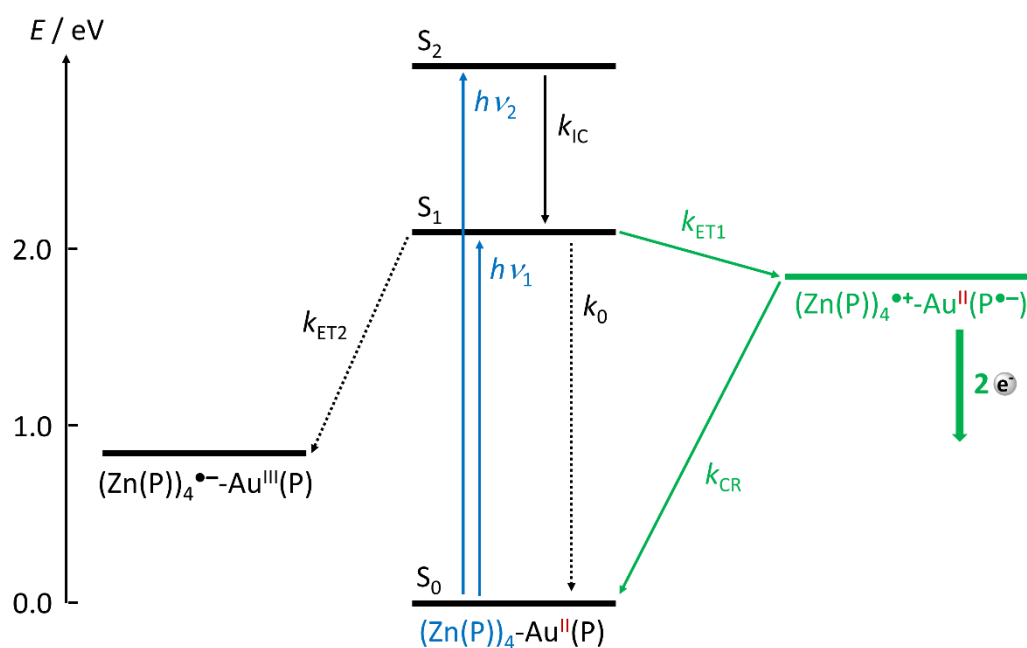


Figure 4.4 Proposed energy level diagram regarding the second photoinduced ET process of the dendritic artificial light-harvesting system $[(\text{Zn}(\text{P}))_4\text{-Au}(\text{P})][\text{PF}_6]$.

5 References

- [1] A. Trebst, M. Avron, *Photosynthesis I*; 118–119, Springer-Verlag Berlin, Heidelberg, **1977**.
- [2] W. Kaim, B. Schwederski, A. Klein, *Bioinorganic Chemistry: Inorganic Elements in the Chemistry of Life*; 57–75, John Wiley, Chichester, 2nd edition, **2013**.
- [3] A. N. Schechter, *Blood* **2008**, *122*, 3927–3938.
- [4] T. Suzuki, K. Imai, *Cell. Mol. Life. Sci.* **1998**, *54*, 979–1004.
- [5] R. Croce, H. von Amerongen, *Photosyn. Res.* **2013**, *116*, 153–166.
- [6] R. van Grondelle, J.P. Dekker, T. Gillbro, V. Sundstorm, *Biochim. Biophys. Acta* **1994**, *1187*, 1–65.
- [7] T. Cardona, A. Sedoud, N. Cox, A. W. Rutherford, *Biochim. Biophys. Acta* **2012**, *1817*, 26–43.
- [8] H. Michel, J. Deisenhofer, *Angew. Chem. Int. Ed.* **1989**, *28*, 829–847; *Angew. Chem.* **1989**, *101*, 872–892.
- [9] G. P. Moss, *Pure Appl. Chem.* **1987**, *59*, 779–832.
- [10] M. O. Senge, M. Davis, *J. Porph. Phthal.* **2010**, *14*, 557–567.
- [11] H. Fischer, W. Gleim, *Justus Liebigs Ann. Chem.* **1936**, *521*, 157–160.
- [12] E. Vogel, *Pure Appl. Chem.* **1993**, *65*, 143–152.
- [13] J. H. Fuhrhop, *Angew. Chem. Int. Ed.* **1974**, *13*, 321–335; *Angew. Chem.* **1974**, *86*, 363–377.
- [14] P. Schaeffer, R. Ocampo, H. J. Callot, P. Albrecht, *Nature* **1993**, *364*, 133–136.
- [15] A. Stone, E. B. Fleischer, *J. Am. Chem. Soc.* **1968**, *90*, 2735–2748.
- [16] L. Bonomo, M. L. Lehaire, E. Solari, R. Scopelliti, C. Floriani, *Angew. Chem. Int. Ed.* **2001**, *40*, 771–774; *Angew. Chem.* **2001**, *113*, 793–796.
- [17] W. Kaim, B. Schwederski, *Coord. Chem. Rev.* **2010**, *254*, 1580–1588.
- [18] D. Hamdane, H. Zhang, P. Hollenberg, *Photosynthesis research* **2008**, *98*, 657–666.
- [19] M. Gouterman, *J. Chem. Phys.* **1959**, *30*, 1139–1161.
- [20] M. Gouterman, *J. Mol. Spectrosc.* **1961**, *6*, 138–163.
- [21] M. Gouterman, G. H. Wagnière, *J. Mol. Spectrosc.* **1963**, *11*, 108–127.
- [22] L. D. Barron, *Molecular Light Scattering and Optical Activity*, Cambridge University Press, New York, **2004**.
- [23] P. J. Spellane, M. Gouterman, A. Antipas, S. Kim, Y. C. Liu, *Inorg. Chem.* **1980**, *19*, 386–391.
- [24] K. S. Suslick, R. A. Watson, *New. J. Chem.* **1992**, *16*, 633–642.
- [25] A. Antipas, J. W. Buchler, M. Gouterman, P. D. Smith, *J. Am. Chem. Soc.* **1978**, *100*, 3015–3024.
- [26] M. Y. R. Wang, B. M. Hoffman, *J. Am. Chem. Soc.* **1983**, *106*, 4235–4240.
- [27] A. Antipas, D. Dolphin, M. Gouterman, E. C. Johnson, *J. Am. Chem. Soc.* **1978**, *100*, 7705–7709.
- [28] M. O. Senge, *Chem. Commun.* **2011**, *47*, 1943–1960.
- [29] R. B. Woodward, *J. Am. Chem. Soc.* **1960**, *82*, 383–404.
- [30] B. C. Milgram, K. Eskildsen, S. M. Richter, W. R. Scheidt, K. A. Scheidt, *J. Org. Chem.* **2007**, *72*, 3941–3944.
- [31] P. Rothmund, *J. Am. Chem. Soc.* **1936**, 625–627.

-
- [32] J. P. Celli, B. Q. Spring, I. Rizvi, C. L. Evans, K. S. Samkoe, S. Verma, B. W. Pogue, T. Hasan, *Chem. Rev.* **2010**, *110*, 2795–2838.
- [33] D. Gust, T. A. Moore, A. L. Moore, *Acc. Chem. Res.* **2009**, *42*, 1890–1898.
- [34] J. Melomedov, J. R. Ochsmann, M. Meister, F. Laquai, K. Heinze, *Eur. J. Inorg. Chem.* **2014**, 1984–2001.
- [35] H. Imahori, Y. Sekiguchi, Y. Kashiwagi, T. Sato, Y. Araki, O. Ito, H. Yamada, S. Fukuzumi, *Chem. Eur. J.* **2004**, *10*, 3184–3196.
- [36] J. S. Lindsey, *Acc. Chem. Res.* **2010**, *43*, 300–311.
- [37] G. P. Arsenault, E. Bullock, S. F. MacDonald, *J. Am. Chem. Soc.* **1960**, *82*, 4384–4389.
- [38] J. Melomedov, A. Wünsche von Leupoldt, M. Meister, F. Laquai, K. Heinze, *Dalton Trans.* **2013**, *42*, 9727–9739.
- [39] K. Heinze, A. Reinhart, *Dalton Trans.* **2008**, 469–480.
- [40] H. Schmidbauer, *Gold Bull* **2000**, *33*, 3–10.
- [41] K. Heinze, *Angew. Chem. Int. Ed.* **2017**, *56*, 16126–16134; *Angew. Chem.* **2017**, *129*, 16342–16350.
- [42] L. F. Pašteka, E. Eliav, A. Borschevsky, U. Kaldor, P. Schwerdtfeger, *Phys. Rev. Lett.* **2017**, *118*, 023002-1–5.
- [43] P. Pyykkö, *Angew. Chem. Int. Ed.* **2004**, *43*, 4412–4456; *Angew. Chem.* **2004**, *116*, 4512–4557.
- [44] H. Schmidbauer, S. Cronje, B. Djordjevic, O. Schuster, *Chem. Phys.* **2005**, *311*, 151–161.
- [45] V. W.-W. Yam, E. C.-C. Cheng, *Chem. Soc. Rev.* **2008**, *37*, 1806–1813.
- [46] M.-C. Gimeno, *Modern Supramolecular Gold Chemistry: Gold-Metal Interactions and Applications*; 1–63, Wiley-VCH, Heidelberg, **2008**.
- [47] H. Schmidbauer, W. Graf, G. Müller, *Angew. Chem. Int. Ed.* **1988**, *27*, 417–419; *Angew. Chem.* **1988**, *100*, 437–439.
- [48] H. Schmidbauer, A. Schier, *Chem. Soc. Rev.* **2012**, *41*, 370–412.
- [49] D. A. Fennell, Y. Summers, J. Cadranel, T. Benepal, D. C. Christoph, R. Lal, M. Das, F. Maxwell, C. Visseren-Grul, D. Ferry, *Cancer Treat. Rev.* **2016**, *44*, 42–50.
- [50] R. W.-Y. Sun, C.-M. Che, *Coord. Chem. Rev.* **2009**, *253*, 1682–1691.
- [51] T. Zou, C. T. Lum, C.-N. Lok, J.-J. Zhang, C.-M. Che, *Chem. Soc. Rev.* **2015**, *44*, 8786–8801.
- [52] S. P. Fricker, *Gold Bull* **1996**, *29*, 53–60.
- [53] D. B. Dell'Amico, F. Calderazzo, F. Marchetti, S. Merlino, *J. Chem. Dalton Trans.* **1982**, 2257–2260.
- [54] J. Strähle, J. Gelinek, M. Kölmel, *Z. Anorg. Allg. Chem.* **1979**, *456*, 241–260.
- [55] D.-A. Roşca, D. A. Smith, D. L. Hughes, M. Bochmann, *Angew. Chem. Int. Ed.* **2012**, *51*, 10643–10646; *Angew. Chem.* **2012**, *124*, 10795–10798.
- [56] T. Dann, D.-A. Roşca, J. A. Wright, G. G. Wildgoose, M. Bochmann, *Chem. Commun.* **2013**, *49*, 10169–10171.
- [57] D.-A. Roşca, M. Bochmann, *Organometallics* **2016**, *35*, 27–31.
- [58] L. Huang, M. Rudolph, F. Rominger, A. S. K. Hashmi, *Angew. Chem. Int. Ed.* **2016**, *55*, 4808–4813; *Angew. Chem.* **2016**, *128*, 4888–4893.
- [59] M. N. Hopkinson, A. Tlahuext-Aca, F. Glorius, *Acc. Chem. Res.* **2016**, *49*, 2261–2272.
- [60] B. Sahoo, M. N. Hopkinson, F. Glorius, *J. Am. Chem. Soc.* **2013**, *135*, 5505–5508.
- [61] X.-Z. Shu, M. Zhang, Y. He, H. Frei, F. D. Toste, *J. Am. Chem. Soc.* **2014**, *136*, 5844–5847.

- [62] A. Tlahuext-Aca, M. N. Hopkinson, B. Sahoo, F. Glorius, *Chem. Sci.* **2016**, *7*, 89–93.
- [63] M. S. Winston, W. J. Wolf, F. D. Toste, *J. Am. Chem. Soc.* **2014**, *136*, 7777–7782.
- [64] E. Göransson, J. Boixel, J. Fortage, D. Jacquemin, H.-C. Becker, E. Blart, L. Hammarström, F. Odobel, *Inorg. Chem.* **2012**, *51*, 11500–11512.
- [65] S. Fukuzumi, K. Ohkubo, E. Wenbo, Z. Ou, J. Shao, K. M. Kadish, J. A. Hutchison, K. P. Ghigino, P. J. Santic, M. J. Crossley, *J. Am. Chem. Soc.* **2003**, *125*, 14984–14985.
- [66] S. Kim, J. Rojas-Martin, F. D. Toste, *Chem. Sci.* **2016**, *7*, 85–88.
- [67] M. D. Levin, F. D. Toste, *Angew. Chem. Int. Ed.* **2014**, *53*, 6211–6215; *Angew. Chem.* **2014**, *126*, 6325–6329.
- [68] C.-Y. Wu, T. Horibe, C. B. Jacobsen, F. D. Toste, *Nature* **2015**, *517*, 449–454.
- [69] R. Casado, M. Contel, M. Laguna, P. Romero, S. Sanz, *J. Am. Chem. Soc.* **2003**, *125*, 11925–11935.
- [70] T. Drews, S. Seidel, K. Seppelt, *Angew. Chem. Int. Ed.* **2002**, *41*, 454–456; *Angew. Chem.* **2002**, *114*, 470–473.
- [71] S. Seidel, K. Seppelt, *Science* **2000**, *290*, 117–118.
- [72] K. Seppelt, *Z. Anorg. Allg. Chem.* **2003**, *629*, 2427–2430.
- [73] S. H. Elder, G. M. Lucier, F. J. Hollander, N. Bartlett, *J. Am. Chem. Soc.* **1997**, *119*, 1020–1026.
- [74] I.-C. Hwang, K. Seppelt, *Z. Anorg. Allg. Chem.* **2002**, *628*, 765–769.
- [75] R. Schmidt, B. G. Müller, *Z. Anorg. Allg. Chem.* **1999**, *625*, 605–608.
- [76] A. J. Blake, J. A. Greig, A. J. Holder, T. I. Hyde, A. Taylor, M. Schröder, *Angew. Chem. Int. Ed.* **1990**, *29*, 197–198; *Angew. Chem.* **1990**, *102*, 203–204.
- [77] M. A. Halcrow, *Chem. Soc. Rev.* **2013**, *42*, 1784–1795.
- [78] J. L. Shaw, J. Wolowska, D. Collison, J. A. K. Howard, E. J. L. McInnes, J. McMaster, A. J. Blake, C. Wilson, M. Schröder, *J. Am. Chem. Soc.* **2006**, *128*, 13827–13839.
- [79] D. Huang, X. Zhang, E. J. L. McInnes, J. McMaster, A. J. Blake, E. S. Davies, J. Wolowska, C. Wilson, M. Schröder, *Inorg. Chem.* **2008**, *47*, 9919–9929.
- [80] M. Baya, A. Pérez-Bitrián, S. Martínez-Salvador, A. Martín, J. M. Casas, B. Menjón, J. Orduna, *Chem. Eur. J.* **2018**, *24*, 1514–1517.
- [81] Z. Qu, L. Giurgiu, E. Roduner, *Chem. Commun.* **2006**, 2507–2509.
- [82] A. MacCragh, W. S. Koski, *J. Am. Chem. Soc.* **1965**, *87*, 2496–2497.
- [83] E. W. Y. Wong, A. Miura, M. D. Wright, Q. He, C. J. Walsby, S. Shimizu, N. Kobayashi, D. B. Leznoff, *Chem. Eur. J.* **2012**, *18*, 12404–12410.
- [84] D. Carrascal, L. Fernández-Seivane, J. Ferrer, *Phys. Rev. B* **2009**, *80*, 1–5.
- [85] W. Sinha, M. G. Sommer, M. van der Meer, S. Plebst, B. Sarkar, S. Kar, *Dalton Trans.* **2016**, *45*, 2914–2923.
- [86] W. Sinha, M. G. Sommer, N. Deibel, F. Ehret, B. Sarkar, S. Kar, *Chem. Eur. J.* **2014**, *20*, 15920–15932.
- [87] W. Sinha, M. G. Sommer, N. Deibel, F. Ehret, M. Bauer, B. Sarkar, S. Kar, *Angew. Chem. Int. Ed.* **2015**, *54*, 13769–13774; *Angew. Chem.* **2015**, *127*, 13973–13978.
- [88] R. A. Marcus, *Angew. Chem. Int. Ed. Engl.* **1993**, *32*, 1111–1121; *Angew. Chem.* **1993**, *105*, 1161–1180.
- [89] C. C. Moser, J. M. Keske, K. Warncke, R. S. Farid, P. L. Dutton, *Nature* **1992**, *355*, 796–802.
- [90] R. A. Marcus, *J. Chem. Phys.* **1956**, *24*, 966–978.

-
- [91] R. A. Marcus, *Annu. Rev. Phys. Chem.* **1964**, *15*, 155–196.
- [92] T. J. Meyer, *Acc. Chem. Res.* **1978**, *11*, 94–100.
- [93] N. S. Hush, *Coord. Chem. Rev.* **1985**, *64*, 135–157.
- [94] B. S. Brunschwig, N. Sutin, *Coord. Chem. Rev.* **1999**, *187*, 233–254.
- [95] M. B. Robin, P. Day, *Adv. Inorg. Chem. Radiochem.* **1967**, *10*, 247–422.
- [96] C. Creutz, H. Taube, *J. Am. Chem. Soc.* **1969**, *91*, 3988–3989.
- [97] C. Creutz, H. Taube, *J. Am. Chem. Soc.* **1973**, *95*, 1086–1094.
- [98] B. S. Brunschwig, C. Creutz, N. Sutin, *N. Chem. Soc. Rev.* **2002**, *31*, 168–184.
- [99] R. Huber, *Angew. Chem. Int. Ed.* **1989**, *28*, 848–869; *Angew. Chem.* **1989**, *101*, 849–871.
- [100] D. Gerster, J. Reichert, H. Bi, J. V. Barth, S. M. Kaniber, A. W. Holleitner, I. Visoly-Fisher, S. Sergani, I. Carmeli, *Nat. Nanotechnol.* **2012**, *7*, 673–676.
- [101] T. Förster, *Naturwissenschaften* **1946**, *33*, 166–175.
- [102] T. Förster, *Ann. Phys.* **1948**, *2*, 55–75.
- [103] R. E. Blankenship, R. C. Prince, *Trends Biochem. Sci.* **1985**, *10*, 382–383.
- [104] Y. Umena, K. Kawakami, J.-R. Shen, N. Kamiya, *Nature* **2011**, *473*, 55–60.
- [105] S. Fukuzumi, K. Ohkubo, T. Suenobu, *Acc. Chem. Res.* **2014**, *47*, 1455–1464.
- [106] B. Albinsson, J. Mårtensson, *J. Photochem. Photobiol. C* **2008**, *9*, 138–155.
- [107] W. B. Davis, W. A. Svec, M. A. Ratner, M. R. Wasielewski, *Nature* **1998**, *396*, 60–63.
- [108] M. U. Winters, E. Dahlstedt, H. E. Blades, C. J. Wilson, M. J. Frampton, H. L. Anderson, B. Albinsson, *J. Am. Chem. Soc.* **2007**, *129*, 4291–4297.
- [109] H. M. McConnell, *J. Chem. Phys.* **1961**, *35*, 508–515.
- [110] P. Siddarth, R. A. Marcus, *J. Phys. Chem.* **1990**, *94*, 2985–2989.
- [111] D. Gust, T. A. Moore, A. L. Moore, A. N. Macpherson, A. Lopez, J. M. DeGraziano, I. Gouni, E. Bittersmann, G. R. Seely, F. Gao, R. A. Nieman, X. C. Ma, L. J. Demanche, S.-C. Hung, D. K. Luttrull, S.-J. Lee, P. K. Kerrigan, *J. Am. Chem. Soc.* **1993**, *115*, 11141–11152.
- [112] D. Gust, T. A. Moore, A. L. Moore, L. Leggett, S. Lin, J. M. DeGraziano, R. M. Hermant, D. Nicodem, P. Craig, G. R. Seely, R. A. Nieman, *J. Phys. Chem.* **1993**, *97*, 7926–7931.
- [113] S. K. Das, B. Song, A. Mahler, V. N. Nesterov, A. K. Wilson, O. Ito, F. D’Souza, *J. Phys. Chem. C* **2014**, *118*, 3994–4006.
- [114] S. Fukuzumi, K. Okamoto, H. Imahori, *Angew. Chem. Int. Ed.* **2002**, *41*, 620–622; *Angew. Chem.* **2002**, *114*, 642–644.
- [115] S. Fukuzumi, K. Okamoto, Y. Yoshida, H. Imahori, Y. Araki, O. Ito, *J. Am. Chem. Soc.* **2003**, *125*, 1007–1013.
- [116] S. L. Gould, G. Kodis, R. E. Palacios, L. de La Garza, A. Brune, D. Gust, T. A. Moore, A. L. Moore, *J. Phys. Chem. B* **2004**, *108*, 10566–10580.
- [117] H. Imahori, D. M. Guldi, K. Tamaki, Y. Yoshida, C. Luo, Y. Sakata, S. Fukuzumi, *J. Am. Chem. Soc.* **2001**, *123*, 6617–6628.
- [118] H. Imahori, Y. Sekiguchi, Y. Kashiwagi, T. Sato, Y. Araki, O. Ito, H. Yamada, S. Fukuzumi, *Chem. Eur. J.* **2004**, *10*, 3184–3196.
- [119] H. Imahori, K. Tamaki, Y. Araki, Y. Sekiguchi, O. Ito, Y. Sakata, S. Fukuzumi, *J. Am. Chem. Soc.* **2002**, *124*, 5165–5174.
- [120] J. Melomedov, J. R. Ochsmann, M. Meister, F. Laquai, K. Heinze, *Eur. J. Inorg. Chem.* **2014**, 2902–2915.

- [121] T. H. Ngo, D. Zieba, W. A. Webre, G. N. Lim, P. A. Karr, S. Kord, S. Jin, K. Ariga, M. Galli, S. Goldup, J. P. Hill, F. D'Souza, *Chem. Eur. J.* **2016**, *22*, 1301–1312.
- [122] C. A. Wijesinghe, M. E. El-Khouly, M. E. Zandler, S. Fukuzumi, F. D'Souza, *Chem. Eur. J.* **2013**, *19*, 9629–9638.
- [123] M. Lauck, C. Förster, D. Gehrig, K. Heinze, *J. of Organomet. Chem.* **2017**, *847*, 33–40.
- [124] M. Natali, S. Campagna, F. Scandola, *Chem. Soc. Rev.* **2014**, *43*, 4005–4018.
- [125] J. Melomedov, J. R. Ochsmann, M. Meister, F. Laquai, K. Heinze, *Eur. J. Inorg. Chem.* **2014**, 1984–2001.
- [126] S. Fukuzumi, Y. Endo, H. Imahori, *J. Am. Chem. Soc.* **2002**, *124*, 10974–10975.
- [127] S. Preiß, J. Melomedov, A. Wünsche von Leupoldt, K. Heinze, *Chem. Sci.* **2016**, *7*, 596–610.
- [128] C.-W. Huang, K. Y. Chiu, S.-H. Cheng, *Dalton Trans.* **2005**, 2417–2422.
- [129] A. Harriman, F. Odobel, and J.-P. Sauvage, *J. Am. Chem. Soc.* **1995**, *117*, 9461–9472.
- [130] A. M. Brun, A. Harriman, V. Heitz, J. P. Sauvage, *J. Am. Chem. Soc.* **1991**, *113*, 8657–8663.
- [131] D. B. Amabilino, J.-P. Sauvage, *New. J. Chem.* **1998**, *22*, 395–409.
- [132] I. M. Dixon, J.-P. Collin, J.-P. Sauvage, F. Barigelletti, L. Flamigni, *Angew. Chem.* **2000**, *112*, 1348–1351; *Angew. Chem. Int. Ed.* **2000**, *39*, 1292–1295.
- [133] V. Heitz, S. Chardon-Noblat, J.-P. Sauvage, *Tetrahedron Lett.* **1991**, *32*, 197–198.
- [134] M. E. El-Khouly, S. Fukuzumi, *Photochem. Photobiol.* **2016**, *15*, 1340–1346.
- [135] K. M. Kadish, W. E. Z. Ou, J. Shao, P. J. Sentic, K. Ohkubo, S. Fukuzumi, M. J. Crossley, *Chem. Commun.* **2002**, 356–357.
- [136] K. Ohkubo, R. Garcia, P. J. Sentic, T. Khoury, M. J. Crossley, K. M. Kadish, S. Fukuzumi, *Chem. Eur. J.* **2009**, *15*, 10493–10503.
- [137] K. Ohkubo, P. J. Sentic, N. V. Tkachenko, H. Lemmetyinen, E. Wenbo, Z. Ou, J. Shao, K. M. Kadish, M. J. Crossley, S. Fukuzumi, *Chem. Phys.* **2006**, *326*, 3–14.
- [138] E. K. L. Yeow, P. J. Sentic, N. M. Cabral, J. N. H. Reek, M. J. Crossley, K. P. Ghiggino, *Phys. Chem. Chem. Phys.* **2000**, *2*, 4281–4291.
- [139] Z. Ou, K. M. Kadish, W. E. J. Shao, P. J. Sentic, K. Ohkubo, S. Fukuzumi, M. J. Crossley, *Inorg. Chem.* **2004**, *43*, 2078–2086.
- [140] J. Fortage, J. Boixel, E. Blart, H. C. Becker, F. Odobel, *Inorg. Chem.* **2009**, *48*, 518–526.
- [141] J. Fortage, J. Boixel, E. Blart, L. Hammarström, H. C. Becker, F. Odobel, *Chem. Eur. J.* **2008**, *14*, 3467–3480.
- [142] J. Fortage, A. Scarpaci, L. Viau, Y. Pellegrin, E. Blart, M. Falkenström, L. Hammarström, I. Asselberghs, R. Kellens, W. Libaers, K. Clays, M. P. Eng, F. Odobel, *Chem. Eur. J.* **2009**, *15*, 9058–9067.
- [143] B. M. Szyja, *ChemElectroChem* **2018**, *5*, 2105–2112.
- [144] S. Karlsson, J. Boixel, Y. Pellegrin, E. Blart, H.-C. Becker, F. Odobel, L. Hammarström, *Faraday Discuss.* **2012**, *155*, 233–252.

6 Appendix

6.1 Supporting Information to 3.1: Gold(III) tetraarylporphyrin amino acid derivatives: ligand or metal centred redox chemistry?

Fig. S01 ^1H NMR spectrum of $[\text{Au}(\text{TPP})](\text{PF}_6)$ in CD_2Cl_2 .

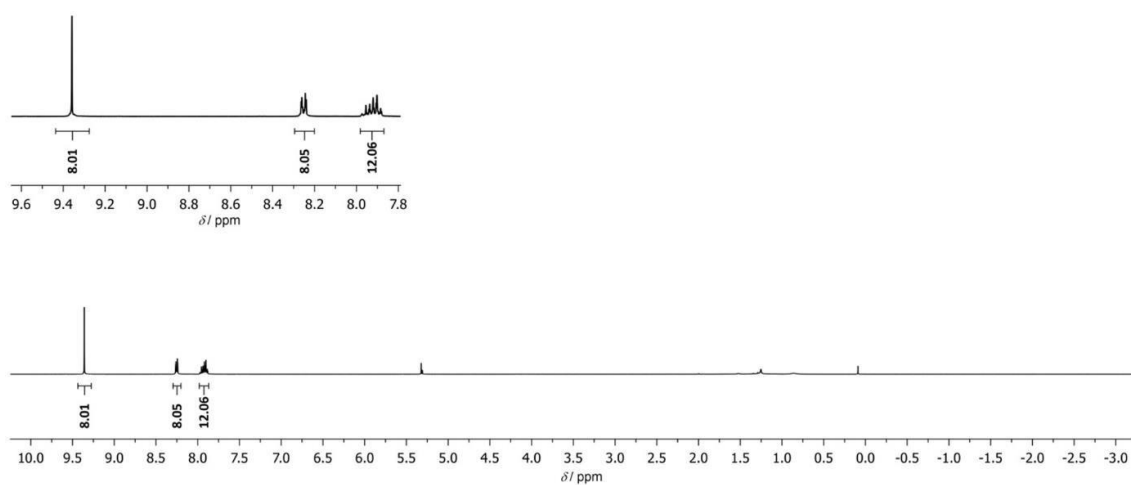


Fig. S02 ^{13}C NMR spectrum of $[\text{Au}(\text{TPP})](\text{PF}_6)$ in CD_2Cl_2 .

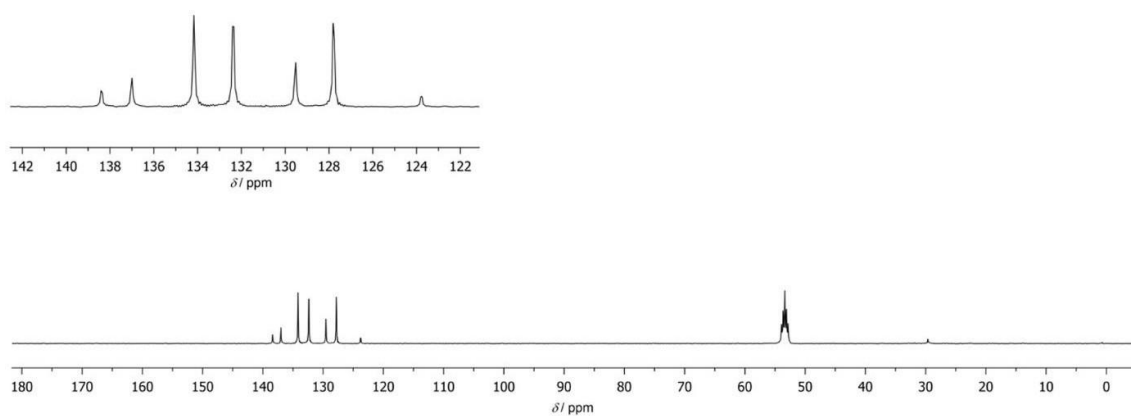


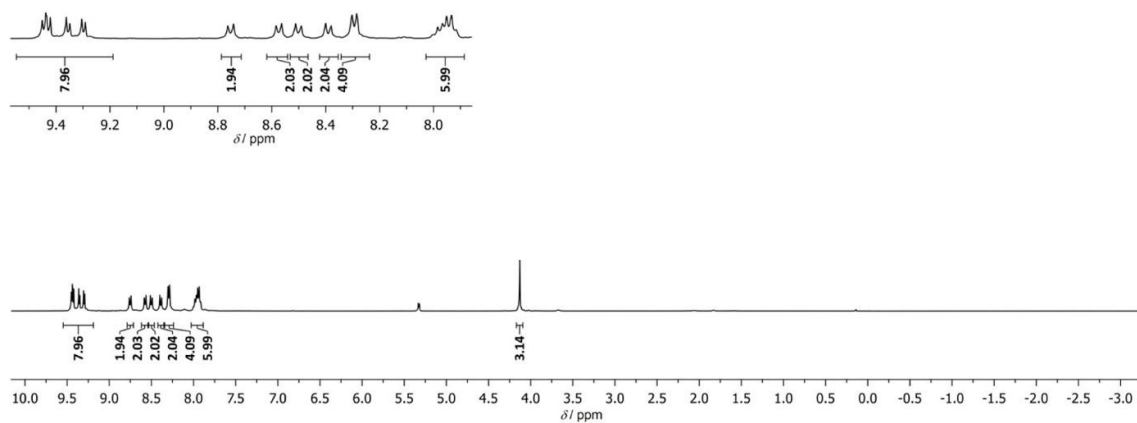
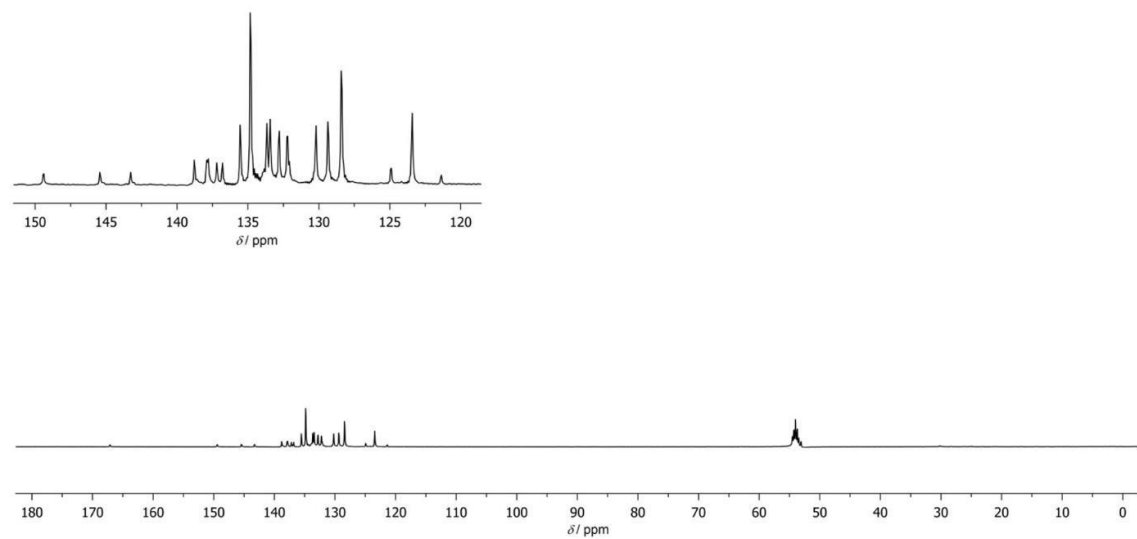
Fig. S03 ^1H NMR spectrum of **[1a](PF₆)** in CD_2Cl_2 .**Fig. S04** ^{13}C NMR spectrum of **[1a](PF₆)** in CD_2Cl_2 .

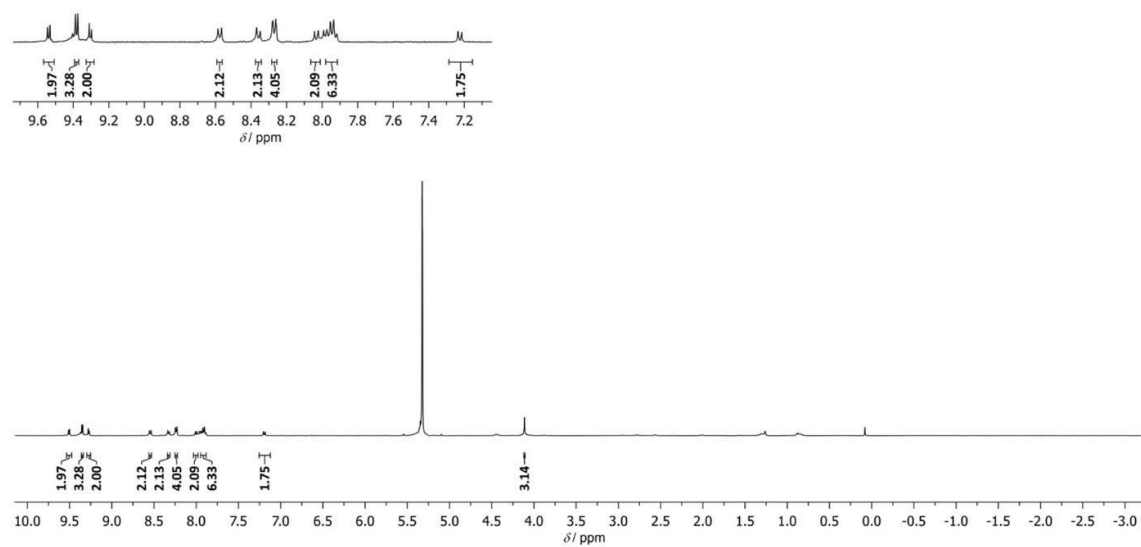
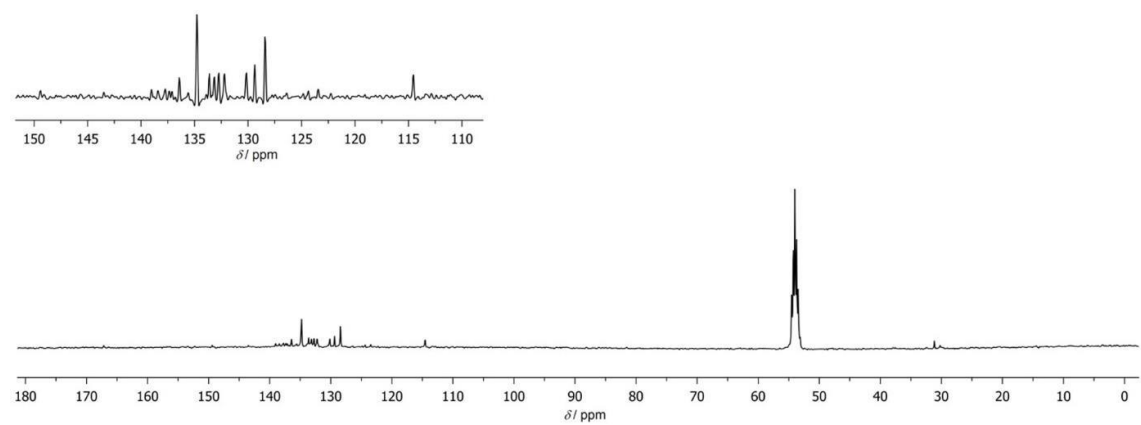
Fig. S05 ^1H NMR spectrum of **[2a](PF₆)** in CD_2Cl_2 .**Fig. S06** ^{13}C NMR spectrum of **[2a](PF₆)** in CD_2Cl_2 .

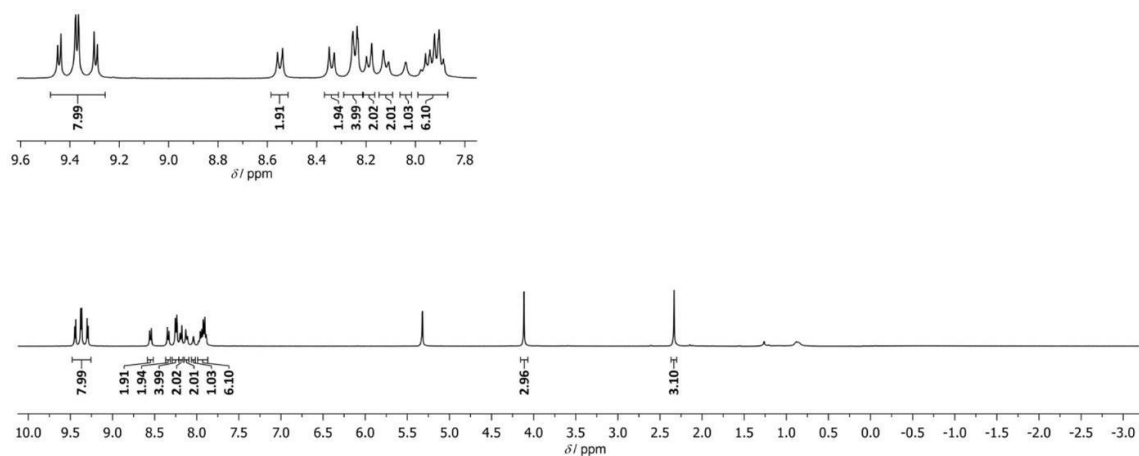
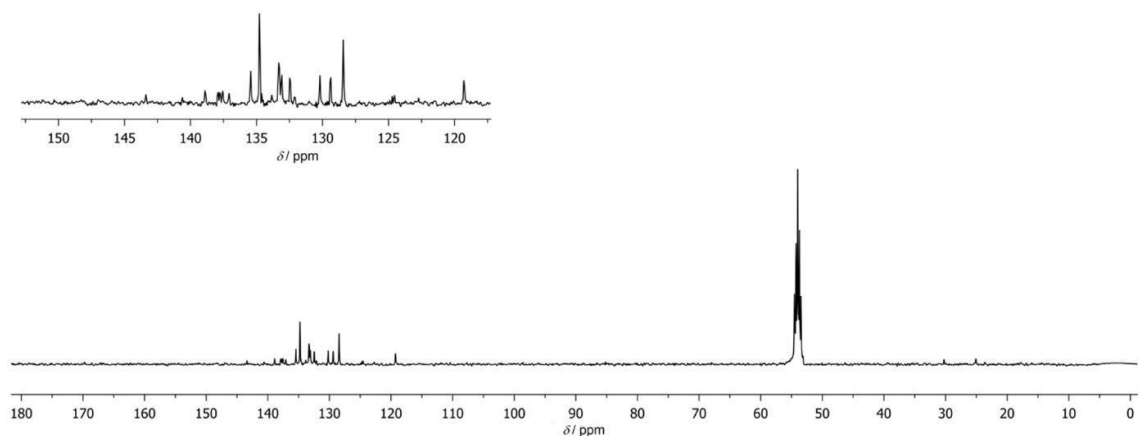
Fig. S07 ^1H NMR spectrum of **[3a](PF₆)** in CD_2Cl_2 .**Fig. S08** ^{13}C NMR spectrum of **[3a](PF₆)** in CD_2Cl_2 .

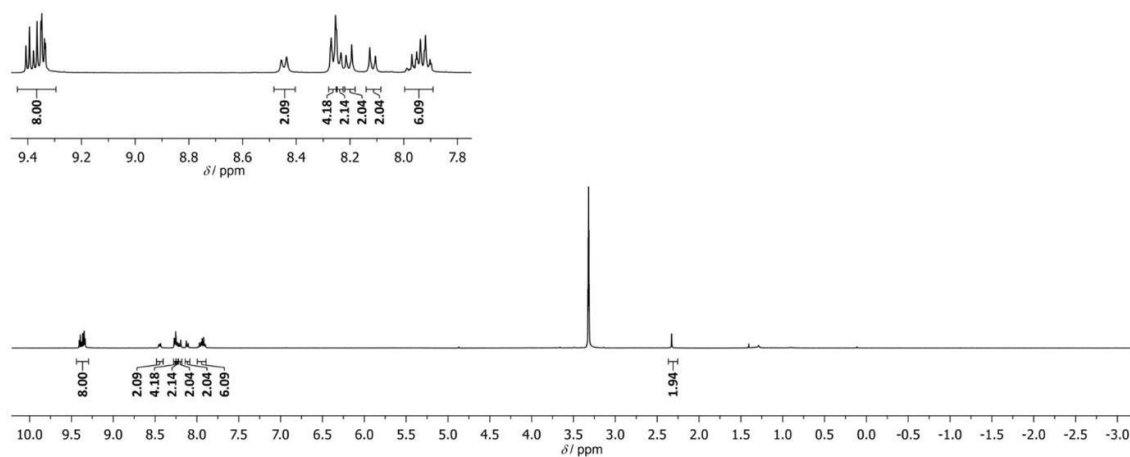
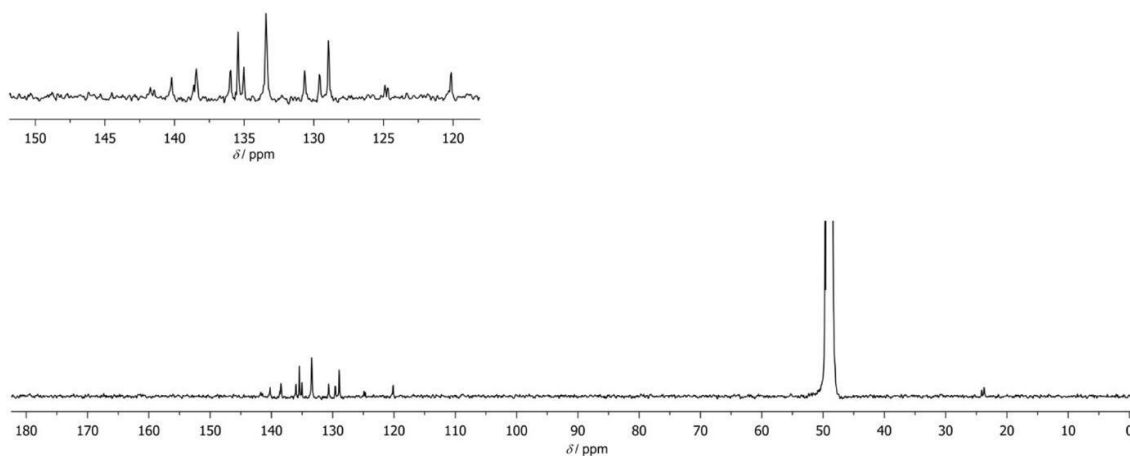
Fig. S09 ^1H NMR spectrum of **[4a](PF₆)** in CD₃OD.**Fig. S10** ^{13}C NMR spectrum of **[4a](PF₆)** in CD₃OD.

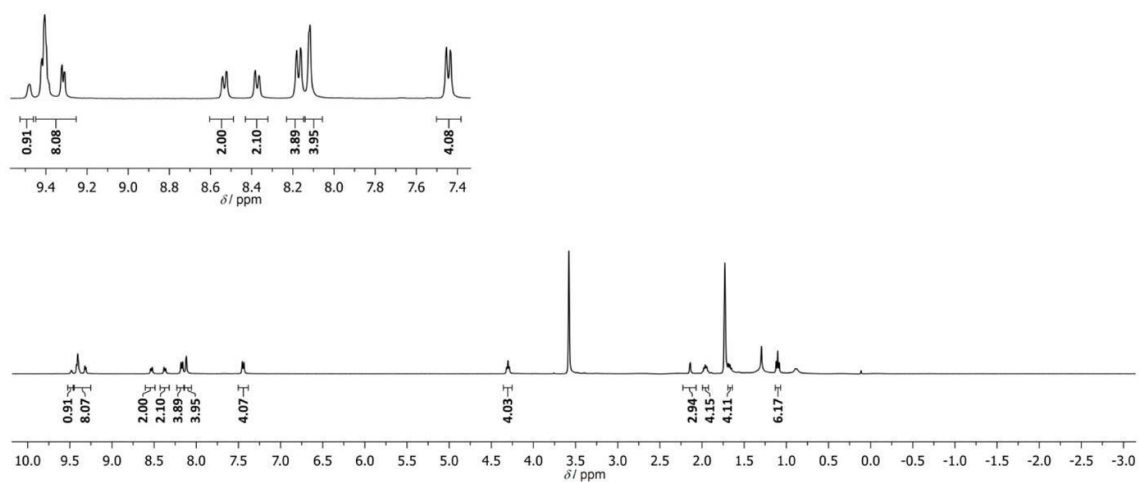
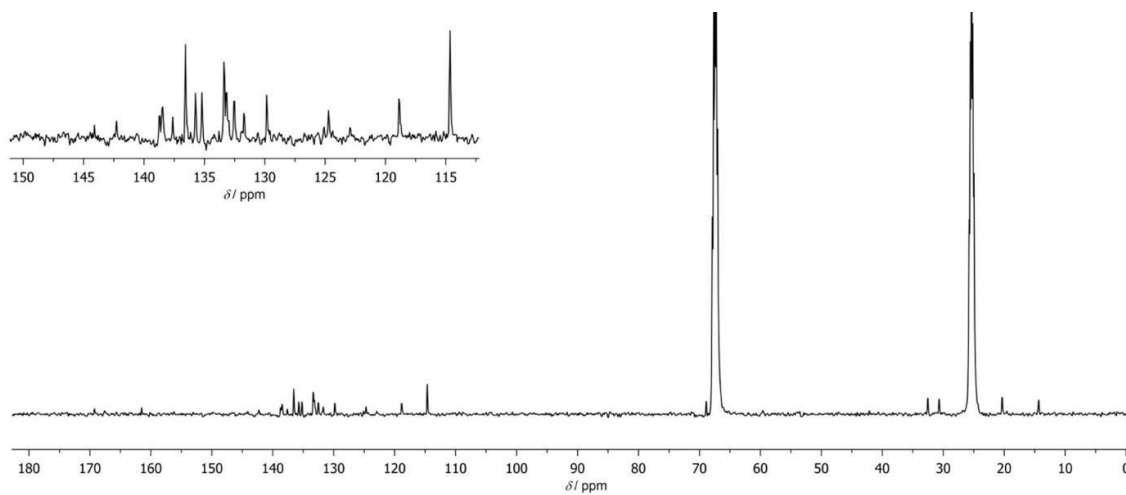
Fig. S11 ^1H NMR spectrum of **[4b](PF₆)** in d_8 -THF.**Fig. S12** ^{13}C NMR spectrum of **[4b](PF₆)** in d_8 -THF.

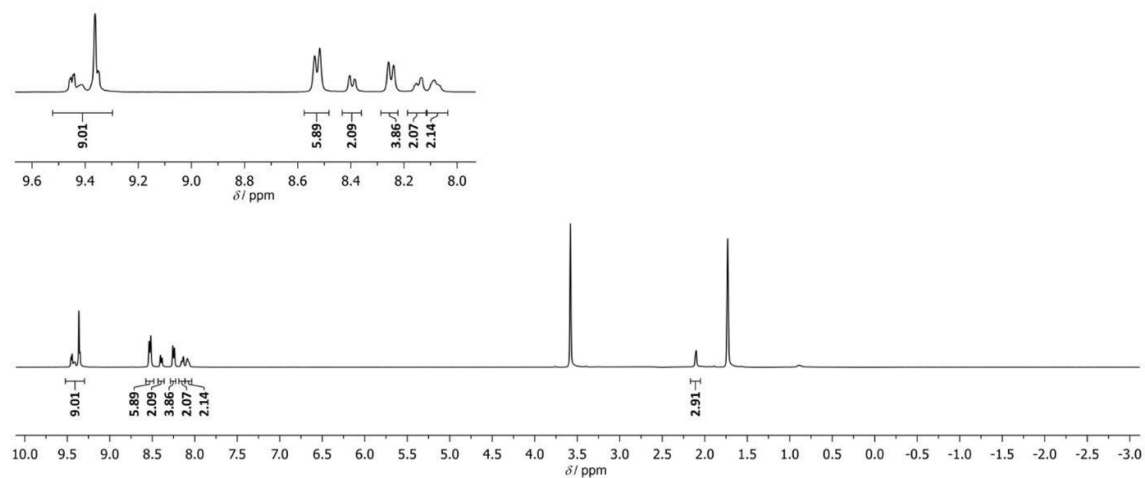
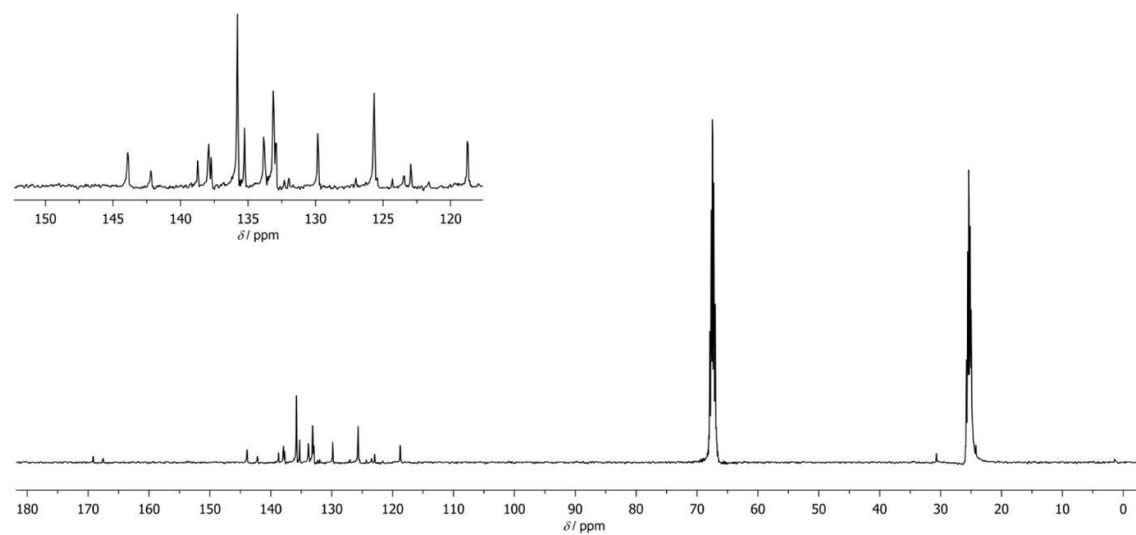
Fig. S13 ^1H NMR spectrum of **[4c](PF₆)** in d_8 -THF.**Fig. S14** ^{13}C NMR spectrum of **[4c](PF₆)** in d_8 -THF.

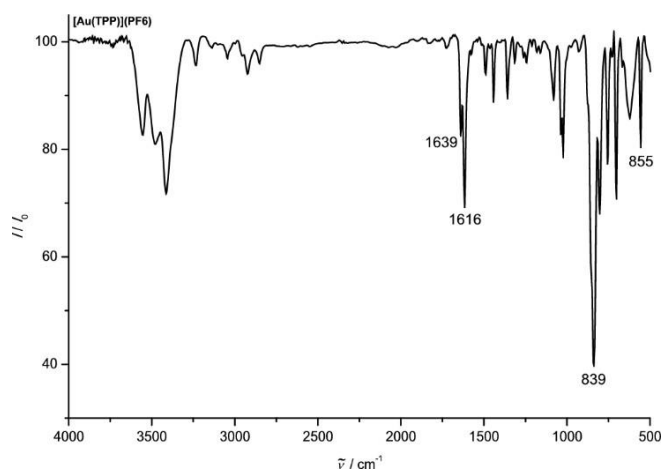
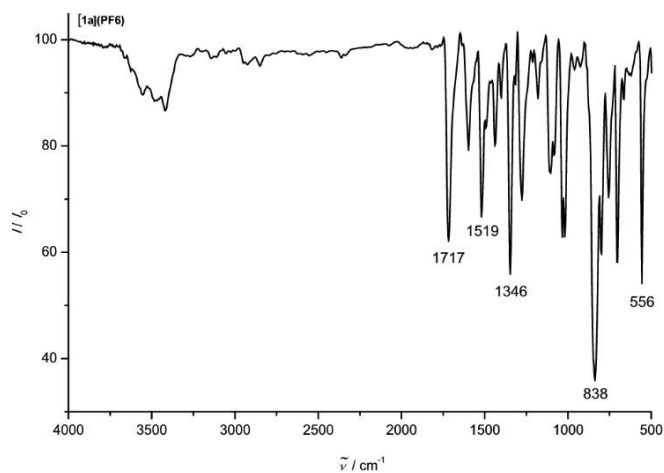
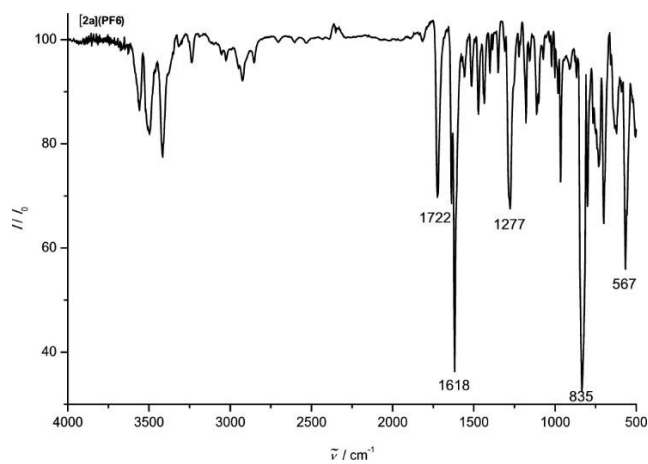
Fig. S15 IR spectrum of [Au(TPP)](PF₆) as KBr disk.**Fig. S16** IR spectrum of [1a](PF₆) as KBr disk.**Fig. S17** IR spectrum of [2a](PF₆) as KBr disk.

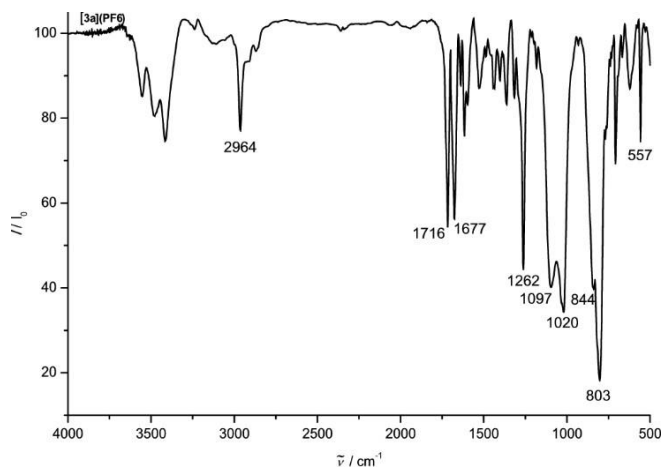
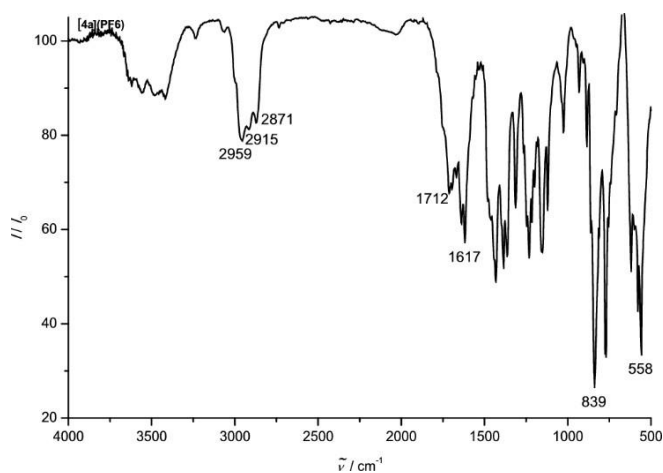
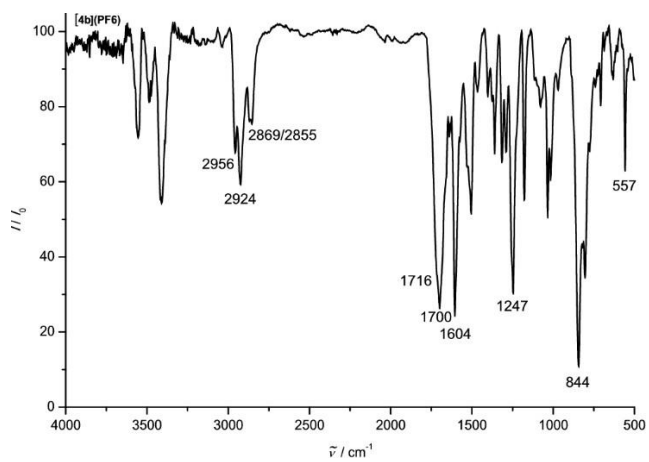
Fig. S18 IR spectrum of **[3a](PF₆)** as KBr disk.**Fig. S19** IR spectrum of **[4a](PF₆)** as KBr disk.**Fig. S20** IR spectrum of **[4b](PF₆)** as KBr disk.

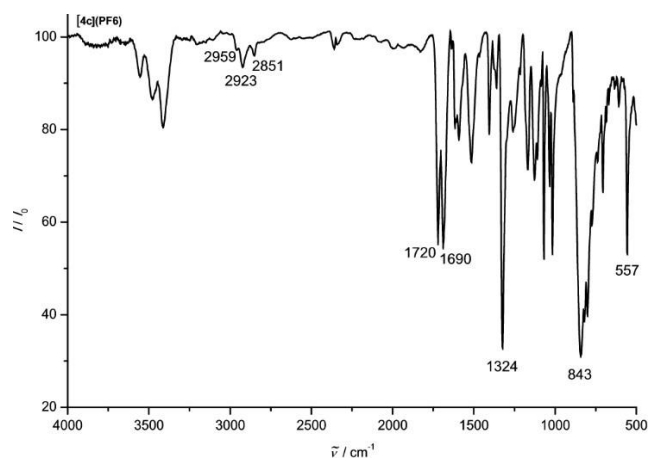
Fig. S21 IR spectrum of **[4c](PF₆)** as KBr disk.

Fig. S22 UV/Vis spectral changes upon the first electroreduction of $[\text{Au}(\text{TPP})]^+$ 10^{-5} M in 0.1 M $[\text{nBu}_4\text{N}](\text{PF}_6)/\text{THF}$ solution (isosbestic points indicated in blue).

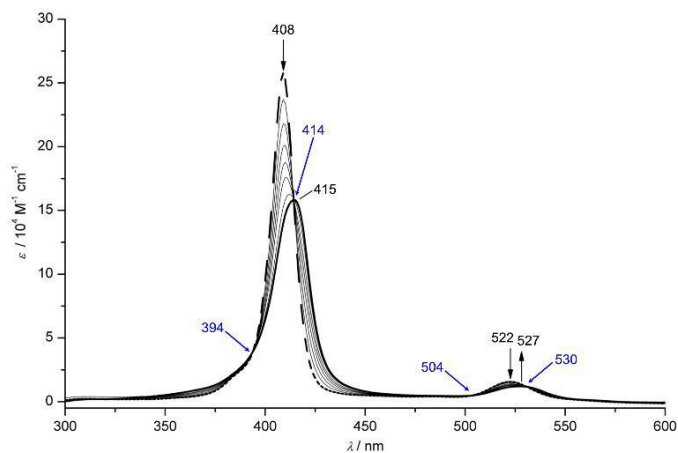


Fig. S23 UV/Vis spectral changes upon the first electroreduction of a) $[\mathbf{4a}]^+$ (in MeOH), b) $[\mathbf{4b}]^+$ and c) $[\mathbf{4c}]^+$ 10^{-5} M in 0.1 M $[\text{nBu}_4\text{N}](\text{PF}_6)/\text{THF}$ solution (isosbestic points indicated in blue).

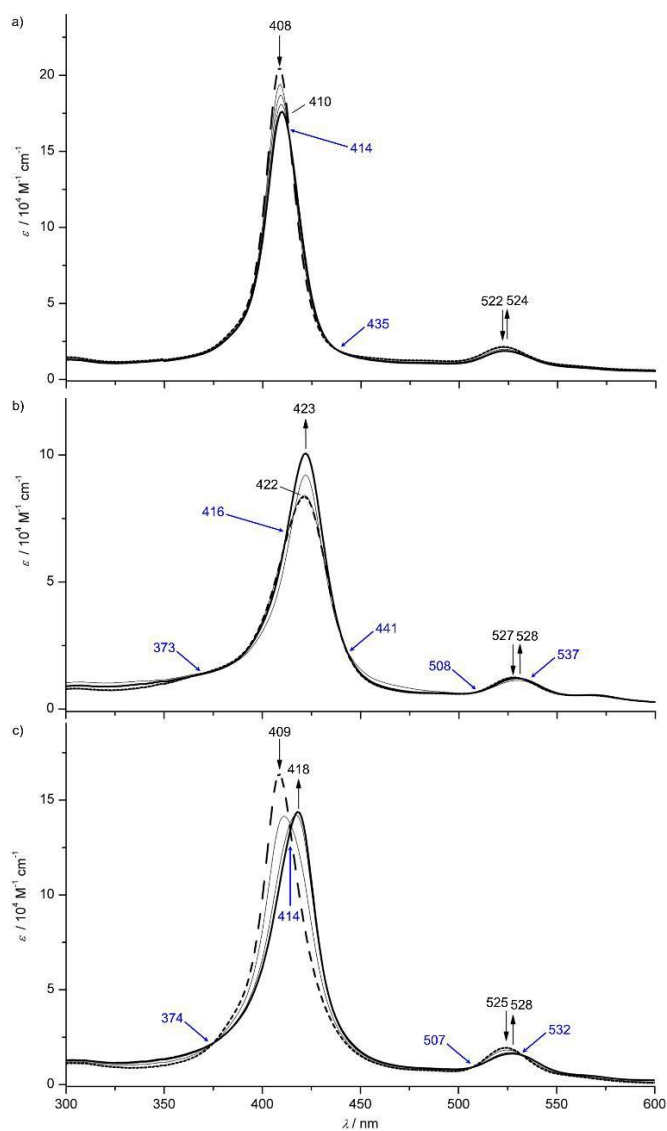


Fig. S24 X-band EPR spectrum of **1a**/**1a'**/**1a''** in frozen CH_2Cl_2 solution (77 K, 9.4 GHz) and deconvolution in the respective component spectra.

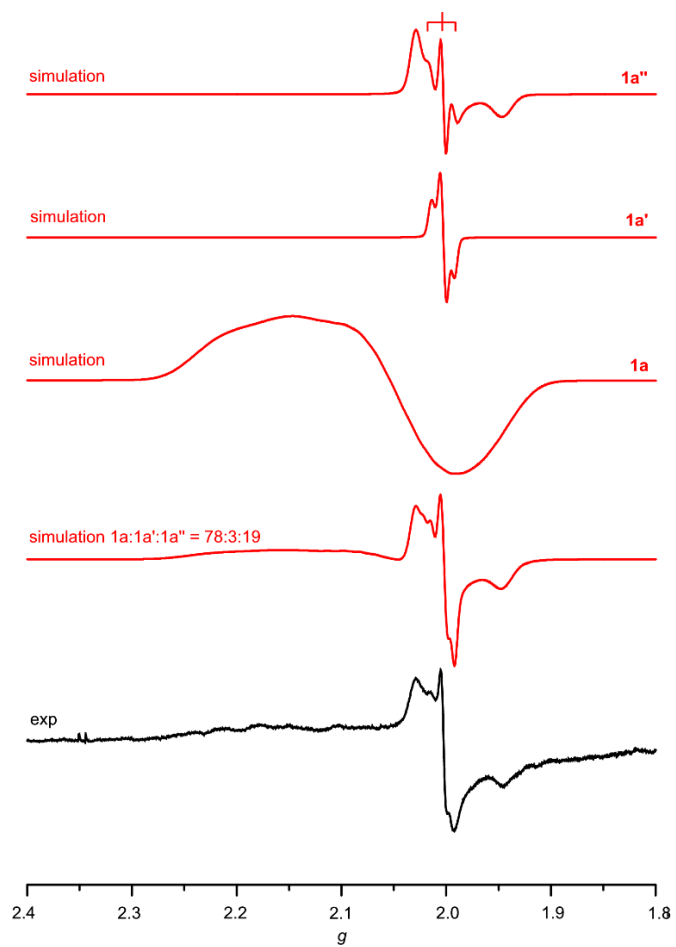


Fig. S25 X-band EPR spectrum of **1a** in frozen CH_2Cl_2 solution (77 K, 9.4 GHz) in the absence and in the presence of two equivalents $[\text{nBu}_4\text{N}]\text{Cl}$.

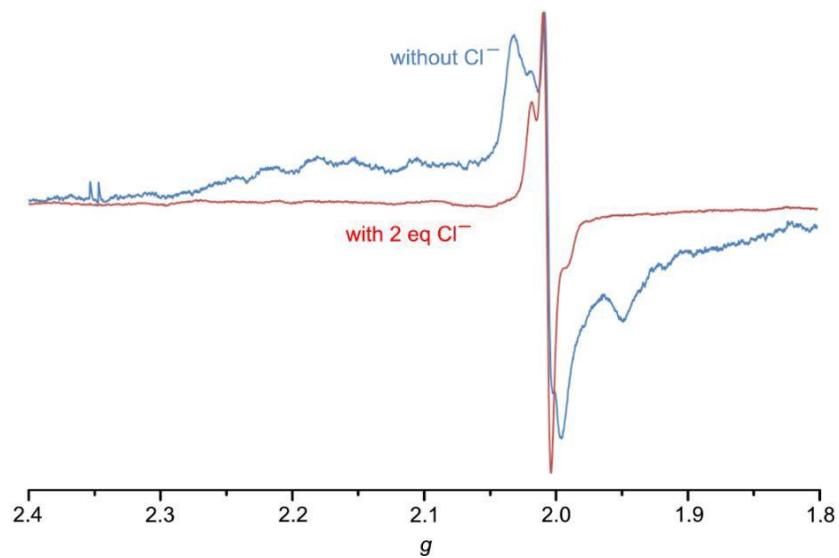


Fig. S26 X-band EPR spectrum of **1a** in frozen CH_2Cl_2 solution (77 K, 9.4 GHz) in the presence of two equivalents $[\text{nBu}_4\text{N}]\text{Cl}$ and corresponding simulation.

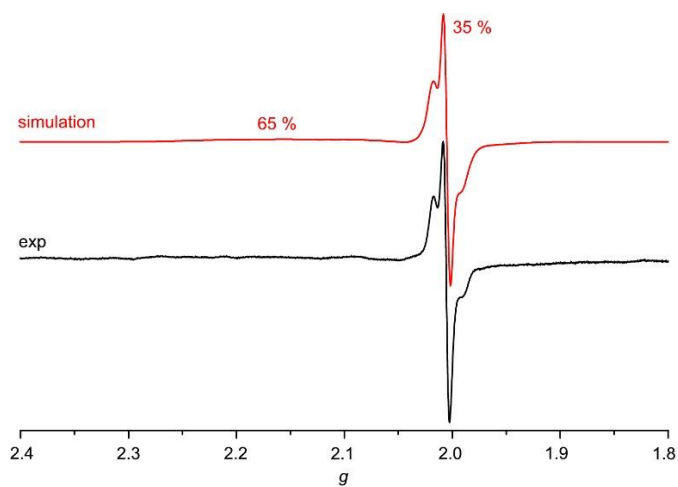


Fig. S27 Spin densities of DFT optimized geometries of Au(TPP) and Cu(TPP) (isosurface value 0.01 a.u.; UB3LYP, LANL2DZ, IEFPCM CH₂Cl₂; Mulliken spin densities in italics).

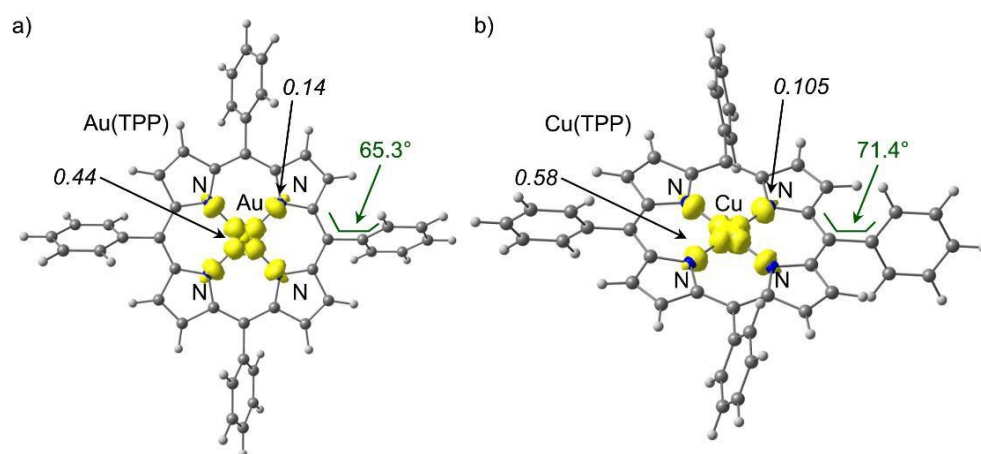


Fig. S28 Spin densities of DFT optimized geometries of **4a**, **4b** and **4c** (isosurface value 0.01 a.u.; UB3LYP, LANL2DZ, IEFPCM CH₂Cl₂; Mulliken spin densities in italics).

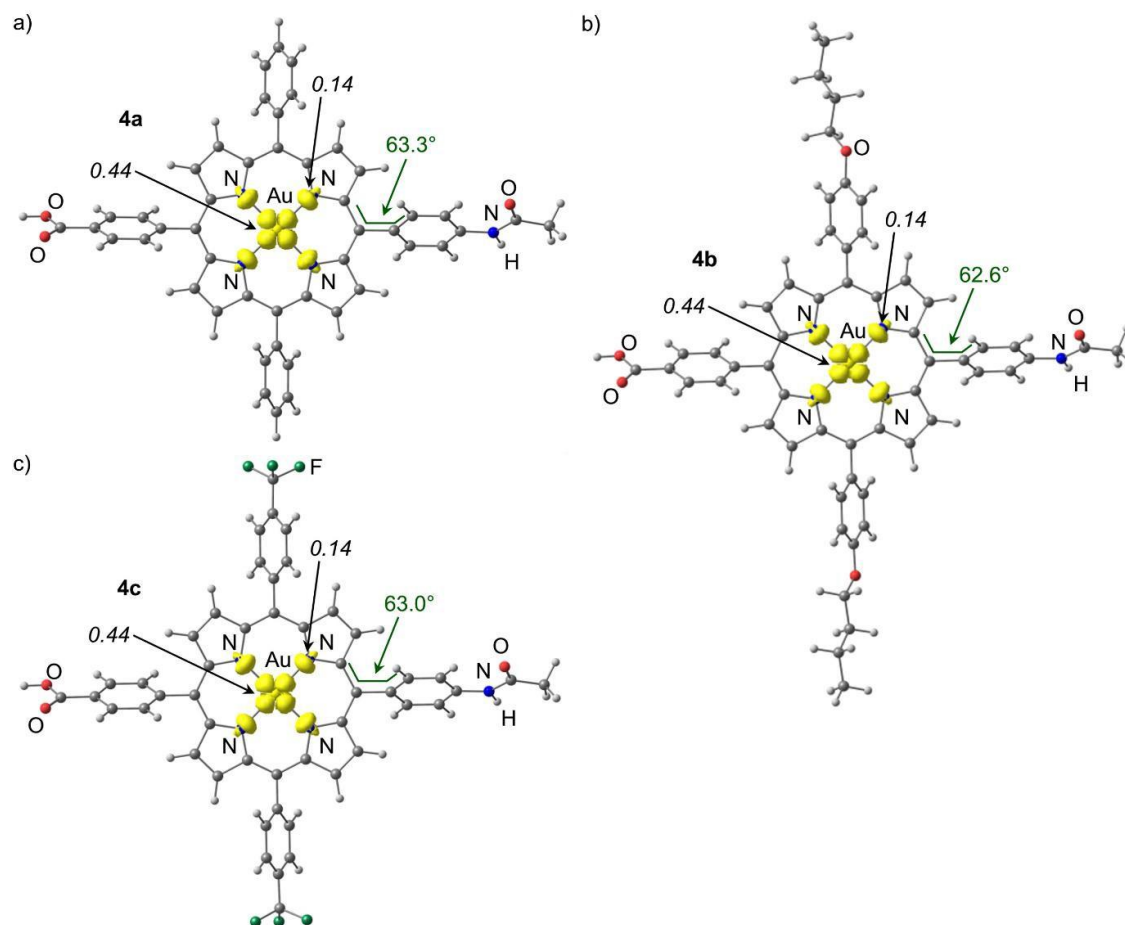


Fig. S29 X-band EPR spectrum of **2a / 2a'** in frozen CH_2Cl_2 (top) and THF (bottom) solution (77 K, 9.4 GHz).

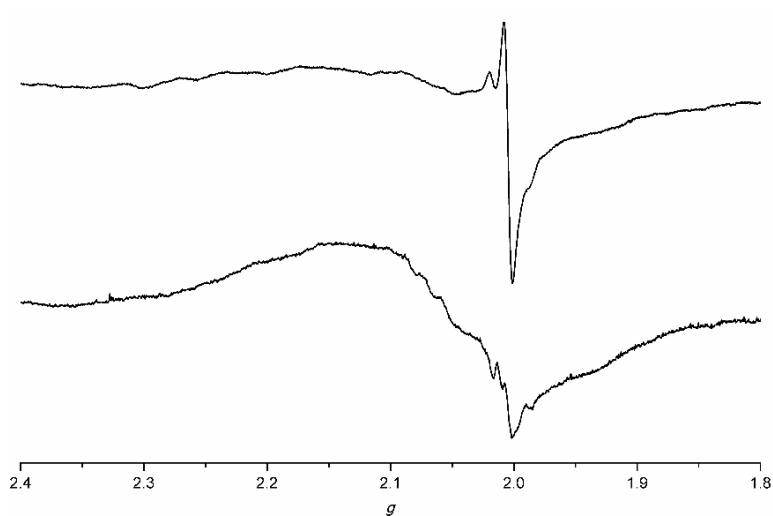
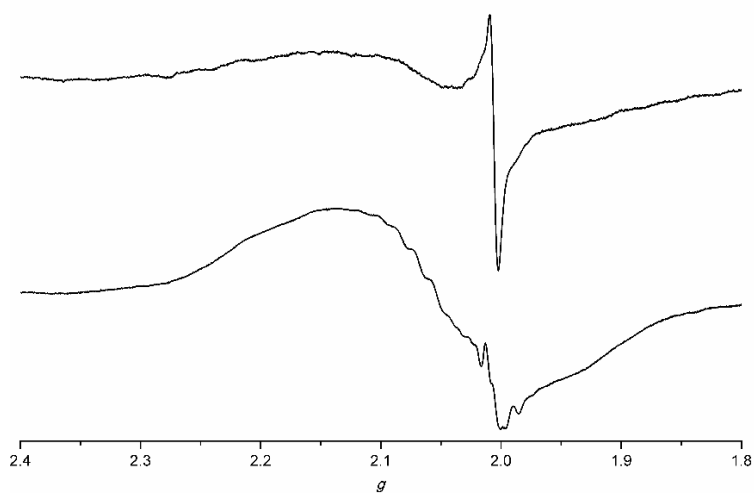


Fig. S30 X-band EPR spectrum of **3a / 3a'** in frozen CH_2Cl_2 (top) and THF (bottom) solution (77 K, 9.4 GHz).



6.2 Supporting Information to 3.2: Structure and reactivity of a mononuclear gold(II) complex

General considerations. All reactions were performed under an argon atmosphere unless otherwise noted. Dichloromethane was dried with CaH_2 and distilled prior to use. THF and toluene were distilled from potassium. All reagents were used as received from commercial suppliers (Acros, Sigma-Aldrich, ABCR). $[\text{Au}(\text{TPP})][\text{PF}_6]$ was prepared according to ref. ^[1].

NMR spectra were recorded on a Bruker DRX 400 spectrometer at 400.31 MHz (^1H) and 100.05 MHz ($^{13}\text{C}\{^1\text{H}\}$). All resonances are reported in ppm vs the solvent signal as internal standard: CD_2Cl_2 (^1H , δ 5.32 ppm; ^{13}C , δ 54.00 ppm); d_8 -THF (^1H , δ 1.73, 3.58 ppm; ^{13}C , δ 25.37, 67.57 ppm); d_8 -toluene (^1H , δ 2.09, 6.98, 7.00, 7.09 ppm; ^{13}C , δ 20.40, 125.49, 128.33, 129.24, 137.86 ppm).^[2]

IR spectra were recorded with a BioRad Excalibur FTS 3100 spectrometer as KBr disks.

UV/vis/near-IR spectra were recorded on a Varian Cary 5000 spectrometer by using 1.0 cm cells (Hellma, Suprasil).

Emission spectra were recorded on a Varian Cary Eclipse spectrometer. X-band (9.4 GHz)

X-band CW EPR spectra (ca. 5×10^{-3} mM) were measured on a Miniscope MS 300 at 77 K cooled by liquid nitrogen in a finger Dewar (Magnettech GmbH, Berlin, Germany). g factors are referenced to external Mn^{2+} in ZnS ($g = 2.118, 2.066, 2.027, 1.986, 1.946, 1.906$).

Q-band (33.9 GHz) CW EPR measurements were conducted on a Bruker EMX-plus spectrometer, using an ER5106QT resonator. All spectra were recorded at 50 K using a mercury iTC temperature controller (Oxford instruments). A microwave power of 1 mW, 100 KHz modulation frequency, modulation amplitude of 0.5 mT and 7858 points were used during measurements. A concentration of 2.5 mM was found to produce the best spectral shape. Samples were prepared by dissolving $[\text{Au}(\text{TPP})][\text{PF}_6]$ and $\text{Co}(\eta^5\text{-C}_5\text{H}_5)_2$ in anhydrous dichloromethane under inert conditions.

Simulations of EPR spectra were performed with EasySpin (v 5.0.0) for MatLab (R2015a).^[3]

Variable-temperature magnetic susceptibility measurements were carried out with a Quantum Design MPMS-XL7 SQUID magnetometer in the temperature range 2–300 K under an applied magnetic field of 1 T. Experimental susceptibility data were corrected by the underlying diamagnetism using Pascal's constants. The temperature dependent magnetic contribution of the holder was experimentally determined and subtracted from the measured susceptibility data.

FD^+ mass spectra were recorded on a Thermo Scientific DFS with LIFDI upgrade (Linden CMS). ESI^+ mass spectra were recorded on a Micromass Q-TOF-Ultima spectrometer.

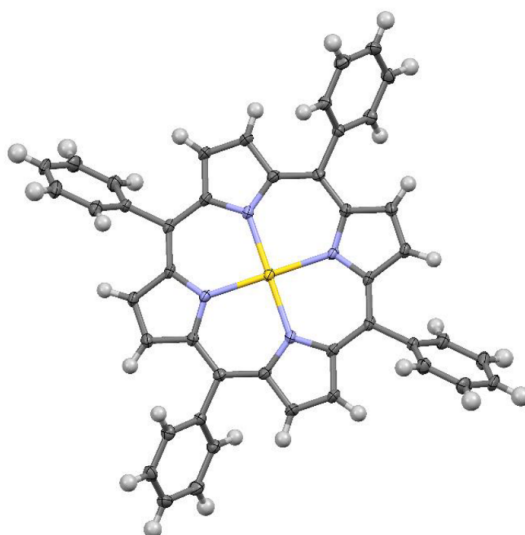
Elemental analyses were performed by the microanalytical laboratory of the chemical institutes of the University of Mainz.

XAS spectral measurements were performed at beamline P65 of PETRA III (Hamburg, Germany) under ambient conditions at 293 K. A Si(111) double crystal monochromator was used for measurements at the Au L₃ edge (11.918 keV). The second monochromator crystal was tilt for optimal harmonic rejection. The spectra were recorded in transmission mode with ionization chambers filled with nitrogen. The individual pressures were adjusted to optimize the signal to noise ratio. Energy calibration was performed with a gold metal foil. The solid samples were handled in a glove box and embedded in an oxygen free boron nitride matrix and pressed into self-supporting pellets. The XANES spectra were analyzed by the peak fitting approach.^[4-8] The edge step in this process is modeled by an arctan function. Only the white line was adjusted after the rising edge, using a Gauss function. All parameters (energy, integral intensity and width) were allowed to float in the fit. Difference spectra were obtained without shifting the energy, followed by numerical integration using the program Athena. To determine the smooth part of the EXAFS spectra^[9], corrected for pre-edge absorption, a piecewise polynomial was used. It was adjusted in such a way that the low-*R* components of the resulting Fourier transform were minimal. After division of the background-subtracted spectrum by its smooth part, the photon energy was converted to photoelectron wave numbers *k*. The resulting $\chi(k)$ -function was weighted with k^3 . Single scattering data analysis was performed in *k*-space according to the curved wave formalism of the EXCURV98 program with XALPHA phase and amplitude functions.^[10] The mean free path of the scattered electrons was calculated from the imaginary part of the potential (VPI set to -4.00). An amplitude reduction factor of 0.8 was used to reproduce the crystallographic coordination numbers in a free floating fit.

Crystal Structure Determination. Intensity data were collected with a Bruker AXS Smart1000 CCD diffractometer with an APEX II detector and an Oxford cooling system and corrected for absorption and other effects using Mo K_{α} radiation ($\lambda = 0.71073 \text{ \AA}$). The diffraction frames were integrated using the SAINT package, and most were corrected for absorption with MULABS^[11,12] The structures were solved by direct methods and refined by the full-matrix method based on F^2 using the SHELXTL software package.^[13,14] All non-hydrogen atoms were refined anisotropically, while the positions of all hydrogen atoms were generated with appropriate geometric constraints and allowed to ride on their respective parent carbon atoms with fixed isotropic thermal parameters.

Crystal data for Au(TPP): $C_{44}H_{28}AuN_4$ (809.67); $T = 173 \text{ K}$; purple plate; $0.20 \times 0.15 \times 0.05 \text{ mm}^3$; triclinic; $P\bar{1}$; $a = 6.1691(2) \text{ \AA}$; $b = 10.6043(4) \text{ \AA}$; $c = 12.4939(5) \text{ \AA}$; $\alpha = 97.4790(10)^\circ$; $\beta = 97.4530(10)^\circ$; $\gamma = 99.9250(10)^\circ$; $V = 788.51(5) \text{ \AA}^3$; $Z = 1$; $F(000) = 399$; $\rho = 1.705 \text{ g cm}^{-3}$; $\mu = 4.705 \text{ mm}^{-1}$; θ range $2.375\text{--}27.939^\circ$; index ranges $-8 \leq h \leq 8$, $-13 \leq k \leq 13$, $-16 \leq l \leq 16$; 9273 reflections collected; 3774 independent reflections; parameters 223; maximum/minimum transmission 1.35416/0.73982; goodness of fit on F^2 1.066; largest difference peak and hole $1.367/-1.006 \text{ e \AA}^{-3}$; $R_1(I > 2\sigma) = 0.0246$; $R_1(\text{all data}) = 0.0249$; $wR_2(I > 2\sigma) = 0.0569$; $wR_2(\text{all data}) = 0.0569$.

Figure 0. Structure of Au(TPP) as determined by X-ray crystallography. Thermal ellipsoids at 50% probability level.



DFT calculations. These were carried out with the ORCA 3.0.2/DFT series of programs.^[15] Tight convergence criteria were chosen for all calculations (Keywords TightSCF and TightOpt). For geometry optimizations and energy calculations, the B3LYP formulation^[16] of density functional theory was used employing the def2-TZVPP basis set with the zeroth order regular approximation (ZORA)^[17], or Schwerdtfeger's ECP basis set for gold,^[18] the RIJCOSX approximation^[19,20], at GRID7 for C, H, N and an even higher accuracy for the gold atom (Keyword SpecialGridIntAcc 20). To account for solvent effects, a conductor-like screening model (COSMO CH₂Cl₂) modelling dichloromethane was used in all calculations.^[21] Grimme's empirical dispersion correction D3(BJ) was employed.^[22,23] No symmetry constraints were imposed on the molecules. Transition state searches were performed at the B3LYP/def2-SVP level (ZORA, COSMO CH₂Cl₂).^[24] The presence of energy minima of the ground states and saddle points for transition states was checked by numerical frequency calculations for the def2-SVP optimized geometries (ZORA, COSMO CH₂Cl₂). The approximate free energies at 298 K were obtained through thermochemical analysis of the frequency calculation, using the thermal correction to Gibbs free energy as reported by ORCA 3.0.2. The calculation of the *g* tensor and the time-dependent DFT calculations were done at the B3LYP, def2-TZVPP, ZORA, D3(BJ), COSMO (CH₂Cl₂) level using the optimized geometry, yet simplified by replacing the Ph groups by hydrogen atoms.

Figure 1. Photograph of **Au(TPP)** sublimed onto the cold finger of the sublimation apparatus.



Figure 2. LIFDI mass spectrum of **Au(TPP)** in THF; inset shows calculated (calcd. for $C_{44}H_{28}N_4Au$) and experimental isotopic pattern.

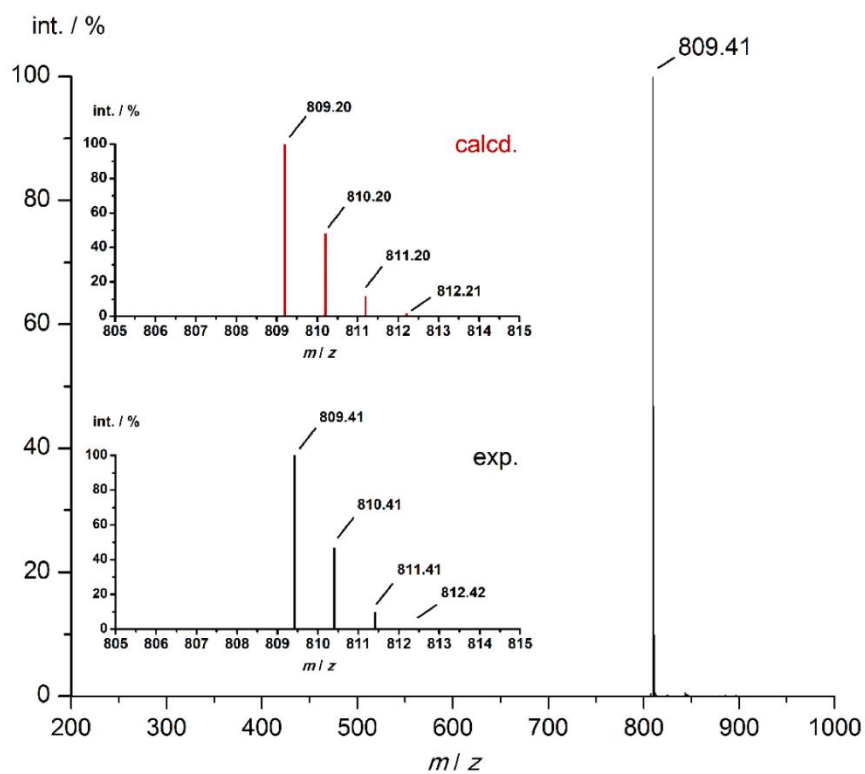


Figure 3. UV/Vis spectra of **Au(TPP)** (red), **[Au(TPP)][PF₆]** (black) and **Cu(TPP)** (blue) in THF. Inset shows expanded low energy region.

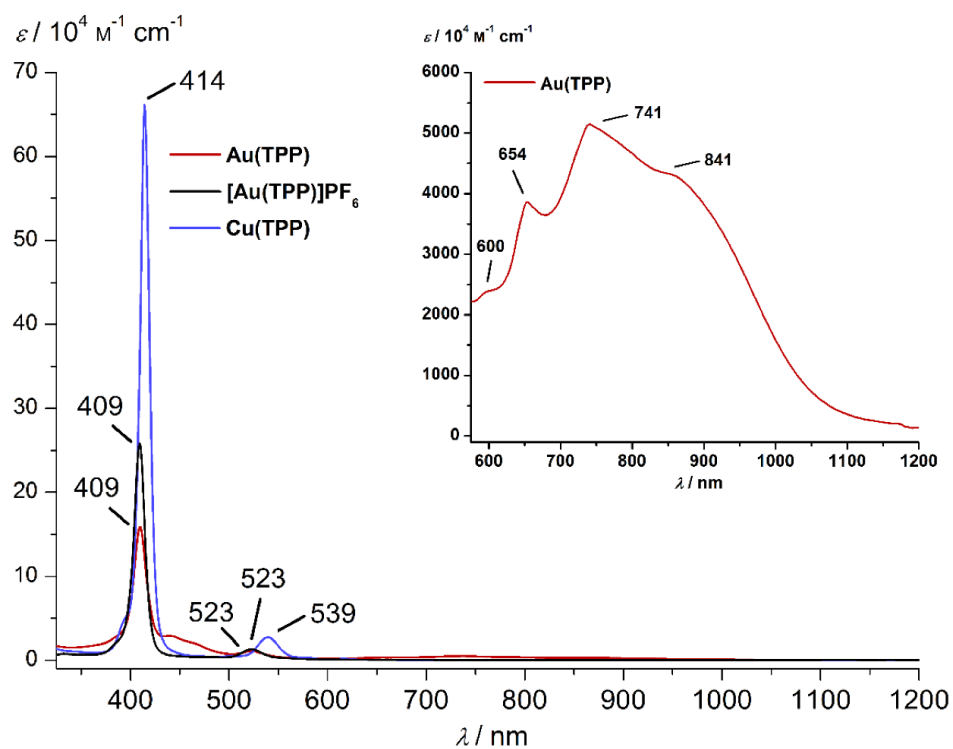


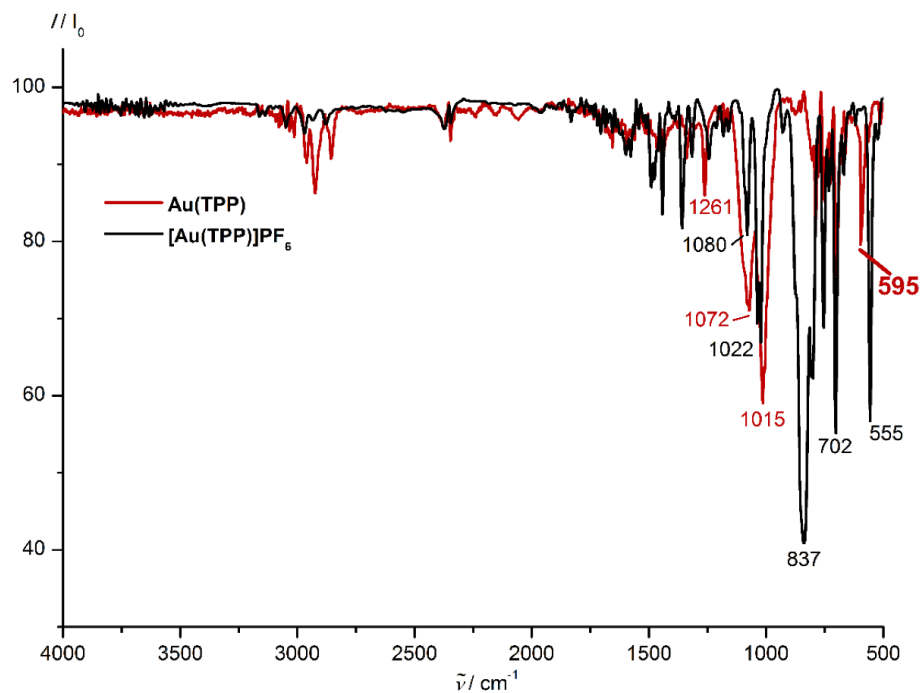
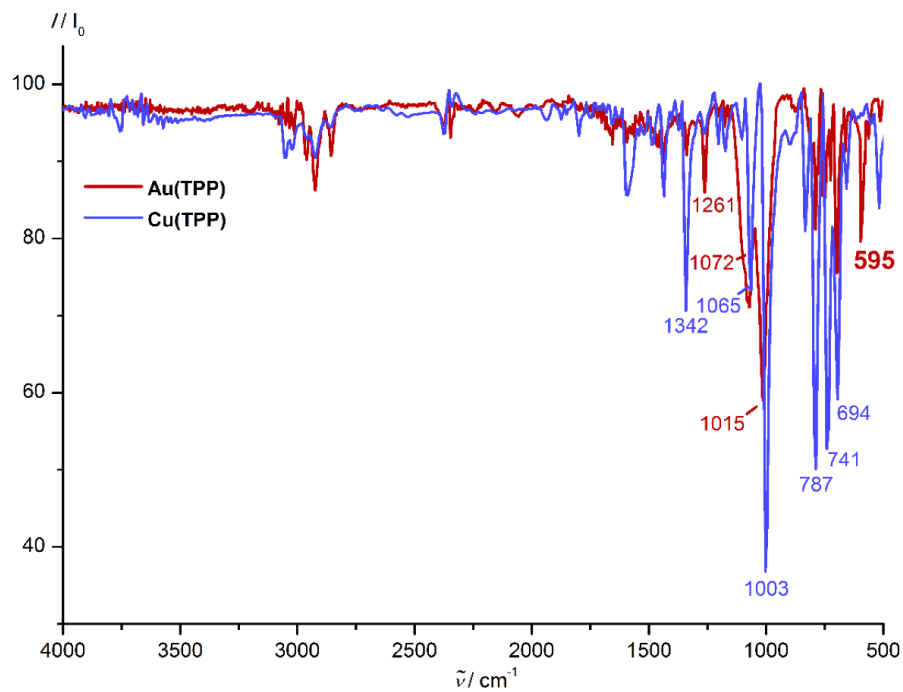
Figure 4. IR spectra of **Au(TPP)** (red) and **[Au(TPP)][PF₆]** (black) as KBr disks.Figure 5. IR spectra of **Au(TPP)** (red) and **Cu(TPP)** (blue) as KBr disks.

Figure 6. Magnetic susceptibility versus temperature plot of **Au(TPP)**; fit to a Hamiltonian with $g = 2.073$ and $zJ = -1.09 \text{ cm}^{-1}$.

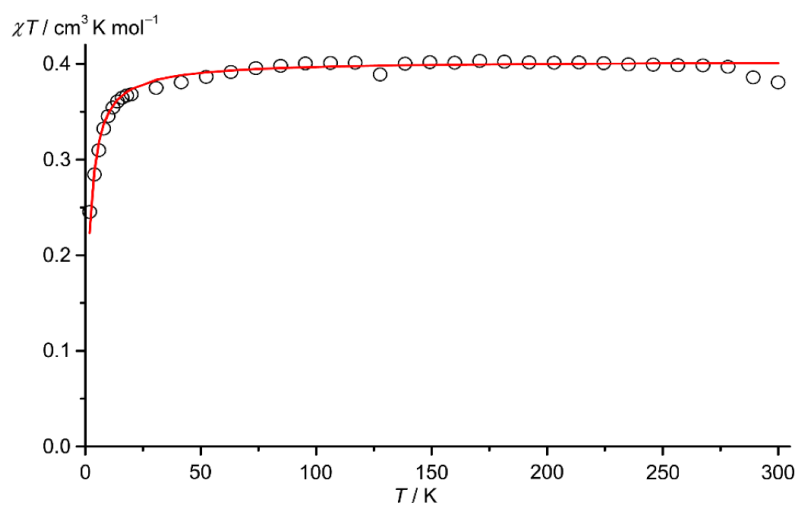


Figure 7. ^1H NMR spectrum of **Au(TPP)** in CD_2Cl_2 at 293 K. Asterisk denotes residual solvent resonance.

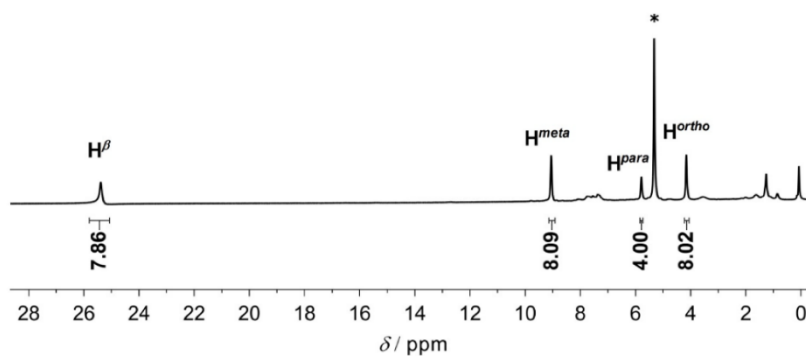


Figure 8. ^1H NMR spectrum of **Au(TPP)** in d_8 -THF at 293 K. Asterisks denote residual solvent resonances.

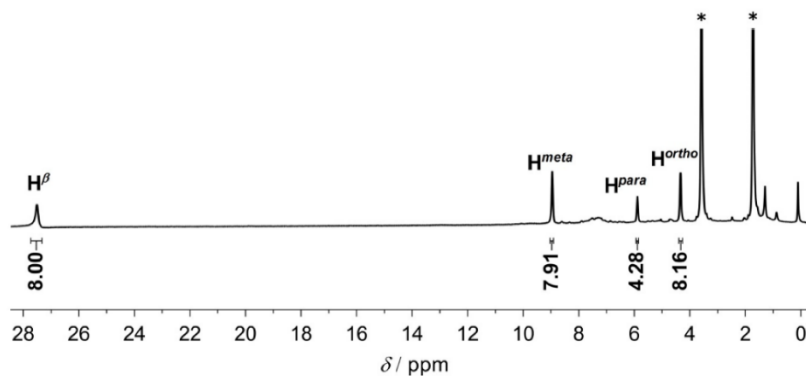


Figure 9. ^1H NMR spectrum of **Au(TPP)** in d_8 -toluene at 293 K. Asterisks denote residual solvent resonances.

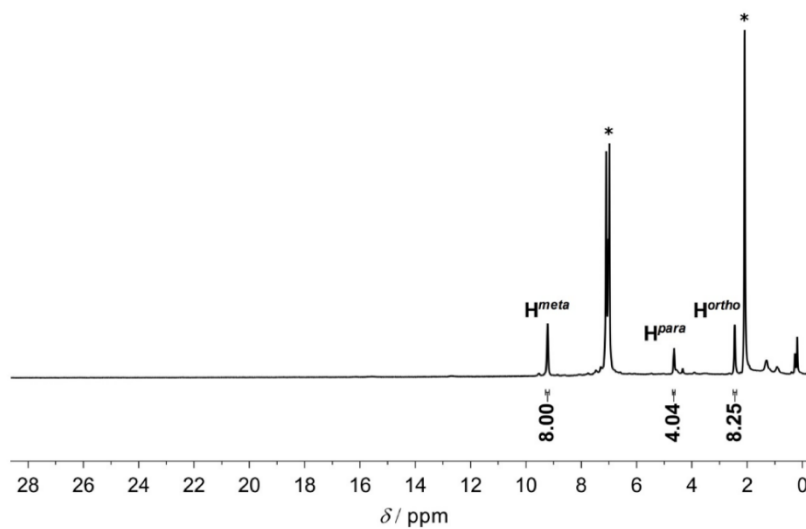


Figure 10. $^1\text{H}^1\text{H}$ COSY of **Au(TPP)** in CD_2Cl_2 at 293 K. Asterisk denotes residual solvent resonance.

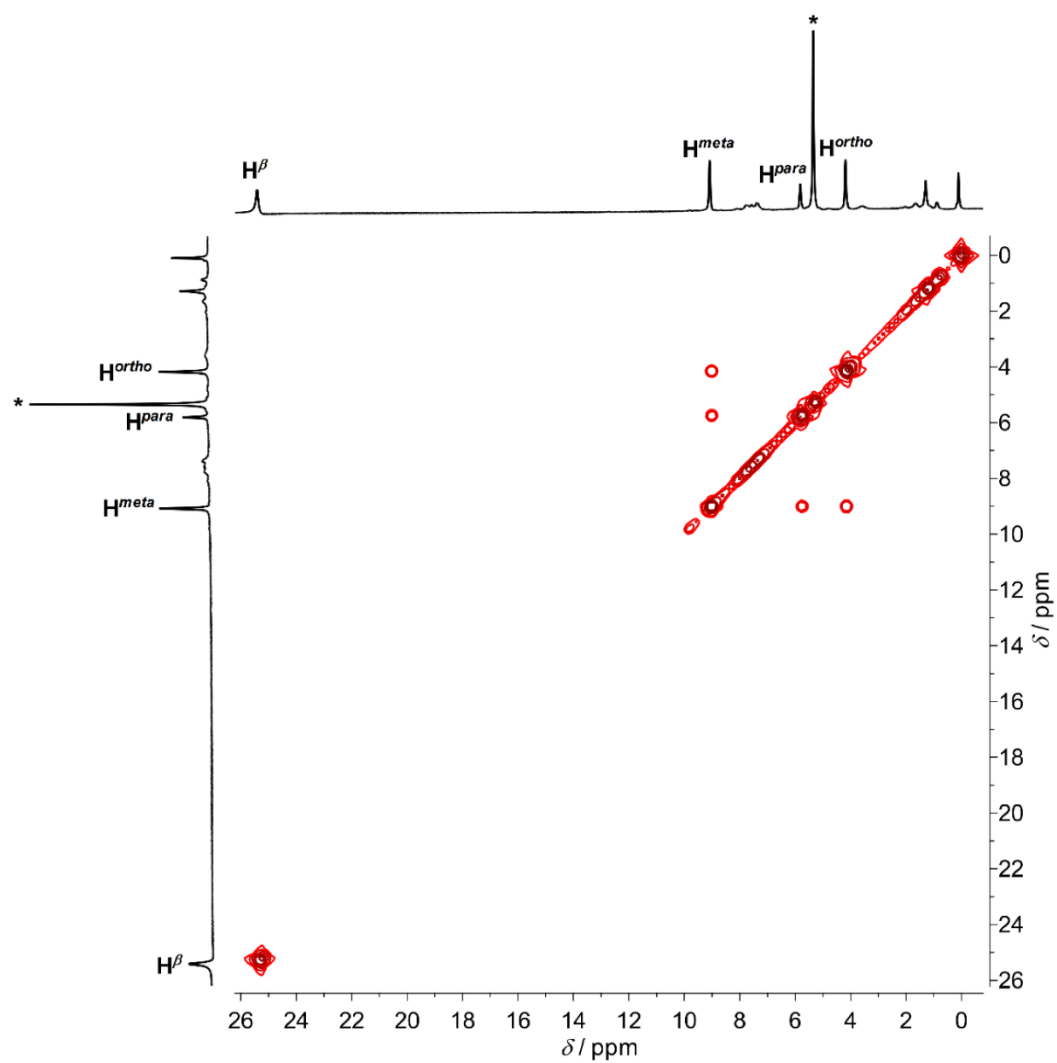


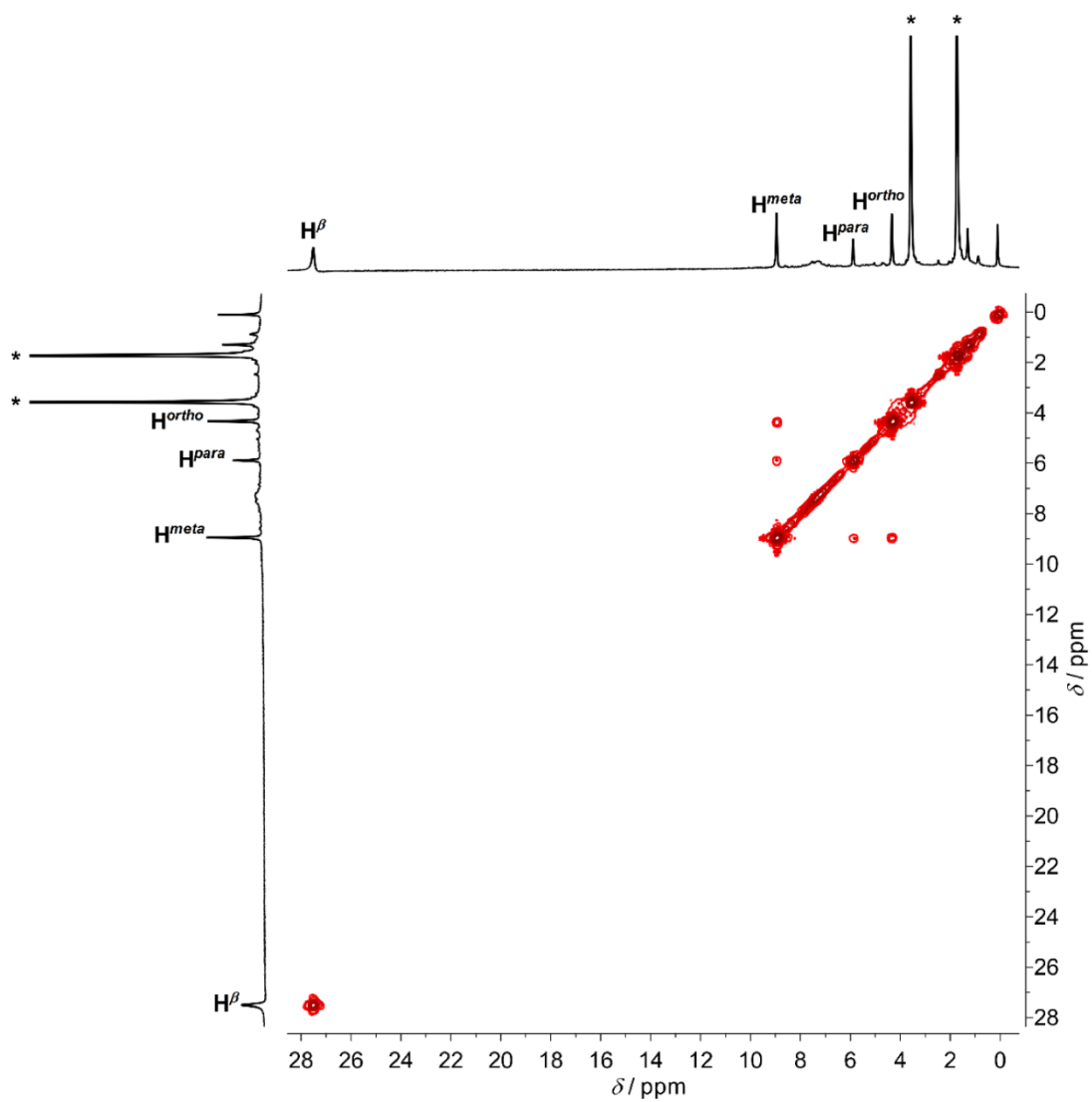
Figure 11. ^1H COSY of **Au(TPP)** in d_8 -THF at 293 K. Asterisks denote residual solvent resonances.

Figure 12. $^1\text{H}^1\text{H}$ COSY of **Au(TPP)** in d_8 -toluene at 293 K. Asterisks denote residual solvent resonances.

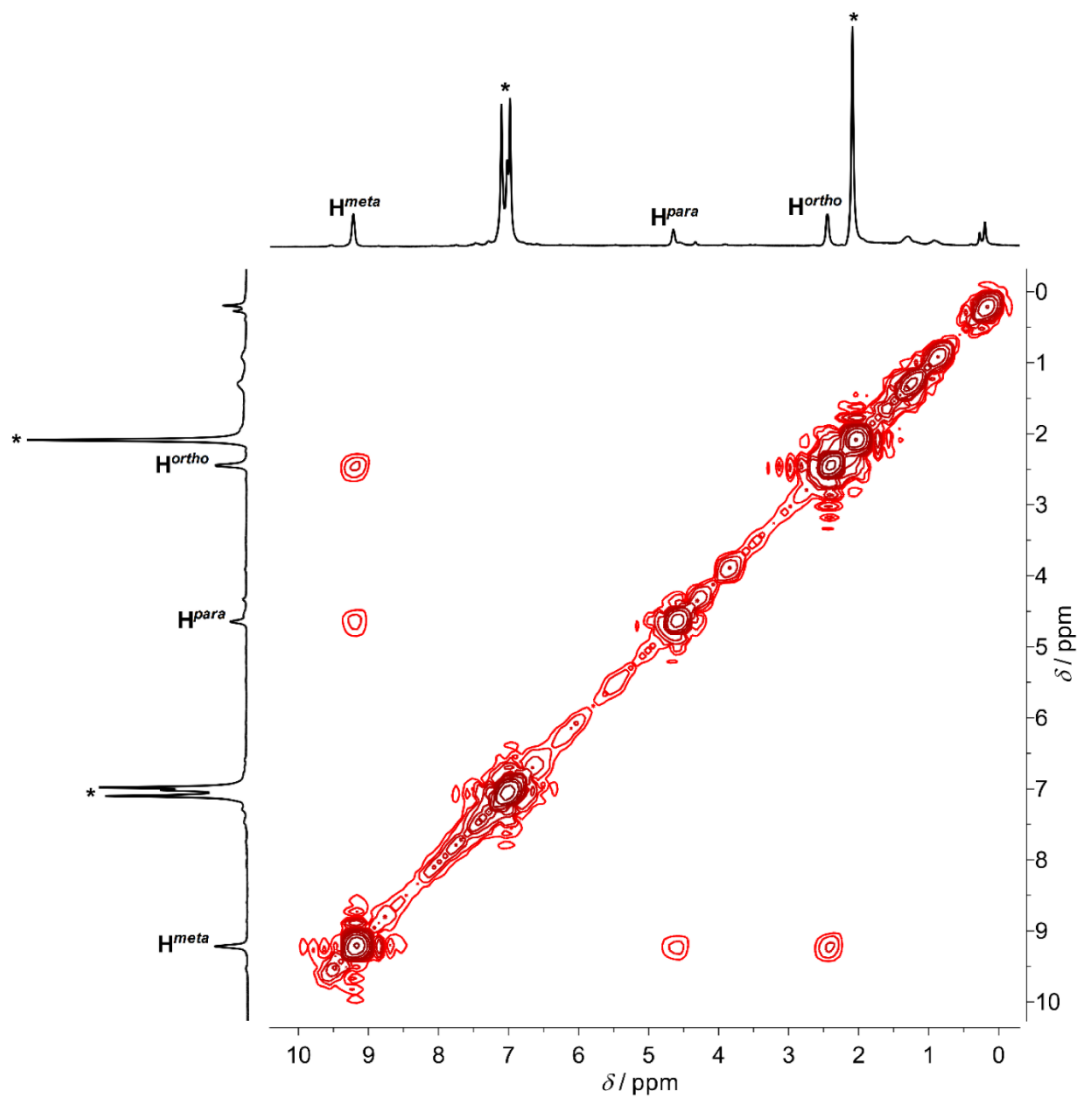


Figure 13. $^{13}\text{C}\{^1\text{H}\}$ NMR spectrum of **Au(TPP)** in d_8 -THF at 293 K. Asterisks denote residual solvent resonances.

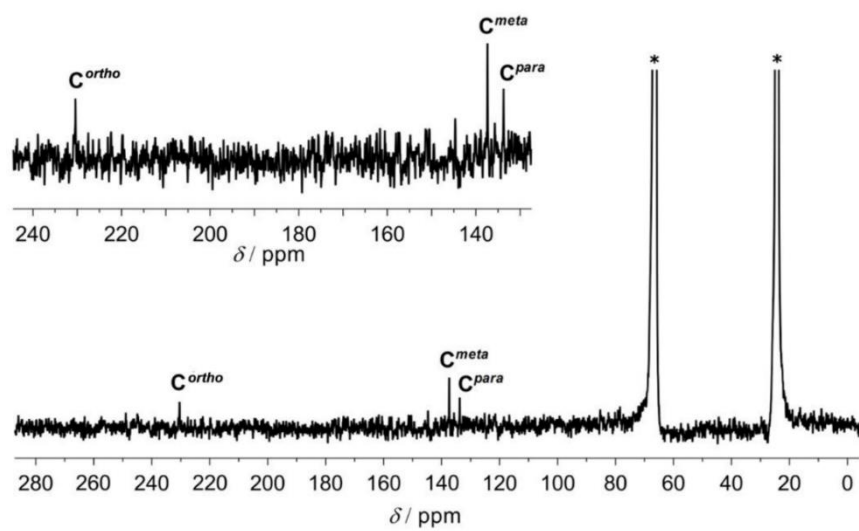


Figure 14. $^1\text{H}^{13}\text{C}$ HSQC of **Au(TPP)** in $\text{d}_8\text{-THF}$ at 293 K. Asterisks denote residual solvent resonances.

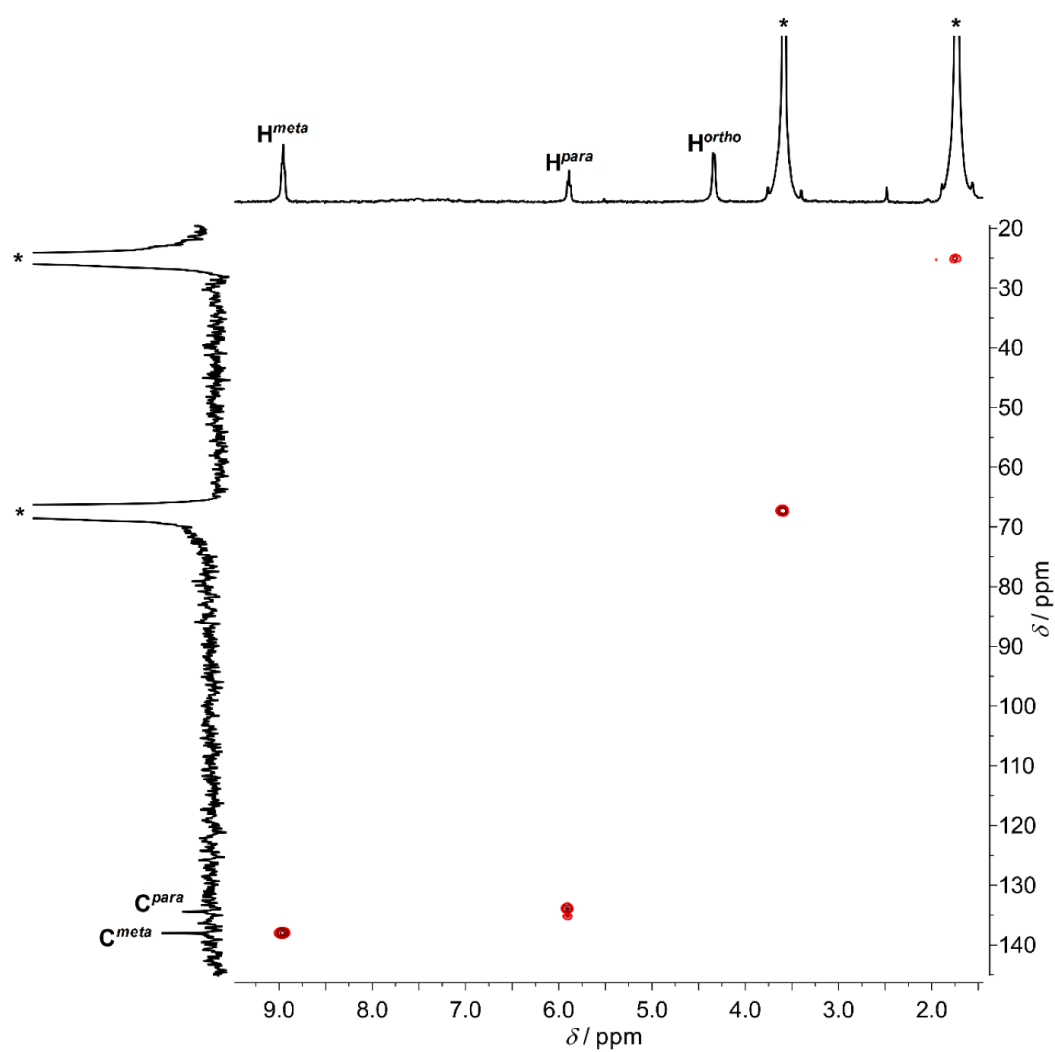


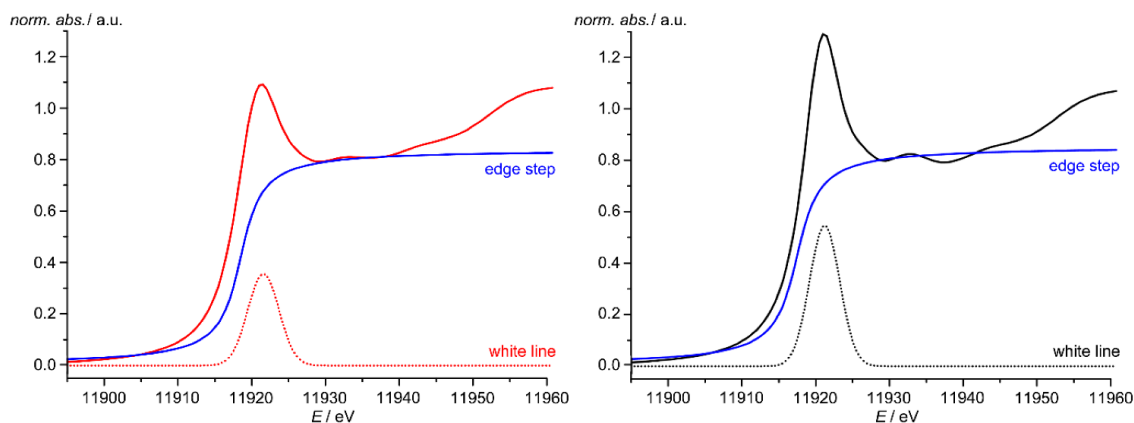
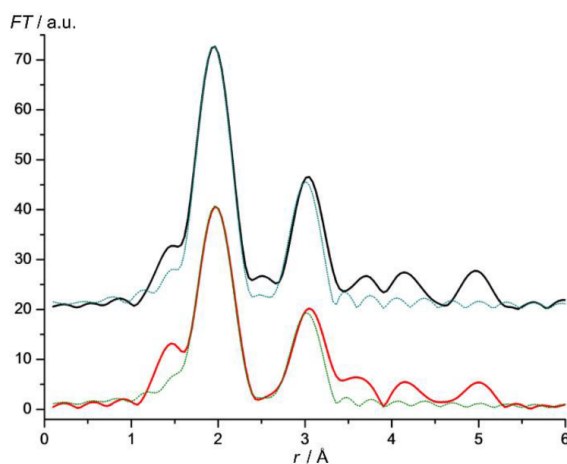
Figure 15: XANES deconvolution of **Au(TPP)** (left, red) and **[Au(TPP)][PF₆]** (right, black).Figure 16. Experimental Fourier transformed EXAFS functions of **[Au(TPP)][PF₆]** (top, black) and **Au(TPP)** (bottom, red) and the calculated functions according to the structural parameters given in Table S1.

Table 1. Structure parameters extracted from analysis of the experimental EXAFS data.

	Abs-Bs ^a	N(Bs) ^b	R(Abs-Bs) ^c [Å]	σ^d [Å ²]	E_f^e [eV] R [%] ^f
Au(TPP)	Au-N	3.9 ± 0.4	2.031 ± 0.020	0.009 ± 0.001	-0.289
	Au-C	4.5 ± 0.5	3.038 ± 0.031	0.006 ± 0.001	27.88
[Au(TPP)][PF₆]	Au-N	4.3 ± 0.4	2.010 ± 0.020	0.007 ± 0.001	-0.384
	Au-C	4.6 ± 0.5	3.025 ± 0.030	0.003 ± 0.001	25.51

^a Abs = X-ray absorbing atom, Bs = backscattering atom. ^b N = Number of neighbor backscattering atoms. ^c Distance between Abs and Bs. ^d σ = Debye-Waller like factor. ^e E_f = Shift between experimental and theoretical EXAFS function. ^f R = Quality of fit.

Figure 17. Molecular structure **Au(TPP)** by DFT calculation (B3LYP, ECP basis set, COSMO CH₂Cl₂) including side view along the N1-Au1-N1a axis. Relevant distances are given in Å, relevant angles are given in deg (H atoms omitted).

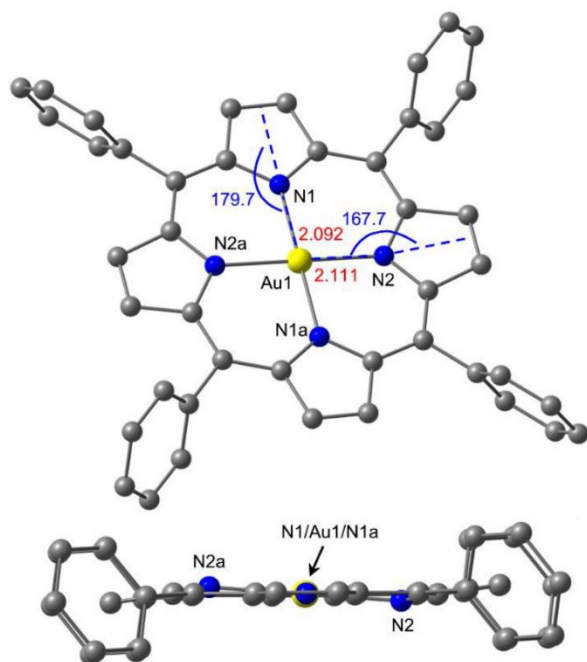


Figure 18. Spin density plots of **Au(TPP)** (in green) calculated by DFT, a) B3LYP, def2-TZVPP, ZORA, D3(BJ), COSMO CH₂Cl₂ and b) B3LYP, ECP, COSMO CH₂Cl₂ (isosurface value in green at 0.01 a.u.; H atoms omitted).

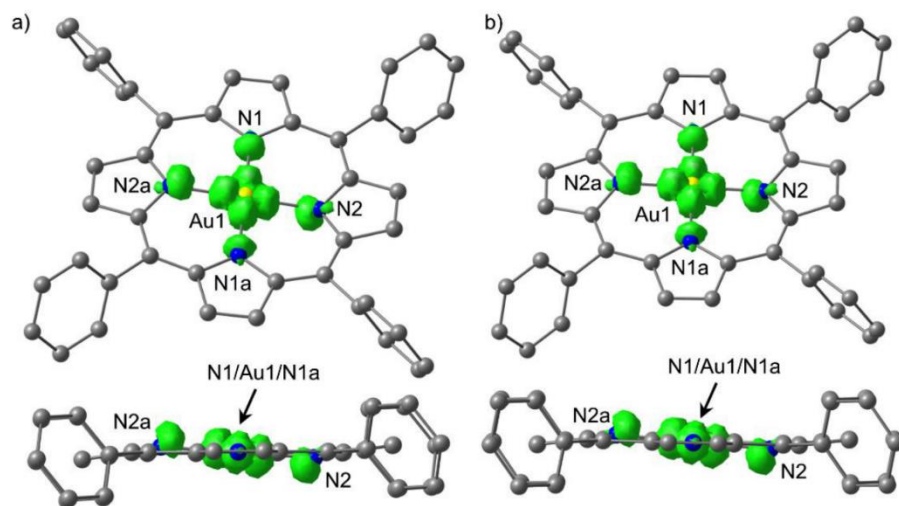


Figure 19. DFT calculated transition state between SOJT isomers of **Au(TPP)** (negative frequency 112 cm^{-1}) (B3LYP, def-SVP, ZORA, COSMO CH_2Cl_2 ; scaled displacement vectors shown; relevant distances are given in Å, relevant angles are given in deg.).

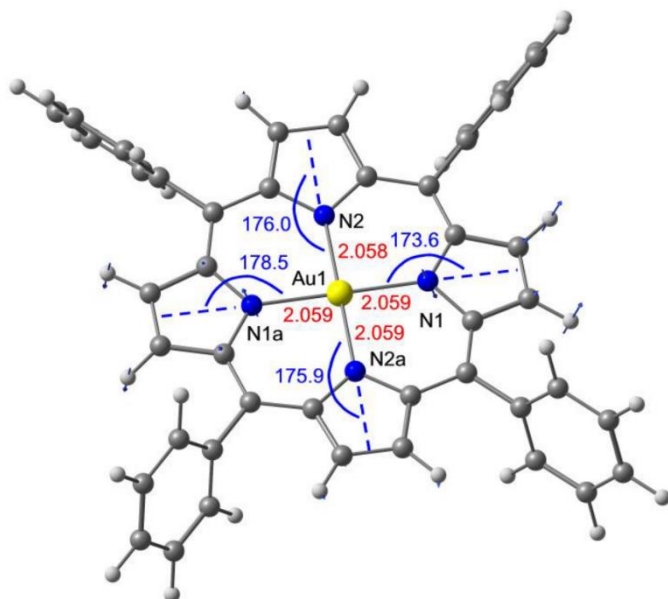


Figure 20. Variable-temperature ^1H NMR spectra of **Au(TPP)** in CD_2Cl_2 (248 – 298 K). Asterisk denotes residual solvent resonance.

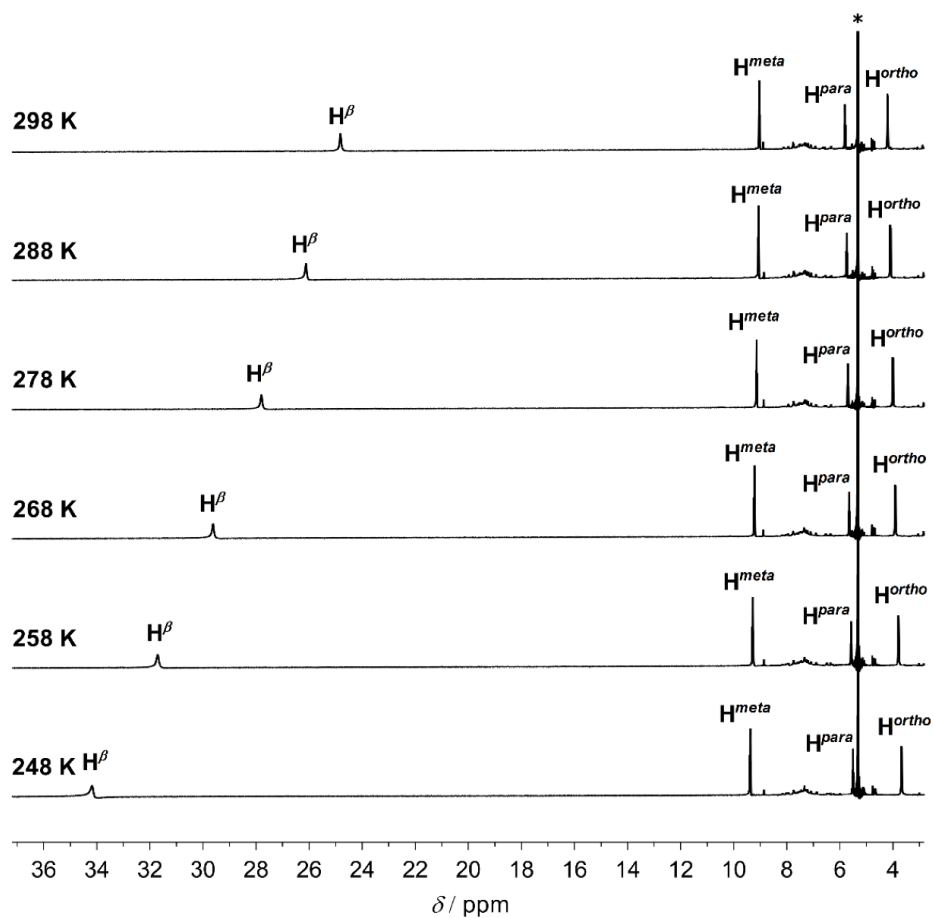


Figure 21. Plot of $\delta(\text{H}^\beta)$ of **Au(TPP)** vs. T^{-1} .

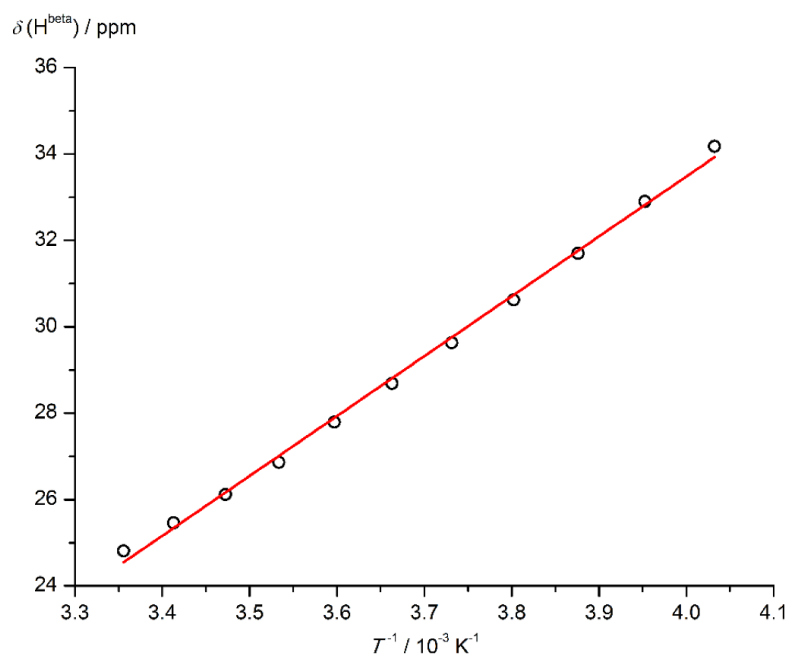


Figure 22. TD-DFT (B3LYP, def2-TZVPP, ZORA, COSMO CH₂Cl₂, D3(BJ)) calculated UV/Vis spectrum of **Au(P)** including electron density difference maps of relevant excited states (isosurface values 0.005 a.u.; purple lobes indicate loss, orange lobes show increase of electron density upon excitation, H atoms omitted). The phenyl rings of optimized **Au(TPP)** have been replaced by hydrogen atoms.

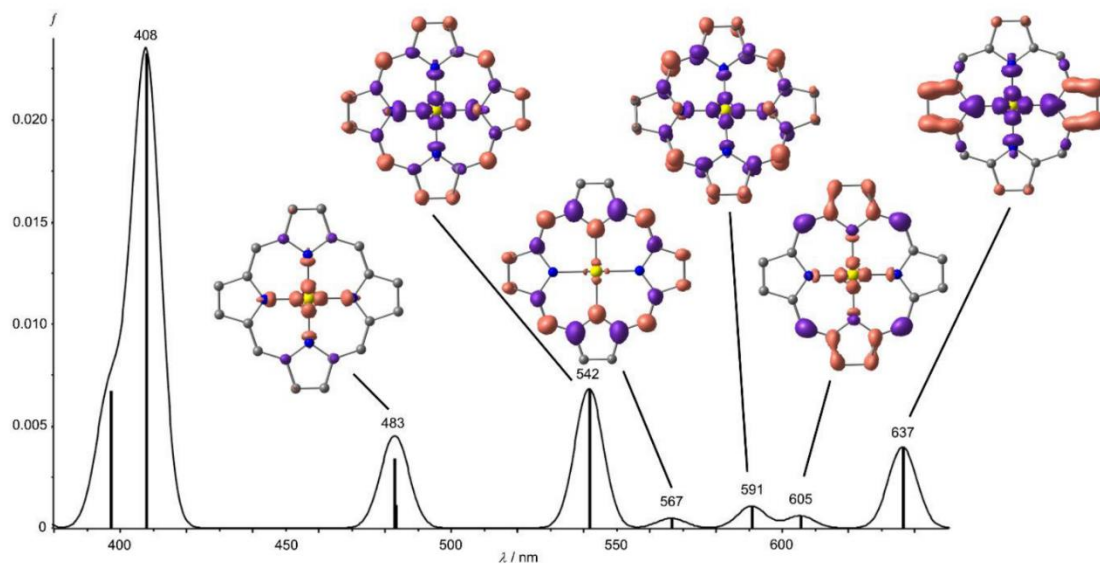


Figure 23. ^1H NMR spectra of $[\text{Au}(\text{TPP})][\text{PF}_6]$ in the presence of increasing amounts of $\text{Au}(\text{TPP})$ in CD_2Cl_2 .

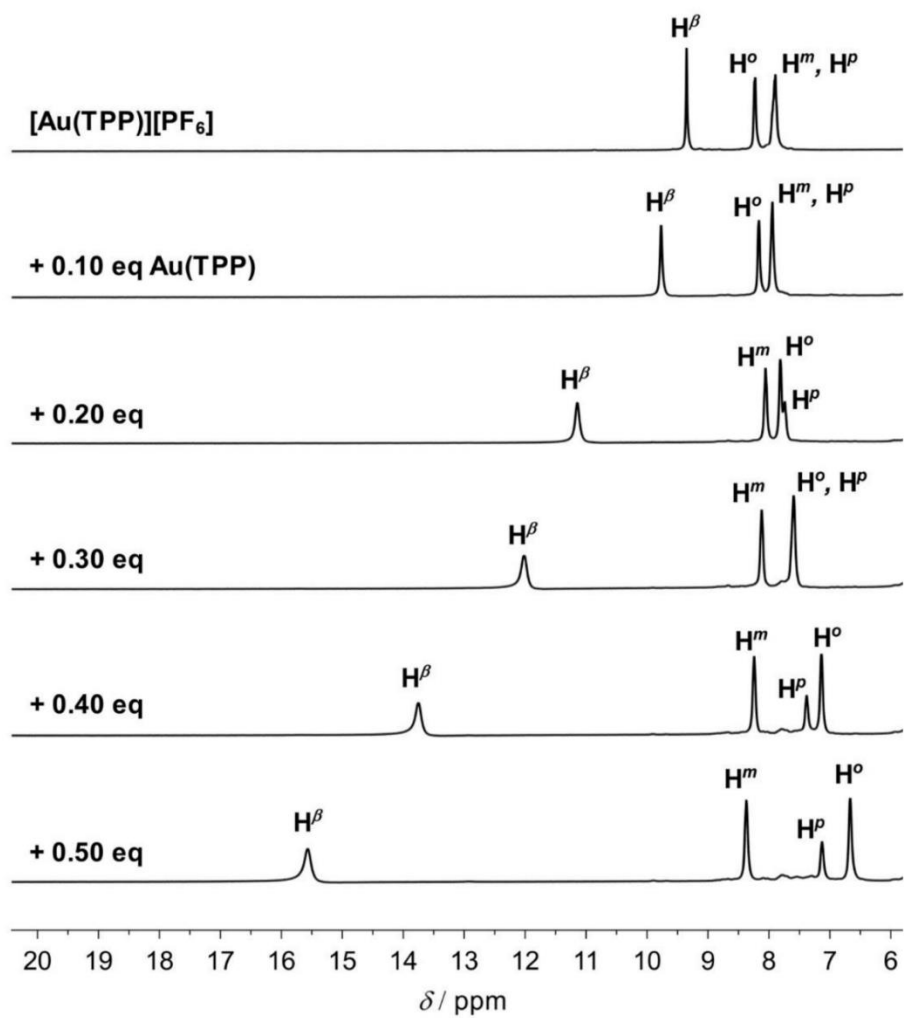


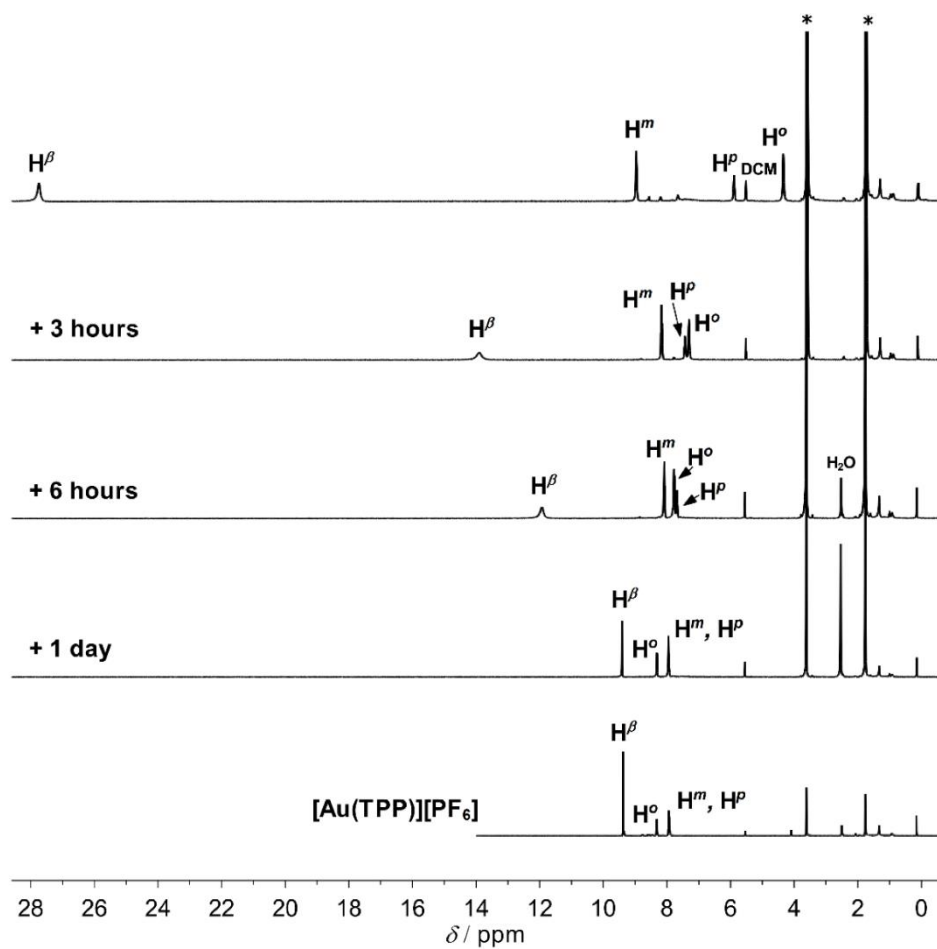
Figure 24. ^1H NMR spectra of **Au(TPP)** in the presence of O_2 / H_2O (open NMR tube) in d_8 -THF.

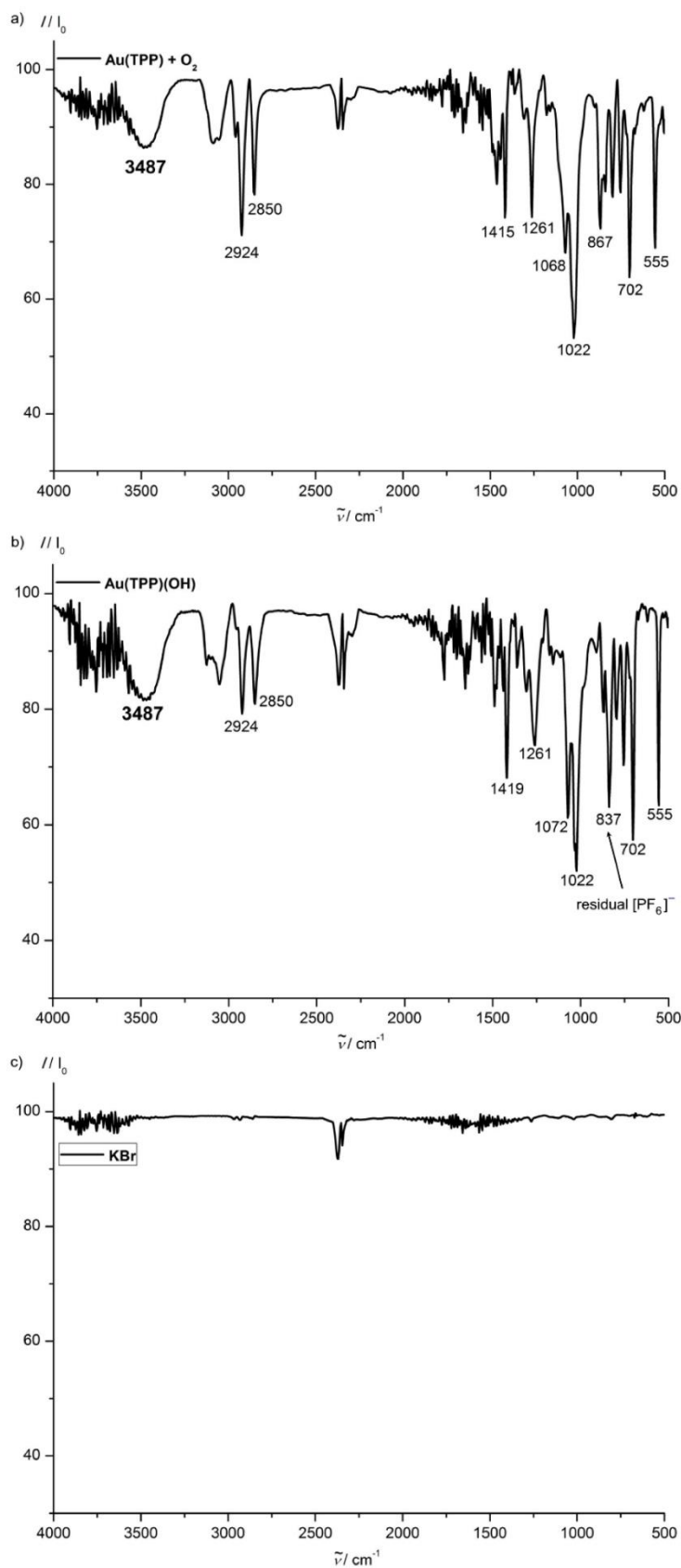
Figure 25. IR spectra (KBr) a) of **Au(TPP)** after reaction with O_2 , b) of **[Au(TPP)](OH)** and c) KBr.

Figure 26. ESI⁺ mass spectrum (THF/MeOH 1:1) a) of **Au(TPP)** after reaction with O₂ and b) of **[Au(TPP)][OH]**.

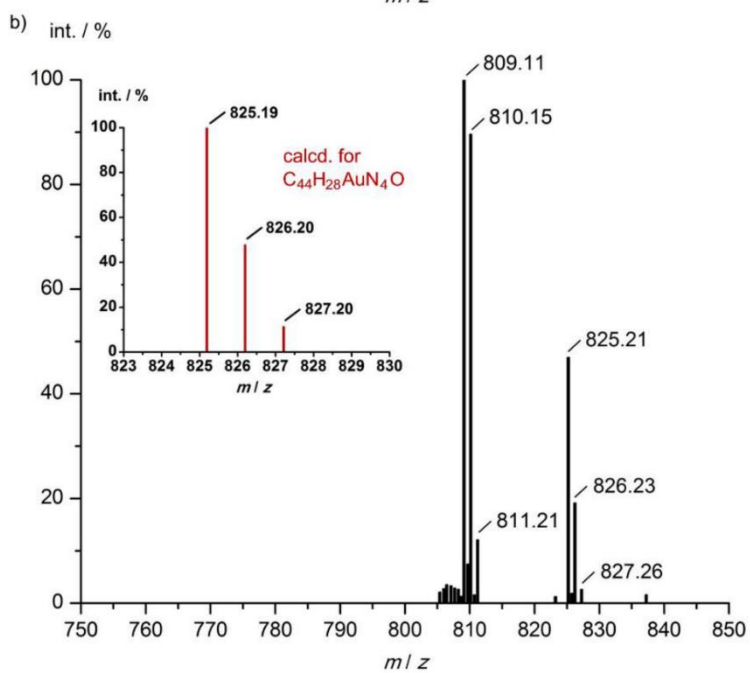
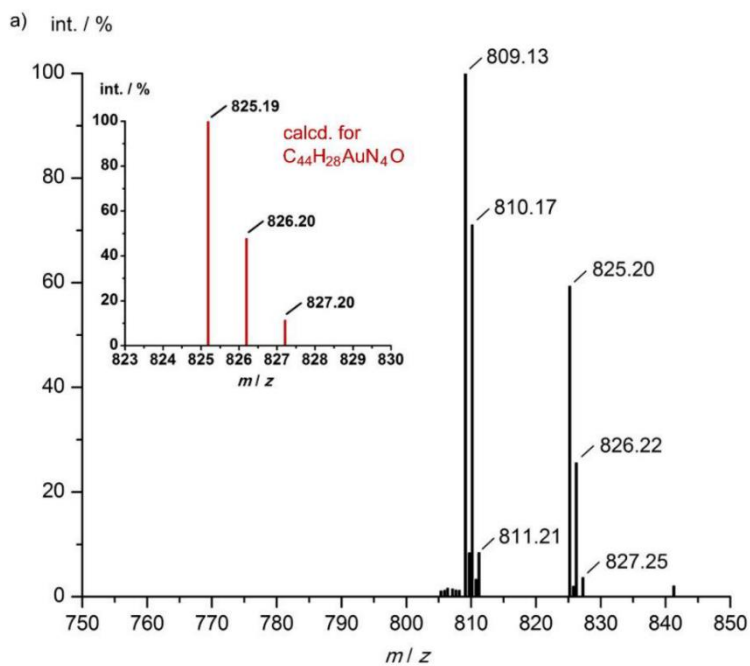


Figure 27. X-band EPR spectrum of **Au(TPP)** and PhNO in CH₂Cl₂ at 77 K (red) including simulation (black) with $g = 2.021, 2.017, 2.003$ and $A(^{14}\text{N}) = 11, 5, 10$ G, linewidth pp Gauss 1.0 MHz; linewidth pp Lorentz 0.1 MHz.

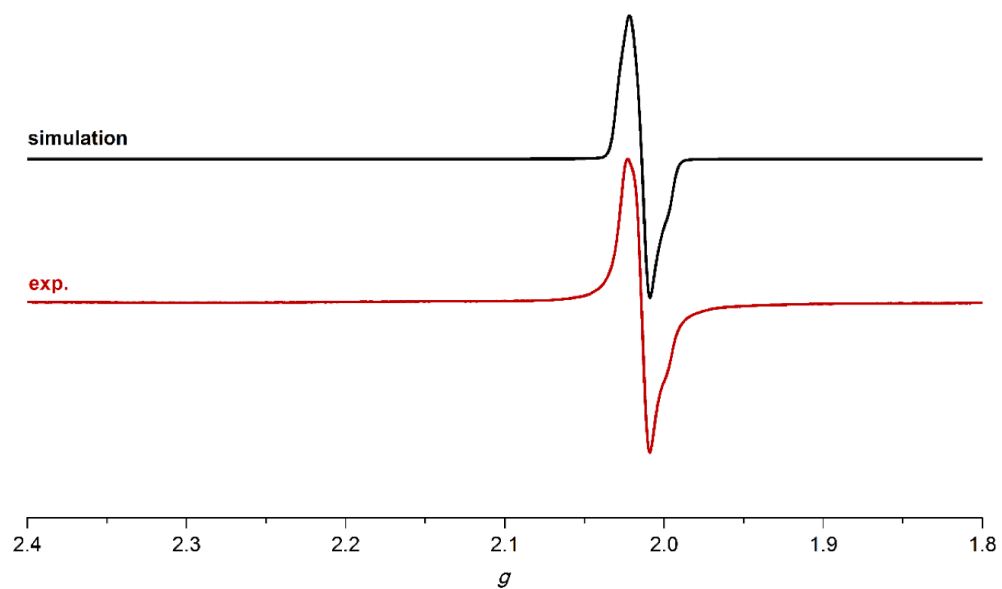


Figure 28. ^1H NMR spectra of a) 1-benzyl-1,4-dihydronicotinamide (BNAH), b) $[\text{Au}(\text{TPP})][\text{OH}] + 2$ eq BNAH, c) $[\text{Au}(\text{TPP})][\text{OH}] + 15$ eq BNAH + 15 eq KOH and d) $[\text{Au}(\text{TPP})][\text{OH}] + 15$ eq BNAH + 15 eq KOH after 6h in d_8 -THF. Asterisks denote residual solvent resonances.

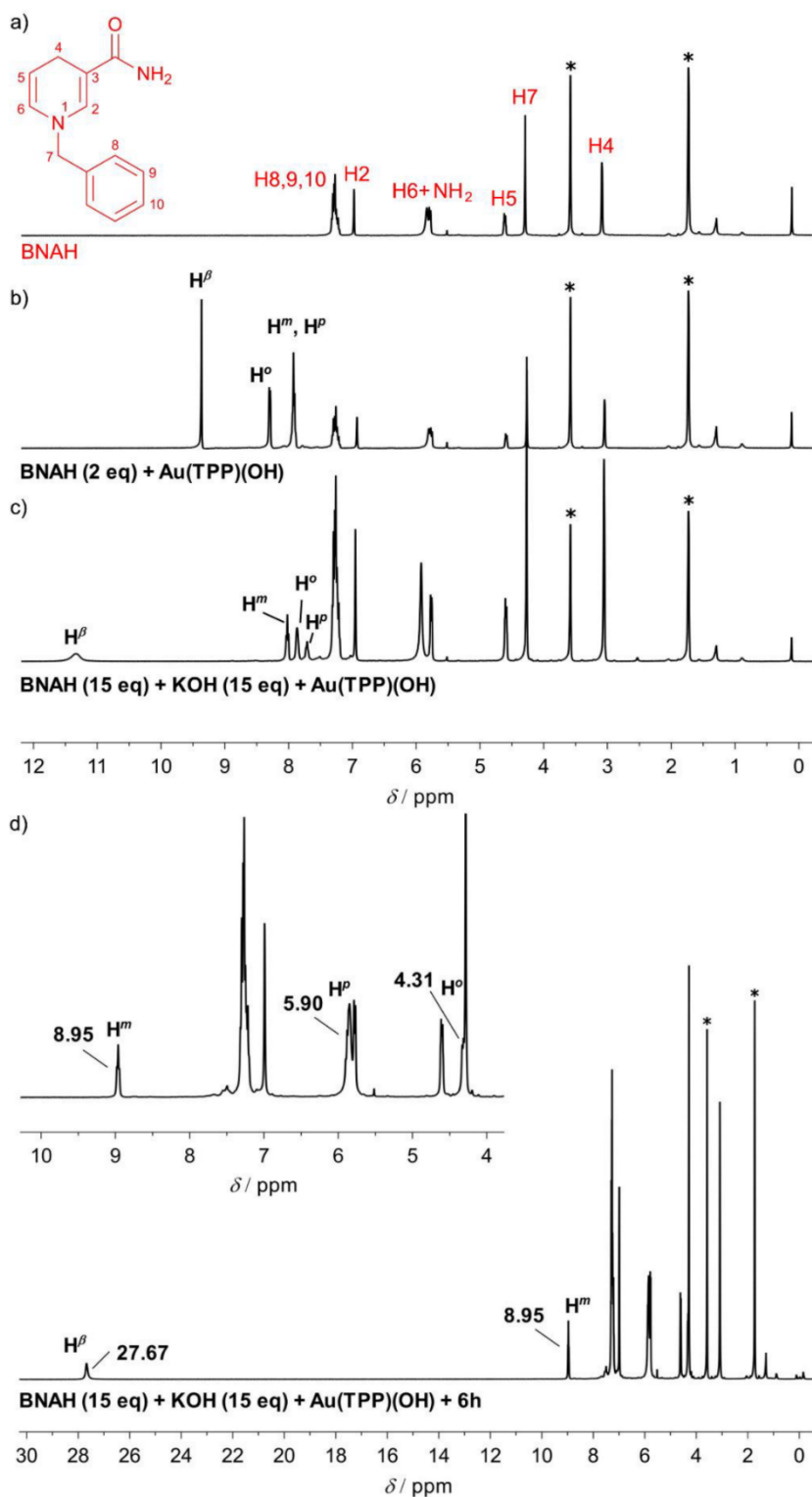


Figure 29. ^1H NMR spectrum of **Au(TPP)** in the presence of excess H_2O in $\text{d}_8\text{-THF}$. Asterisks denote residual solvent resonances.

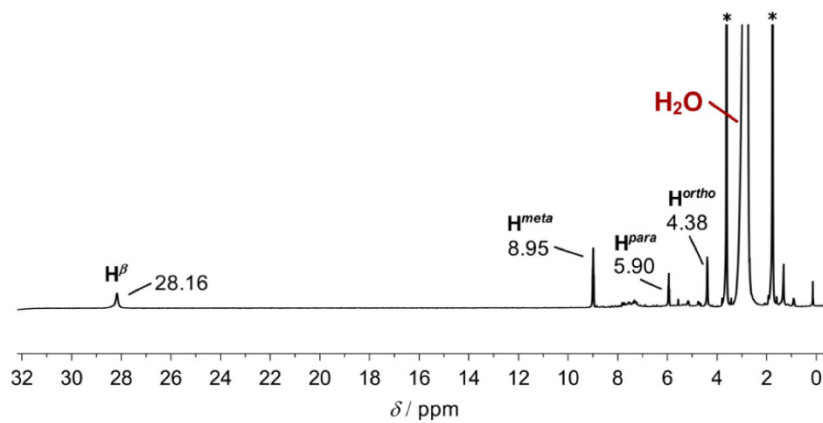
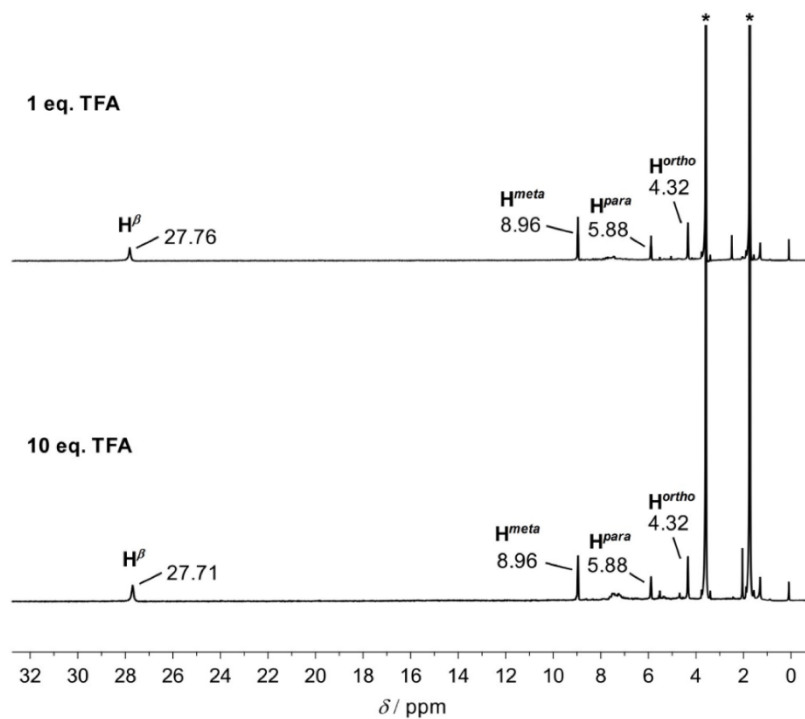


Figure 30. ^1H NMR spectra of **Au(TPP)** in the presence of increasing amounts of TFA in $\text{d}_8\text{-THF}$. Asterisks denote residual solvent resonances.



Cartesian Coordinates of DFT calculated compounds:**Au(TPP) [B3LYP, ECP, COSMO CH₂Cl₂]**

79	1.360403000	4.255488000	6.118248000
7	0.109603000	2.843312000	5.214163000
7	0.322107000	4.009871000	7.939408000
6	0.127478000	2.497925000	3.887823000
6	-0.890263000	1.503375000	3.676657000
1	-1.105458000	1.022344000	2.738516000
6	-1.495589000	1.272526000	4.874721000
1	-2.313021000	0.600308000	5.068850000
6	-0.865220000	2.120507000	5.851268000
6	-1.204231000	2.193779000	7.219156000
6	-2.271343000	1.262743000	7.705084000
6	-2.039843000	-0.113162000	7.788694000
1	-1.075195000	-0.509784000	7.500105000
6	-3.031020000	-0.973629000	8.248813000
1	-2.831666000	-2.035410000	8.313269000
6	-4.272536000	-0.471825000	8.627294000
1	-5.044560000	-1.141204000	8.983415000
6	-4.514915000	0.895692000	8.545706000
1	-5.478333000	1.294984000	8.834932000
6	-3.520824000	1.756006000	8.090881000
1	-3.716337000	2.818621000	8.028095000
6	-0.610383000	3.031356000	8.175483000
6	-0.837479000	2.967696000	9.601856000
1	-1.511105000	2.287490000	10.093551000
6	-0.025168000	3.882289000	10.188378000
1	0.078402000	4.078218000	11.241527000
6	0.726214000	4.536002000	9.140615000
6	1.729779000	5.496241000	9.337634000
6	1.928889000	5.989244000	10.737466000
6	0.984853000	6.830044000	11.333312000
1	0.109196000	7.129572000	10.772216000
6	1.163953000	7.290986000	12.633541000
1	0.425089000	7.945915000	13.076705000
6	2.288145000	6.912772000	13.360716000
1	2.426924000	7.268915000	14.373050000
6	3.232799000	6.073030000	12.778539000
1	4.108092000	5.769685000	13.338093000
6	3.055520000	5.617481000	11.476416000
1	3.792242000	4.961560000	11.031237000
7	2.611247000	5.667688000	7.022316000
7	2.398591000	4.501303000	4.297011000
6	2.593364000	6.013074000	8.348657000
6	3.611266000	7.007446000	8.559866000
1	3.826571000	7.488366000	9.498035000
6	4.216615000	7.238277000	7.361817000
1	5.034104000	7.910429000	7.167728000
6	3.586118000	6.390457000	6.385214000
6	3.925074000	6.317268000	5.017297000
6	4.992192000	7.248251000	4.531331000
6	4.761182000	8.624313000	4.448887000
1	3.796930000	9.021113000	4.738537000
6	5.752334000	9.484724000	3.988617000
1	5.553337000	10.546625000	3.925052000
6	6.993332000	8.982694000	3.608726000
1	7.765320000	9.652012000	3.252412000
6	7.235235000	7.615018000	3.689132000
1	8.198256000	7.215546000	3.398839000
6	6.241188000	6.754787000	4.144198000
1	6.436298000	5.692048000	4.206044000
6	3.331103000	5.479795000	4.060934000
6	3.557996000	5.543610000	2.634533000
1	4.231588000	6.223831000	2.142826000
6	2.745616000	4.629081000	2.048006000
1	2.641878000	4.433307000	0.994840000
6	1.994398000	3.975241000	3.095798000

6	0.990927000	3.014908000	2.898814000
6	0.791772000	2.521934000	1.498971000
6	1.735597000	1.680840000	0.903210000
1	2.611118000	1.381017000	1.464368000
6	1.556425000	1.219906000	-0.397014000
1	2.295129000	0.564769000	-0.840137000
6	0.432433000	1.598489000	-1.124296000
1	0.293634000	1.242388000	-2.136643000
6	-0.511995000	2.438542000	-0.542208000
1	-1.387130000	2.742194000	-1.101844000
6	-0.334696000	2.894023000	0.759938000
1	-1.071256000	3.550203000	1.205013000

Au(TPP) [B3LYP, def2-SVP/ZORA, COSMO CH₂Cl₂]

79	1.360625000	4.255308000	6.118274000
7	0.098067000	2.830951000	5.206632000
7	0.349382000	3.971837000	7.961646000
6	0.113660000	2.491206000	3.877720000
6	-0.907046000	1.485342000	3.661881000
1	-1.127406000	1.005714000	2.715377000
6	-1.513331000	1.251455000	4.866564000
1	-2.332549000	0.570052000	5.064397000
6	-0.872393000	2.103918000	5.847859000
6	-1.207380000	2.173711000	7.224887000
6	-2.284912000	1.249015000	7.710951000
6	-2.079232000	-0.142367000	7.750893000
1	-1.122198000	-0.551840000	7.429214000
6	-3.084177000	-1.000810000	8.209702000
1	-2.904278000	-2.075218000	8.239235000
6	-4.313792000	-0.482435000	8.632790000
1	-5.097175000	-1.151016000	8.988452000
6	-4.530610000	0.900001000	8.596963000
1	-5.485643000	1.312636000	8.921260000
6	-3.523608000	1.758302000	8.142185000
1	-3.700025000	2.833152000	8.112432000
6	-0.604295000	3.013060000	8.192398000
6	-0.856800000	2.965695000	9.621702000
1	-1.551407000	2.295539000	10.114899000
6	-0.038412000	3.887287000	10.212310000
1	0.050678000	4.100484000	11.271304000
6	0.734490000	4.520519000	9.158601000
6	1.743021000	5.494543000	9.353810000
6	1.934448000	5.996520000	10.755284000
6	0.954272000	6.799498000	11.366851000
1	0.055291000	7.063500000	10.810654000
6	1.127319000	7.268806000	12.673511000
1	0.359594000	7.894309000	13.128376000
6	2.282123000	6.938746000	13.392440000
1	2.416487000	7.302485000	14.410655000
6	3.263031000	6.137767000	12.795755000
1	4.162863000	5.871222000	13.349607000
6	3.091259000	5.672239000	11.487645000
1	3.855548000	5.043871000	11.031470000
7	2.622917000	5.679946000	7.029831000
7	2.371615000	4.539059000	4.274802000
6	2.607239000	6.019772000	8.358725000
6	3.627915000	7.025666000	8.574546000
1	3.848291000	7.505310000	9.521031000
6	4.234229000	7.259522000	7.369878000
1	5.053379000	7.941003000	7.172061000
6	3.593355000	6.407006000	6.388588000
6	3.928350000	6.337223000	5.011551000
6	5.005774000	7.262002000	4.525434000
6	4.800335000	8.653449000	4.486411000
1	3.843585000	9.062925000	4.808914000
6	5.805156000	9.511978000	4.027500000
1	5.625428000	10.586435000	3.998694000

6	7.034394000	8.993617000	3.603291000
1	7.817669000	9.662248000	3.247485000
6	7.250976000	7.611115000	3.638174000
1	8.205725000	7.198486000	3.313044000
6	6.244124000	6.752749000	4.093152000
1	6.420347000	5.677849000	4.122153000
6	3.325227000	5.497893000	4.044028000
6	3.577569000	5.545380000	2.614694000
1	4.272139000	6.215543000	2.121464000
6	2.759123000	4.623837000	2.024093000
1	2.669846000	4.410781000	0.965083000
6	1.986357000	3.990508000	3.077833000
6	0.977832000	3.016487000	2.882635000
6	0.786283000	2.514607000	1.481136000
6	1.766061000	1.711031000	0.869719000
1	2.664816000	1.446497000	1.426032000
6	1.592834000	1.241707000	-0.436913000
1	2.360219000	0.615717000	-0.891682000
6	0.438311000	1.572423000	-1.155988000
1	0.303845000	1.208695000	-2.174192000
6	-0.542165000	2.374048000	-0.559466000
1	-1.441789000	2.641080000	-1.113421000
6	-0.370267000	2.839520000	0.748650000
1	-1.134246000	3.468360000	1.204704000

Au(TPP) [B3LYP, def2-TZVPP/ZORA, D3(BJ), COSMO CH₂Cl₂]

79	1.360160000	4.255798000	6.118159000
7	0.113477000	2.848413000	5.217549000
7	0.308034000	4.029716000	7.927828000
6	0.136611000	2.496187000	3.892230000
6	-0.882045000	1.504159000	3.679960000
1	-1.090306000	1.020208000	2.742003000
6	-1.495966000	1.281162000	4.877522000
1	-2.317718000	0.615031000	5.073100000
6	-0.867470000	2.130600000	5.852685000
6	-1.212490000	2.209822000	7.214813000
6	-2.274039000	1.281878000	7.700593000
6	-2.064213000	-0.098531000	7.716453000
1	-1.118696000	-0.495717000	7.372300000
6	-3.052548000	-0.959303000	8.179067000
1	-2.872241000	-2.026102000	8.191428000
6	-4.267480000	-0.451215000	8.628448000
1	-5.037636000	-1.121126000	8.987011000
6	-4.486291000	0.922465000	8.615100000
1	-5.429164000	1.325737000	8.960188000
6	-3.494984000	1.782569000	8.156618000
1	-3.667467000	2.850538000	8.145669000
6	-0.623647000	3.049404000	8.165422000
6	-0.848169000	2.983061000	9.592194000
1	-1.518682000	2.298019000	10.080980000
6	-0.035476000	3.898899000	10.178935000
1	0.074312000	4.094344000	11.231361000
6	0.712848000	4.554944000	9.130332000
6	1.716475000	5.507616000	9.329021000
6	1.914621000	5.996829000	10.724044000
6	0.937519000	6.778525000	11.343086000
1	0.038376000	7.033327000	10.798012000
6	1.115075000	7.234588000	12.644316000
1	0.350953000	7.844089000	13.108362000
6	2.271202000	6.909630000	13.346370000
1	2.409277000	7.262187000	14.359841000
6	3.248989000	6.128026000	12.738718000
1	4.148714000	5.866316000	13.279770000
6	3.072300000	5.676936000	11.436006000
1	3.831920000	5.065787000	10.967263000
7	2.606960000	5.663050000	7.018820000
7	2.412434000	4.481683000	4.308567000

6	2.583904000	6.015183000	8.344168000
6	3.602627000	7.007141000	8.556451000
1	3.810999000	7.490985000	9.494431000
6	4.216511000	7.230174000	7.358887000
1	5.038246000	7.896321000	7.163320000
6	3.587973000	6.380792000	6.383702000
6	3.933043000	6.301511000	5.021588000
6	4.994707000	7.229280000	4.535788000
6	4.785308000	8.609760000	4.520404000
1	3.840077000	9.007171000	4.865065000
6	5.773722000	9.470357000	4.057639000
1	5.593730000	10.537212000	4.045620000
6	6.988288000	8.962007000	3.607559000
1	7.758483000	9.631766000	3.248794000
6	7.206690000	7.588256000	3.620454000
1	8.149287000	7.184776000	3.274864000
6	6.215331000	6.728344000	4.079167000
1	6.387494000	5.660323000	4.089734000
6	3.344187000	5.461917000	4.070976000
6	3.568774000	5.528167000	2.644204000
1	4.239377000	6.213107000	2.155411000
6	2.756090000	4.612319000	2.057465000
1	2.646311000	4.416838000	1.005039000
6	2.007682000	3.956388000	3.106068000
6	1.004070000	3.003713000	2.907392000
6	0.806109000	2.514284000	1.512410000
6	1.782948000	1.731798000	0.893965000
1	2.681682000	1.476524000	1.439495000
6	1.605579000	1.275469000	-0.407197000
1	2.369483000	0.665371000	-0.870818000
6	0.449948000	1.601010000	-1.109801000
1	0.312063000	1.248295000	-2.123241000
6	-0.527544000	2.383452000	-0.502760000
1	-1.426873000	2.645626000	-1.044244000
6	-0.351078000	2.834747000	0.799918000
1	-1.110469000	3.446547000	1.268196000

Au(TPP) [B3LYP, def2-SVP/ZORA, COSMO CH₂Cl₂]

79	1.360625000	4.255308000	6.118274000
7	0.098067000	2.830951000	5.206632000
7	0.349382000	3.971837000	7.961646000
6	0.113660000	2.491206000	3.877720000
6	-0.907046000	1.485342000	3.661881000
1	-1.127406000	1.005714000	2.715377000
6	-1.513331000	1.251455000	4.866564000
1	-2.332549000	0.570052000	5.064397000
6	-0.872393000	2.103918000	5.847859000
6	-1.207380000	2.173711000	7.224887000
6	-2.284912000	1.249015000	7.710951000
6	-2.079232000	-0.142367000	7.750893000
1	-1.122198000	-0.551840000	7.429214000
6	-3.084177000	-1.000810000	8.209702000
1	-2.904278000	-2.075218000	8.239235000
6	-4.313792000	-0.482435000	8.632790000
1	-5.097175000	-1.151016000	8.988452000
6	-4.530610000	0.900001000	8.596963000
1	-5.485643000	1.312636000	8.921260000
6	-3.523608000	1.758302000	8.142185000
1	-3.700025000	2.833152000	8.112432000
6	-0.604295000	3.013060000	8.192398000
6	-0.856800000	2.965695000	9.621702000
1	-1.551407000	2.295539000	10.114899000
6	-0.038412000	3.887287000	10.212310000
1	0.050678000	4.100484000	11.271304000
6	0.734490000	4.520519000	9.158601000
6	1.743021000	5.494543000	9.353810000
6	1.934448000	5.996520000	10.755284000

6	0.954272000	6.799498000	11.366851000
1	0.055291000	7.063500000	10.810654000
6	1.127319000	7.268806000	12.673511000
1	0.359594000	7.894309000	13.128376000
6	2.282123000	6.938746000	13.392440000
1	2.416487000	7.302485000	14.410655000
6	3.263031000	6.137767000	12.795755000
1	4.162863000	5.871222000	13.349607000
6	3.091259000	5.672239000	11.487645000
1	3.855548000	5.043871000	11.031470000
7	2.622917000	5.679946000	7.029831000
7	2.371615000	4.539059000	4.274802000
6	2.607239000	6.019772000	8.358725000
6	3.627915000	7.025666000	8.574546000
1	3.848291000	7.505310000	9.521031000
6	4.234229000	7.259522000	7.369878000
1	5.053379000	7.941003000	7.172061000
6	3.593355000	6.407006000	6.388588000
6	3.928350000	6.337223000	5.011551000
6	5.005774000	7.262002000	4.525434000
6	4.800335000	8.653449000	4.486411000
1	3.843585000	9.062925000	4.808914000
6	5.805156000	9.511978000	4.027500000
1	5.625428000	10.586435000	3.998694000
6	7.034394000	8.993617000	3.603291000
1	7.817669000	9.662248000	3.247485000
6	7.250976000	7.611115000	3.638174000
1	8.205725000	7.198486000	3.313044000
6	6.244124000	6.752749000	4.093152000
1	6.420347000	5.677849000	4.122153000
6	3.325227000	5.497893000	4.044028000
6	3.577569000	5.545380000	2.614694000
1	4.272139000	6.215543000	2.121464000
6	2.759123000	4.623837000	2.024093000
1	2.669846000	4.410781000	0.965083000
6	1.986357000	3.990508000	3.077833000
6	0.977832000	3.016487000	2.882635000
6	0.786283000	2.514607000	1.481136000
6	1.766061000	1.711031000	0.869719000
1	2.664816000	1.446497000	1.426032000
6	1.592834000	1.241707000	-0.436913000
1	2.360219000	0.615717000	-0.891682000
6	0.438311000	1.572423000	-1.155988000
1	0.303845000	1.208695000	-2.174192000
6	-0.542165000	2.374048000	-0.559466000
1	-1.441789000	2.641080000	-1.113421000
6	-0.370267000	2.839520000	0.748650000
1	-1.134246000	3.468360000	1.204704000

Transition state **Au(TPP)** [B3LYP, def2-SVP/ZORA, COSMO CH₂Cl₂]

79	1.364397000	4.251975000	6.119462000
7	0.120803000	2.869681000	5.236237000
7	0.438453000	3.927600000	7.929393000
6	0.145582000	2.480060000	3.906558000
6	-0.793471000	1.426623000	3.722457000
1	-0.970408000	0.908513000	2.787774000
6	-1.390910000	1.185416000	4.944540000
1	-2.160320000	0.457242000	5.171650000
6	-0.824449000	2.092724000	5.883099000
6	-1.190292000	2.174363000	7.253296000
6	-2.282501000	1.263009000	7.730476000
6	-1.985859000	0.112857000	8.483098000
1	-0.947541000	-0.118519000	8.719569000
6	-3.007541000	-0.735146000	8.926066000
1	-2.758846000	-1.622540000	9.507700000
6	-4.342598000	-0.446393000	8.621029000
1	-5.138411000	-1.105978000	8.965853000

6	-4.649874000	0.694527000	7.869909000
1	-5.686960000	0.928330000	7.630100000
6	-3.627560000	1.540870000	7.427081000
1	-3.872329000	2.428973000	6.844998000
6	-0.581787000	3.018103000	8.171941000
6	-0.913166000	3.074959000	9.580673000
1	-1.690422000	2.486039000	10.053063000
6	-0.079095000	3.973635000	10.167896000
1	-0.044227000	4.260930000	11.212109000
6	0.792435000	4.505610000	9.141015000
6	1.801136000	5.431468000	9.366651000
6	2.022466000	5.921271000	10.767516000
6	1.597517000	7.205622000	11.152427000
1	1.100384000	7.845604000	10.423876000
6	1.800501000	7.663853000	12.458760000
1	1.459897000	8.659747000	12.741083000
6	2.435640000	6.845417000	13.400661000
1	2.594023000	7.202001000	14.418088000
6	2.866101000	5.566865000	13.028143000
1	3.363507000	4.924021000	13.754029000
6	2.661601000	5.109338000	11.721229000
1	3.002003000	4.114586000	11.434822000
7	2.602327000	5.639495000	7.003566000
7	2.302727000	4.565648000	4.313844000
6	2.661140000	5.935052000	8.354624000
6	3.724541000	6.854153000	8.575993000
1	4.001477000	7.262546000	9.540479000
6	4.297739000	7.127812000	7.349133000
1	5.143660000	7.773081000	7.145303000
6	3.595030000	6.369923000	6.370612000
6	3.885312000	6.368233000	4.980574000
6	4.938010000	7.315346000	4.490590000
6	4.727035000	8.706487000	4.523464000
1	3.784174000	9.095766000	4.906244000
6	5.707814000	9.590079000	4.061191000
1	5.523110000	10.663816000	4.087514000
6	6.920302000	9.098009000	3.562695000
1	7.685076000	9.786309000	3.204085000
6	7.143948000	7.716924000	3.528156000
1	8.085992000	7.324538000	3.145834000
6	6.160607000	6.833625000	3.987856000
1	6.342841000	5.759567000	3.963984000
6	3.242270000	5.556445000	4.054091000
6	3.446148000	5.624882000	2.622753000
1	4.114061000	6.320754000	2.129238000
6	2.640875000	4.695470000	2.042825000
1	2.525186000	4.488336000	0.985605000
6	1.908641000	4.024891000	3.095733000
6	0.961517000	3.030656000	2.883590000
6	0.763012000	2.522646000	1.487677000
6	1.758567000	1.754712000	0.856558000
1	2.676984000	1.523402000	1.395362000
6	1.577917000	1.280263000	-0.447592000
1	2.359284000	0.684066000	-0.918370000
6	0.397899000	1.567471000	-1.143012000
1	0.256927000	1.199544000	-2.158855000
6	-0.600727000	2.330606000	-0.525573000
1	-1.520853000	2.562953000	-1.061281000
6	-0.420504000	2.801501000	0.779138000
1	-1.199660000	3.398215000	1.252302000

-
- [1] Preiß, S., Melomedov, J., Wünsche von Leupoldt, A. & Heinze, K. Gold(III) tetraarylporphyrin amino acid derivatives: ligand or metal centred redox chemistry?. *Chem. Sci.* **7**, 596–610 (2016).
- [2] Fulmer, G. R., Miller, A. J. M., Sherden, N. H., Gottlieb, H. E., Nudelman, A., Stoltz, B. M., Bercaw, J. E. & Goldberg, K. I. NMR Chemical Shifts of Trace Impurities: Common Laboratory Solvents, Organics, and Gases in Deuterated Solvents Relevant to the Organometallic Chemist. *Organometallics* **29**, 2176–2179 (2010).
- [3] Stoll, S. & Schweiger, A. EasySpin, a comprehensive software package for spectral simulation and analysis in EPR. *J. Magn. Reson.* **178**, 42–55 (2006).
- [4] Bauer, M., Heusel, G., Mangold, S. & Bertagnolli, H. Spectroscopic set-up for simultaneous UV-Vis/(Q)EXAFS in situ and in operando studies of homogeneous reactions under laboratory conditions. *J. Synchr. Rad.* **17**, 273–279 (2010).
- [5] Villa, A., Dimitratos, N., Chan-Thaw, C. E., Hammond, C., Veith, G. M., Wang, D., Manzoli, M., Prati, L. & Hutchings, G. J. Characterisation of gold catalysts. *Chem. Soc. Rev.* **45**, 4953–4994 (2016).
- [6] van Bokhoven, J. A. & Miller, J. T. d Electron Density and Reactivity of the d Band as a Function of Particle Size in Supported Gold Catalysts. *J. Phys. Chem. C* **111**, 9245–9249 (2007).
- [7] Serrano-Becerra, J. M., Maier, A. F. G., González-Gallardo, S., Moos, E., Kaub, C., Gaffga, M., Niedner-Schatteburg, G., Roesky, P. W., Breher, F. & Paradies, J. Mono- vs. Dinuclear Gold-Catalyzed Intermolecular Hydroamidation. *Eur. J. Org. Chem.* 4515–4522 (2014).
- [8] Bus, E., Miller, J. T. & van Bokhoven, J. A. Hydrogen Chemisorption on Al₂O₃-Supported Gold Catalysts. *J. Phys. Chem. B* **109**, 14581–14587 (2005).
- [9] Bauer, M. & Bertagnolli, H. in *Methods in Physical Chemistry*, Wiley-VCH, 231–269 (2012).
- [10] Gurman, S. J., Binsted, N. & Ross, I. A rapid, exact curved-wave theory for EXAFS calculations. *J. Phys. C: Solid State Phys.* **17**, 143–151 (1984).
- [11] SMART Data Collection and SAINT-Plus Data Processing Software for the SMART System (various versions); Bruker Analytical X-Ray Instruments, Inc., Madison, WI (2000).
- [12] Blessing, R. H. An empirical correction for absorption anisotropy. *Acta Cryst. A* **51**, 33–38 (1995).
- [13] Sheldrick, G. M. Crystal structure refinement with SHELXL. *Acta Cryst. C* **71**, 3–8 (2015).
- [14] Sheldrick, G. M. SHELXL-2014/7, University of Göttingen, Germany (2014).
- [15] Neese, F. The ORCA program system. *WIREs Comput Mol Sci* **2**, 73–78 (2012).
- [16] Becke, A. D. Density-functional thermochemistry. III. The role of exact exchange. *J. Chem. Phys.* **98**, 5648–5652 (1993).
- [17] Pantazis, D. A., Chen, X.-Y., Landis, C. R. & Neese, F. All-Electron Scalar Relativistic Basis Sets for Third-Row Transition Metal Atoms. *J. Chem. Theory Comput.* **4**, 908–919 (2008).
- [18] Theilacker, K., Schlegel, H. B., Kaupp, M. & Schwerdtfeger, P. Relativistic and Solvation Effects on the Stability of Gold(III) Halides in Aqueous Solution. *Inorg. Chem.* **54**, 9869–9875 (2015).

-
- [19] Neese, F., Wennmohs, F., Hansen, A. & Becker, U. Efficient, approximate and parallel Hartree–Fock and hybrid DFT calculations. A ‘chain-of-spheres’ algorithm for the Hartree–Fock exchange. *Chem. Phys.* **356**, 98–109 (2009).
- [20] Izsák, R. & Neese, F. An overlap fitted chain of spheres exchange method. *J. Chem. Phys.* **135**, 144105 (2011).
- [21] Sinnecker, S., Rajendran, A., Klamt, A., Diedenhofen, M. & Neese, F. Calculation of Solvent Shifts on Electronic g-Tensors with the Conductor-Like Screening Model (COSMO) and Its Self-Consistent Generalization to Real Solvents (Direct COSMO-RS). *J. Phys. Chem. A* **110**, 2235–2245 (2006).
- [22] Grimme, S., Ehrlich, S. & Goerigk, L. Effect of the damping function in dispersion corrected density functional theory. *J. Comput. Chem.* **32**, 1456–1465 (2011).
- [23] Grimme, S., Antony, J., Ehrlich, S. & Krieg, H. A consistent and accurate ab initio parametrization of density functional dispersion correction (DFT-D) for the 94 elements H–Pu. *J. Chem. Phys.* **132**, 154104 (2010).
- [24] Petrenko, T., Kossmann, S. & Neese, F. Efficient time-dependent density functional theory approximations for hybrid density functionals: Analytical gradients and parallelization. *J. Chem. Phys.* **134**, 054116 (2011).

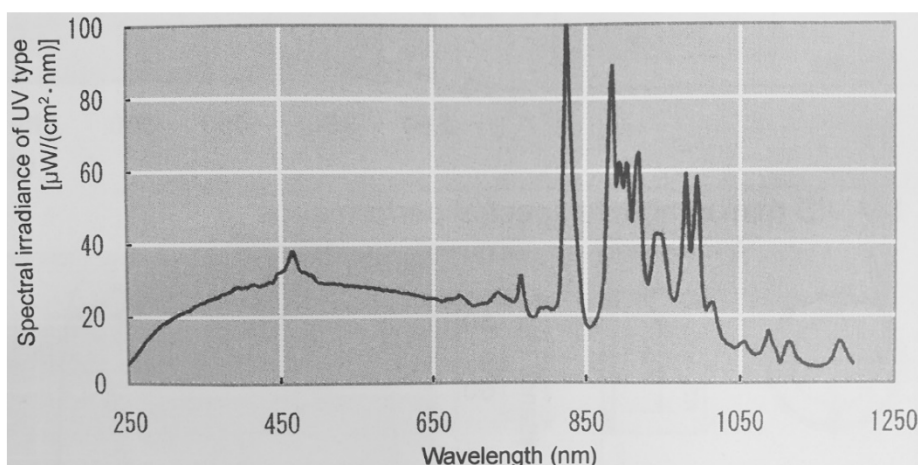
6.3 Supporting Information to 3.3: Gold(II) porphyrins in photoinduced electron transfer reactions

General considerations: All reactions were performed under an argon atmosphere unless otherwise noted. Dichloromethane was dried with CaH₂ and distilled prior to use. THF was distilled from potassium. Absolute DMF was used as received from Acros. 1-[Bis(dimethylamino)methylene]-1H-1,2,3-triazolo[4,5-b]pyridinium 3-oxidehexafluorophosphate (HATU) was commercially available from Novabiochem. *N,N*-diisopropylethylamine (DIPEA) was commercial available from Sigma-Aldrich and dried with NaOH overnight under argon prior to use. All other reagents were used as received from commercial suppliers (Acros, Sigma-Aldrich, ABCR). Porphyrins **Ia**, **Ila**, **Illa**, **[Ib][PF₆]**, **[IIb][PF₆]**, **[IIIb][PF₆]**, and reference porphyrins **Zn-Ac-Ia**, **Zn-Ac-Ila**, **Zn-Ac-Illa**, **[Au-Ac-Ib][PF₆]**, **[Au-Ac-IIb][PF₆]**, **[Au-Ac-IIIb][PF₆]** were prepared according to ref.^[1] NMR spectra were recorded on a Bruker DRX 400 spectrometer at 400.31 MHz (¹H) and 100.05 MHz (¹³C{¹H}). All resonances are reported in ppm vs. the solvent signal as internal standard: *d*₇-*N,N*-dimethylformamide (¹H: δ = 8.03, 2.92, 2.75 ppm; ¹³C: δ = 163.2, 34.9, 29.8 ppm)^[2]; UV/Vis/NIR spectra were recorded on a Varian Cary 5000 spectrometer using 1.0 cm cells. Steady state emission spectra were recorded on a Varian Cary Eclipse spectrometer in 1.0 cm cells. Quantum yields Φ were determined by comparing the areas under the emission spectra on an energy scale [cm⁻¹] recorded for optically matched solutions (absorption intensity below 0.05) of the samples and the reference (Φ (H₂TPP) = 0.13 in benzene)^[3] using the equation^[4] $\Phi = \Phi_{\text{ref}} \times I_{\text{ref}} \times \eta^2 / \eta_{\text{ref}}^2$ with η (benzene) = 1.5011, η (CH₂Cl₂) = 1.4242; experimental uncertainty 15 %. IR spectra were recorded on a Bruker Alpha FTIR spectrometer with ATR unit containing a diamond crystal. HR-ESI⁺ mass spectra were recorded with a Micromass Q-TOF-Ultima spectrometer. Electrochemical experiments were carried out with a BioLogic SP-50 voltammetric analyser using a platinum working electrode, a platinum wire as counter electrode, and a 0.01 M Ag/AgNO₃ electrode as reference electrode. The measurements were carried out at a scan rate of 100 mV s⁻¹ for cyclic voltammetry experiments using 0.1 M [ⁿBu₄N][PF₆] as supporting electrolyte and 0.001 M of the sample in tetrahydrofuran. Potentials are given relative to the ferrocene / ferrocenium couple. X-band CW EPR spectra (ca. 5 × 10⁻³ M, 9.4 GHz) were measured on a Miniscope MS 300 at 77 K cooled by liquid nitrogen in a finger Dewar (Magnettech GmbH, Berlin, Germany). *g* factors are referenced to external Mn²⁺ in ZnS (*g* = 2.118, 2.066, 2.027, 1.986, 1.946, 1.906). Time-resolved luminescence was measured by a streak camera system (C10627, Hamamatsu Photonics) using 160 fs pulses of a Ti:sapphire laser (CPA 2001, Clark MXR, Inc.). The transient absorption spectra were recorded using laser pulses with a time resolution of ca. 200 fs in a pump-probe setup. For these measurements, a Ti:sapphire laser system (Spectra-Physics, Spitfire Pro) with a center wavelength of 800 nm and a repetition rate of 1 kHz was used. By applying a BBO-crystal for frequency doubling the pump-wavelength of 400 nm was generated. The white light continuum for the probe was generated with a CaF₂ crystal. Both beams were focussed into the sample with the magic angle and overlapped with a diameter of 108 μ m for the pump and 75 μ m for the probe. The sample was dissolved in THF and filled into a 1 mm fused silica cuvette. The optical density was set at 400 nm to 0.7–1.0 to obtain transient spectra with a good signal to noise ratio. This corresponds to different concentrations for the various compounds due to the differences in the absorption spectra. XAS spectral measurements were performed at beamline P64 of PETRA III (Hamburg, Germany) under ambient conditions at 293 K. A Si(111) double crystal

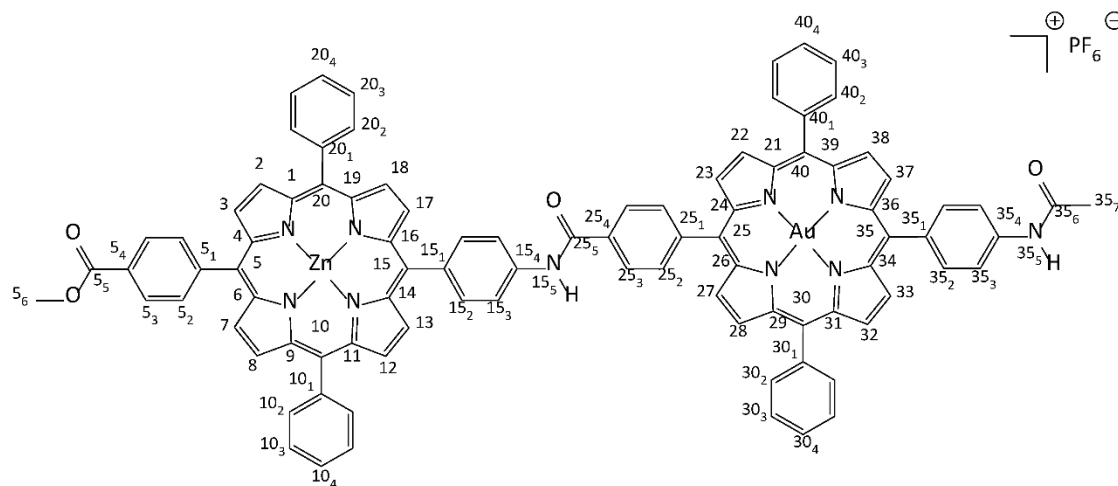
monochromator was used for measurements at the Au L₃ edge (11.918 keV). The second monochromator crystal was tilt for optimal harmonic rejection. Energy calibration was performed with a gold metal foil. The samples were handled in a glove box. A reduced sample of **[3][PF₆]** (NEt₃, 420±5 nm; 64 % reduction, 3 mg) was dissolved in DMF (2 ml). The spectra were recorded in fluorescence mode using a PIPS detector, employing a Schlenk tube like cell that allows measuring under fully inert conditions. After the measurement under inert conditions, oxygen was allowed to oxidise the sample and the measurement was repeated.

DFT calculations: DFT calculations were carried out using the ORCA program package (version 4.0.1.2).^[6] Tight convergence criteria were chosen for all calculations (keywords TightSCF and TightOpt). For geometry optimizations and energy calculations, the B3LYP formulation^[7] of density functional theory was used employing the ZORA-def2-SVP basis set for the porphyrin macrocycle and Au-SARC-ZORA-def2-TZVP basis set for the gold centre with the zeroth order regular approximation (keyword: ZORA)^[8], the RIJCOSX approximation^[9], at GRID4 for C, H, N, O, Zn and a higher accuracy for the gold atom (keyword: SpecialGridIntAcc 7). To account for solvent effects, a conductor-like polarizable continuum model (CPCM, CH₂Cl₂) modelling dichloromethane was used in all calculations.^[10] Grimme's empirical dispersion correction D3BJ was employed.^[11] No symmetry constraints were imposed on the molecules. The presence of energy minima of the ground states and excited states was checked by numerical frequency calculations. Explicit counterions and/or solvent molecules were not taken into account.

PET and catalysis experiments: The experiments were carried out using an Asahi Spectra Max-303 Xenon Light Source (300 W), together with 420 nm±5 nm filters (Soret band) and 560 nm±5 nm filters (Q band), respectively.



Experimental Section:



[1][PF₆]: The free-base porphyrin acid component **[1b][PF₆]** (71.1 mg, 0.068 mmol, 0.9 eq) was dissolved in anhydrous DMF (5 mL). HATU (28.5 mg, 0.075 mmol, 1.0 eq) and DIPEA (14.5 mg, 0.118 mmol, 1.5 eq) were added and the reaction mixture was stirred for 5 min at room temperature. The solution was added dropwise to a solution of the porphyrin amino component **1a** (51.5 mg, 0.075 mmol, 1.0 eq) in DMF (5 mL). The mixture was stirred for 2 d at room temperature, diluted with CH₂Cl₂ (50 mL) and washed with water (3×10 mL). The organic phase was separated, dried with MgSO₄ and concentrated under reduced pressure. After column chromatography (silica, CH₂Cl₂/methanol 10:1) the intermediate free-base gold bis(porphyrin) in 38 % yield (44.1 mg, 0.026 mmol; *R_f* = 0.32) was dissolved in CH₂Cl₂ (200 mL). Zinc acetate dihydrate (27.4 mg, 0.125 mmol) was added to the solution and the solution was stirred for 1 d. Subsequently, a saturated aqueous solution of potassium hexafluorophosphate (20 mL) was added to the mixture and it was stirred for 2 d. The organic phase was separated, washed with water (3×20 mL), dried with MgSO₄ and concentrated under reduced pressure. After column chromatography (silica, CH₂Cl₂/methanol 10:1; *R_f* = 0.32) **[1][PF₆]** was isolated as purple powder in 98 % yield (45.6 mg, 0.025 mmol). Yield over all steps was 37 %. C₉₃H₆₀AuF₆N₁₀O₄PZn (1788.88 g mol⁻¹).

¹H NMR (d₇-DMF): δ(ppm) = 2.34 (s, 3H, H^{35₇}), 4.13 (s, 3H, H^{5₆}), 7.88 (m, 6H, H^{10/20_{3/4}}), 8.04 (m, 6H, H^{30/40_{3/4}}), 8.32 (m, 6H, H^{10/20/35_{2/2/3}}), 8.37 (d, 2H, ³*J*_{HH} = 8.5 Hz, H^{35₂}), 8.41 (d, 2H, ³*J*_{HH} = 8.3 Hz, H^{15₂}), 8.45 (m, 4H, H^{30/40_{2/2}}), 8.47 (s, 4H, H^{5_{2/3}}), 8.60 (d, 2H, ³*J*_{HH} = 8.2 Hz, H^{15₃}), 8.68 (d, 2H, ³*J*_{HH} = 7.8 Hz, H^{25₂}), 8.84 (d, 2H, ³*J*_{HH} = 7.9 Hz, H^{25₃}), 8.90 (m, 4H, H^β), 8.95 (d, 2H, ³*J*_{HH} = 4.6 Hz, H^β), 9.06 (d, 2H, ³*J*_{HH} = 4.7 Hz, H^β), 9.49 (d, 2H, ³*J*_{HH} = 5.2 Hz, H^β), 9.54 (d, 2H, ³*J*_{HH} = 5.3 Hz, H^β), 9.60 (m, 4H, H^β), 10.68 (s, 1H, H^{35₅}), 11.29 (s, 1H, H^{15₅}).

¹³C NMR (d₇-DMF): Poor solubility of **[1][PF₆]** in DMF.

³¹P NMR (d₇-DMF): δ(ppm) = -143.0 (sept, ¹*J*_{PF} = 710 Hz).

HR MS (ESI): *m/z* (%) = 1641.3703 (calcd for C₉₃H₆₀AuN₁₀O₄Zn: 1641.3756).

UV/vis/NIR (CH₂Cl₂): λ (nm) (ε / (M⁻¹ cm⁻¹)) = 421 (408.980), 525 (16.411), 548 (20.026), 586 (7.497).

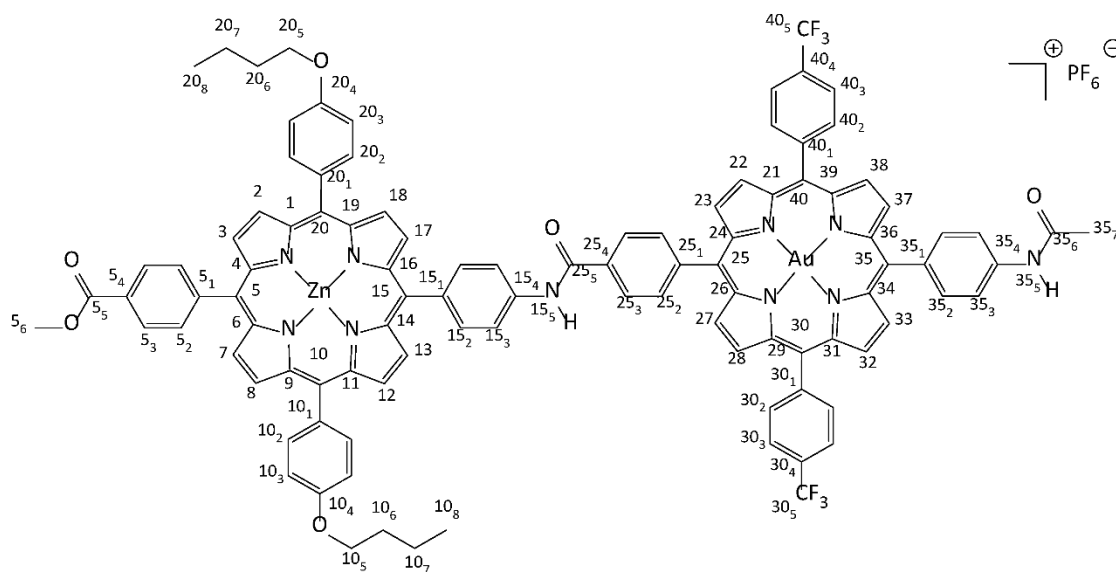
Fluorescence (CH₂Cl₂): λ (nm) (relative intensity) = 599 (1.00), 646 (0.85).

Quantum yield: $\Phi = 0.0029$.

Lifetime: τ (ns) = 1.6.

IR: $\tilde{\nu}$ (cm⁻¹) = 2956 (CH, w), 2923 (CH, w), 2851 (CH, w), 1717 (CO, w), 1667 (CO, w), 1593 (m), 1507 (m), 1322 (m), 1245 (OCO, m), 1171 (s), 1107 (m), 1068 (m), 841 (PF, s), 798, s), 556 (PF, m).

CV (Fch/Fch⁺, 100 mV s⁻¹, DMF, 0.1 M [ⁿBu₄N][PF₆]): $E_{1/2}$ (V) = 0.42 (rev.), -0.95 (rev.), -1.44 (rev.), -1.77 (rev.).



[2][PF₆]: The free-base porphyrin acid component **[Iib][PF₆]** (36.5 mg, 0.049 mmol, 0.9 eq) was dissolved in anhydrous DMF (5 mL). HATU (20.5 mg, 0.054 mmol, 1.0 eq) and DIPEA (10.0 mg, 0.081 mmol, 1.5 eq) were added and the reaction mixture was stirred for 5 min at room temperature. The solution was added dropwise to a solution of the porphyrin amino component **Ila** (45.0 mg, 0.054 mmol, 1.0 eq) in DMF (5 mL). The mixture was stirred for 2 d at room temperature, diluted with CH₂Cl₂ (50 mL) and washed with water (3×10 mL). The organic phase was separated, dried with MgSO₄ and concentrated under reduced pressure. After column chromatography (silica, CH₂Cl₂/methanol 10:1) the intermediate free-base gold bis(porphyrin) in 22 % yield (21.3 mg, 0.011 mmol; *R_f* = 0.40) was dissolved in CH₂Cl₂ (200 mL). Zinc acetate dihydrate (12.1 mg, 0.055 mmol) was added to the solution and the solution was stirred for 1 d. Subsequently, a saturated aqueous solution of potassium hexafluorophosphate (20 mL) was added to the mixture and it was stirred for 2 d. The organic phase was separated, washed with water (3×20 mL), dried with MgSO₄ and concentrated under reduced pressure. After column chromatography (silica, CH₂Cl₂/methanol 10:1; *R_f* = 0.40) **[2][PF₆]** was isolated as purple powder in 98 % yield (22.3 mg, 0.011 mmol). Yield over all steps was 21 %. C₁₀₃H₇₄AuF₁₂N₁₀O₆PZn (2066.43 g mol⁻¹).

¹H NMR (d₇-DMF): δ(ppm) = 1.10 (t, 6H, ³J_{HH} = 7.2 Hz, H^{10/20}₈), 1.68 (tq, 4H, ³J_{HH} = 7.1 Hz, H^{10/20}₇), 1.97 (p, 4H, ³J_{HH} = 7.0 Hz, H^{10/20}₆), 2.34 (s, 3H, H³⁵₇), 4.14 (s, 3H, H⁵₆), 4.35 (t, 4H, ³J_{HH} = 6.5 Hz, H^{10/20}₅), 7.44 (d, 4H, ³J_{HH} = 8.1 Hz, H^{10/20}₃), 8.21 (d, 4H, ³J_{HH} = 7.9 Hz, H^{10/20}₂), 8.36 (m, 6H, H^{15/35/35}_{2/2/3}), 8.42 (d, 4H, ³J_{HH} = 8.4 Hz, H^{30/40}_{2/2}), 8.47 (s, 4H, H⁵_{2/3}), 8.58 (d, 2H, ³J_{HH} = 8.2 Hz, H¹⁵₃), 8.69 (d, 2H, ³J_{HH} = 7.8 Hz, H²⁵₂), 8.72 (d, 4H, ³J_{HH} = 7.8 Hz, H^{30/40}_{3/3}), 8.85 (d, 2H, ³J_{HH} = 7.9 Hz, H²⁵₃), 8.89 (d, 2H, ³J_{HH} = 4.4 Hz, H^β), 8.97 (m, 4H, H^β), 9.04 (d, 2H, ³J_{HH} = 4.5 Hz, H^β), 9.54 (d, 2H, ³J_{HH} = 5.3 Hz, H^β), 9.62 (m, 6H, H^β), 10.69 (s, 1H, H³⁵₅), 11.29 (s, 1H, H¹⁵₅).

¹³C NMR (d₇-DMF): δ(ppm) = 13.7 (s, C^{10/20}_{8/8}), 19.5 (s, C^{10/20}_{7/7}), 22.7 (s, C³⁵₇), 31.7 (s, C^{10/20}_{6/6}), 52.3 (s, C⁵₆), 68.0 (s, C^{10/20}_{5/5}), 112.9 (s, C^{10/20}_{3/3}), 118.2 (s, C¹⁵₃), 118.8 (s, C³⁵₃), 119.1 (s, C⁵₁), 120.9 (s, C^{10/20}₂), 122.2 (s, C^{30/40}_{1/1}), 122.9 (s, C²⁵₂), 123.7 (s, C^{30/40}_{2/2}), 124.4 (s, C³⁵₂), 125.1 (s, C^{30/40}_{2/2}), 126.4 (s, C¹⁵₂), 127.6 (s, C²⁵₃), 127.7 (s, C⁵₂), 129.3 (s, C⁵₂), 131.0–133.7 (multiple s, C^{2/3/7/8/12/13/17/18/22/23/27/28/32/33/37/38}), 133.4

(s, C³⁵₁), 134.8 (s, C⁵₃), 135.3 (m, C^{10/15/20/25/30/35/40}_{1/2/1/2/3/2/3}), 135.8 (s, C^{10/20}_{2/2}), 136.2–137.8 (multiple s, C^{21/24/26/29/31/34/36/39}), 136.4 (s, C²⁵₄), 139.0 (s, C¹⁵₄), 139.5 (s, C¹⁵₁), 141.4 (s, C³⁵₄), 142.0 (s, C¹⁵₄), 143.1 (s, C^{30/40}_{4/4}), 148.6 (s, C⁵₄), 149.1–151.2 (multiple s, C^{1/4/6/9/11/14/16/19}), 159.1 (s, C^{10/20}_{4/4}), 166.0 (s, C²⁵₅), 167.1 (s, C⁵₅), 169.5 (s, C³⁵₆).

³¹P NMR (d₇-DMF): δ (ppm) = –143.9 (sept, ¹J_{PF} = 711 Hz).

HR MS (ESI): *m/z* (%) = 1921.4610 (calcd. for C₁₀₃H₇₄AuF₆N₁₀O₆Zn: 1921.4654).

UV/vis/NIR (CH₂Cl₂): λ (nm) (ϵ / (M⁻¹ cm⁻¹)) = 424 (470.593), 523 (15.457), 549 (18.676), 590 (5.267).

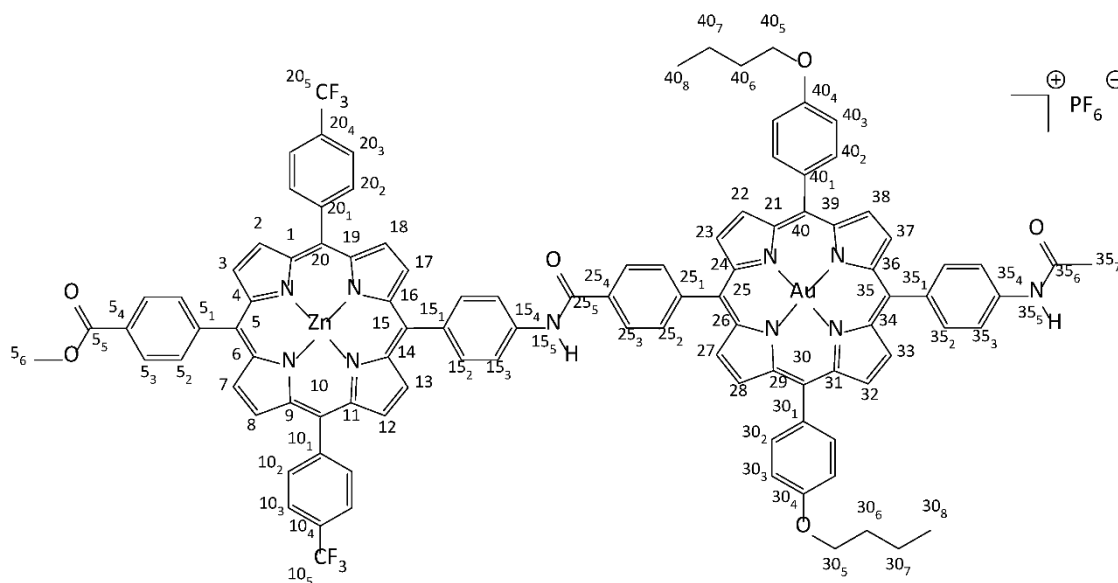
Fluorescence (CH₂Cl₂): λ (nm) (relative intensity) = 601 (1.00), 649 (0.69).

Quantum yield: Φ = 0.0017.

Lifetime: τ (ns) = 1.3.

IR: $\tilde{\nu}$ (cm⁻¹) = 2957 (CH, w), 2919 (CH, w), 2849 (CH, w), 1715 (CO, w), 1668 (CO, w), 1589 (m), 1519 (m), 1260 (OCO, m), 1096 (m), 1016 (s), 841 (PF, s), 796 (s), 556 (PF, m).

CV (Fc/FcH⁺, 100 mV s⁻¹, THF): $E_{1/2}$ (V) = $E_{1/2}$ (V) = 0.68 (rev.), 0.33 (rev.), –0.92 (rev.), –1.53 (rev.), –1.93 (rev.).



[3][PF₆]: The free-base porphyrin acid component **[IIb][PF₆]** (54.6 mg, 0.045 mmol, 0.9 eq) was dissolved in anhydrous DMF (5 mL). HATU (20.0 mg, 0.050 mmol, 1.0 eq) and DIPEA (9.3 mg, 0.075 mmol, 1.5 eq) were added and the reaction mixture was stirred for 5 min at room temperature. The solution was added dropwise to a solution of the porphyrin amino component **IIa** (41.2 mg, 0.050 mmol, 1.0 eq) in DMF (5 mL). The mixture was stirred for 2 d at room temperature, diluted with CH₂Cl₂ (50 mL) and washed with water (3×10 mL). The organic phase was separated, dried with MgSO₄ and concentrated under reduced pressure. After column chromatography (silica, CH₂Cl₂/methanol 10:1) the intermediate free-base gold porphyrin, yield 51 % (46.7 mg, 0.023 mmol; *R_f* = 0.41) was dissolved in CH₂Cl₂ (200 mL). Zinc acetate dihydrate (12.1 mg, 0.055 mmol) was added to the solution and the solution was stirred for 1 d. Subsequently, a saturated aqueous solution of potassium hexafluorophosphate (20 mL) was added to the mixture and it was stirred for 2 d. The organic phase was separated, washed with water (3×20 mL), dried with MgSO₄ and concentrated under reduced pressure. After column chromatography (silica, CH₂Cl₂/methanol 10:1; *R_f* = 0.41) **[3][PF₆]** was isolated as purple powder in 98 % yield (47.5 mg, 0.023 mmol). Yield over all steps was 50 %. C₁₀₃H₇₄AuF₁₂N₁₀O₆PZn (2066.43 g mol⁻¹).

¹H NMR (d₇-DMF): δ(ppm) = 1.10 (t, 6H, ³J_{HH} = 7.4 Hz, H^{30/40}₈), 1.68 (tq, 4H, ³J_{HH} = 7.1 Hz, H^{30/40}_{7/7}), 1.99 (p, 4H, ³J_{HH} = 7.4 Hz, H^{30/40}_{6/6}), 2.32 (s, 3H, H³⁵₇), 4.11 (s, 3H, H⁵₆), 4.39 (t, 4H, ³J_{HH} = 6.4 Hz, H^{30/40}_{5/5}), 7.59 (d, 4H, ³J_{HH} = 8.7 Hz, H^{30/40}_{3/3}), 8.26 (d, 4H, ³J_{HH} = 8.7 Hz, H^{10/20}_{2/2}), 8.35 (m, 10H, ³J_{HH} = 8.5 Hz, H^{15/30/35/35/40}_{2/2/2/3/2}), 8.45 (s, 4H, H⁵_{2/3}), 8.57 (m, 6H, H^{10/15/20}_{3/3/3}), 8.65 (d, 2H, ³J_{HH} = 7.7 Hz, H²⁵₂), 8.81 (d, 2H, ³J_{HH} = 7.6 Hz, H²⁵₃), 8.92 (m, 6H, H^β), 9.09 (d, 2H, ³J_{HH} = 4.7 Hz, H^β), 9.56 (m, 8H, H^β), 10.67 (s, 1H, H³⁵₅), 11.25 (s, 1H, H¹⁵₅).

¹³C NMR (d₇-DMF): δ(ppm) = 13.9 (s, C^{30/40}_{8/8}), 19.5 (s, C^{30/40}_{7/7}), 22.7 (s, C³⁵₇), 31.7 (s, C^{30/40}_{6/6}), 52.4 (s, C⁵₆), 68.3 (s, C^{30/40}_{5/5}), 114.2 (s, C^{30/40}_{3/3}), 118.3 (s, C¹⁵₃), 118.9 (s, C³⁵₃), 119.5 (s, C^{10/20}_{1/2}), 119.9 (s, C⁵₁), 121.6 (C³⁵), 122.5 (s, C²⁵), 123.9 (s, C^{10/20}_{2/2}), 124.1 (s, C^{10/20}), 125.2 (s, C^{30/40}), 126.8 (s, C¹⁵), 127.6 (s, C²⁵₃), 127.9 (s, C⁵₂), 129.5 (s, C⁵), 131.1 (s, C^{30/40}_{1/1}), 131.5–133.7 (multiple s, C^{2/3/7/8/12/13/17/18/22/23/27/28/32/33/37/38}), 134.9 (s, C³⁵₁), 135.1 (s, C⁵₃), 135.4 (m, C^{10/15/20/25/30/35/40}_{3/2/3/2/1/2/1}),

136.1 (s, C^{30/40}_{2/2}), 136.4 (C²⁵₄), 136.7–137.9 (multiple s, C^{21/24/26/29*/31/34/36/39}), 138.8 (s, C¹⁵₁), 139.7 (s, C¹⁵₄), 141.4 (s, C³⁵₄), 142.3 (C²⁵₁), 147.8 (s, C^{10/20}_{4/4}), 148.4 (s, C⁵₄), 149.3–151.2 (multiple s, C^{1/4/6/9/11/14/16/19}), 160.5 (s, C^{30/40}_{4/4}), 166.1 (s, C²⁵₅), 167.1 (s, C⁵₅), 169.5 (s, C³⁵₆).

³¹P NMR (*d*₇-DMF): δ (ppm) = -143.9 (sept, ¹J_{PF} = 710 Hz).

HR MS (ESI): *m/z* (%) = 1921.4605 (calcd. for C₁₀₃H₇₄AuF₆N₁₀O₆Zn: 1921.4654).

UV/vis/NIR (CH₂Cl₂): λ (nm) (ϵ / (M⁻¹ cm⁻¹)) = 421 (561.246), 526 (18.896), 548 (24.593), 584 (5.654).

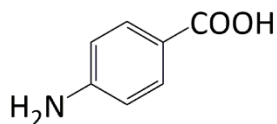
Fluorescence (CH₂Cl₂): λ (nm) (relative intensity) = 599 (0.42), 647 (1.00).

Quantum yield: Φ = 0.0011.

Lifetime: τ (ns) = 1.7.

IR: $\tilde{\nu}$ (cm⁻¹) = 2954 (CH, w), 2921 (CH, m), 2851 (CH, m), 1711 (CO, w), 1661 (CO, w), 1593 (m), 1515 (m), 1319 (s), 1247 (OCO, m), 1065 (m), 1000 (s), 839 (PF, vs), 798 (s), 557 (PF, m).

CV (FcH/FcH⁺, 100 mV s⁻¹, THF, 0.1 M [ⁿBu₄N][PF₆]): *E*_{1/2} (V) = 0.49 (rev.), -0.99 (rev.), -1.63 (rev.), -1.83 (rev.).



4-Aminobenzoic acid was prepared analogously to the literature, but using **[3][PF₆]** as sensitizer.^[12] To a solution of **[3][PF₆]** (0.2 mg, 0.010 μmol, 0.01 eq), DIPEA (17.5 μL, 0.1 mmol, 10 eq) and CH₃COOH (6.3 μL, 0.1 mmol, 10 eq) in 0.5 mL dry *d*₇-DMF was added 4-azidobenzoic acid (1.6 mg, 0.01 mmol, 1.0 eq). The slightly red solution was transferred into a Young NMR tube and irradiated with a Xenon Light Source (300 W, Asahi Spectra Max-303, 420±5 nm) for 72 h, spectroscopic yield 50 % (0.005 mmol). The yield was determined via ¹H NMR spectroscopy using 1,4-bis(trimethylsilyl)benzene as internal standard.

¹H NMR (*d*₇-DMF): δ (ppm) = 6.69 (d, 2H, ³J_{HH} = 8.5 Hz), 7.74 (d, 2H, ³J_{HH} = 8.5 Hz).

The spectroscopic data is in agreement with those previously reported.^[12]

Figure S1: ^1H NMR spectrum of $[\mathbf{1}][\text{PF}_6]$ in d_7 -DMF at 293 K. Asterisks denote residual solvent resonances.

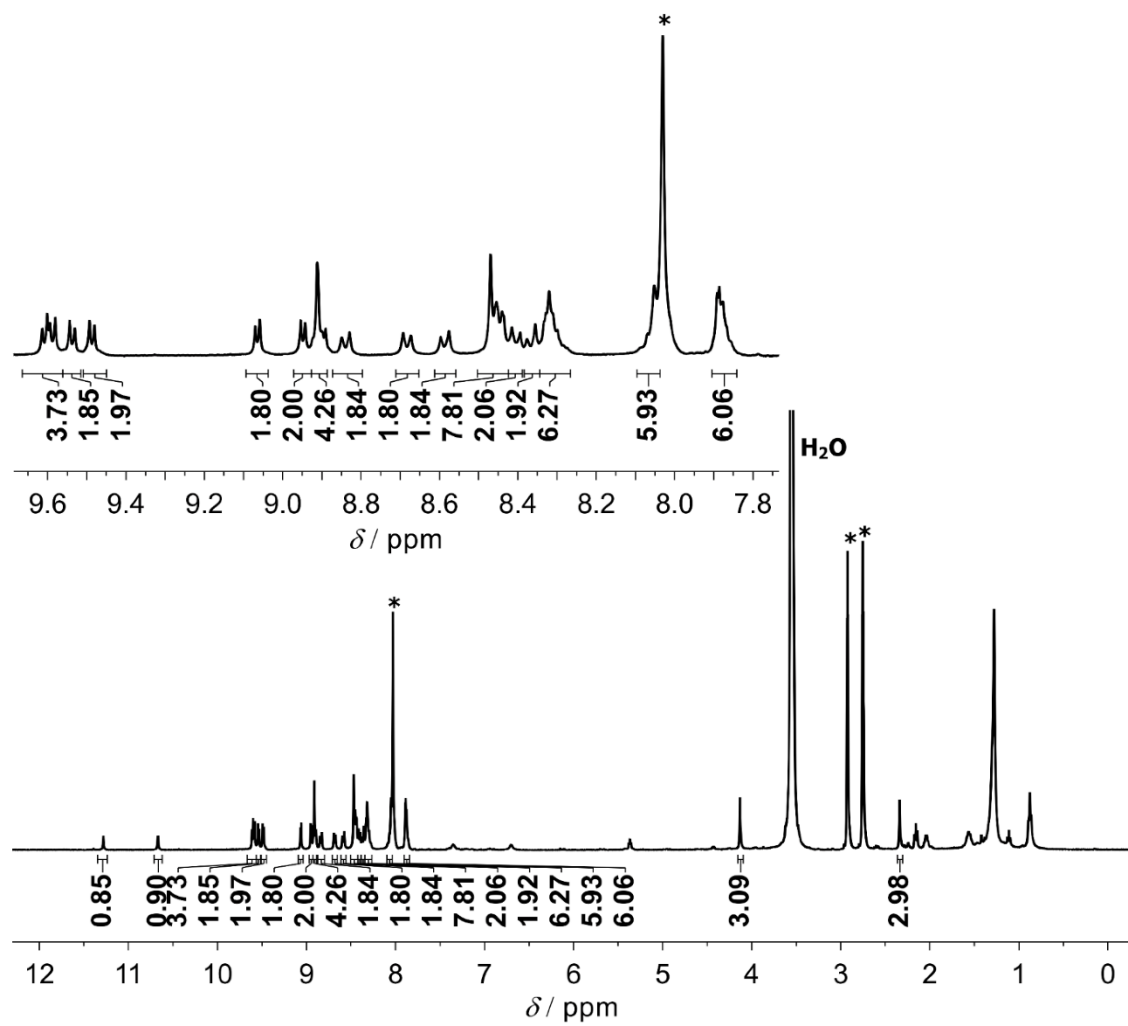


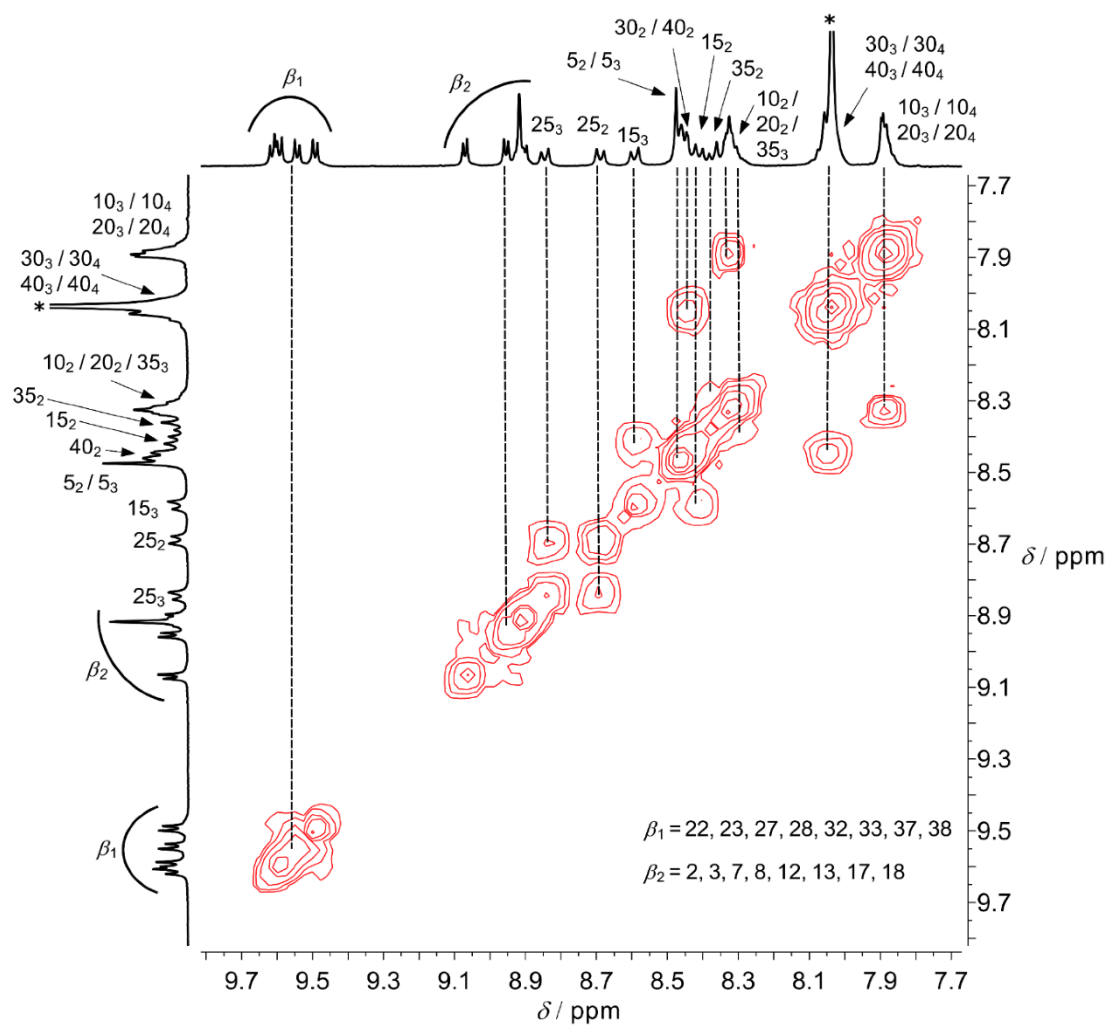
Figure S2: $^1\text{H}^1\text{H}$ COSY of $[\mathbf{1}][\text{PF}_6]$ in d_7 -DMF at 293 K. Asterisks denote residual solvent resonances.

Figure S3: ^1H NMR spectrum of **[2][PF₆]** in d_7 -DMF at 293 K. Asterisks denote residual solvent resonances.

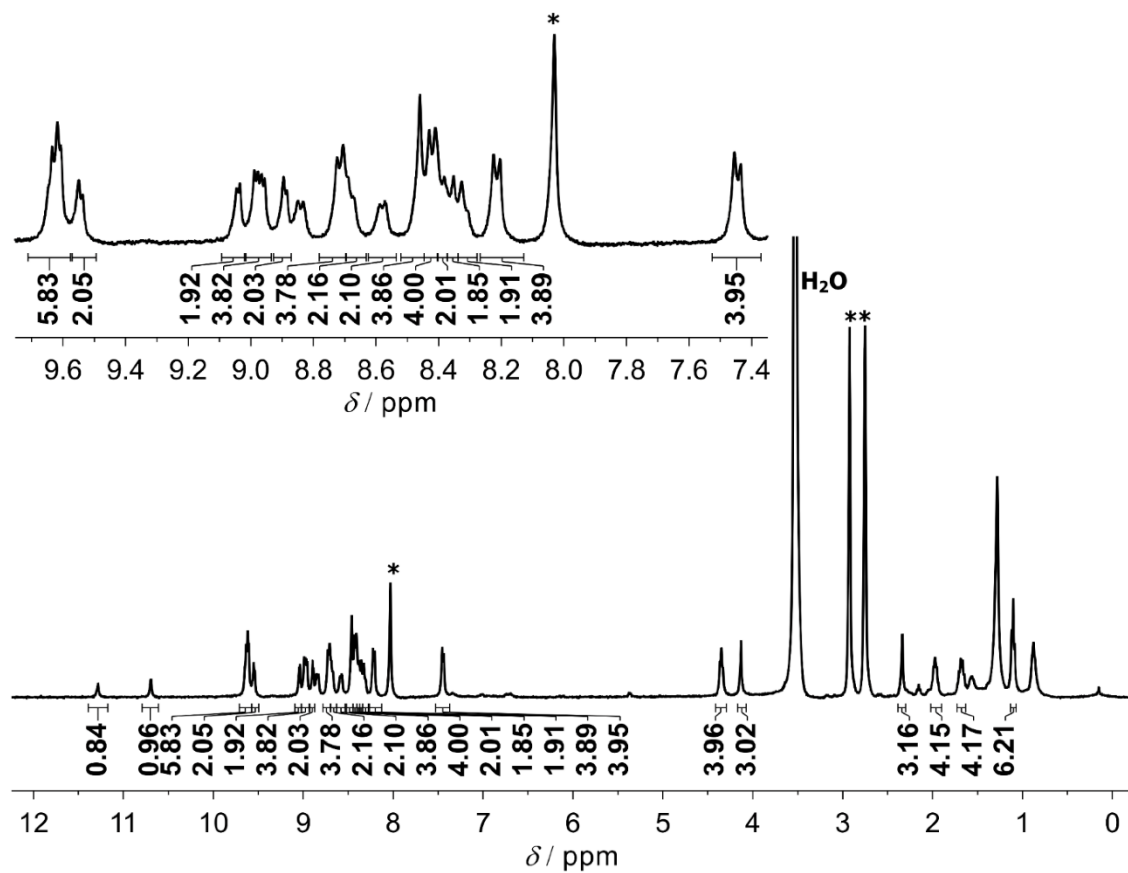


Figure S4: $^1\text{H}^1\text{H}$ COSY of **[2][PF₆]** in d_7 -DMF at 293 K. Asterisks denote residual solvent resonances.

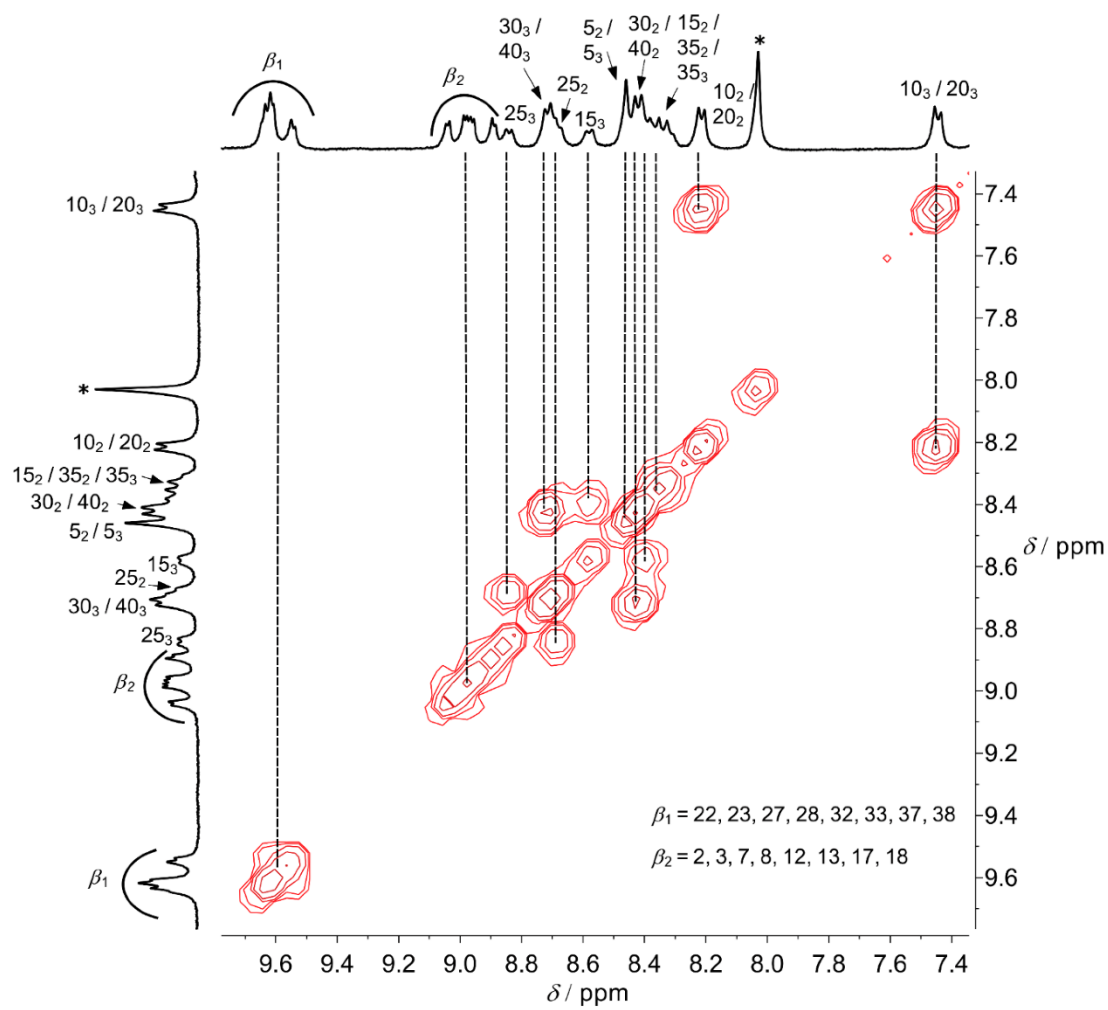


Figure S5: $^{13}\text{C}\{^1\text{H}\}$ NMR spectrum of **[2][PF₆]** in d_7 -DMF at 293 K. Asterisks denote residual solvent resonances.

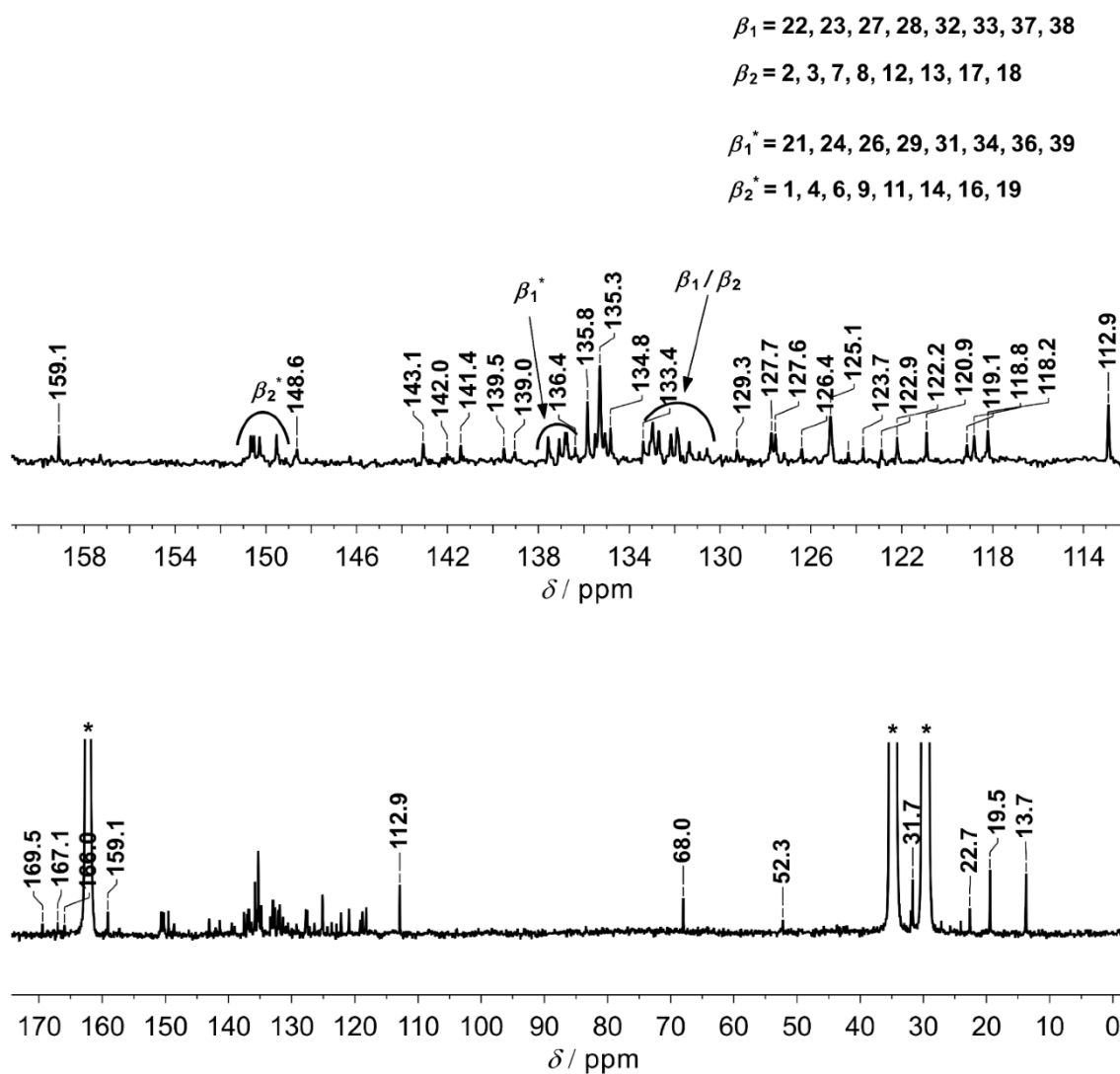


Figure S6: ^1H NMR spectrum of **[3][PF₆]** in d_7 -DMF at 293 K. Asterisks denote residual solvent resonances.

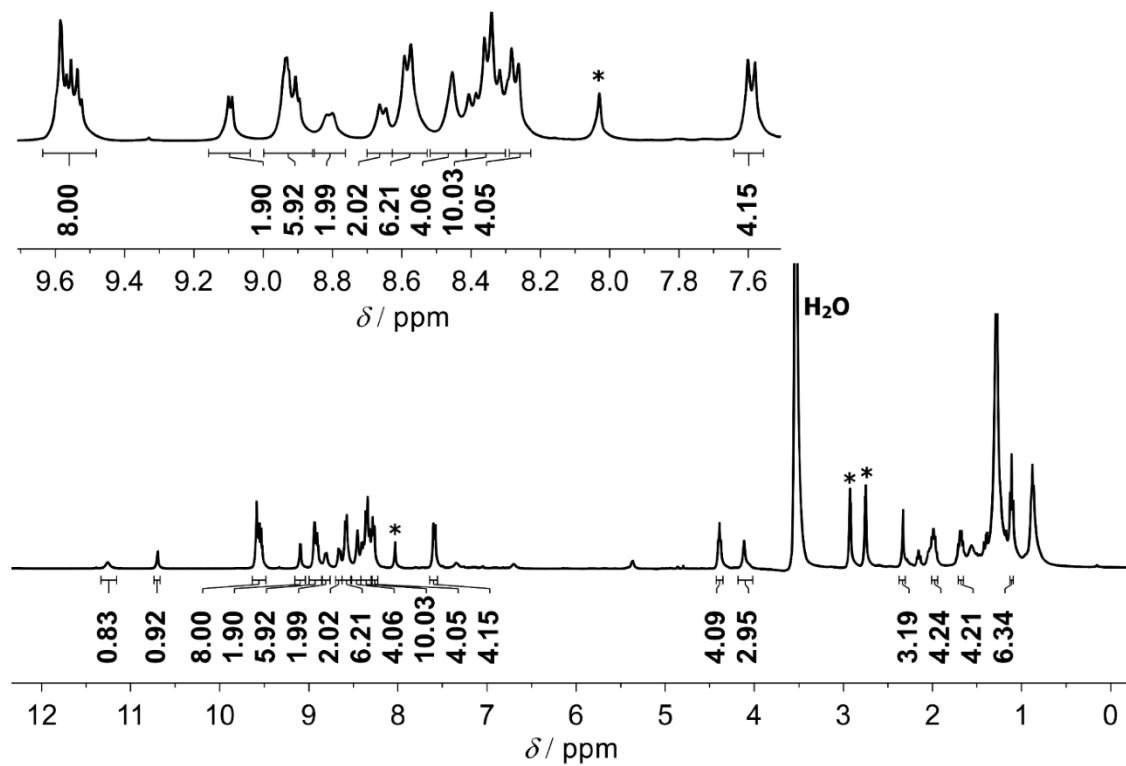


Figure S7: ^1H COSY of **[3][PF₆]** in d_7 -DMF at 293 K. Asterisks denote residual solvent resonances.

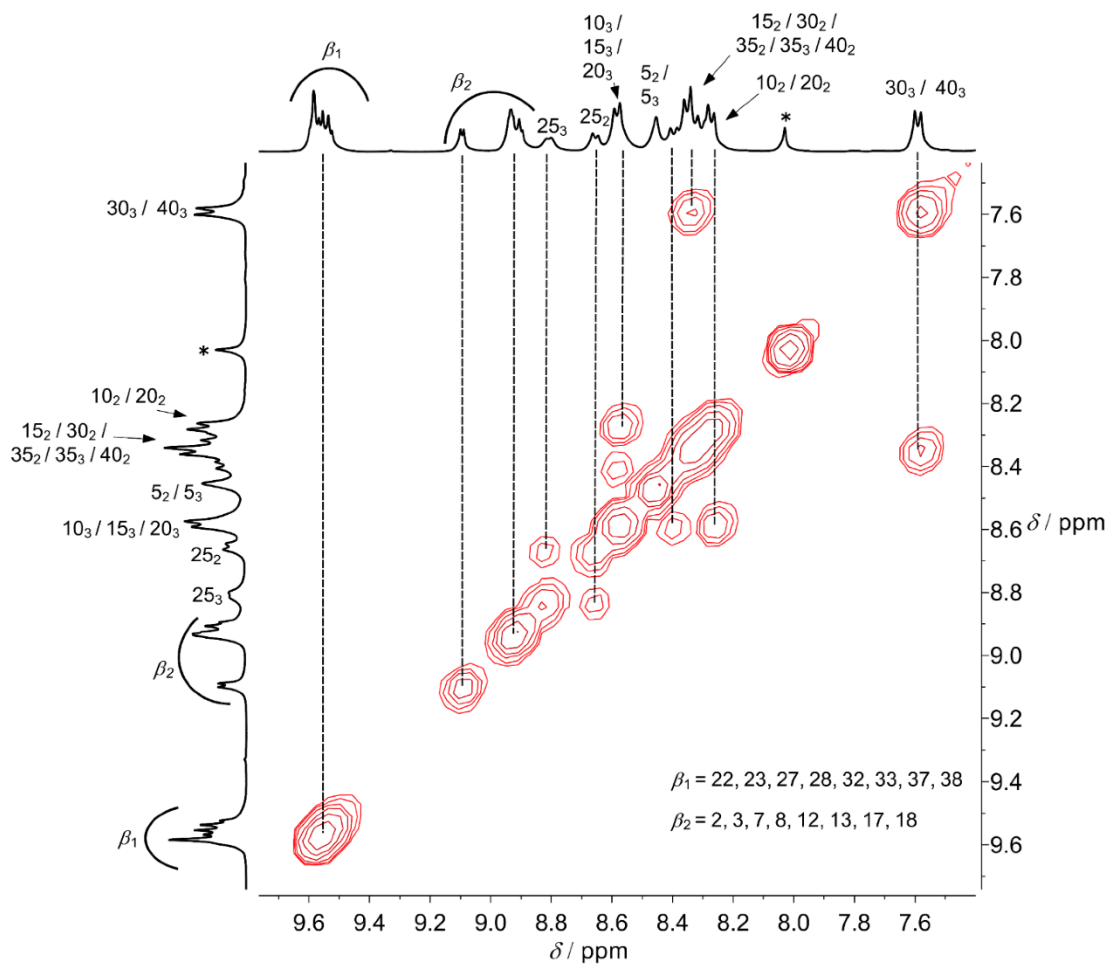


Figure S8: $^{13}\text{C}\{^1\text{H}\}$ NMR spectrum of **[3][PF₆]** in d_7 -DMF at 293 K. Asterisks denote residual solvent resonances.

$\beta_1 = 22, 23, 27, 28, 32, 33, 37, 38$

$\beta_2 = 2, 3, 7, 8, 12, 13, 17, 18$

$\beta_1^* = 21, 24, 26, 29, 31, 34, 36, 39$

$\beta_2^* = 1, 4, 6, 9, 11, 14, 16, 19$

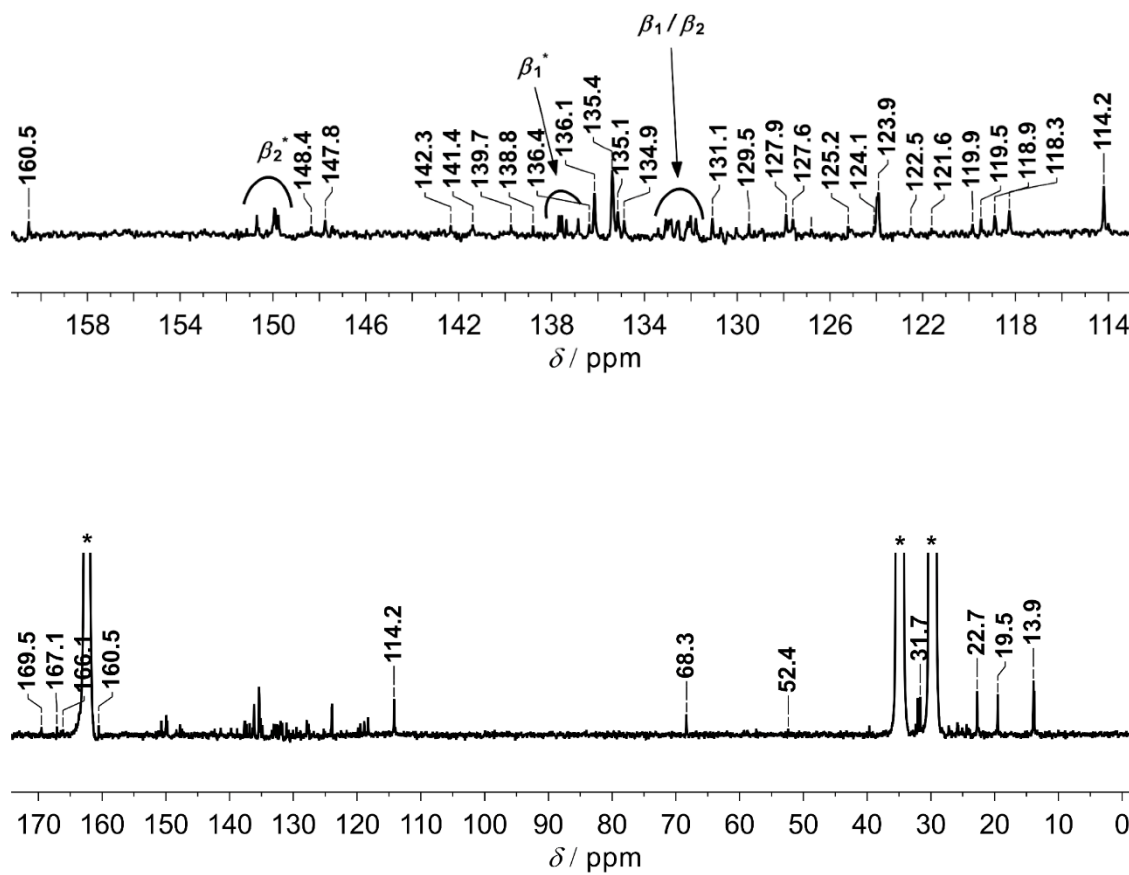


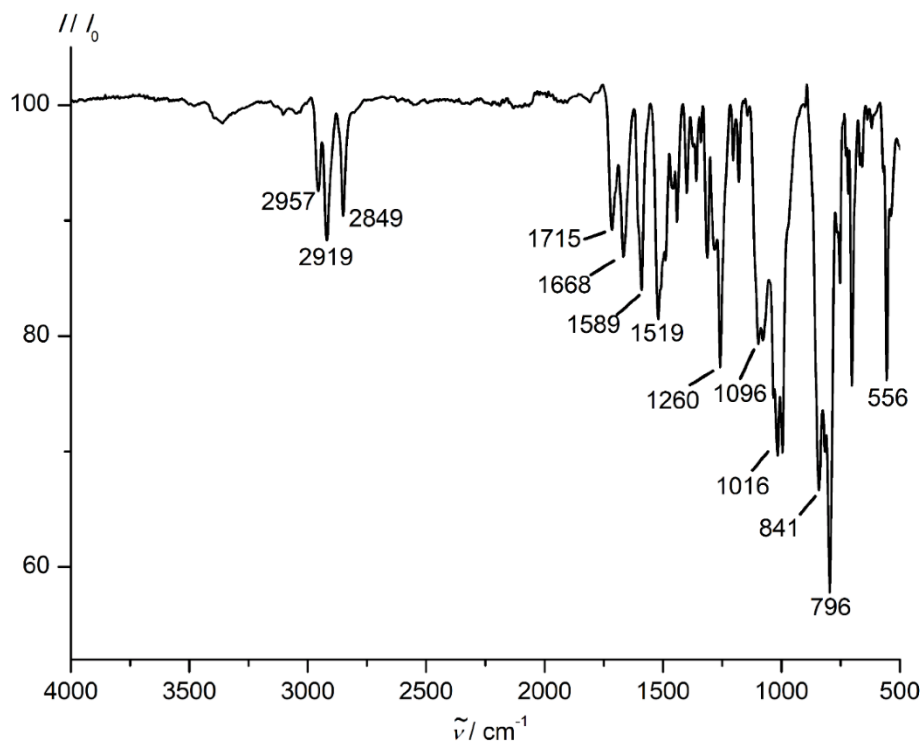
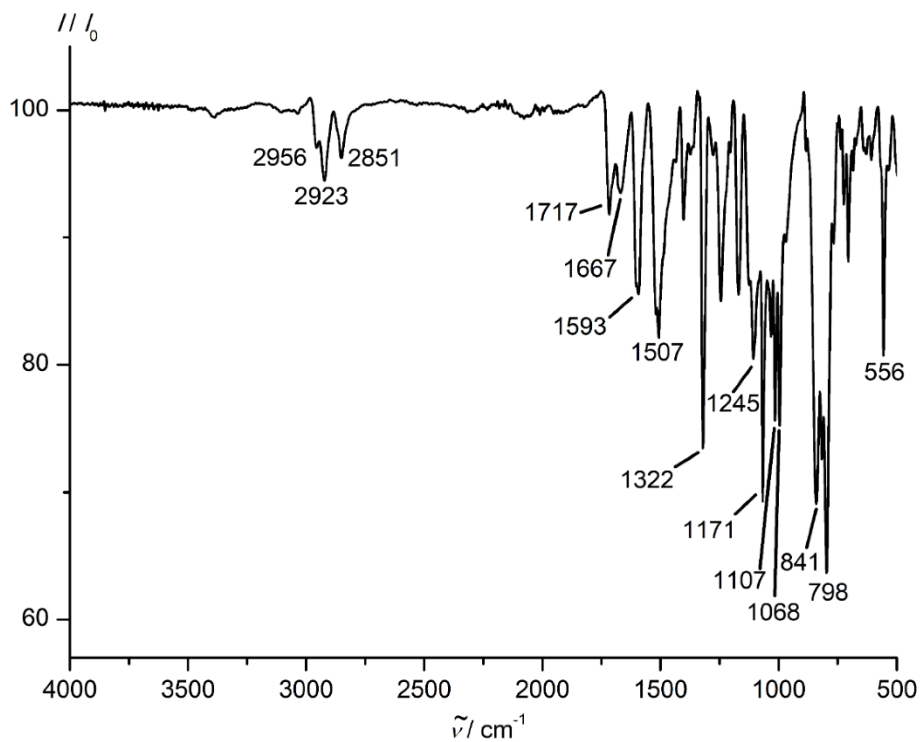
Figure S9: ATR-IR spectrum of **[1][PF₆]** as a solid.**Figure S10:** ATR-IR spectrum of **[2][PF₆]** as a solid.

Figure S11: ATR-IR spectrum of [3][PF₆] as a solid.

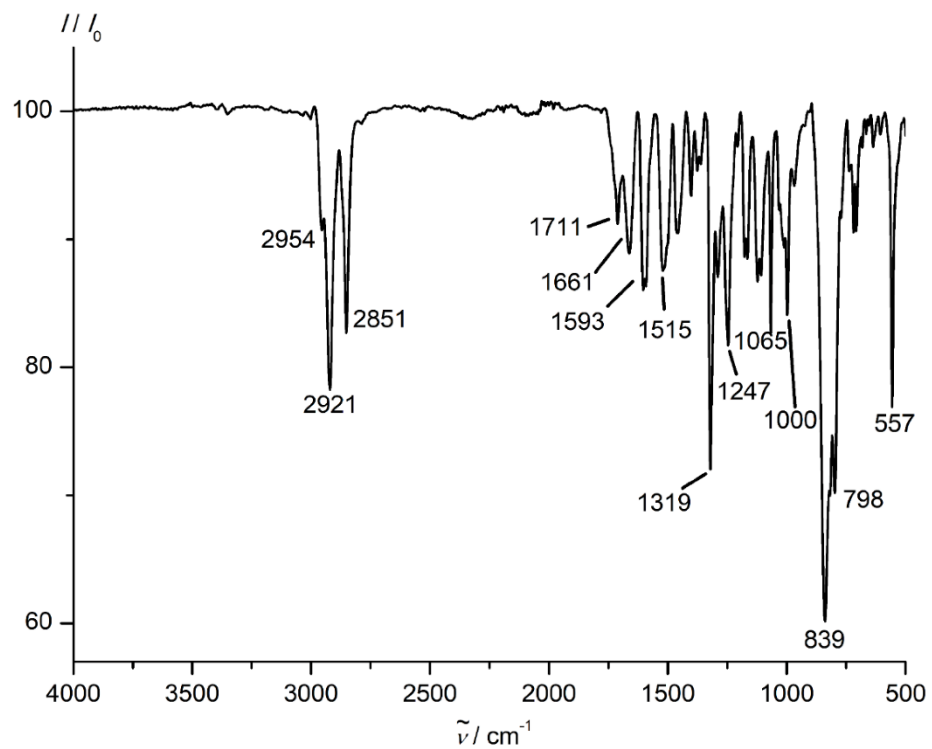


Figure S12: Absorption and emission spectra of **[2][PF₆]**, **Zn-Ac-IIa** and **[Au-Ac-IIb][PF₆]** in CH₂Cl₂ at room temperature.

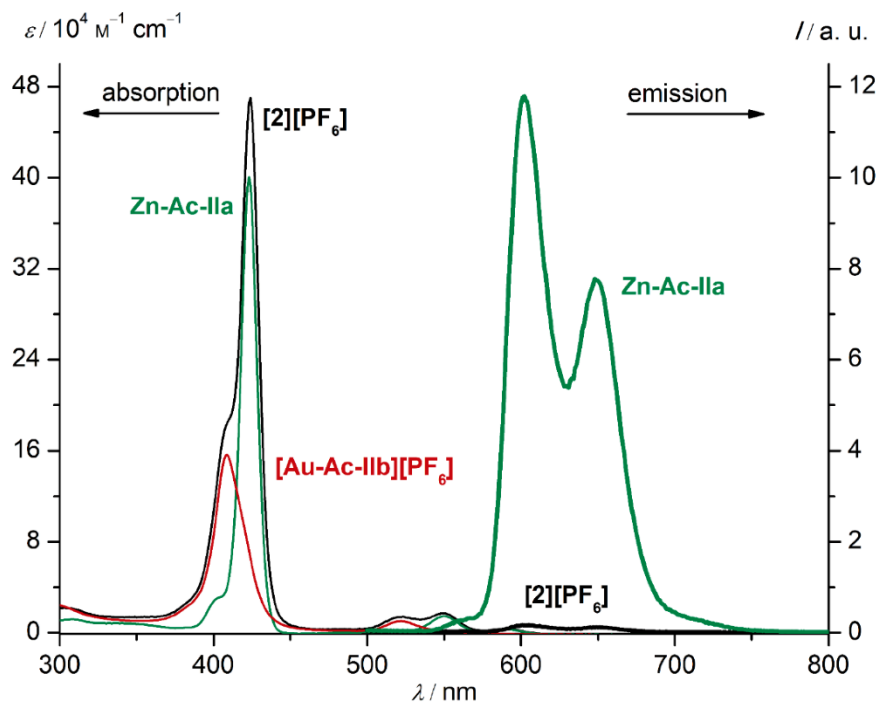


Figure S13: Absorption and emission spectra of **[3][PF₆]**, **Zn-Ac-IIIa** and **[Au-Ac-IIIb][PF₆]** in CH₂Cl₂ at room temperature.

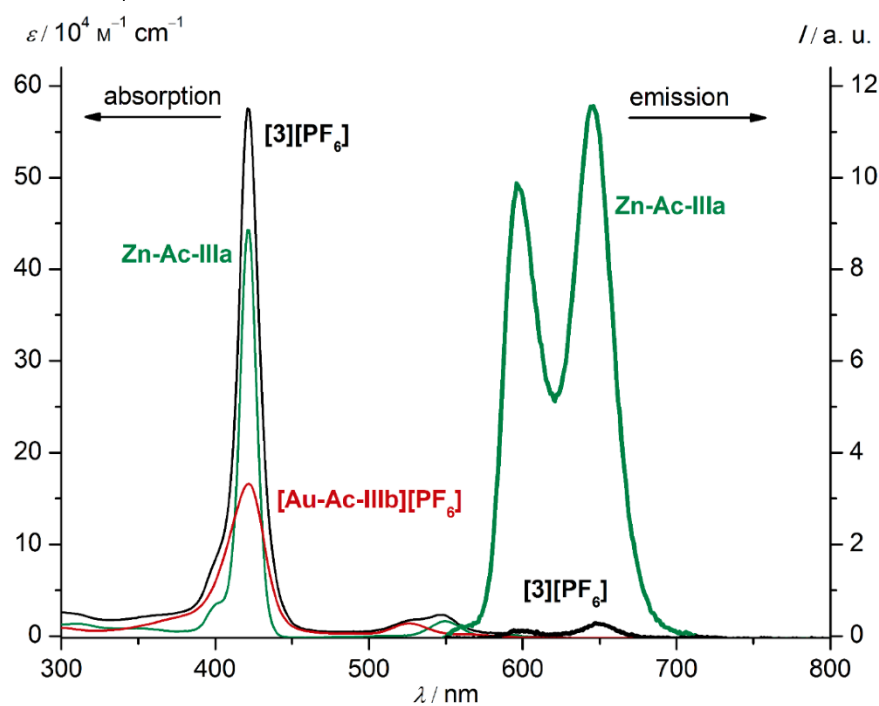


Figure S14: High resolution ESI⁺ mass spectrum of **[1][PF₆]** in DMF/MeCN; calculated (calcd. for C₉₃H₆₀AuN₁₀O₄Zn) and experimental isotopic pattern.

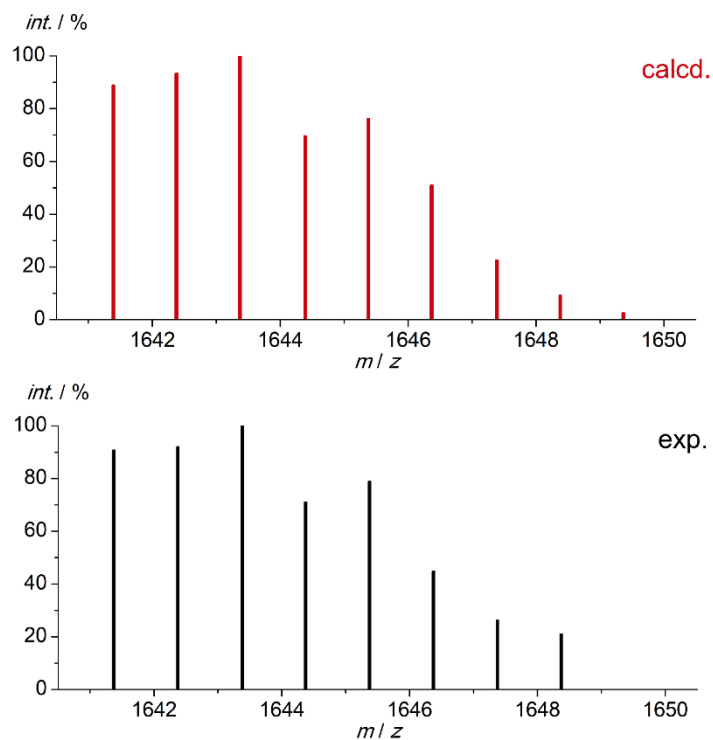


Figure S15: High resolution ESI⁺ mass spectrum of **[2][PF₆]** in DMF/MeCN; calculated (calcd. for C₁₀₃H₇₄AuF₆N₁₀O₆Zn) and experimental isotopic pattern.

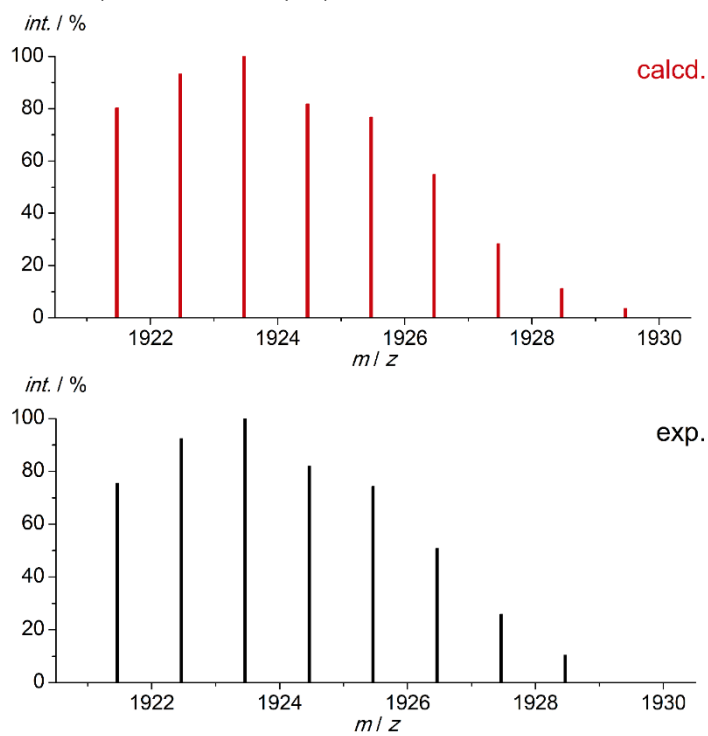


Figure S16: High resolution ESI⁺ mass spectrum of [3][PF₆] in DMF/MeCN; calculated (calcd. for C₁₀₃H₇₄AuF₆N₁₀O₆Zn) and experimental isotopic pattern.

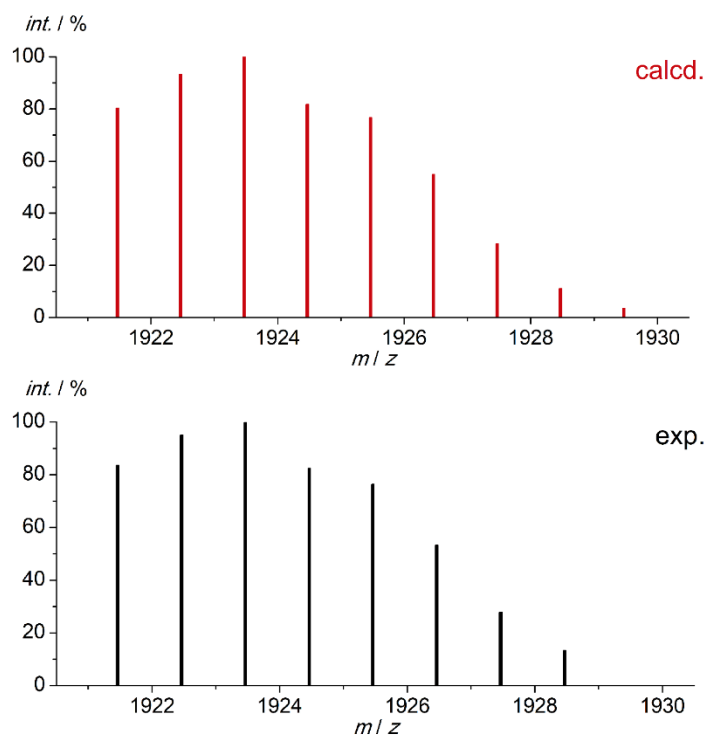


Figure S17: Cyclic voltammogram of [1][PF₆] in DMF/[ⁿBu₄N][PF₆] (scan rate 100 mV s⁻¹).

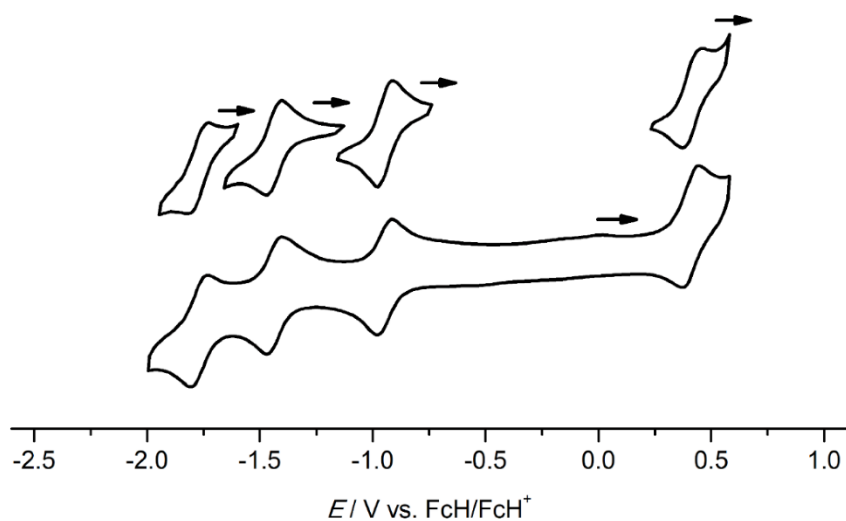


Figure S18: Cyclic voltammogram of **[2][PF₆]** in THF/[ⁿBu₄N][PF₆] (scan rate 100 mV s⁻¹).

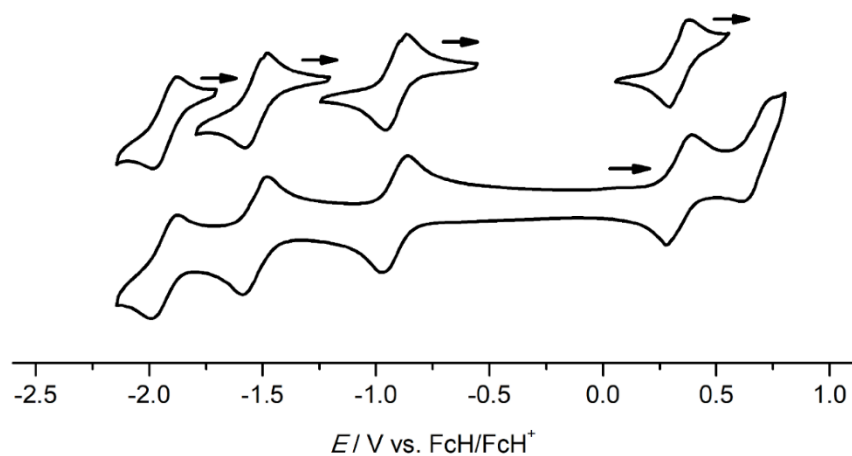


Figure S19: Cyclic voltammogram of **[3][PF₆]** in THF/[ⁿBu₄N][PF₆] (scan rate 100 mV s⁻¹).

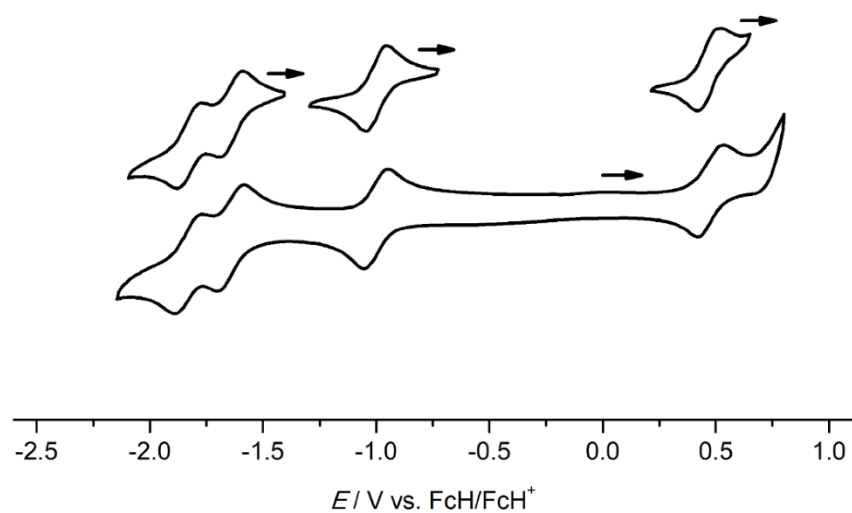


Figure S20: Fluorescence decays and lifetimes of a) **[1][PF₆]**, b) **[2][PF₆]** and c) **[3][PF₆]** in THF after excitation with 410 nm (monoexponential decay in all cases; the fluorescence at initial times is likely due to stray light).

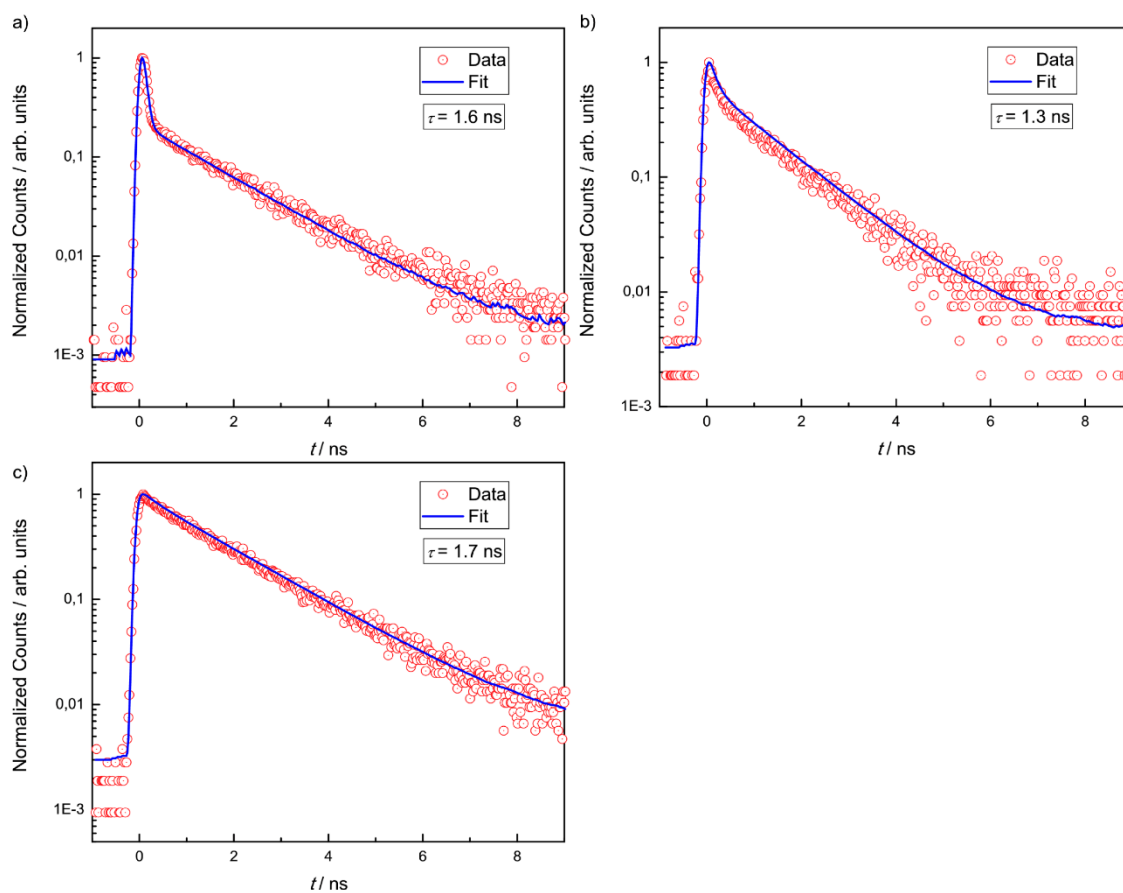


Figure S21: fs-Transient absorption spectra in THF at different time points after excitation with 400 nm of a) **[2][PF₆]** and b) **[3][PF₆]** and amplitude spectra of the components labelled with the respective time constants of c) **[2][PF₆]** and d) **[3][PF₆]**.

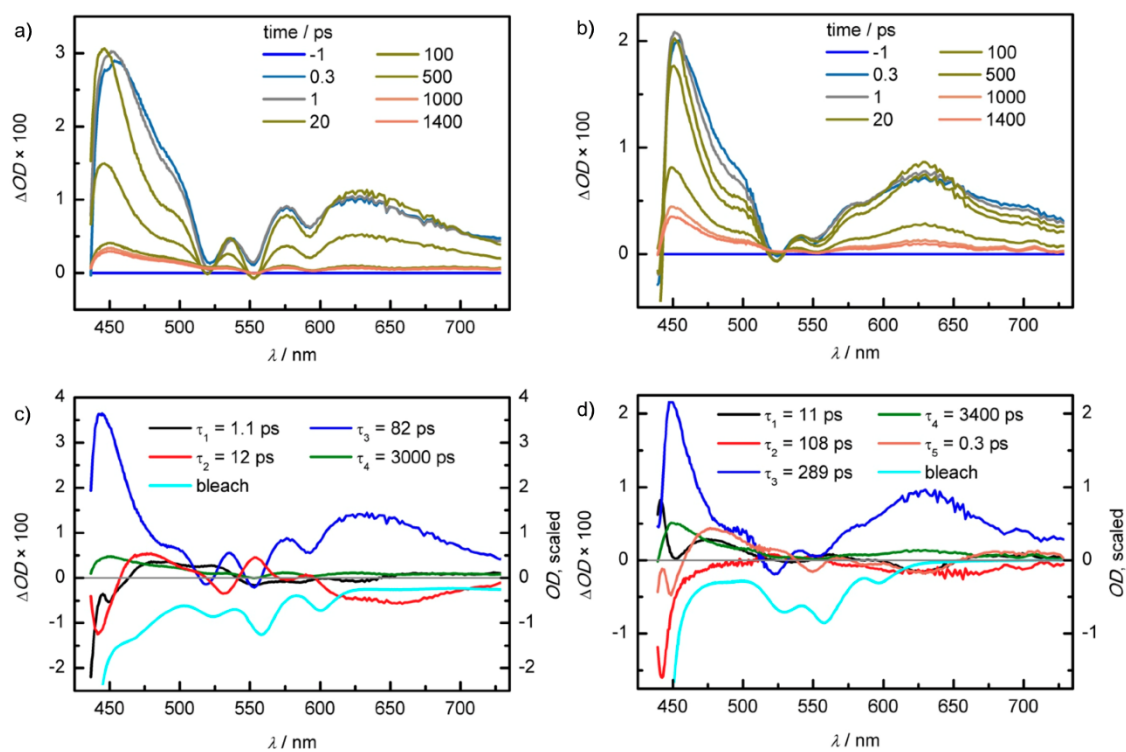


Figure S22: Normalised UV/Vis spectral changes of **[3][PF₆]** in CH₂Cl₂ (black) after a) irradiation at 420±5 nm in the presence of NEt₃ (10 eq, red) and b) chemical reduction with 1.0 eq. KC₈ (red).

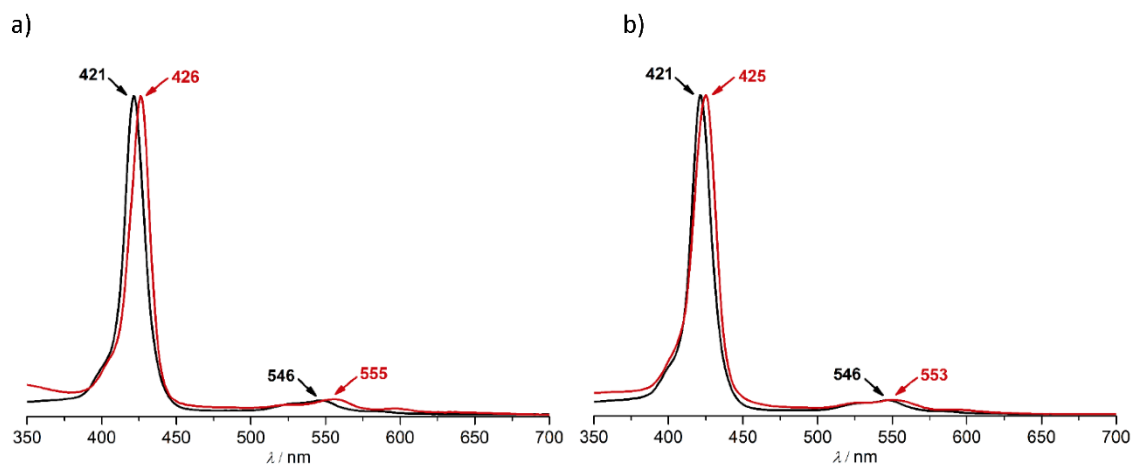


Figure S23: a) Normalised UV/Vis spectral changes in CH₂Cl₂ of **[1][PF₆]** (black) after irradiation at 420±5 nm in the presence of NEt₃ (10 eq, red) and b) simulation of the final Soret band via superposition of the curve-fitted [Au^{III}(P)]⁺/Au^{II}(P) and Zn^{II}(P) components.

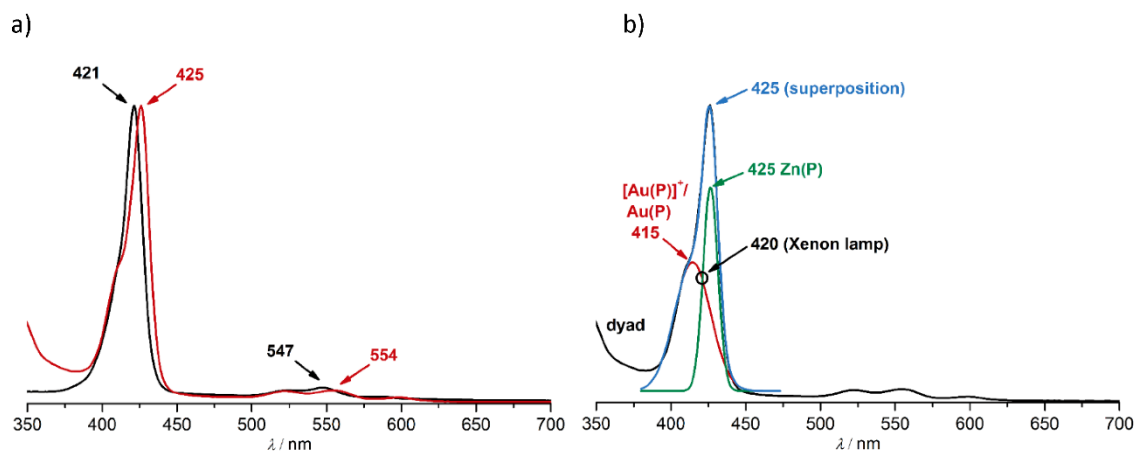


Figure S24: X-band EPR spectra (9.4 GHz, 77 K) of a) $[\text{Au}(\text{TPP})][\text{PF}_6]^{[1a]}$ + 0.9 eq. CoCp_2 in CH_2Cl_2 , b) $[\mathbf{3}][\text{PF}_6]$ + 0.9 eq. KC_8 in DMF (superimposed is a weak, sharp resonance of an organic radical species) and c) $[\mathbf{3}][\text{PF}_6]$ after irradiation at 420 ± 5 nm in the presence of NEt_3 (10 eq) in DMF (superimposed is a resonance of radical species derived from NEt_3).

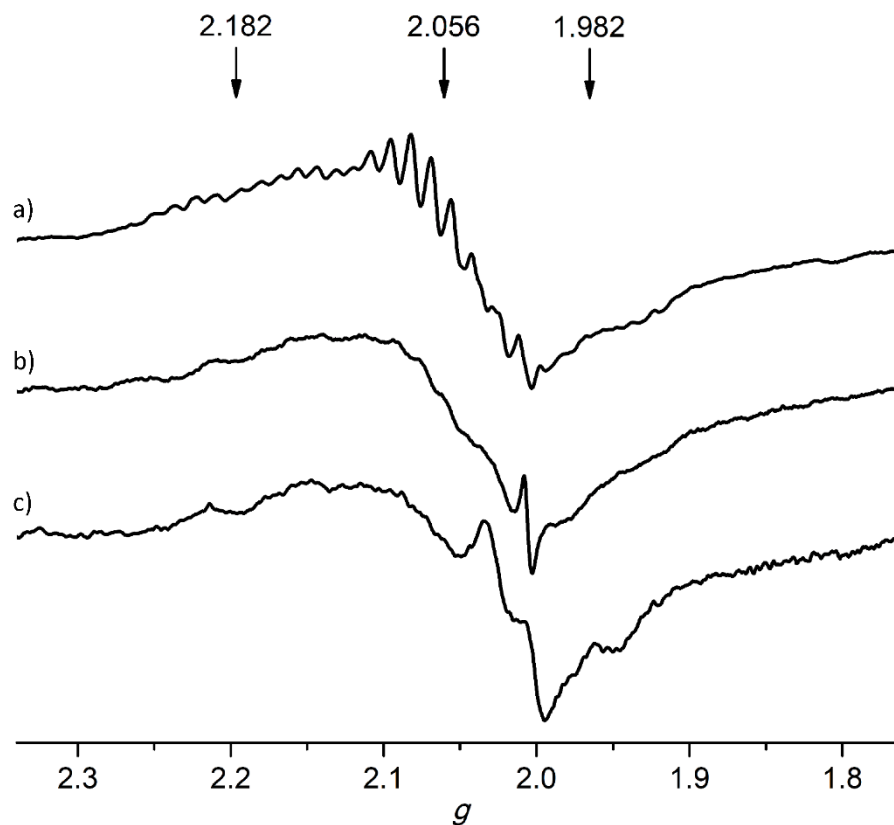


Figure S25: Normalised XANES spectra of $[\mathbf{3}][\text{PF}_6]$ after irradiation at 420 ± 5 nm in the presence of NEt_3 (10 eq, black) in DMF (64 % reduced) and b) after introduction of oxygen to the sample (red).

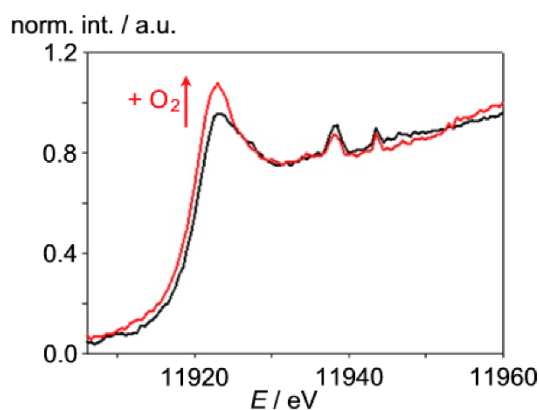


Figure S26: ^1H NMR spectra of **[1][PF₆]** after irradiation at a) 420 ± 5 nm (Soret band), b) 560 ± 5 nm (Q band) in d_7 -DMF, in the presence of NEt_3 (10 eq) and c) ^1H NMR spectrum of **[1][PF₆]** after reduction with 1.0 eq. KC_8 .

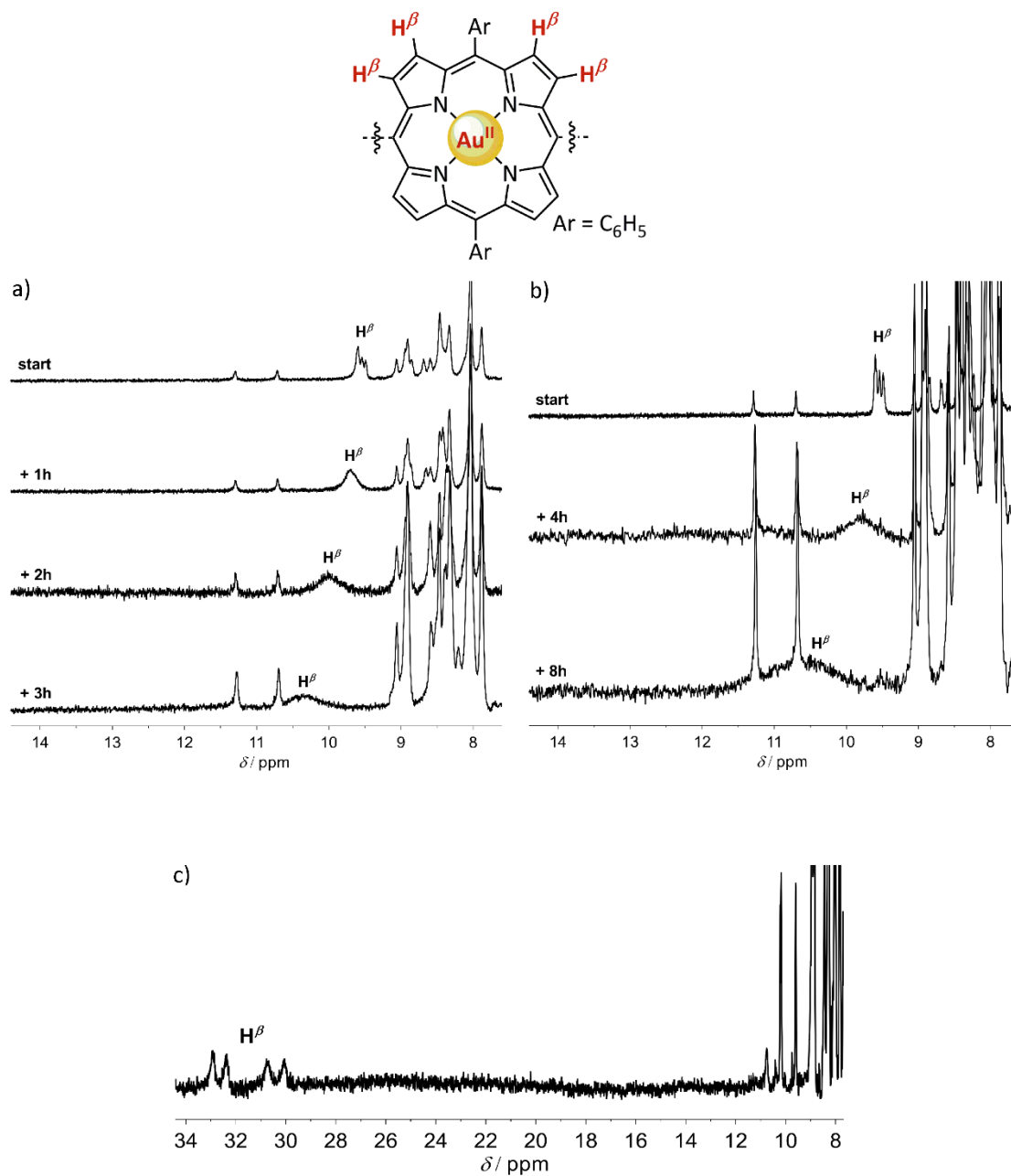


Figure S27: Paramagnetic shift of H^β resonances during irradiation at 420 ± 5 nm in d_7 -DMF of a) **[1][PF₆]** and immediate addition of NEt₃ (black) and b) **[1][PF₆]** with addition of NEt₃ after 3 h of irradiation (green) and c) **[3][PF₆]** and direct addition of NEt₃ (red).

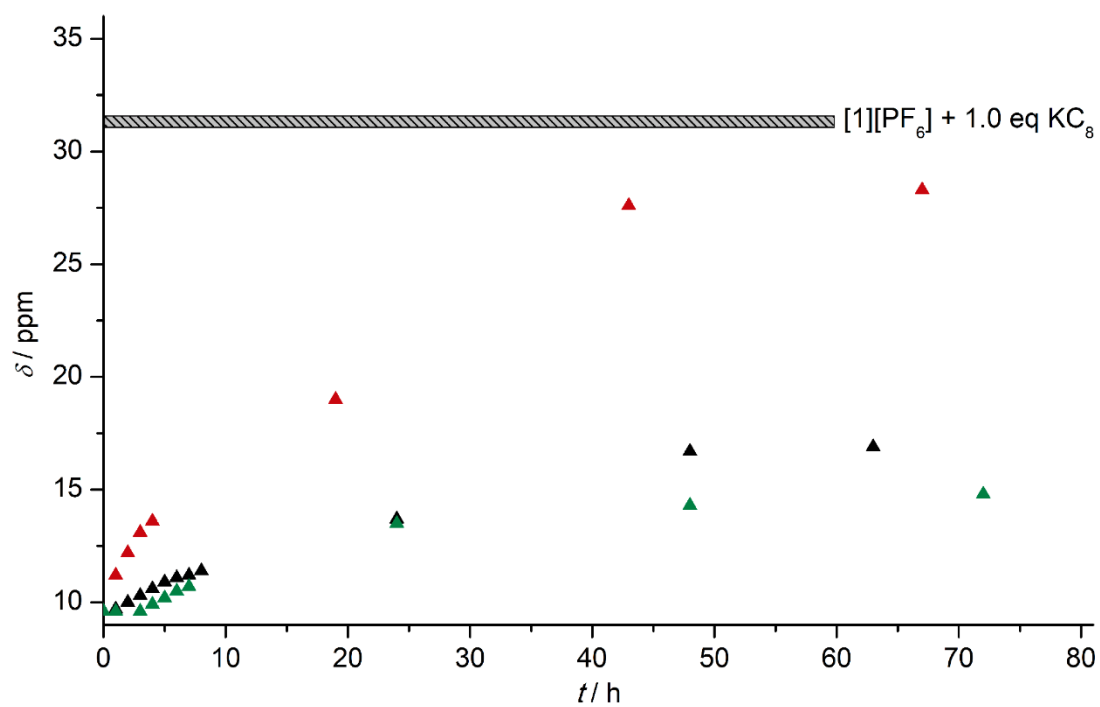
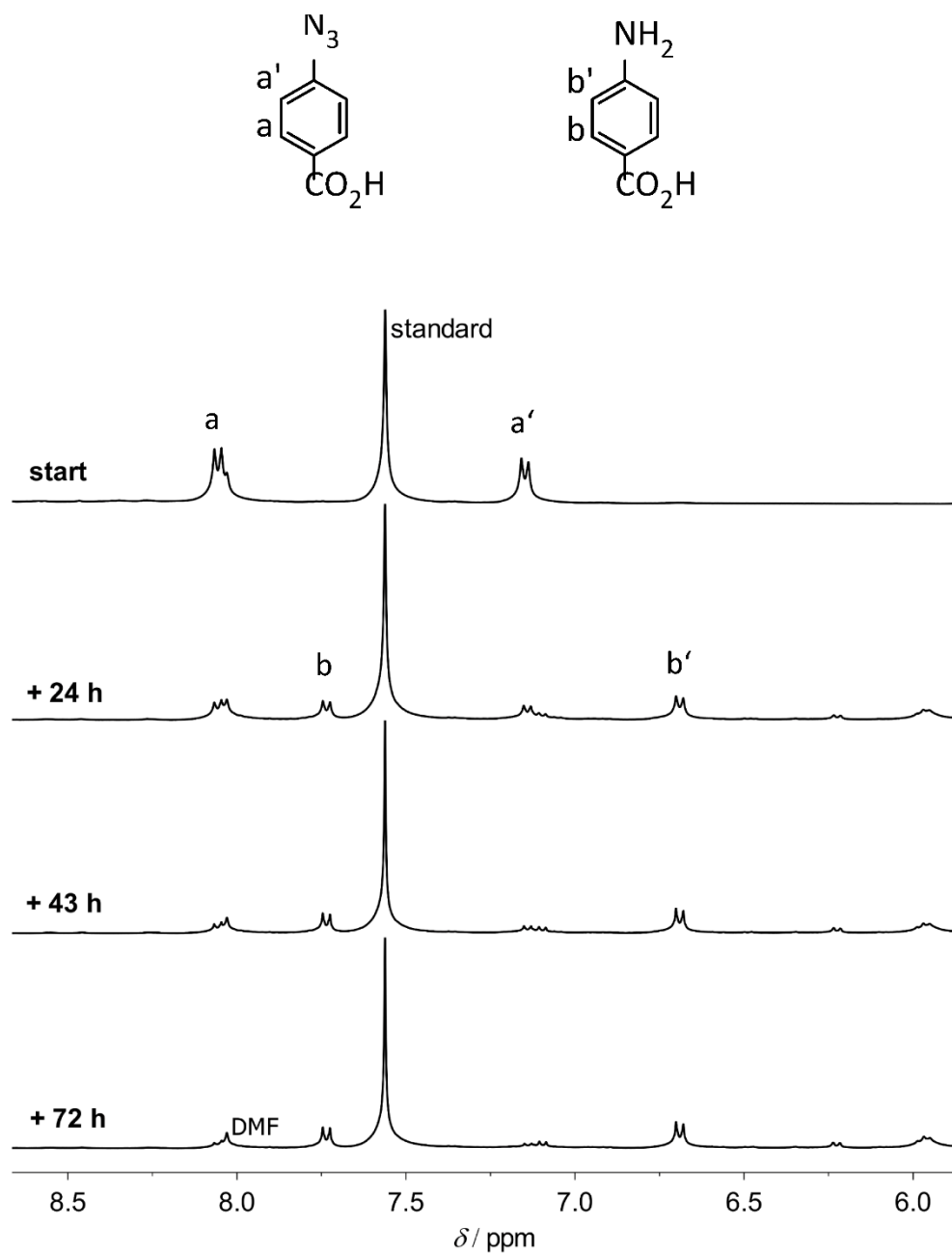


Figure S28: ^1H NMR spectra during the light-sensitized (420 ± 5 nm) formation of 4-aminobenzoic acid from 4-azidobenzoic acid in d_7 -DMF in the presence of 1 mol-% $[\mathbf{3}][\text{PF}_6]$, DIPEA (10 eq) and $\text{CH}_3\text{CO}_2\text{H}$ (10 eq). Internal standard was 1,4-bis(trimethylsilyl)benzene.



-
- [1] a) S. Preiß, J. Melomedov, A. Wünsche von Leupoldt and K. Heinze, *Chem. Sci.* 2016, **7**, 596–610; b) J. Melomedov, J. R. Ochsmann, M. Meister, F. Laquai and K. Heinze, *Eur. J. Inorg. Chem.* 2014, 1984–2001.
- [2] G. R. Fulmer, A. J. M. Miller, N. H. Sherden, H. E. Gottlieb, A. Nudelman, B. M. Stoltz, J. E. Bercaw and K. I. Goldberg, *Organometallics* 2010, **29**, 2176–2179.
- [3] A. Rosa, G. Ricciardi, E. J. Baerends, A. Romeo and M. L. Scolaro, *J. Phys. Chem. A* 2003, **107**, 11468–11482.
- [4] J. R. Lakowicz, *Principles of Fluorescence Spectroscopy*, third ed., Springer, New York, 2006.
- [5] M. Bauer, G. Heusel, S. Mangold and H. Bertagnolli, *J. Synchrotron Rad.* 2010, **17**, 273–279.
- [6] F. Neese, *WIREs Comput. Mol. Sci.* 2012, **2**, 73–78.
- [7] a) A. D. Becke, *J. Chem. Phys.* 1993, **98**, 5648–5652; b) C. Lee, W. Yang, and R. G. Parr, *Phys. Rev. B* 1988, **37**, 758–789; c) B. Mihlich, A. Savin, H. Stoll and H. Preuss, *Chem. Phys. Lett.* 1989, **157**, 200–206.
- [8] D. A. Pantazis, X.-Y. Chen, C. R. Landis and F. Neese, *J. Chem. Theory Comput.* **2008**, **4**, 908–919.
- [9] a) F. Neese, F. Wennmohs, A. Hansen and U. Becker, *Chem. Phys.* 2009, **356**, 98–109; b) R. Izsák and F. Neese, *J. Chem. Phys.* 2011, **135**, 144105.
- [10] V. Barone, M. Cossi, *J. Phys. Chem. A* 1998, **102**, 1995–2001.
- [11] a) S. Grimme, J. Antony, S. Ehrlich and H. Krieg, *J. Chem. Phys.* 2010, **132**, 154104; b) S. Grimme, S. Ehrlich and L. Goerigk, *J. Comput. Chem.* 2011, **32**, 1456–1465.
- [12] Y. Chen, A. S. Kamlet, J. B. Steinman and D. R. Liu, *Nat. Chem.* 2011, **3**, 146–153.
- [13] S. Preiß, C. Förster, S. Otto, M. Bauer, P. Müller, D. Hinderberger, H. Hashemi Haeri, L. Carella and K. Heinze, *Nat. Chem.* 2017, **9**, 1249–1255.

6.4 Supporting Information to 3.4: Intrinsic superoxide dismutase activity of MnO nanoparticles enhances magnetic resonance imaging contrast

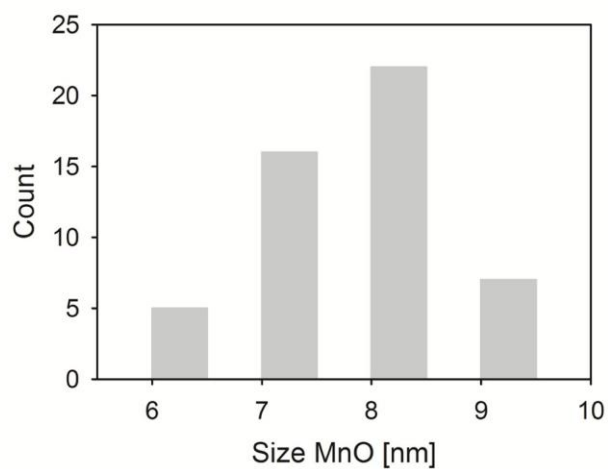


Fig. S1. Size distribution for MnO NPs determined by TEM (size of 50 individual NPs), revealing an average diameter of 7.6 ± 0.7 nm.

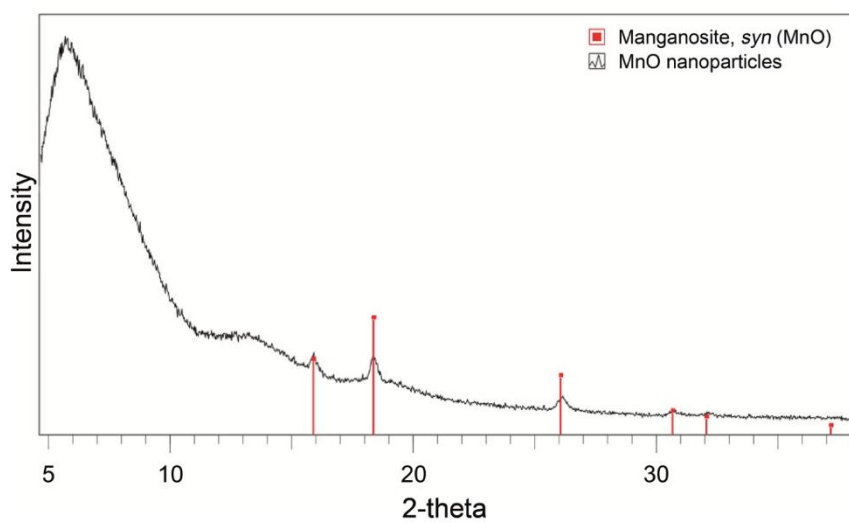


Fig. S2. P-XRD of MnO NPs (black) showing the formation of phase-pure face-centered cubic manganosite, *syn*-MnO (red).

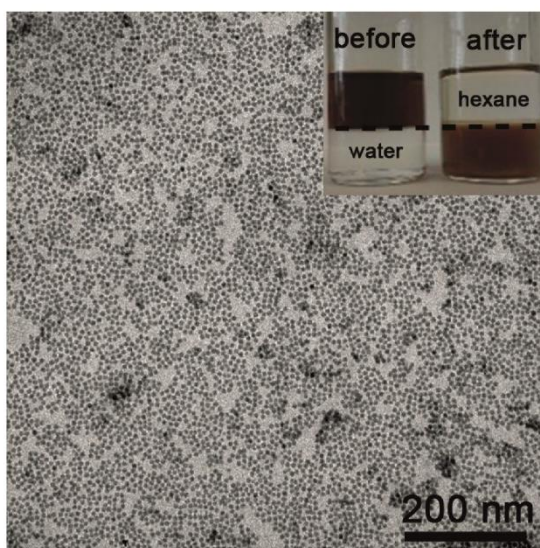


Fig. S3. Water soluble surface functionalized 8 nm MnO NPs with C-PEG. NPs retain size and shape during the functionalization process. Scale bar: 200 nm. Inset: Phase transfer of the MnO NPs in hexane/water before (left) and after (right) the functionalization with C-PEG.

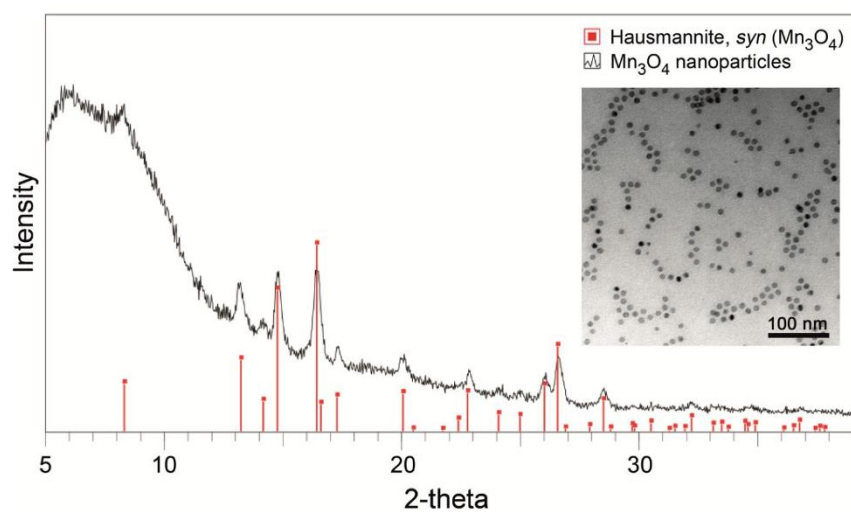


Fig. S4. Synthesis of Mn₃O₄ NPs. P-XRD of Mn₃O₄ NPs (black) showing the formation of phase-pure body-centered tetragonal hausmannite, *syn*-Mn₃O₄ (red). Inset: TEM Image of monodisperse 8 nm Mn₃O₄ NPs. Scale bar: 100 nm.

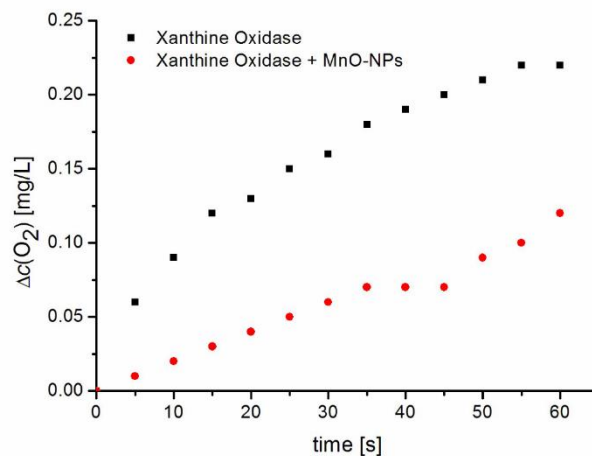


Fig. S5. Oxygen evolution of MnO NPs when exposed to superoxide radicals generated by xanthine/xanthine oxidase (XO) without addition of cytochrome c (pH 7.4). Molecular oxygen (O₂) is depleted by enzymatic activity of XO (black) forming superoxide radicals. In general superoxide dismutation by SOD-active materials leads to the formation of hydrogen peroxide and oxygen (50% each). MnO NPs reduce the oxygen depletion to approx. 50% (red), which is equivalent to the formation of an equivalent amount of O₂.

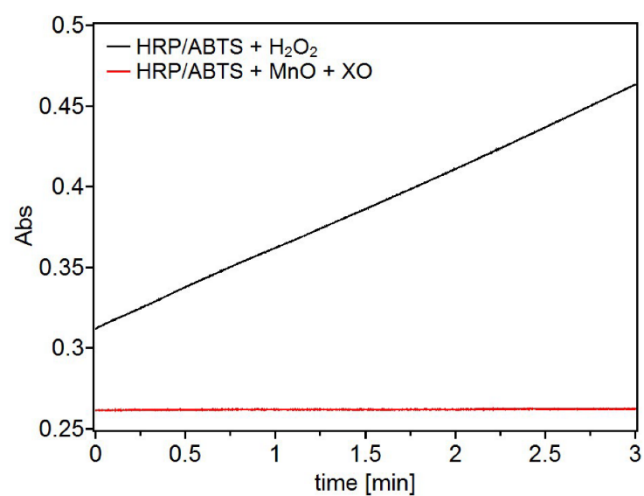


Fig. S6. Formation of H₂O₂ during the SOD-reaction of MnO NPs (red) cannot be demonstrated using the classical HRP/ABTS assay due to the intrinsic catalase-like activity of MnO NPs. As a positive control H₂O₂ has been added to the reaction mixture without addition of MnO (black).

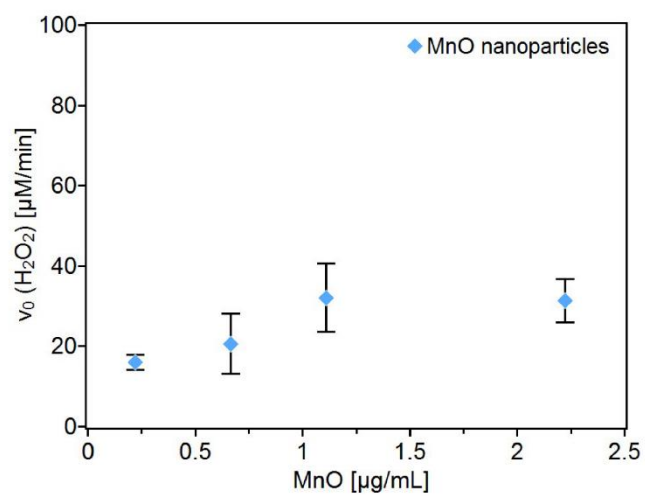


Fig. S7. Catalase-like reaction of MnO NPs monitored by disappearance of peroxide at 240 nm for 3 min at RT. Concentrations of 10mM H_2O_2 and 50 mM PBS pH 7.4 were used, while varying amounts of MnO nanoparticles (0.2, 0.7, 1.1, 2.2 $\mu\text{g}/\text{mL}$).

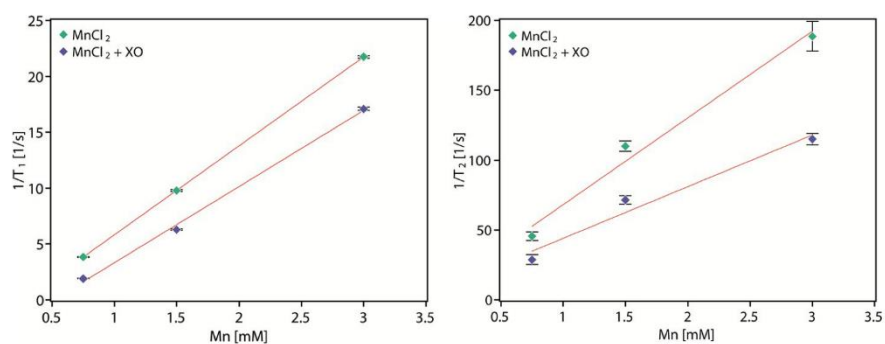


Fig. S8. Specific relaxivities r_1 and r_2 of Mn^{2+} ion a without and b with addition of superoxide generated by xanthine/xanthine oxidase (XO). Relaxivities were determined by linear regression and show values for a $r_1 = 7.95 \pm 0.01 \text{ mM}^{-1}\text{s}^{-1}$ and $r_2 = 62.07 \pm 8.26 \text{ mM}^{-1}\text{s}^{-1}$, b $r_1 = 6.81 \pm 0.34 \text{ mM}^{-1}\text{s}^{-1}$ and $r_2 = 36.95 \pm 6.88 \text{ mM}^{-1}\text{s}^{-1}$, respectively.

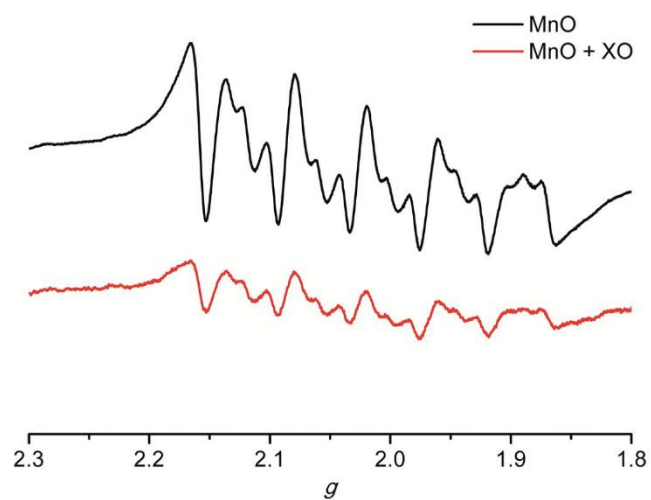


Fig. S9. X-band EPR spectra of MnO NPs in a frozen 50/50 mixture water/glycerol (77 K, 9.4 GHz) without (black) and with addition of superoxide generated by xanthine/xanthine oxidase (XO, red) after 30 min. Both spectra show the characteristic anisotropic six line pattern of Mn²⁺ (⁵⁵Mn; $I = 5/2$; 100%) with a reduction in signal intensity due to the superoxide treatment (red).

7 Acknowledgements

First and foremost, my sincere thanks go to [REDACTED] for giving me the opportunity to work in the very interesting field of artificial photosynthesis. I am particularly grateful for the fruitful discussions, her countless ideas and constructive feedback she always had to offer. This has been fundamental for the outcome of this work. Her way to communicate scientific competences is excellent and it has been a pleasure to work in her group.

Thanks also go to [REDACTED] for solving my crystal structures and reviewing my manuscripts.

I would like to thank [REDACTED] for the XRD sample preparation and data collection and the analytical department of the chemistry institutes for the fast and accurate measurement of all mass spectra and elemental analyses.

I would like to thank [REDACTED] for the very competent assistance when I had a specific issue to resolve using NMR spectroscopy.

Special thanks to:

[REDACTED] for providing me with “good” music during lab work, especially the widely known pirate metal won over my heart quickly. I want to thank him for sharing a beer or two every now and then and especially for introducing me to the dark side of the Force. Furthermore, for being a valuable member of the fabled KCT triumvirate.

[REDACTED] for being always straightforward and providing me with countless stories about the Bundeswehr. He represents the other crucial member of the KCT triumvirate and together with Oliver Back, I want to thank you guys for the splendid companionship during the KCT meetings and the everyday lab life.

[REDACTED] for being always helpful and trying to optimise the working conditions for everybody.

[REDACTED] for trying to make the world a better place. My profound respect for being so consequent.

[REDACTED] alias TomTom alias TCI-Thomas alias Lügen-Thomas alias Tdog for enduring my daily quips with a charming smile and for walking the mile down to the bus stop.

██████████ for delivering the hard-hitting truth, especially in the morning.

██████████ for filling up my inbox with funny “pöbel” mails about the laboratory conditions.

██████████ for convincing me that “magic” is real, even in the dangerous streets of Mainz-Gonsenheim.

██████████ for being a bottomless pit of knowledge and for always giving competent advice.

██████████ ██████████ and ██████████ for countless funny conversations that helped me not to go insane and to survive everyday life.

██████████ and ██████████ for following the “golden” path. It is my pleasure, to leave my golden legacy to two such competent and ambitious colleagues.

██████████ and ██████████ for introducing me to the porphyrin lifestyle.

██████████ for testing my knowledge with millions of tiny questions.

my research students for their support regarding the synthesis and characterisation of my precious porphyrins.

I would like to thank all current and former members of the ██████████ group. It was a pleasure to work with you and to solve the everyday problems. The cohesion and the atmosphere within the group is unique. I wish you all the best!

Special thanks go to my parents ██████████ and ██████████, my sister ██████████, my grandmother ██████████ and my brother-in-law ██████████ for the endless love and support. You will always be in my heart.

Finally, I would like to thank my second half ██████████ with all my heart for her love. Thank you for giving me the most wonderful years and the most beautiful life.

8 Curriculum Vitae

Sebastian Preiß



PERSÖNLICHES

	Geb. 01.03.1984 In Wuppertal
	Goldenluftgasse 11 55116 Mainz
	s_preiss@hotmail.de
	+49 151 75041234
	xing.com/profile/ Sebastian_Preiss6

SPRACHEN

Deutsch – Muttersprache
 Englisch – verhandlungssicher
 Französisch – Grundkenntnisse

KENNTNISSE

EDV

MS Excel	●●●●●
MS Powerpoint	●●●●●
MS Word	●●●●●
Chemdraw	●●●●●
Origin	●●●●●
MestreNova	●●●●●
ORCA	●●●●●
Chemcraft	●●●●●

Spektroskopie

^1H / ^{13}C / ^{31}P NMR	●●●●●
UV-Vis / Emission	●●●●●
IR / Raman	●●●●●
EPR	●●●●●

WISSENSCHAFTLICHE AUSBILDUNG

PROMOTION

Johannes Gutenberg-Universität, Mainz, [REDACTED] 11/2013 – 02/2019

Projekt: „Gold-Porphyrine als Akzeptoren bei photoinduzierten Elektronentransferprozessen“

- Gezielte Planung und Synthese künstlicher Photosynthese-Systeme zur Untersuchung von Elektronentransferprozessen
- Spezifische Kenntnisse in der organischen Synthese
- Elektrochemische und spektroskopische Charakterisierung
- Betreuung von Bacheloranden/Masteranden im Bereich der anorganischen und organischen Synthese und Anleitung zur selbstständigen und zielgerichteten Arbeitsweise

Nachhilfelehrer Chemie, Physik 06/2012 – 11/2013

DIPLOMARBEIT

Max-Planck-Institut für Polymerforschung, Mainz, [REDACTED] 06/2011 – 05/2012

Projekt: „Monomere Bausteine zur Synthese von zickzack-Graphennanostreifen“

- Monomersynthese und vollständige Charakterisierung
- Aufbau eines Referenzsystems zur Untersuchung der chemischen und physikalischen Eigenschaften von Graphennanostreifen, Stichwort: organische Halbleiter

STUDIUM CHEMIE

Johannes Gutenberg-Universität, Mainz 10/2004 – 05/2011

Studium der Chemie mit Schwerpunkten:

- Makromolekulare Chemie
- Bioanorganische Chemie

Abschluss Vordiplom 10/2007

Nachhilfelehrer Chemie, Physik 01/2004 – 09/2004

AUSLANDSERFAHRUNG

AUSLANDSSEMESTER - DAAD

University of Toronto, Toronto – Kanada, [REDACTED] 07/2008 – 03/2009

Projekt: „Synthese von Latexfilmen mittels Emulsionspolymerisation zur Untersuchung der Polymer Diffusion“

- Einbau von Donor/Akzeptor Co-Monomeren
- Untersuchung der Polymer Diffusion via Förster-Resonanzenergietransfer (FRET)

AUSZEICHNUNGEN

BESTER VORTRAG**03/2017**13. Koordinationschemietreffen,
Potsdam**BESTES POSTER****09/2016**18. Tagung der Wöhler-Vereinigung,
Berlin**BESTES POSTER****03/2015**11. Koordinationschemietreffen,
Paderborn**DAAD STIPENDIUM****07/2008 – 03/2009**

INTERESSEN

Segeln
Ski fahren
Tennis

BUNDESWEHR

- **FALLSCHIRMJÄGERBATALLION 263**

*Zweibrücken***04/2003 – 12/2003**

SCHULISCHE AUSBILDUNG

- **GYMNASIUM**

*Burggymnasium, Kaiserslautern***09/1994 – 03/2003**

PUBLIKATIONEN

- **NATURE CHEMISTRY**

S. Preiß, C. Förster, S. Otto, M. Bauer, P. Müller, D. Hinderberger, H. H. Haeri, L. Carella, K. Heinze, *Nat. Chem.* 2017, 9, 1249-1255.

„Structure and reactivity of a mononuclear gold(II) complex”

[DOI: 10.1038/NCHEM.2836]

Pressemitteilungen:

- uni-mainz.de/presse/aktuell/2351_ENG_HTML.php
- onlinelibrary.wiley.com/doi/full/10.1002/nadc.20184071717

- **CHEMICAL SCIENCE**

S. Preiß, J. Melomedov, A. Wünsche von Leupoldt, K. Heinze, *Chem. Sci.* 2016, 7, 596-610.

„Gold(III) tetraarylporphyrin amino acid derivatives: ligand or metal centred redox chemistry?”

[DOI: 10.1039/c5sc03429a]

- **JOURNAL OF MATERIALS CHEMISTRY B**

R. Ragg, A. M. Schilmann, K. Korschelt, C. Wieseotte, M. Kluncker, M. Viel, L. Völker, S. Preiß, J. Herzberger, H. Frey K. Heinze, P. Blümler, M. N. Tahir, F. Natalio, W. Tremel, *J. Mater. Chem. B* 2016, 4, 7423-7428.

„Intrinsic superoxide dismutase activity of MnO nanoparticles enhances magnetic resonance imaging contrast”

[DOI: 10.1039/C6TB02078J]

- **CHEMISTRY - A EUROPEAN JOURNAL**

S. Preiß, A. Pöpcke, L. Burkhardt, L. Großmann, S. Lochbrunner, M. Bauer, T. Opatz, K. Heinze, *Chem. Eur. J.* 2019, accepted.

„Gold(II) porphyrins in photoinduced electron transfer reactions”

[DOI: 10.1002/chem.201900050]

8.1 List of Publications

S. Preiß, J. Melomedov, A. Wünsche von Leupoldt, K. Heinze, Gold(III) tetraarylporphyrin amino acid derivatives: ligand or metal centred redox chemistry. *Chem. Sci.* **2016**, *7*, 596–610.

R. Ragg, A. M. Schilman, K. Korschelt, C. Wieseotte, M. Kluncker, M. Viel, L. Völker, **S. Preiß**, J. Herzberger, H. Frey, K. Heinze, P. Blümli, M. N. Tahir, F. Natalio, W. Tremel, Intrinsic superoxide dismutase activity of MnO nanoparticles enhances magnetic resonance imaging contrast. *J. Mater. Chem. B* **2016**, *4*, 7423–7428.

S. Preiß, C. Förster, S. Otto, M. Bauer, P. Müller, D. Hinderberger, H. H. Haeri, L. Carella, K. Heinze, Structure and reactivity of a mononuclear gold(II) complex. *Nat. Chem.* **2017**, *9*, 1249–1255.

S. Preiß, A. Pöpcke, L. Burkhardt, L. Großmann, S. Lochbrunner, M. Bauer, T. Opatz, K. Heinze, Gold(II) Porphyrins in Photoinduced Electron Transfer Reactions. *Chem. Eur. J.* **2019**, accepted.

8.2 Conference Contributions

- 03/2015 **11. Koordinationschemie-Tagung**, Paderborn, Germany
Poster presentation
„Gold(III) porphyrin amino acid derivatives as one-electron acceptors“
Best poster award
- 03/2016 **12. Koordinationschemie-Tagung**, Kiel, Germany
Poster presentation
„Gold(III) tetraarylporphyrin amino acid derivatives: ligand or metal centred redox chemistry?“
- 09/2016 **18. Wöhler-Tagung**, Berlin, Germany
Poster presentation
„Mononuclear Au^{II} trapped in a square: a missing link between Au^I and Au^{III}“
Best poster award
- 03/2017 **13. Koordinationschemie-Tagung**, Potsdam, Germany
Oral presentation
„Mononuclear Au^{II} trapped in a square: a missing link between Au^I and Au^{III}“
Best oral presentation award